UNIVERSITY OF CALIFORNIA

Los Angeles

Multimedia Environmental Distribution of Nanomaterials

A dissertation submitted in partial satisfaction of the

requirements for the degree Doctor of Philosophy

in Chemical Engineering

by

Haoyang Haven Liu

2015

ABSTRACT OF THE DISSERTATION

Multimedia Environmental Distribution of Nanomaterials

by

Haoyang Haven Liu

Doctor of Philosophy in Chemical Engineering

University of California, Los Angeles, 2015

Professor Yoram Cohen, Chair

Engineered nanomaterials (ENMs), which may be released to the environment due to human-related activities, can move across environmental phase boundaries and be found in most media. Given the rapid development and growing applications of nanotechnology, there is concern and thus the need to assess the potential environmental impact associated with ENMs. Accordingly, a modeling platform was developed to enable evaluation of the dynamic multimedia environmental distribution of ENMs (MendNano) and the range of potential exposure concentrations of ENMs.

The MendNano was based on a dynamic multimedia compartmental modeling approach that was guided by detailed analysis of the agglomeration of ENMs, life-cycle analysis based estimates of their potential release to the environment, and incorporation of mechanistic sub-

models of various intermedia transport processes. Model simulations for various environmental scenarios indicated that ENM accumulation in the sediment increased significantly with increased ENMs attachment to suspended solids in water. Atmospheric dry and wet depositions can be important pathways for ENMs input to the terrestrial environment in the absence of direct and distributed ENM release to soil. Increased ENM concentration in water due to atmospheric deposition (wet and dry) is expected as direct ENM release to water diminishes. However, for soluble ENMs dissolution can be the dominant pathway for suspended ENM removal from water even compared to advective transport. For example, simulations for Los Angeles showed that dry deposition, rain scavenging, and wind dilution can remove 90% of ENMs from the atmospheric airshed in ~100-230 days, ~2-6 hrs, and ~0.5-2 days, respectively. For the evaluated ENMs (metal, metal oxides, carbon nanotubes (CNT), nanoclays), mass accumulation in the multimedia environment was mostly in the soil and sediment. Additionally, simulation results for TiO_2 in Los Angeles demonstrates that the ENM concentrations in air and water increases rapidly to reach steady state, in 72 hrs and 8 days after the start of source release, respectively. After termination of source release, ENM concentrations would decrease by 90% in ~1 and ~4 days. In contrast, steady state for ENM concentrations in soil would not be expected to occur until after about 10 years. MendNano was further integrated with a sub-model of lifecycle environmental assessment for the release of ENMs (LearNano). Estimation of the releases of various ENMs and their environmental distributions in various regions in the U.S. and countries throughout the world revealed that the exposure concentrations for most ENMs (e.g., metal, metal oxides and carbon nanotubes) are expected to be in the range of 0.0003 – 30 ng m^{-3} (air), 0.006 – 150 ng L^{-1} (water), 0.01 – 40 μg kg^{-1} (soil), and 0.005 – 100 mg kg^{-1} (sediment).

It is important to note that the environmental transport of ENMs is governed by particulate transport processes; and thus the transport rates of ENMs are dependent on their particle size distribution. Accordingly, a computational constant-number Direct Simulation Monte Carlo (DSMC) model was also developed to assess the ENM agglomeration in aqueous systems, by solving the Smoluchowski coagulation equation coupled with particle-particle interaction energies provided by the classical Derjaguin-Landau-Verwey-Overbeek (DLVO) theory and non-DLVO hydration repulsion interaction energy. Prediction of ENM agglomerate PSDs demonstrated excellent agreement with experimental measurements for TiO_2, CeO_2, α-Fe_2O_3, SiO_2, and C_{60} ENMs over a wide range suspension conditions. Simulations also demonstrated, in quantitative agreement with DLS measurements, that nanoparticle agglomerate size increased both with ionic strength (IS) and as the solution pH approached the isoelectric point (IEP). Additionally, evaluation of experimental DLS measurements for TiO_2, CeO_2, SiO_2, and α-Fe_2O_3 (hematite) at high IS (up to 900 mM) or low |ζ-potential| ($\geqslant$1.35 mV) revealed that non-DLVO hydration repulsion energy can be above electrostatic repulsion energy such that the increased overall repulsion energy (contributed by hydration repulsion energy) can significantly lower the agglomerate diameter relative to the classical DLVO prediction. The classical DLVO theory, which is reasonably applicable for agglomeration of NPs of high |ζ-potential| (~>35 mV) in suspensions of low IS (~<1 mM), can overpredict agglomerate sizes by up to a factor of 5 at high IS (~>1 mM) or low |ζ-potential| (~< 40 mV) conditions.

In summary, the MendNano-LearNano integrated modeling platform was implemented as a web-based software application that enables rapid “what-if?” scenario analysis, in order to assess the response of environmental system to various scenarios of ENM releases, investigate the

impact of geographical and meteorological parameters on ENM distribution in the environment, compare the impact of ENM production and potential releases on different regions, as well as estimate source release rates based on monitored ENM concentrations. It is envisioned that the present integrated modeling platform can serve as a decision support tool to rapidly and critically assess the potential environmental implications of ENMs and thus ensure that nanotechnology is developed in a productive and environmentally responsible manner.

The dissertation of Haoyang Haven Liu is approved.

Panagiotis D. Christofides

Harold G. Monbouquette

Michael K. Stenstrom

Yoram Cohen, Committee Chair

University of California, Los Angeles

2014

To my wife Shirley.

Table of Contents

List of Tables

List of Figures

Acknowledgements

I am most grateful for my advisor Dr. Yoram Cohen for his patience and inspiration during my pursuit of the degree. I am especially thankful for his persistent demand for achieving excellence. I also thank Dr. Cohen for his guidance and many long discussions throughout my research projects. I would like to also thank Dr. Robert Rallo for helpful discussions regarding high performance computing, and for advices on computational modeling techniques. I would like to thank my colleagues in Dr. Cohen's group for their help, support, and friendship, without whom I would not have succeeded. In particular, I thank Dr. Rong Liu for his expert assistance in numerical modeling and computation, as well as in statistical analyses. I would like to thank Sirikarn Surawanvijit for her help with reviewing my writings, collaboration in experimental work, and continued support and encouragement during the course of my graduate career. I also thank Dr. Muhammad Bilal for the opportunities to work together on many coding projects. Additionally, I thank the administrative staff of UCLA Chemical and Biomolecular Engineering department and UC CEIN, especially John Berger, Miguel Perez, Victoria Ybiernas, and David Avery, for their tremendous support, as well as funding from the National Science Foundation and the U.S. Environmental Protection Agency for making the research work possible.

I would like to thank my parents for their love and support throughout my life. Words can never be sufficient in conveying my gratitude toward them.

Finally, I thank my wife, Shirley, for her unwavering love and sacrifice.

Vita

2007	Bachelor of Science, Chemical Engineering Washington University in Saint Louis Saint Louis, Missouri
2008–2015	Research Assistant Department of Chemical and Biomolecular Engineering University of California, Los Angeles
2008–2014	Teaching Assistant Department of Chemical and Biomolecular Engineering University of California, Los Angeles

Publications

Liu, H. H.; Surawanvijit, S.; Rallo, R.; Orkoulas, G.; Cohen, Y., Analysis of Nanoparticle Agglomeration in Aqueous Suspensions via Constant-Number Monte Carlo Simulation. Environmental Science & Technology 2011, 45, 9284-9292.

Cohen, Y.; Rallo, R.; Liu, R.; **Liu, H. H.**, *In Silico* Analysis of Nanomaterials Hazard and Risk. Accounts of Chemical Research 2013, 46, 802-812.

Surawanvijit, S.; **Liu, H. H.**; Kim, M.; Cohen, Y., Removal of Metal Oxide Nanoparticles From Aqueous Suspensions. Separation Science and Technology 2013. 2014, 49, 161-170.

Liu, H. H.; Cohen, Y., Multimedia Environmental Distribution of Engineered nanomaterials. Environmental Science & Technology. 2014, 48, 3281-3292.

Liu, H. H.; Lanphere, J.; Walker, S.; Cohen, Y., Effect of Hydration Repulsion on Nanoparticle Agglomeration Evaluated via a Constant Number Monte Carlo Simulation. Nanotechnology. 2015, 26(4).

Liu, H. H.; Bilal, M.; Lazareva, A.; Keller, A.; Cohen, Y., Simulation Tool for Assessing the Releases and Multimedia Environmental Distribution of Nanomaterials. *In Review*.

Liu, R., **Liu, H. H.**, Ji, Z., Xia, T., Nel, A., Cohen, Y., Potential Impact of ENMs Sedimentation on High Throughput Toxicity Screening of ENMs. *In preparation*.

Conference Proceedings

Liu, H. H.; Surawanvijit, S.; Orkoulas, G.; Cohen, Y., Modeling Aggregation and Size Distribution of Nanoparticles with Monte Carlo Simulation. NSTI - Nanotech 2010 Conference Proceeding. 2010, 3.

Liu, H. H.; Cohen, Y., Multimedia Environmental Distribution of Nanomaterials. NSTI - Nanotech 2012 Conference Proceeding. 2012, 3.

Liu, H. H.; Bilal, M., Lazareva, A., Keller, A., Cohen, Y., Regional multimedia distribution of nanomaterials and associated exposures: A software platform. 2014 IEEE International Conference on Bioinformatics and Biomedicine. 2014, 10.

Conference Presentations

"Computational Model of Nanoparticle Aggregation Kinetics", NSTI - Nanotech 2010 Conference, Jun. 24, 2010, Anaheim, CA

"Computational Model of Nanoparticle Aggregation Kinetics", International Conference on Environmental Implication of Nanotechnology 2010, May 12, 2010, Los Angeles, CA

"Computational Model of Nanoparticle Aggregation Kinetics", AIChE Annual Meeting, Nov. 10, 2010, Salt Lake City, UT.

"Modeling Agglomeration and Size Distribution of Nanoparticles in Aqueous Suspensions", AIChE Annual Meeting, Oct. 19, 2011, Minneapolis, MN.

"Multimedia Environmental Distribution of Nanomaterials", ACS National Meeting, Aug. 22, 2012, Philadelphia, PA

"Multimedia Environmental Distribution of Nanomaterials", AIChE Annual Meeting, Oct. 29, 2012, Pittsburgh, PA.

"Multimedia Environmental Distribution of Nanomaterials", AIChE Annual Meeting, Nov. 6, 2013, San Francisco, CA

"Probabilistic nanoinformatics modeling platform for assessing the potential environmental impact of engineered nanomaterials", ACS National Meeting, Aug. 11, 2014, San Francisco, CA

"Nanoinformatics platform for assessing the potential environmental distribution and exposure levels of engineered nanomaterials (ENMs)", ACS National Meeting, Aug. 11, 2014, San Francisco, CA

"Regional multimedia distribution of nanomaterials and associated exposures: A software platform", IEEE International Conference on Bioinformatics and Biomedicine, Nov. 2, 2014, Belfast, UK

"Probabilistic Assessment of Potential Environmental Impact of Engineered Nanomaterial", Nanoinformatics 2015 Workshop, Jan. 28, 2015, Arlington, VA

"Nanoinfo.org: An integrated Nanoinformatics Web Portal", Nanoinformatics 2015 Workshop, Jan. 28, 2015, Arlington, VA

Chapter 1. Introduction

1.1 Background

Nanomaterials are defined as a class of materials with at least one dimension at the nanoscale, in the range of 1 to 100 nm [1]. These nanomaterials are often considered to be the building block of nanotechnology [2]. While natural nanomaterials have existed for millenniums [3], engineered nanomaterials (ENMs) have gained popularity in the last decade and being increasingly utilized in many modern consumer and industrial products, primarily due to the ability to synthesis and control their unique nanoscale properties such as high surface area to mass ratio [2, 4-7]. ENMs are estimated to be components of more than 1,000 consumer and industrial products [8], with estimated annual global production exceeding 340,00 metric tons in 2016 [9]. TiO_2, SiO_2, and ZnO are among the most widely used ENMs incorporated into the consumer products [10]. For example, TiO_2 ENMs have been incorporated in coating, paints, and pigments, as well as cosmetic products, and SiO_2 have been used in energy and environment, electronic and optics, and automotive applications, [10] while ZnO ENMs are increasingly utilized for its antibacterial, antifungal, and UV blocking properties [11]. Other ENMs usages include consumer oriented products such as clothing, and sporting goods [2], as well as in industrial applications such as abrasive and other construction materials, see Table 1-1 [12-18].

Table 1-1: Usages of nanomaterials [9].

Application areas; Estimated production volume (per yr)[a]	**Nanomaterial Usage**	**Nanomaterials**
Catalysts; 43,200 ton yr^{-1}	Catalyst, diesel fuel additive, molecular sieves	Al_2O_3, CeO_2, CuO, Fe_2O_3, SiO_2, ZnO
Composites and plastics; 27,000 ton yr^{-1}	Conductive polymer, sporting goods, caulks and sealants,	CNT, Nanoclays
Consumer Products (including textile, packaging); 10,800 ton yr^{-1}	Electronic textiles, anti-bacterial coating, packaging films, UV-protective textiles, oxygen barrier	Ag, CNT, Nanoclays, SiO_2
Electronics and optics; 56,700 ton yr^{-1}	Dielectrics, IR imaging, optoelectronics, semiconductors, electromagnetic shielding, microwave antennas, Li ion batteries, touchscreen displays	Al_2O_3, CNT, CeO_2, CuO, Fe_2O_3, Ag, SiO_2, ZnO
Energy and the environment (including filtration); 37,800 ton yr^{-1}	Fuel cells, rocket propellant, heavy metal contaminants removal, thermal insulator, infrared absorbent, air purification, water treatment	Al_2O_3, CNT, CeO_2, CuO, Fe_2O_3, Ag, SiO_2, ZnO
Medical and cosmetics; 32,400 ton yr^{-1}	Cosmetic filter, medical implants, drug delivery, anti-microbial/biotic/fungal agents, biosensor, MRI, sunscreen, toothpaste	Al_2O_3, CeO_2, CuO, Fe_2O_3, Nanoclays, Ag, TiO_2, ZnO
Paints, pigments, coatings; 40,500 ton yr^{-1}	UV filter, printing ink, paints, anti-corrosion coating, anti-bacterial coating, conductive coating, flame retardant	Al_2O_3, CNT, CeO_2, CuO, Fe_2O_3, Nanoclays, Ag, SiO_2, TiO_2, ZnO
Other (including aerospace and sensors); 21,600 ton yr^{-1}	Microscope probe tip, gas leak detector, oxygen sensor	CNT, CuO, Fe_2O_3, Nanoclays, SiO_2

[a] Estimated production volume as of 2011;

Given the rapid growth of the nanotechnology market, there is growing concern that ENMs could be released to the environment [19]. ENMs that may be released to the environment (e.g., air emissions, direct discharge to surface water) are likely to move across environmental boundaries and thus will be found in most media [20]. While the potential environmental and health risks of ENMs are still being investigated [7], preliminary *in vivo* and *in vitro* studies have revealed that various organisms exhibit toxic responses when exposed to these ENMs [5]. For

example, high throughput screening (HTS) assays have demonstrated sub-lethal cellular inflammatory responses as a result of metal and metal oxide nanoparticles (e.g. Al_2O_3, Ag, Au, SiO_2), as well as lethal genotoxic responses as result of ZnO and Pt nanoparticles [21]. Animal studies have revealed that inhalation exposure to ENMs can lead to pneumonia, fibrosis, granuloma formation, alveolar proteinosis, and pleural injury [22]. In addition to respiratory effects, ENMs have been reported able to access the central nervous system and ganglia via translocation along axons and dendrites of neurons [23]. C_{60} fullerenes were found to be highly toxic to *E. coli* [24] and *B. subtilis* [25]. Additionally, it has also been argued that ENMs may have detrimental effects on ecosystems via their interactions with existing environmental contaminants [26]. An example of the above interaction is the "Trojan Horse" effects, wherein compounds that might not normally enter a cell are internalized when associated with ENMs [27]. Also, Hg adsorbed onto ENMs could become bioavailable and thus result in toxicity risk if introduced into natural systems [28]. Thus, there is an increased public concern regarding the potential adverse impacts of exposure to ENMs that may take place in the workplace, during product use and disposal, and in the environment [2, 7, 14, 29-34].

In order to interpret the toxicity of ENMs in the context of their environmental and health risks, it is crucial to assess the potential exposure levels to ENMs in the various environment media (e.g. air, water, soil, sediment) [34]. Field monitoring of the concentrations of ENMs would clearly be valuable for assessing the environmental multimedia distribution of ENMs. However, current technology for environmental detection and measurements of ENMs is still in the developing stage [35-38]. Preliminary environmental monitoring of ENM reported concentration levels of $\sigma(10^0)\ \mu g\ L^{-1}$ in surface water (for TiO_2 in UK) [39], and $\sigma(10^{-1})\ \mu g\ m^{-3}$ in the atmosphere (for fullerene in the Mediterranean Sea) [40]. Additionally,

even with the availability of advanced monitoring methods, deployment of a multimedia monitoring strategy would be a daunting and costly endeavor that may be impractical for the increasingly large number of ENMs. In this regard, estimation methods based on life-cycle assessment (LCA) can inform decision makers as to potential environmental releases of ENMs during manufacturing, use and product disposal [10, 19, 41-43]. In order to assess the likely ENM release rates to various environmental compartments, life cycle inventory assessment (LCIA) based approaches have been utilized to track the mass of ENM throughout its life cycle from production, through use, to final disposal and release to the environment, based on ENM production rates and heuristic quantification of the fraction of mass transferred between compartments (environmental or technical) [10, 42]. Although there have been attempts to estimate ENM media concentrations based on the above (also known as material flow analysis), such estimates are not based on fundamental multimedia fate and transport (F&T) analysis; thus, one is not assured of overall mass balance consistency and adherence to constraints that may be imposed by intermedia transport mechanisms.

Multimedia F&T models have been developed to assess the potential impact of chemical pollutants. Such models have relied on mathematical constructs to describe the entry, movement, and distribution of chemicals within the environment [32], in order to estimate their media concentrations and mass distributions. Multimedia analysis is typically a tiered process, which ranges from use of simple models consisting of well-mixed environmental compartments linked by intermedia transport processes [44] (first tier), to complex single medium models at various levels of spatial resolution of predicted contaminant distribution, coupled (where feasible) with field monitoring [44]. First tier screening-level multimedia analysis [32] has been utilized for order-of-magnitude (or better) analysis of exposure concentrations and mass distribution of

chemical pollutants in specific regions [45-48]. When warranted, higher tier models can be used for site-specific exposure analyses, but often at the expense of significant parameter inputs that are typically required (e.g., source emissions rates, local geography and meteorology) for spatial models [32, 48]. However, the multimedia compartment models for chemical contaminants are not directly applicable to ENMs. Unlike gaseous and dissolved chemical pollutants, for which interphase mass transport rates are governed by chemical potential (fugacity) driving forces that are constrained by thermodynamic equilibrium [44], the transport behavior of ENMs is governed by physical transport processes of particulate matter. Fundamentally, transport properties of particles are governed by their particle size distribution (PSD) [49]. For example, mass diffusivity, sedimentation velocity, deposition velocity, and attachment efficiency of nanoparticles onto solid and biological surfaces are significantly influenced by their size [50-53]. Thus, the environmental transport and fate of ENMs [6, 54] as well as their behavior at the bio–nano interface [2, 6, 55] are affected by their physicochemical properties [2] with the particle size being a major factor [5, 54]. For example, there is a growing interest and effort in the toxicology community to determine whether *in vitro* toxicity induced by ENMs should be attributed to settled ENM or the conventional metric of administered concentration [56-59]. Since settling velocity of a particle is a function of its size, quantifying the size distribution of ENMs is clearly desirable in order to understand the *in vitro* toxicity mechanism.

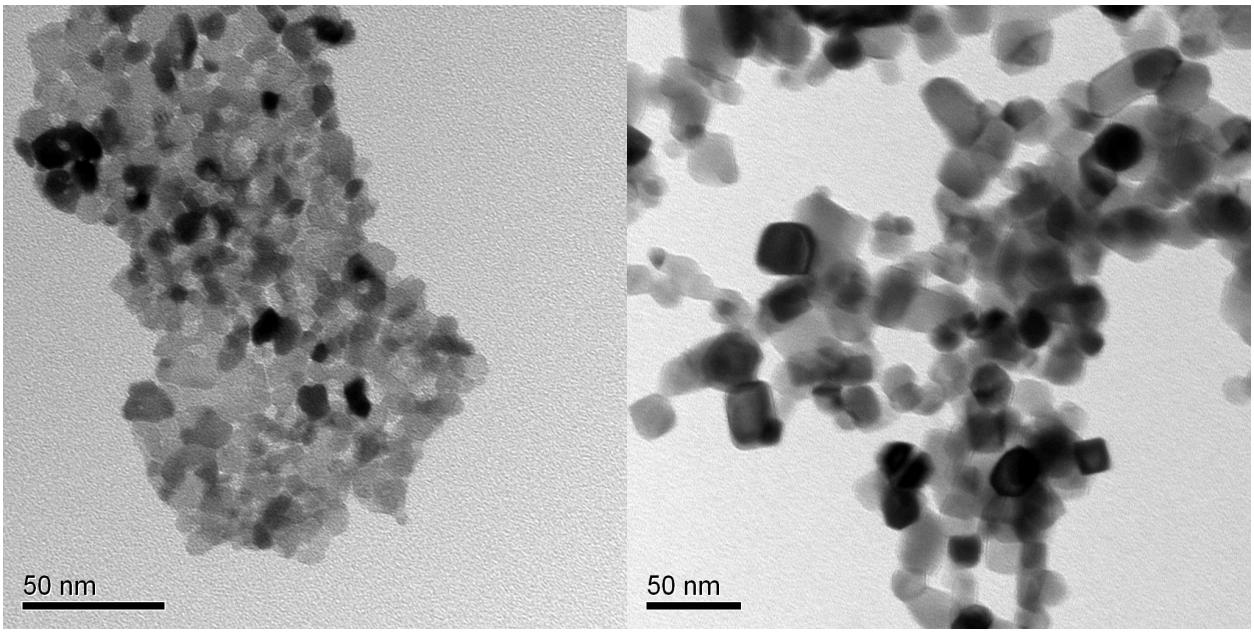

Figure 1-1. Sample transmission electron microscopy (TEM) images of (left) CeO_2 and (right) TiO_2 nanoparticles used in the experimental portion of the present study. The primary sizes of the nanoparticles were: 21 nm (TiO_2) and 15 nm (CeO_2). Samples for TEM (TEM, JEOL 1200 EX, accelerating voltage 80 kV) imaging were prepared by placing a drop of the aqueous nanoparticle suspension on a carbon coated TEM grid, and allowing the water to evaporate. [60]

As has been shown in numerous studies, ENMs generally do not exist as segregated primary nanoparticles [54, 60-66]. This is particularly the case in aqueous systems under environmental conditions where the ionic strength of natural water sources is sufficiently high, thus ENMs are expected to form agglomerates with diameters exceeding $10^2 – 10^3$ nm (Figure 1-1) [61-63, 65]. In recent years, efforts to quantify the agglomeration state of ENMs in aqueous systems have intensified [54, 61, 62, 64, 67-69]. However, comprehensive experimental mapping of ENMs agglomeration for the large number of present and anticipated emerging nanoparticles, over wide ranges of possible environmental water chemistries and nanoparticle properties, is a daunting and possibly impractical task. Thus, there has been a growing interest to explore various approaches

[61, 68, 70, 71] to better understand and generalize the agglomeration behavior of NP in aqueous suspensions. The majority of studies on the environmental or toxic impact of NP have focused on qualitative interpretation of observed agglomeration behavior of nanoparticles via the classical Derjaguin–Landau–Verwey–Overbeek (DLVO) theory [60-62, 64] and its various extensions (e.g., incorporating steric, geometric, hydrodynamic, hydration, and magnetic interaction energies) [72-76]. However, quantitative predictive models for ENM agglomeration state have not been reported.

1.2 Problem Statement

Given the rapid development of nanotechnology, it is critical that this technology growth is accomplished in an environmentally compatible manner, whereby the potential environmental impacts of ENM are properly assessed. In order to facilitate ENM environmental impact assessment, it is imperative to quantify the potential environmental concentrations of ENM under realistic regional and ENM release scenarios. In order to understand the fate and transport behavior of ENMs in the environment, it is necessary to evaluate the effect of various transport processes, as well as geographical and meteorological parameters on the environmental distribution of ENMs. Prediction of ENM environmental exposure levels requires information regarding release rates of ENM. Thus, assessing the effect of ENM release kinetics, which may be dependent on ENM applications, on its temporal environmental distribution is crucial. Since transport behavior of ENMs in the environment is governed by physical transport mechanism of particulates, evaluation of multimedia environmental distribution of ENMs requires mechanistic quantification of intermedia transport rates that are affected by their particle size distribution. Experimentally measurements of the particle size distributions of the growing number of ENMs in a wide range of environmental conditions are likely to be costly and impractical. Therefore,

numerical simulations of ENM agglomeration are a practical alternative for assessing the particle size distributions (PSDs). Lastly, in order to enable comparison of predictions of ENM PSDs with experimental dynamic light scattering measurements, which measures ENM sizes in suspension, the effect of gravitational settling on ENM particle size distribution must also be assessed. A flowchart of the dissertation work is presented in Figure 1-2. First, a computational model for predicting the ENM agglomerates size distribution was developed based on the classical DLVO theory and validated using experimental data. The model was then used to quantify the effect of ENM properties and suspension conditions on agglomeration behavior, as well as to evaluate impact of non-DLVO hydration repulsion energy on ENM agglomeration over a wide range of suspension conditions. Subsequently, potential environmental exposure levels of ENMs were predicted using a multimedia compartmental model (MendNano) validated using reported environmental monitoring data. Finally, the effects of various intermedia transport processes and release rates of various ENMs release scenarios on their environmental distribution were evaluated to assess the potential level of exposure concentrations.

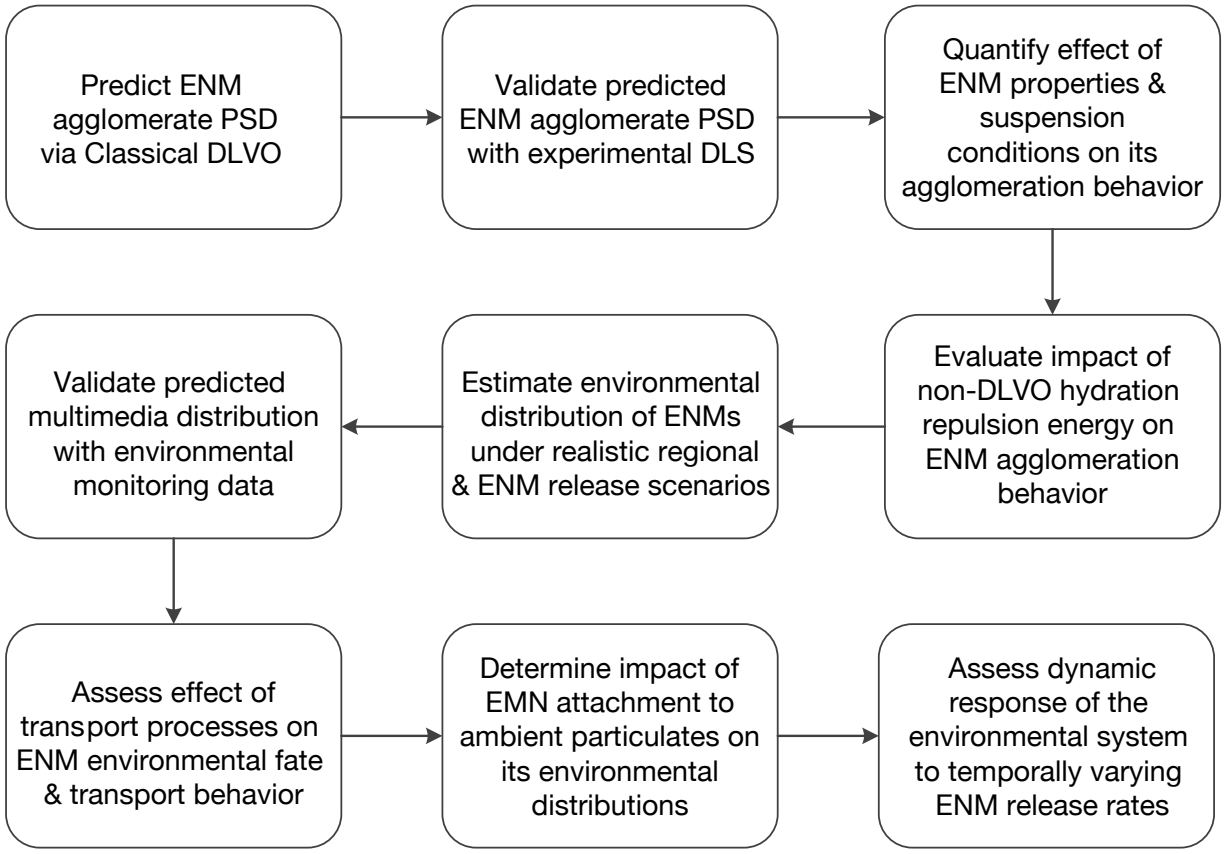

Figure 1-2. Research flowchart.

1.3 Research Objectives

The major goals of the dissertation were to: a) evaluate ENM agglomeration behavior in aqueous suspensions, and b) assess multimedia environmental distribution of ENMs. First, the agglomeration behavior of ENMs was investigated using the classical DLVO theory and its extensions. The accuracy of predicted ENM agglomerate size distribution was assessed via comparison with dynamic light scattering (DLS) measurements. Subsequently, the environmental distributions and exposure levels of ENMs were estimated based on fundamental modeling of mechanistic transport processes pertinent to ENMs, while accounting for their complete PSDs. The effect of intermedia transport processes, geographical and meteorological

parameters, ENM and ambient particulate properties, and source release scenarios on the fate and transport behavior of ENMs was also evaluated. The specific objectives of the research are listed below:

1. Evaluate ENM agglomeration in aqueous suspensions
    a. Demonstrate the applicability of classical DLVO theory in prediction of ENM agglomeration behavior,
    b. Analyze the importance of accounting for gravitational settling in enabling comparison between prediction of ENM agglomeration size distribution with experimental DLS measurements,
    c. Quantify the dependence of ENM agglomeration behavior on ENM properties and suspension conditions (e.g., primary size, Hamaker constant, ionic strength, ζ-potential),
    d. Evaluate the effect of non-DLVO hydration repulsion interaction energy on the predicted ENM agglomerate diameter,
    e. Estimate fraction of ENMs that may settle during *in vitro* toxicological experiments.
2. Assess multimedia environmental distribution of ENMs
    a. Predict environmental concentrations and mass distributions of ENMs under realistic regional and ENM release scenarios, considering the size distributions of ENMs and ambient particulate matter,
    b. Evaluate the importance of accounting for ENMs attachment to ambient particulates to environmental distribution of ENMs,

c. Investigate the effect of various transport processes on the temporal kinetics of ENMs environmental fate and transport behavior, and quantify the relative importance of the various transport processes,

d. Assess the dynamic response of the environmental system to temporally varying ENM release rates,

e. Demonstrate ranking of the potential environmental impact of ENMs based on exposure concentration and toxicity metrics.

1.4 Research Focus

The research objectives were accomplished through a combination of various numerical modeling approaches and experimental measurements. ENM agglomeration behavior was evaluated using a Monte Carlo simulation of particles in a box, which was validated using experimental dynamic light scattering (DLS) measurements. The dynamic environmental concentration and mass distribution of ENMs was assessed using a multimedia compartmental modeling platform, which incorporates mechanistic intermedia transport processes, while accounting for complete particle size distribution for the ENMs as well as ambient particulates.

The modeling approach for simulating ENM agglomeration is described in Chapter 3. A direct simulation Monte Carlo method was used to solve the Smoluchowski coagulation equation, in which the particle–particle interaction energy was quantified by the classical DLVO theory. The above model was validated using experimental DLS measurements of particle size distributions over a wide range of ENM types (i.e., metal oxide, carbonaceous) and aqueous suspension conditions (i.e., pH, ionic strength). The above approach was also used to evaluate the agglomeration behavior of ENMs as a function of various suspension conditions and material

properties. The agglomeration modeling approach described in Chapter 3 is expanded to include non-DLVO hydration repulsion interaction energy in Chapter 4. The hydration repulsion energy was quantified based on analysis of DLS measurements of particle size distribution in relation to the primary particle size. Using the extracted hydration repulsion energy parameters, the effect of hydration repulsion on ENMs agglomeration was evaluated over a wide range of suspension conditions and material properties, in order to quantify the impact of hydration repulsion on ENM agglomeration. As an illustration of the importance of ENM particle size distributions, a modeling approach is provided in Chapter 5 that quantifies the fraction of ENMs that may sedimented in *in vitro* toxicological studies. The modeling approach combines Brownian diffusion and Stokes' settling velocity, which was modified to account for the effective particle density and permeability within the ENM agglomerate. The modeling approach was validated using sedimentation experiments, where ENM suspension concentrations were obtained via ICP measurements.

Chapter 6 presents the modeling platform for assessing the dynamic multimedia environmental distribution of ENMs, which incorporates mechanistic intermedia transport processes, while accounting for complete PSD for the ENMs, as well as ambient particulates. The above modeling platform was validated using reported concentrations of semi-volatile organic compounds, which tend to attach to ambient particulates due to their low volatility and solubility [77-79]; thus, their transport behavior is that of particulate matter. Test cases of predicted environmental concentration of 10 ENM types in Los Angeles (using reported release rates), and evaluation of the impact of material properties (e.g., solubility) on the predicted ENM mass distribution are also presented in Chapter 6.

Chapter 7 describes an expansion of the multimedia modeling platform presented in Chapter 6, to incorporate a sub-model for estimating ENM release rates to the various environmental compartments, which is based on lifecycle inventory assessment approach. The software implementation of the integrated modeling platform as a web application, including accompanying parameter and scenario database is also described in Chapter 7, which also describes a number of typical use cases for the present modeling platform.

Chapter 2. Literature Review

2.1 ENM Environmental Impact Assessment Framework

ENMs may be released to the various environment media due to anthropogenic activities [19, 20, 80, 81], and can also cross media boundaries as a result of intermedia transport processes [82]. Thus, it is expected that ENMs may be found in most environmental media [20]. Consequently, there is an urgent need to assess the potential impact of ENMs in the multimedia environment [82]. Environmental impact (or risk) due to ENMs is only present if there is hazard due to ENMs at the environmentally expected concentrations. In other words, in the absence of either (or both) exposure or hazard to a given ENM, the environmental impact to such ENM is expected to be negligible. Accordingly, in order to assess the potential environmental impact and risk of ENMs, it is crucial to identify potential hazards due to the ENMs, as well as evaluate the expected environmental concentration and exposure levels of the ENMs [7, 82-84]. A recently proposed conceptual assessment framework for the environmental impact of ENMs [82] (Figure 2-1) recognizes the need to account for both potential hazards and exposure levels of ENMs in the environment. Another important element to impact assessment recognized in the above framework is the proper physicochemical characterization (e.g., size distribution, shape, composition, surface properties) for the ENMs of concern [82], which is the basis for evaluating the hazard and exposure levels of ENMs. For example, it is well known that particle size distributions (PSD) of ENMs (primary particles and agglomerates) are an important factor that affects the potential toxicity [6, 55, 84] and transport [6, 54] behaviors of ENMs. The above framework also acknowledges that while the experimentally measured ENM hazards and exposure levels may be desirable in some situations, such measurements may be impractical or

infeasible over a wide range of existing and future ENMs and environmental conditions, and cannot be used for predictive purposes. For example, reported environmental monitoring measurements of ENM exposure levels, as distinguished from the exposure levels of non-ENM form with the same chemical composition, are currently lacking due to the difficulty in the present instruments to differentiate between ENMs and non-ENM materials of same chemical composition (e.g., natural NM, bulk derived NM) [40, 85]. As a reasonable alternative, computational modeling approaches, based on established theories for transport of environmental contaminants, can be developed to complement experimental and monitoring techniques to predict the potential environmental concentration of ENMs in the environmental impact assessment.

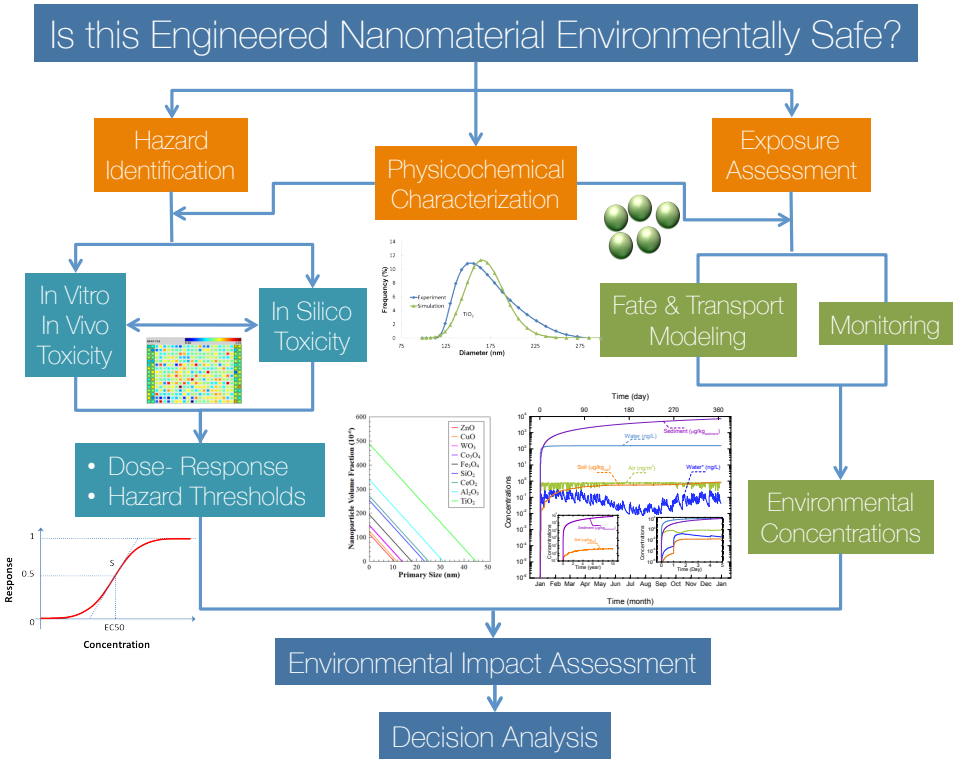

Figure 2-1. Illustration of conceptual environmental impact assessment framework. Adapted from [82].

2.2 Modeling Fate and Transport of Environmental Contaminants

It has been proposed that analysis of the multimedia environmental distribution and exposure concentrations of contaminants can be accomplished via a tiered approach [44]. A screening level assessment (tier-1 analysis) can be carried out based on multimedia compartmental models (MCMs) [44] to identify major exposure pathways and monitoring data gaps. In such analysis, the entry to the environment, movement, and distribution of contaminants in the environment are described by a set of mathematical expressions. Specifically, the MCMs requires mechanistic quantification of the intermedia transport rates (e.g., dry and wet deposition, sedimentation, dissolution) and rates of contaminant releases to the various environmental media. Typically, such a screening level analysis is expected to provide order of magnitude (or better) assessment. For example, the MCM approach was used in the Lake Michigan Mass Balance study [86] to determine the concentrations of PCBs, atrazine, *trans*-nonachlor, and mercury in air, water, and sediment and their effect on river organisms.

Screening level (i.e., first tier) multimedia compartmental models are intended to provide regional compartmental average concentrations, but do not provide detailed spatial description of concentration fields. However, spatial resolution may be increased by further divide the environmental media into subcompartments [32]. Higher tier analyses, which may include the use of detailed single medium models, can provide higher spatial resolution of predicted contaminant distribution for the studied region (in contrast to regional average ENM media concentrations). However, such an approach would require extensive site-specific geographical information and meteorological data for the target region (i.e., $\mathcal{O}(10^1) - \mathcal{O}(10^2)$ higher relative to the tier-1 approach [32]), and thus can be much more complex and computationally demanding.

2.2.1 Multimedia Models for Dissolved Chemicals

Computational methods for evaluating the distribution of chemical contaminants in the multimedia environments have been developed over the last few decades in support of environmental management and risk assessment (e.g., Mend-Tox [32, 33], CalTOX [87], TRIM.FaTE [88], SimpleBox [89]). In this regard, compartmental or "well-mixed" media models (i.e., with uniform concentration) [32] have been used extensively for environmental impact assessment [32]. In such models, a given compartment may consist of a number of well-mixed subcompartments, linked via intermedia transport processes that are governed by the thermodynamic partitioning between the adjoining media (Figure 2-2). For example, the dynamic chemical mass in a uniform compartment (e.g., air, water) may be expressed as [32]

$$\frac{d}{dt}[C_i V_i] = \sum_{k=1}^{N}\left(Q_{k,i}^{in} C_{k,i}^{in} - Q_i^{out} C_i\right) + \sum_{\substack{l=1 \\ i\neq l}}^{M}\sum_{j=1}^{P(l)} I_{i,l}^{j} - \sum_{\substack{l-1 \\ i\neq l}}^{M} K_{i,l} A_{i,l}\left(C_i - C_i H_{i,l}\right) + \zeta_i k_i^r C_i V_i + S_i; \qquad i = 1, \ldots, M \quad [2\text{-}1]$$

where V_i is the volume [m^3] of compartment *i*, and C_i [gmol m^{-3}] is the concentration of chemical in compartment *i*. The first term on the RHS is the advective flow transport, where Q [m^3 h^{-1}] is the convective flow rate in (with superscript *in*, from adjacent compartment *k*) or out (with superscript *out*) of compartment *i*. The second term on the RHS describes the intermedia transport (other than interfacial diffusion) between compartments *i* and *l*, where intermedia transport rate between compartments *i* and *l*, via transport process *j*, given by $I_{i,l}^{j}$ [gmol h^{-1}], is summed over all processes (P) from all compartments (M). The third term on the RHS represents

the interfacial diffusion between compartments i and l, where $K_{i,l}$ [m h^{-1}] is the overall mass transfer coefficient, $A_{i,l}$ [m^2] is the interfacial area, and $H_{i,l}$ is the dimensionless partition coefficient (e.g., Henry's Law constant). It is noted that although the driving forces for interphase transport is expressed in terms of chemical concentrations in the above expression, some models in the literature express the driving forces in terms of the chemical fugacity (or chemical potential), which may be useful for interpret the tendency for pollutants to accumulate in various compartment [32]. However, under environmental conditions, where contaminants concentrations are expected to be low, thus a linear concentration gradient driving force is typically considered as adequate [32]. The various reaction (and dissolution) processes are described by the fourth term on the RHS, where ζ_i is the reaction coefficient, signify chemical producing (+1) or consuming (-1) reactions, and k_i^r [h^{-1}] is the first order reaction rate constant. Lastly, the $S_{i,k}$ [g s^{-1}] is the source release rate. Although the above model is designed for chemical contaminants, the association (e.g., adsorption) of chemical to ambient particulate is tracked in order to account for intermedia transport processes of particulate-bound chemicals (e.g., dry/wet deposition of particulate-bound chemicals, sedimentation). It is noted that while the intermedia transport processes of particulates are unconstrained by thermodynamic equilibrium, the association of chemical to ambient particulates is a function of the solubility and volatility of the chemical.

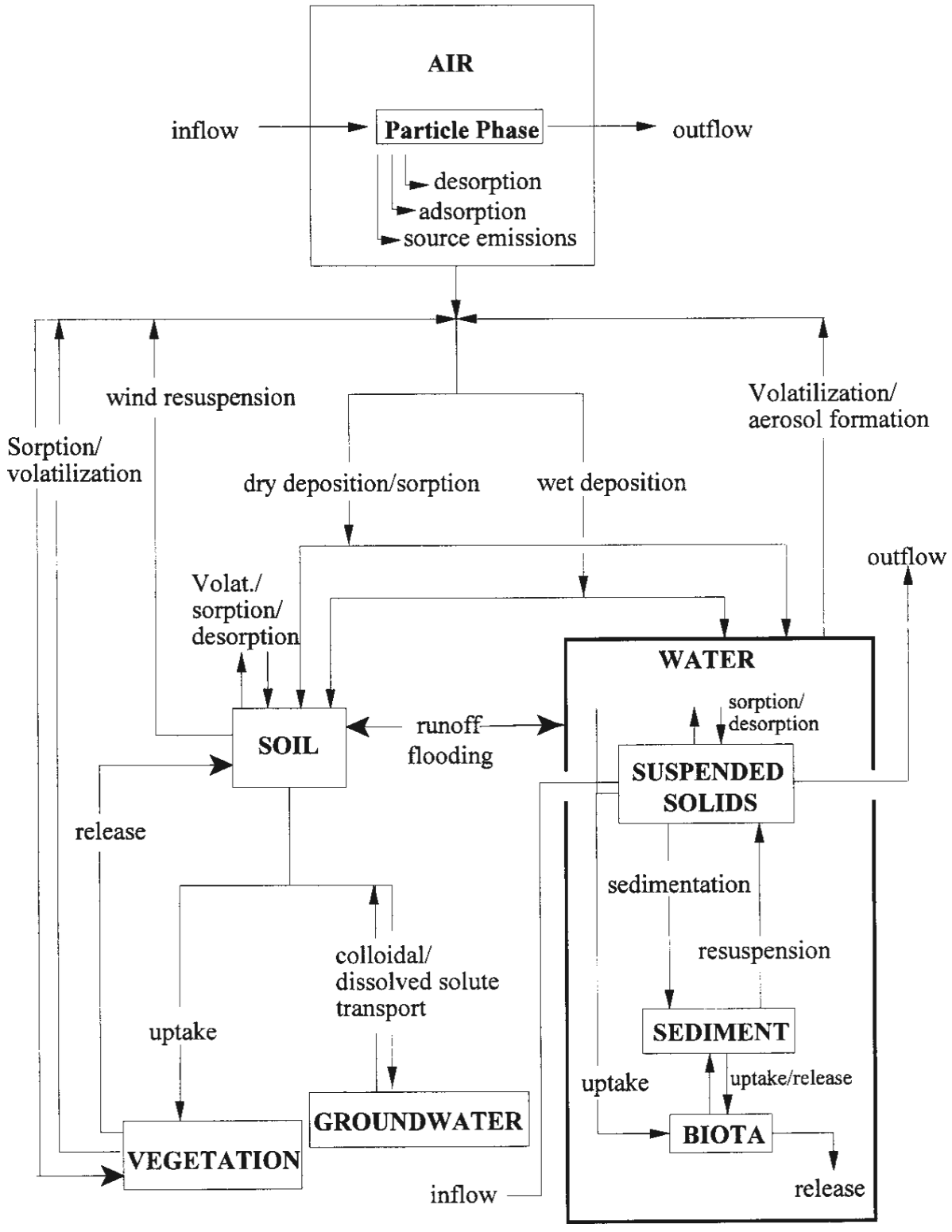

Figure 2-2. Intermedia transport processes in multimedia system. Adapted from [32].

In multimedia fate and transport models for chemical contaminants, reasonable simplifications were made in order to balance the model generality and temporal/spatial resolution with parameter data requirement and computational burden. For example, in SimpleBox [89], temporal variation of source release rates and meteorological parameters, which may significantly affect the environmental concentration of chemicals, are often neglected to reduce needed number of input parameters [32, 44]. Additionally, the complete particle size distributions of ambient particles are typically not considered in determining the intermedia transport rate of particulate-bound chemicals [32]. Further, some multimedia models require manual specification of intermedia transport flux or associated parameters (e.g., dry deposition velocity) [32], as opposed to computing these at run time, in order to lessen the computational burden during model execution.

2.2.2 ENM Transport Processes

Fate and transport models developed for chemical contaminants are not directly applicable to assess the multimedia distribution of ENMs. This is because the transport rate of gaseous and dissolved chemicals are governed by their chemical potential driving forces that are constrained by thermodynamic equilibrium, whereas that of ENMs are governed by the transport mechanisms of particulate matters. Environmental transport processes for ENMs can be organized into 3 categories: 1) intermedia transport processes (between adjoining environmental compartments), 2) Reaction/dissolution, and 3) advective transport (Figure 2-3). A summary of the various transport processes is provided below.

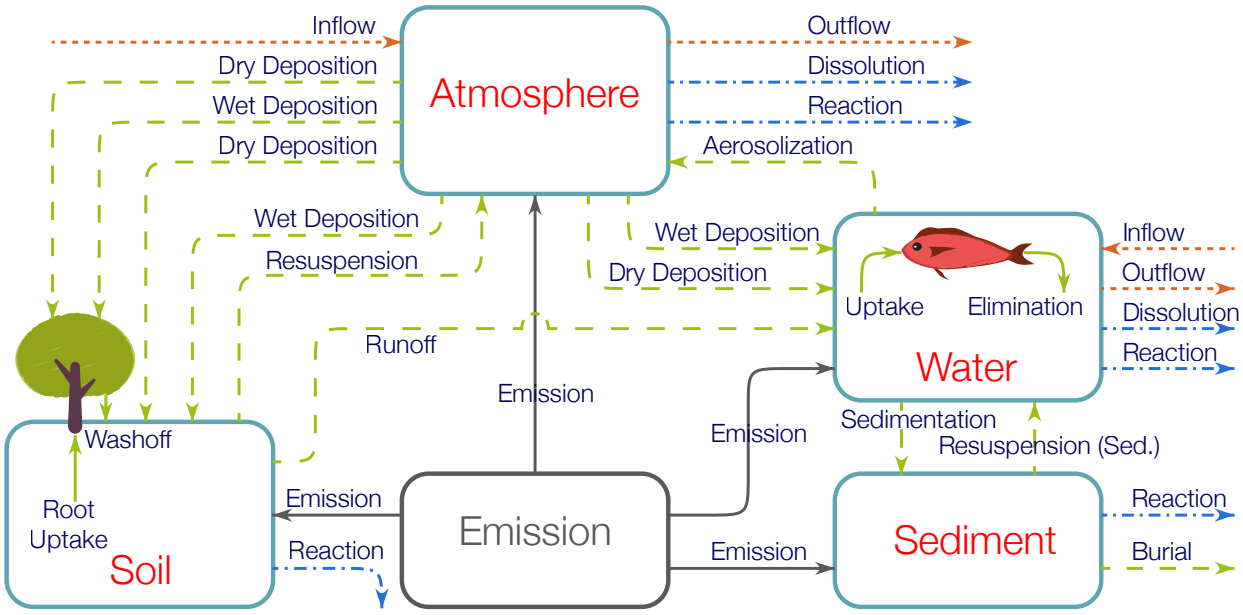

Figure 2-3. Transport processes for ENMs. Green lines represent intermedia transport processes, blue lines represent reactions (including dissolution) within the compartments that eliminate the ENM from particle phase, orange lines represent advection (i.e., transport of ENM via flow of air and water) into and out of the given compartment, and gray lines represent emissions (i.e., ENM releases to the compartments).

Table 2-1: Summary of transport and transformation processes

Transport pathways	Transport rates expression	Key parameters and sub-model source
Air → Surface water		
Dry Deposition	$v_{w,k}^{dry} \cdot C_{a,k} \cdot A_{a,w}$	Dry deposition velocity (water) ($v_{w,k}^{dry}$) – Giorgi (1986)[90], Williams (1982)[91]
Wet Deposition	$\Lambda_k \cdot J_{rain} \cdot C_{a,k} \cdot A_{a,w}$	Scavenging ratio (Λ_k) – Tsai, et al. (1991)[92]
Surface Water → Air		
Aerosolization	$F^{aerosol} \cdot A_{a,w} \cdot C_{w,k}$	Volumetric flux of aerosolized water ($F^{aerosol}$) – O'Dowd and de Leeuw (2007)[93]
Air → Soil		
Dry Deposition	$v_{s,k}^{dry} \cdot C_{a,k} \cdot A_{a,s}$	Dry deposition velocity (soil) ($v_{s,k}^{dry}$) – Giorgi (1986) [90], Sehmel and Hodgson (1978)[94]
Wet Deposition	$\Lambda_k \cdot J_{rain} \cdot C_{a,k} \cdot A_{a,s}$	Scavenging ratio (Λ_k) – Tsai, et al. (1991) [92]
Soil → Air		
Wind Resuspension	$F^{resusp} \cdot A_{a,s} \cdot C_s$	Wind resuspension mass flux (F^{resusp}) – USDA (1961)*[95]*

Transport pathways	Transport rates expression	Key parameters and sub-model source
Soil → Surface Water		
Runoff	$F^{runoff} \cdot A_{a,s} \cdot C_s$	Soil runoff mass flux (F^{runoff}) – Renard, et al. (1997)[96], Wishmeier and Smith (1978)[97]
Air → Foliage		
Dry Deposition	$v_{f,k}^{dry} \cdot C_{a,k} \cdot A_{a,f}$	Dry deposition velocity (foliage) ($v_{f,k}^{dry}$) – Giorgi (1986)[90], Slinn (1982)*[98]*
Wet Deposition	$\Lambda_k \cdot J_{rain} \cdot C_{a,k} \cdot A_{a,f}$	Scavenging ratio (Λ_k) – Tsai, et al. (1991) [92]
Foliage → Soil		
Washoff	$F^{washoff} \cdot m_f / L$	Volumetric flux of washoff water from foliage ($F^{washoff}$) – Cohen and Cooter (2002)[32] Foliage holding capacity (L) – User input
Soil → Plant root		
Root Uptake	$k^{root} \cdot C_s \cdot A_r$	Root uptake rate constant (k^{root}) – User input
Water → Sediment		
Sedimentation	$v_k^{sed} \cdot C_{w,k} \cdot A_{w,sed}$	Setting velocity (v_k^{sed}) – Liu, et al. (2011)*[49]*

Transport pathways	Transport rates expression	Key parameters and sub-model source
Sediment → Water		
Sediment Resuspension	$F^{sed\ resusp} \cdot A_{w,sed} \cdot C_{sed}$	Sediment resuspension mass flux ($F^{sed\ resusp}$) – Luettich (1990)*[99]*, Grant and Madsen (1979)[100]
Water → Biota		
Biota Uptake	$k_{b,k}^{uptake} \cdot C_{w,k} \cdot m_b \cdot I_b$	Biota uptake rate constant ($k_{b,k}^{uptake}$) – User input Surface area per unit mass of biota (I_b) – User input
Biota → Water		
Biota Elimination	$k_e \cdot m_b / M_b$	ENM elimination rate constant (k_e) – User input
Sediment → Deep Sediment		
Sediment Burial	$v^{burial} \cdot m_{sed} / d_{sed}$	Sediment burial velocity (v^{burial}) – User input
Transformations		
Dissolution	$K_{w,k}^{diss}\left(C_w^{(s)} - C_w^{(diss)}\right)A_{T,k}$	Mass transfer coefficient for dissolution ($K_{w,k}^{diss}$) – Bird, et al. (2007)[101] ENM Solubility ($C_w^{(s)}$) – User input Concentration of (background) dissolved species ($C_w^{(diss)}$) – User input Surface area of ENM ($A_{T,k}$) – eq [2-16]
Reaction (1st Order)	$\zeta_i K_{i,k}^r C_{i,k} V_{i,k}$	Reaction rate constant ($K_{i,k}^r$) – User input

2.2.2.1 Intermedia Transport Processes

Dry deposition of nanomaterial onto terrestrial (e.g. soil, vegetative canopy) and aquatic surfaces is due to collection by surface by Brownian diffusion, impaction, and interception [90]. The intermedia transport rate due to dry deposition, $I_{a,j,k}^{dry}$ [g s^{-1}], is expressed as:

$$I_{a,j,k}^{dry} = v_{j,k}^{dry} \cdot C_{a,k} \cdot A_{a,j} \quad [2\text{-}2]$$

where $v_{j,k}^{dry}$ [m s^{-1}] is the dry deposition velocity of particles in size fraction *k* from the atmosphere (denoted by subscript *a*) to target compartment *j*. The dry deposition velocity is described by various models, depending on the target compartment (e.g. to water [90, 91], to soil [90, 94], to vegetative canopy [90, 98]). $C_{a,k}$ [g m^{-3}] is the atmospheric concentration of nanomaterial in size fraction *k*, and $A_{a,j}$ is the interfacial area between atmosphere and compartment *j*.

Wet deposition removes of particles from the atmosphere by falling rain, hail, and snow and subsequent deposition onto the ground below, its rate, $I_{a,j,k}^{wet}$, is given by [92]:

$$I_{a,j,k}^{wet} = \Lambda_k \cdot J_{rain} \cdot C_{a,k} \cdot A_{a,j} \quad [2\text{-}3]$$

where J_{rain} [m s^{-1}] is the rainfall intensity, and Λ_k is the dimensionless scavenging ratio for nanomaterial in size fraction *k*, representing the ratio of nanomaterial concentration in the raindrop at the ground level to that in the atmosphere [92].

Particles suspended in the water column can be transported into air via the process of aerosolization. Particles can be aerosolized at the water surface by bursting of bubbles [102, 103] that are formed by wave breaking as well as impinging precipitation (i.e. rain and snow) [102,

103]. As bubbles burst into small jet drops (~μm size [104]), and are ejected into the air, the particles contained within the drops become airborne [102, 103], where the rate of nanomaterial aerosolization, $I_{wa}^{aerosol}$, is expressed by:

$$I_{w,a,k}^{aerosol} = F^{aerosol} \cdot A_{a,w} \cdot C_{w,k} \quad [2\text{-}4]$$

where $F^{aerosol}$ [m s^{-1}] is the volumetric flux of water (injected into air) due to aerosolization[93], $A_{a,w}$ [m^2] is the interfacial area between the atmosphere and water, and $C_{w,k}$ is the nanomaterial concentration in size fraction *k* in the water.

Soil particles-bound nanomaterial are transported to the atmosphere during episodic wind induced resuspension of soil, and the average rate of wind resuspension of nanomaterial, $I_{s,a}^{resusp}$, can be quantified by:

$$I_{s,a}^{resusp} = F^{resusp} \cdot A_{a,s} \cdot C_s \quad [2\text{-}5]$$

where F^{resusp} [g m^{-2} s^{-1}] is the mass flux of soil loss due to wind resuspension, which can be obtained via the Wind Erosion Equation (WEQ) [95], $A_{a,s}$ [m^2] is the interfacial area between soil and the atmosphere, and C_s [$g_{ENM}\,kg^{-1}{}_{soil}$] is the nanomaterial concentration in the soil. It has been reported that the WEQ predictions of wind erosion for periods of a year or longer compare favorably with field measurements [105]. It is noted that a revised WEQ (or RWEQ) was proposed [106] as a potential improvement over the WEQ, particularly for assessing the impact of single wind resuspension events [105]. It is important to stress that required model input information by RWEQ is significantly higher than that which is needed by WEQ [105]. Moreover, predictions of wind resuspension with WEQ do not appear to present an inherent bias when compared to RWEQ predictions [107].

Runoff occurs during precipitation events after water infiltrates the soil column up to its holding capacity [108], after which excess water can flow to water bodies in the region under consideration. The rate of nanomaterial runoff (from soil to water), $I_{s,w}^{runoff}$, can be expressed as:

$$I_{s,w}^{runoff} = F^{runoff} \cdot A_{a,s} \cdot C_s \text{ , for } t_{rain} > t_{ponding} \quad [2\text{-}6]$$

where F^{runoff} [g m^{-2} s^{-1}] is the mass flux of soil loss due to runoff that can be estimated by the Universal Soil Loss Equation [96, 97], and the time-to-ponding, $t_{ponding}$ [s], is the time for the soil to reach its water holding capacity [108].

Nanomaterials (freely suspended and bound to ambient particulates) in water can deposit onto the sediment surface due to gravitational sedimentation, and the rate of nanomaterial sedimentation, $I_{w,sed,k}^{sed}$, can be estimated from:

$$I_{w,sed}^{sed} = v_k^{sed} \cdot C_{w,k} \cdot A_{w,sed} \quad [2\text{-}7]$$

where v_k^{sed} [m s^{-1}] is the Stokes' settling velocity that accounts for the porosity of the nanomaterial agglomerate [49], and $A_{w,sed}$ is the water-sediment interfacial area.

Similar to wind induced soil resuspension, sediment particles can be resuspended as the result of water current or wave action, and thereby transfer nanomaterial from the sediment to the water compartment. The rate of sediment nanomaterial resuspension, $I_{sed,w}^{sed\ resusp}$, is expressed as:

$$I_{sed,w}^{sed\ resusp} = F^{sed\ resusp} \cdot A_{w,sed} \cdot C_{sed} \quad [2\text{-}8]$$

where C_{sed} [g_{ENM} kg^{-1}_{sed}] is the nanomaterial concentration in the sediment, and $F^{sed\ resusp}$ [g m^{-2} s^{-1}] is the mass flux of sediment loss due to sediment resuspension [99]. When considering

sediment resuspension in natural water bodies, it is noted that wind-induced current and waves govern resuspension primarily in areas that are of depth that is at about 10 m or less [99, 109] ,and suitable modeling approach have been proposed for the above [99]. Resuspension rates of sediment from greater depths and where bottom current (not arising from waves or wind flow) is responsible for sediment resuspension can be estimated from different models (e.g., the approach of Grant and Madsen [100]).

ENMs associated with sediment particles can be transported to deeper sediment via sediment burial, and are thus removed from the surface sediment. Sediment burial typically accounts only a small fraction (3-13%) [38] of ENMs entering the sediment compartment. Mechanistic modeling such process requires solution of diffusion-convection equations for the different particle size range, and the complexity of such approach is disproportionally greater than the other components of the modeling framework. However, recent studies have utilized "burial velocity" to estimate the rate of sediment burial [38]. While such approach is a non-mechanistic approximation, it can be used to provide a first tier estimation of the contribution by sediment burial. Accordingly, the rate of sediment burial can be expressed by:

$$I_{sed}^{burial} = v^{burial} \cdot \frac{m_{sed}}{d_{sed}} \qquad [2\text{-}9]$$

where v^{burial} [m s^{-1}] is the sediment burial velocity, m_{sed} [g] is the total ENM mass in the sediment, and d_{sed} [m] is the sediment depth.

Washoff of nanomaterial from foliage can occur due to rainfall when foliage water retention capacity is exceeded. The rate for nanomaterial washoff from foliage to soil is:

$$I_{f,s}^{washoff} = F^{washoff} \cdot \frac{m_f}{L} \quad [2\text{-}10]$$

where $F^{washoff}$ [m s^{-1}] is the volumetric flux of the precipitated water transfer from foliage to soil [32]. m_f [g] is the mass of nanomaterial deposited onto the foliage surface, and L [m] is the foliage holding capacity of rain water that is a function of leaf structure and hydrophobicity [110].

It has been reported that ENM uptake by plant can also occur via the plant root [111-114]. Given the current absence of predictive mechanistic root uptake models [115], it may be sufficient, at the screening level, to approximate the root uptake rate (I_s^{root}) by a first order uptake process:

$$I_s^{root} = K_r^{uptake} \cdot C_s \cdot A_r \quad [2\text{-}11]$$

where K_r^{uptake} [m s^{-1}] is the root uptake rate constant that can be obtained from experimental root uptake data if available, C_s [$g_{ENM}\,kg^{-1}{}_s$] is ENM concentration in the soil, and A_r [m^2] is the surface area of the plant root, which in principle can be a function of time as the plant roots network evolves over time.

Finally, in the absence of specific mechanistic models of ENM uptake by biota, the rate of biota uptake of ENM ($I_{w,b,k}^{uptake}$) and elimination (I_b^{elim}) of nanomaterial can also be approximated by:

$$I_{w,b,k}^{uptake} = K_{b,k}^{uptake} \cdot C_{w,k} \cdot m_b \cdot a_b \quad [2\text{-}12]$$

$$I_b^{elim} = K_e \frac{m_b}{M_b} \quad [2\text{-}13]$$

where M_b [kg] is the total biota mass, $K_{b,k}^{uptake}$ [m s^{-1}] is the biota uptake rate constant, a_b [m^2 kg] is the surface area per unit mass of biota, K_e [s^{-1}] is the nanomaterial elimination rate constant, and m_b is the mass of nanomaterial in biota. In order to account for growth dilution, the biota growth may be approximated by [116]

$$M_b(t) = M_b^o + (M_b^\infty - M_b^o)\left(1 - e^{-\frac{t}{\tau}}\right) \quad [2\text{-}14]$$

where $M_b(t)$ is the mass of the biota organism at t, M_b^o is the initial biota mass, and M_b^∞ is the mass of fully grown biota, and τ is the growth time constant [s].

It is important to recognize that sub-models for assessing the uptake of ENMs by plant roots and by biota required parameters (i.e., in eq [2-11]-[2-14]) that need to be extracted from experimental kinetic uptake data, which are at present either unavailable or insufficient resolution to establish accurate kinetics. In the absence of information regarding uptake kinetics, one may estimate the range of magnitude of concentrations in biota, using bioconcentration factors (BCFs, Table 2-2), in conjunction with predicted ENM concentrations in water.

Table 2-2. Bioconcentration Factors of Select ENMs and Organisms.

Organism	ENM	Exposure Concentration (mg L^{-1})	Mean BCF (L kg^{-1})[a] [110]
Daphnid	TiO_2	0.1-01	81,283 (56,234-112,202)
	Ag	0.002-0.5	10,965 (1,445-45,709)
	nC_{60}	0.2-2	33,113 (15,136-95,499)
	CNT	0.004-0.4	50,119 (5,495-436,516)
Fish	TiO_2	0.5-10	214 (25-617)
	CeO_2	0.5-5	741 (204-2,692)
	Ag	0.01-0.1	19 (7-42)
	Au	0.0057	479

[a] Values in the parentheses represent range of reported BCFs.

2.2.2.2 Dissolution

For nanomaterials that exhibit significant aqueous solubility (e.g., ZnO, Ag, CuO, Fe_3O_4) [117-121], dissolution of ENMs solids can increase the rate of loss of suspended solids nanomaterial from the water column. The rate of ENM dissolution is governed by the concentration driving force for the dissolving species:

$$R_{w,k}^{diss} = -K_{w,k}^{diss}\left(C_w^{(s)} - C_w^{(diss)}\right)A_{T,k} \quad [2\text{-}15]$$

where $R_{w,k}^{diss}$ [g s^{-1}] is the rate of dissolution of ENM in water size fraction k, $A_{T,k}$ is the total surface area of the ENM in size fraction k, $C_w^{(diss)}$ [g m^{-3}] is the background concentration of the dissolved species, and $C_w^{(s)}$ [g m^{-3}] is the solubility of the dissolved species. It should be noted that (equilibrium) aqueous solubility of the dissolving species (of the ENM) can be affected by various factors such as pH, temperature, surface chemistry, and the presence of various ions. The rate of dissolution for an ENM in a given size fraction k is also governed by the mass transfer coefficient, $K_{w,k}^{diss}$ [m s^{-1}], that can be expressed in terms of the dimensionless Sherwood number

[101] (i.e., $Sh = \frac{K_{w,k}^{diss} d_k}{D}$, in which D [m^2 s^{-1}] is the mass diffusivity of the dissolved species and d_k [m] is average particle diameter for ENM in size fraction k). The Sherwood number, for a dissolving spherical particle, is given as $Sh = 2 + 0.60Re^{1/2}Sc^{1/3}$ [101], where the Schmidt number is defined as $Sc = \mu/\rho D$, μ is the fluid dynamic viscosity [kg m^{-1} s^{-1}] and ρ is the fluid density [kg m^{-3}]. The Reynolds number is defined as $Re = \rho v d_k/\mu$, where v is the absolute particle relative velocity [m s^{-1}]. It is noted that in the absence of forced convection, $Sh = 2$ [101], and thus $K_{w,k}^{diss} = 2D/d_k$. In calculating the rate of dissolution the surface area of particle size fraction k, $A_{T,k}$, in size fraction is determined as:

$$A_{T,k} = n_{\mathrm{k}} \cdot (\pi \cdot d_k^2) \qquad [2\text{-}16]$$

where the total number of particles in size fraction k, n_k, is given by:

$$n_{\mathrm{k}} = \frac{m_k}{\rho \left(\frac{d_k}{d_{pri}}\right)^{d_f} \left(\frac{\pi d_{pri}^3}{6}\right)} \qquad [2\text{-}17]$$

where d_{pri} is the primary ENM diameter [m], and d_f is the dimensionless fractal dimension of the ENM. Therefore, the rate of dissolution is expressed as:

$$\frac{dm_k}{dt} = \frac{12D}{\rho}\left(C_w^{(s)} - C_w^{(diss)}\right) m_k d_k \left(\left(\frac{d_k}{d_{pri}}\right)^{d_f} \left(d_{pri}^3\right)\right)^{-1} \qquad [2\text{-}18]$$

It is noted that, when the dissolved phase concentration of the ENM is significant (e.g., about 0.1% of the solubility limit or higher), it is necessary to track the mass concentration of the dissolved species by introducing the following mass balance equation for the dissolved species(s).

$$\frac{d\left(VC_w^{(diss)}\right)}{dt} = \left(Q^{in}C_w^{(diss),in} - Q^{out}C_w^{(diss)}\right) + \sum_k K_{w,k}^{diss}\left(C_w^{(s)} - C_w^{(diss)}\right)A_{T,k} \quad [2\text{-}19]$$

Additionally, given the low environmental concentrations of ENMs expected from anthropogenic sources [42], it is reasonable to expect that the concentration of ENM in its dissolved form would generally be significantly lower than the ENM solubility. In addition, the background (or ambient) concentration of dissolved ENM species (e.g., zinc ions in the case of ZnO) would be a few orders of magnitude lower than their solubility. Therefore, it is reasonable to assume that $C_w^{(s)} \gg C_w^{(diss)}$).

2.2.2.3 Advective Transport

The effective volumetric flow rates (Q_i^c, [m3 s^{-1}]) into and out of the atmosphere and water compartments is typically determined by the average time for a unit volume of air or water to reside in the simulated region, which is known as the convective residence time ($\tau_{i_{res}}$, [s]). Under ideal conditions (i.e., in a compartment with perfect mixing), the $\tau_{i_{res}}$ is calculated by $\tau_{i_{res}} = V_i/Q_i$, where V_i and Q_i are the volume [m^3] and actual inflow/outflow rate [m^3 s^{-1}] for the compartment. However, non-ideal mixing can occur due to flow recirculation or shortcuts in the region, which can increase or decrease the apparent residence time. In such a case a correction factor (f_c) can be used for the convective residence time ($\tau_{i_{res}}^c$): $\tau_{i_{res}}^c = f_c\tau_{i_{res}}$. The correction factor may be obtained from tracer studies or determined using various dispersion models. For example, the residence time in a flow system (e.g. river, airshed) can be approximated based on dispersion in plug flow reactor [122]:

$$f_c = \left(1 + \frac{2D}{uL}\right) \quad [2\text{-}20]$$

in which D is the eddy dispersion coefficient [$m^2\ s^{-1}$], u is the linear flow velocity [$m\ s^{-1}$], and L is the length of compartment in the direction of flow [m]. For atmospheric dispersion, the eddy dispersion coefficient can be expressed as [123]:

$$D = 0.1 \cdot H_{mix}^{\frac{3}{4}} (-\kappa \cdot L_{MO})^{-\frac{1}{3}} \cdot u^* \quad [2\text{-}21]$$

where H_{mix} is the mixing height [m] of the compartment, κ is the Von Kármán constant (0.4), L_{MO} is the Monin-Obukhov length [m], and u^* is the friction velocity [$m\ s^{-1}$]. For dispersion in river flow, the eddy dispersion coefficient is given by [124]:

$$D = 0.6 \cdot h \cdot u^* \quad [2\text{-}22]$$

where h is the depth of the river [m]. Friction velocity (u^*) [$m\ s^{-1}$] equals to $\sqrt{g \cdot h \cdot S}$ for a river with slope S [$m\ m^{-1}$], where g is the gravitational acceleration (9.8 $m\ s^{-2}$).

The convective residence time in a river estuary can be approximated by [125]:

$$\tau = \frac{(V + P)T}{(1 - b)P + RT} \quad [2\text{-}23]$$

where V is the low tide volume [m^3], P is the tidal prism [m^3], T is the tidal period [s], b is the return flow factor, and R is the discharge rate [$m^3\ s^{-1}$].

2.2.3 Multimedia Compartmental Models for ENMs

Although multimedia models that incorporate mechanistic description of intermedia transport processes and temporal dynamics of source release and meteorology are yet to emerge, some efforts are underway to provide preliminary information on the expected exposure levels of ENMs in the environment. An important factor in assessing the environmental multimedia distribution of ENMs is their release rates. In order to estimate ENMs release rates, life cycle inventory assessment (LCIA) based approaches have been developed to track the target ENM mass throughout its life cycle from production, through use, to final disposal and/or release to the environment. LCIA approaches are based on ENM production rates and empirical transfer coefficients that quantify the fraction of mass transferred between compartments (including technical compartments, such waste processing facilities, as well as environmental compartments, such as air, water and soil) [10, 41-43, 126]. Although there are uncertainties in LCIA approaches, primarily due to the inherent uncertainty in estimated ENM production rates and inter-compartmental transfer coefficients [10], such methods are considered at present as reasonably suitable for assessing potential ENM release rates [10, 42].

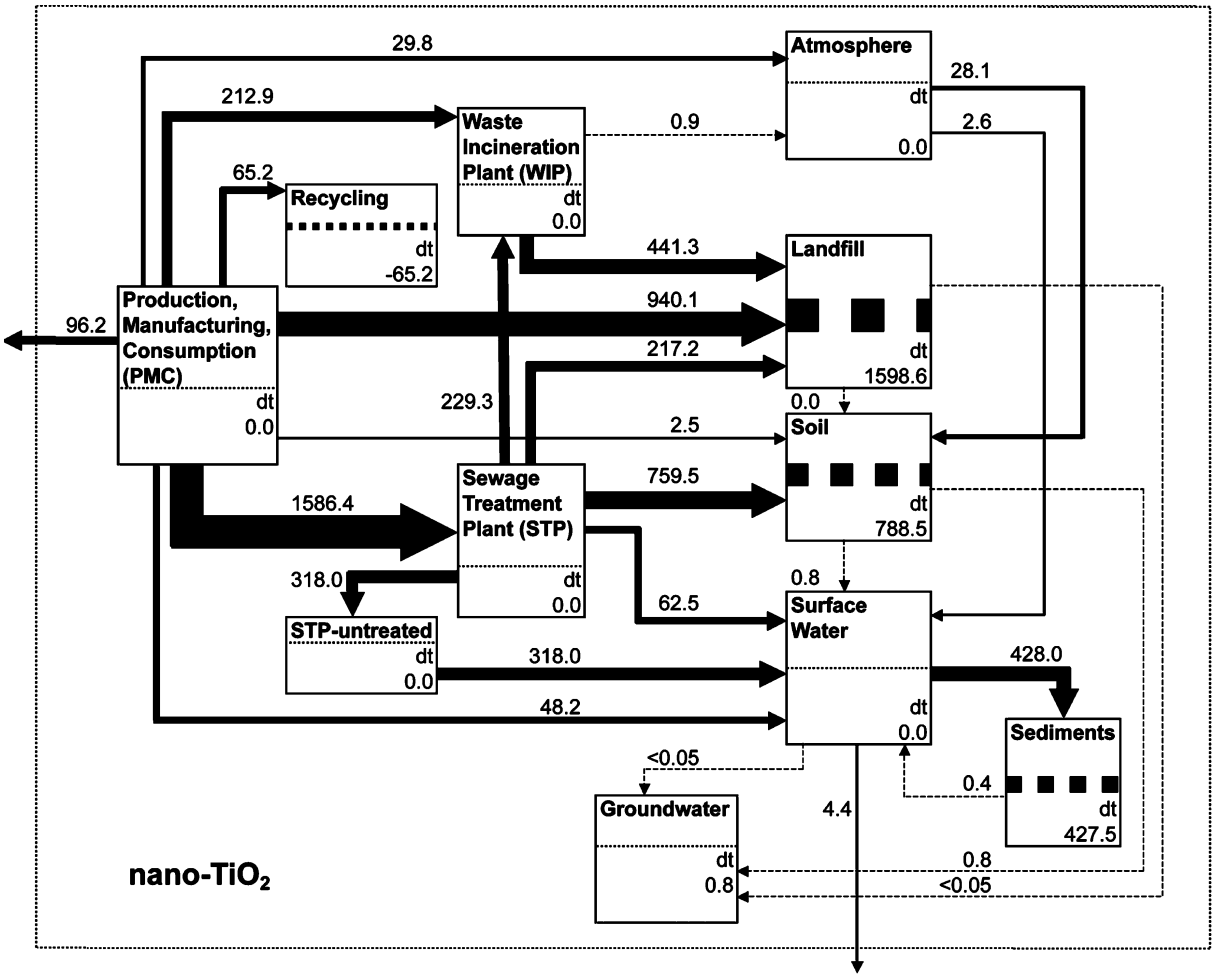

Figure 2-4. Simulation results of TiO_2 mass flow for the U.S., based on material flow analysis. The numerical values have units of metric ton yr^{-1}. The thickness of arrows and horizontal lines (within compartments) are proportional to the magnitude of mass transfer and accumulation rate. Adapted from [42].

There have also been attempts to extend LCIA based methods to predict ENMs media concentrations (e.g., via material flow analysis (MFA)) [41-43] relying on empirically estimated media transfer coefficients under laboratory (i.e., not environmental) conditions (Figure 2-4) [42]. However, instead of calculating transport "flow" rates of ENMs between environmental compartments based on mechanistic models, MFA estimates these values based on values

reported in literature, expert opinion, or other heuristics [42]. Additionally, the transport rates used in MFA were typically extracted from experimental studies conducted in laboratory conditions (i.e., not environmental conditions expected at the modeled region). For example, the fraction of ENMs deposited (via sedimentation in the water column) was determined in a number of studies [61, 127-130] in laboratory bench scale experiments, in which the water column depth is significantly lower compared to environmental systems. As a consequence, such studies report higher fraction of deposited ENMs than would be expected under environmental conditions. Thus, when the fraction of ENM deposited is applied directly to environmental systems, as is the case with MFA, the sedimentation rate is likely to be overestimated. Consequently, in the above MFA methodology, estimated transport rates may violate constraints imposed by intermedia transport mechanisms [131]. In fact, while comparisons with measured concentrations show that modeled concentrations are within an order of magnitude of the measurements for ENMs in technical compartments (e.g., sewerage treatment plant), MFA prediction of Ag concentration in water was a factor of 10–100 lower than reported in the literature [42]. Some MFA studies have estimated the uncertainty in predicted ENM media concentrations based on uncertainties in the input parameters (i.e., transport fraction). This is accomplished by executing the model many times with varying input parameters (within its uncertainty range) based on a Markov Chain Monte Carlo (MCMC) algorithm.

Subsequent to the modeling platform developed in the present dissertation (described in Chapter 6), an approximate treatment to estimate steady-state ENM multimedia concentrations was recently proposed in [132]. The proposed SimpleBox4nano approach [132], which is yet to be validated against environmentally measured concentrations of particulate matter, relied on a compartmental mass balance approach coupled with intermedia transport processes. In

SimpleBox4nano, the steady state ENM mass distribution in the various compartments are obtained via [132]

$$\boldsymbol{m} = -\mathbf{A}^{-1}\boldsymbol{e} \qquad [2\text{-}24]$$

where $\boldsymbol{m}$ [kg] is a vector of ENM mass in the various compartments, $\boldsymbol{e}$ [kg s^{-1}] is a vector of ENM source release rates, and $\mathbf{A}$ [s^{-1}] is a matrix of rate constants for ENM transport between compartments, removal of ENM by advection, reaction (including dissolution), as well as homogeneous and heterogeneous agglomeration.

SimpleBox4nano considers episodic events (e.g., rain scavenging) as continuous processes over the simulation period, with time invariant rate coefficients (i.e., elements of **A** in eq [2-24]) throughout the simulation period [132], while neglecting important intermedia transport processes (e.g., wind resuspension, aerosolization). Predicted concentration profiles, given the above assumption, neglects the temporal dynamics due to episodic intermedia transport processes such as rain scavenging [44], as well as intermedia transport rates that are dependent on temporally varying meteorological parameters (e.g., dry deposition velocity is a function of wind speed [90]).

Further, instead of accounting for the complete PSDs of ENMs and ambient particulates, SimpleBox4nano only considers the average particle size in each of three particle classes (primary ENM (with size of 10 nm), ENM attached to colloids, and ENM attached to larger particles), while assuming an arbitrary constant value of 0.1 for both aggregation and attachment efficiencies [132]. As a consequence the above approach did not account for the temporal dynamics of the multimedia distribution of ENMs that considers the strong dependence of intermedia transport on the complete PSDs [131].

A summary of prior work for modeling environmental ENM concentrations is provided in Table 2-3. Boxall et al. [20] used a simple compartmental model to estimate ENM concentrations in UK. Blaser et al. [133] and Praetorius et al. [38] used estimated steady-state concentrations of Ag and TiO_2, respectively, in the Rhine River, using a spatial compartmental model. Mueller et al. [19], Gottschalk, et al. [42], Gottschalk, et al. [41], and Sun et al. [126] used life cycle assessment based approach (referred in the literatures as substance flow analysis and material flow analysis) to estimate ENM concentrations at various regions. In all of the above prior modeling work, the intermedia transport rates were not determined mechanistically heuristically. After the publication of the work described in the present dissertation, Meesters et al. [132] estimated steady-state ENM concentrations using a compartmental model coupled with mechanistic transport processes.

Table 2-3. Relevant prior work for modeling environmental ENM concentrations

Citation	ENMs	Region; *Compartments*	Contributions	Major Shortcomings
Boxall, et al., (2007) [20]	metal, metal oxide, C_{60}, SiO_2	UK	- ENM average concentrations in water and soil were estimated using a simple compartmental model - Concentration for selected ENMs in air was estimated using empirical dispersion expressions	- Surface water depth was assumed to be 30 cm, without mixing - Intermedia transport rates were heuristically estimated - Advective transport, dissolution, and sedimentation of ENM were not considered - Effects of ambient particulates were not considered
Blaser, et al., (2008) [133]	Ag	Rhine River; *water, sediment*	- Ag concentration in Rhine River was estimated via a spatial compartmental model (with subcompartments), linked via empirical transport rates. - Ag source releases were modeled for cities near river, estimated based on per capita Ag release rates, in 3 release scenarios (minimum, intermediate, and high)	- Intermedia transport rates are not calculated based on mechanistic models - Dynamics of dissolution and reaction were not modeled - Validation via measured concentrations was with respect to Ag in other regions (i.e., with different source release and regional characteristics)
Mueller, et al., (2008) [19]	Ag, TiO_2, CNT	Switzerland; *air, soil, water*	- Substance flow analysis was used to model release and distribution of ENMs in 2 release scenarios ("realistic" release rates and high release rates) - Predicted environmental concentration (PEC) of TiO_2 in	- Sedimentation was not considered; thus ENM concentration in water may be overestimated - Assumed all particles in air are deposited (dry or wet) to soil and water, yet ENM concentration in air is non-zero. This indicates problem with

Citation	ENMs	Region; *Compartments*	Contributions	Major Shortcomings
			water may exceed the Predicted No Effect Concentration (PNEC)	mass balance calculation - Dissolution of Ag was not considered, thus Ag concentration in water may be overestimated - Effects of ambient particulates were not considered
Gottschalk, et al., (2009), Gottschalk, et al., (2010), Sun, et al., (2013) [41, 42, 126]	TiO_2, ZnO, Ag, CNT, C_{60}	Europe, U.S., Switzerland; *air, surface water, soil, sediment*	- Probabilistic material flow analysis was developed to estimate environmental concentrations of ENMs, and associated uncertainties - Predicted environmental concentration for all ENMs modeled were found to be below Predicted No Effect Concentration in environmental compartments	- Intermedia transport rates were obtained from empirical studies, where similarity in experimental condition and expected environmental condition was not ensured - Reported concentration does not correspond to mass accumulation in some cases, indicating problem with bass balance calculation (see §C.2) - Effects of ambient particulates were not considered
Gottschalk, et al, 2011 [134]	TiO_2, ZnO, Ag	Switzerland; *water*	- ENM concentrations in Swiss rivers was estimated using MFA coupled with high spatial resolution geographical description of the Swiss river system, while considering temporal variability of source releases - Spatial and temporal variability results in factor of 10-1000 variation in predicted environmental concentration	- Arbitrary transport scenarios were evaluated, where transformation and deposition of ENMs in river is either absent, or complete removal is assumed. - Effects of ambient particulates were not considered

Citation	ENMs	Region; *Compartments*	Contributions	Major Shortcomings
Praetorius, et al., 2012 [38]	TiO_2	Rhine River; *water, sediment*	- Expanding on Blaser et al [133], steady-state TiO_2 concentration in Rhine River was evaluated using spatial compartmental model (with subcompartments), linked via empirical transport rates. - ENMs in water was found to be rapidly attached to suspended solids - ENM in water column eventually accumulate in the sediment	Various fundamental and calculation errors exist in this work: - ENM mass input (release) rate at the domain inlet (i.e., first box) was inconsistent with that which was calculated based on reported source input rate for each bin size - Reported ENM number concentrations do not correspond to the reported mass concentration - The numerical solution provided was not at steady-state, as reported – i.e., mass inflow rate did not equal sum of mass outflow rate.
Meesters, et al., 2014 [132]	TiO_2	Switzerland; *air, water, soil*	- Steady state environmental TiO_2 concentration was evaluated using a simple box model, where intermedia transport rates were computed based on mechanistic models - Homogeneous and heterogeneous agglomeration was incorporated	- Temporal variation in release rates and meteorological parameters were not considered - Episodic events were modeled as time-continuous processes - The complete particle size distribution was not considered - Agglomerations were modeled using arbitrary attachment efficiencies, which were not calculated based on particle-particle interaction theories, - Model was not validated based on monitored environmental concentrations.

2.3 Agglomeration in Aqueous Suspension

Particle size distributions of ENMs have a marked impact on both their fate and transport in the environment, as well as their behavior at the bio–nano interface [6, 54, 55, 84]. Due to the impracticality to experimentally mapping of agglomeration state for the growing number of ENMs in all relevant environmental conditions, as well as the need to evaluate dynamic ENM agglomeration behavior as a function of their properties and water chemistry, various computational modeling approaches for the above purpose have been proposed, and are discussed below.

2.3.1 Quantitative Modeling Approach for Evaluating Particle Agglomeration

Quantitative simulation methods to describe agglomeration of nanoparticles can be implemented while accounting for particle–particle interactions [51, 135-138]. Indeed, molecular dynamics (MD) and Brownian dynamics (BD) simulations have been used to study details of nanoparticle agglomeration kinetics and agglomerate morphology [135-137]. In MD simulations, the motion of each individual atom or molecule (i.e., that of the particles, medium, dissolved ions, etc.) is determined based on Newton's second law, i.e., $F = m \cdot a$, where F [N] is the force acting on the atom/molecule, m [kg] is the mass of the atom/molecule, and a [m s^{-2}] is acceleration experienced by the atom/molecule. In contrast to MD simulations, where the medium is treated as consisting of discrete atoms/molecules, BD simulations consider the medium to be a stochastic continuum, but still calculate the motion (i.e., trajectory) of each particle due to the forces exerted on the particles by the medium. BD simulations of nanoparticle agglomeration in aqueous suspensions have demonstrated that the DLVO theory can provide a reasonable description of nanoparticle agglomeration [139]. It has been shown that that BD type

simulations can track the temporal change in nanoparticle suspension concentration due to sedimentation [140]. While MD and BD methods provide detailed information regarding particle agglomeration/disagglomeration via tracking of individual particles, they do so at the expense of significant computational resources. Thus, these methods place a limit on the practical number of particles that can be effectively modeled (typically $\sigma(10^0) - \sigma(10^2)$ with modern computers) [136, 139, 141-143].

Another popular approach is the direct simulation Monte Carlo (DSMC) method which treats the simulation domain as a particle ensemble where each agglomeration event has a probability of occurrence quantified via frequency functions calculated based on particle-particle interaction energies [136, 144, 145]. In contrast to BD and MD methods, trajectory of particles due to the forces exerted on the particles by the medium is not explicitly calculated in DSMC simulations. Instead, particle-particle interaction energies, which implicitly consider the effect of the medium and other dissolved species in the medium, are used to determine the agglomeration rate of particle pairs in the DSMC approach. Because of the above, the DSMC approach can simulate a much higher number of particles (up to $\sigma(10^5)$), compared to MD and BD methods, at the same level of computational resources. The DSMC simulation approach [69, 136, 138, 144-148] is a convenient method for describing particle agglomeration whereby the population balance equations (PBEs) are solved as described by the Smoluchowski coagulation theory [149, 150] or its extensions to include disagglomeration [146] nucleation and surface growth [136]. In the DSMC approach, advancement of time is treated in two ways: a) time-driven: the length of a time step is pre-specified, and all events (e.g., agglomeration) expected to occur during that time step are implemented, and b) event-driven: a specific event is chosen (e.g., based on agglomeration likelihood) and implemented, and the time expected for that event to occur, since

the previous event, is advanced [138, 148]. Additionally, since agglomeration events decrease particle number (i.e., number of primary particle and particle agglomerates), DSMC simulations can be categorized as either: a) constant volume, or b) constant number. In constant volume simulations, a fixed volume of the simulation domain is considered, and particle numbers can decrease (e.g., due to agglomeration) or increase (e.g., due to disagglomeration) [138, 148]. With such an approach, the simulation accuracy cannot be maintained if the particle number tracked in the simulation changes significantly, since the simulation accuracy varies with the number of particles, N, in the simulation domain with error $\propto 1/\sqrt{N}$ [147]. Alternatively, in constant-number MC simulations, the number of particles is held constant, and the size of simulation box is enlarged or reduced to account for changes in particle mass and number concentration, and thus ensure that the simulation accuracy is maintained.

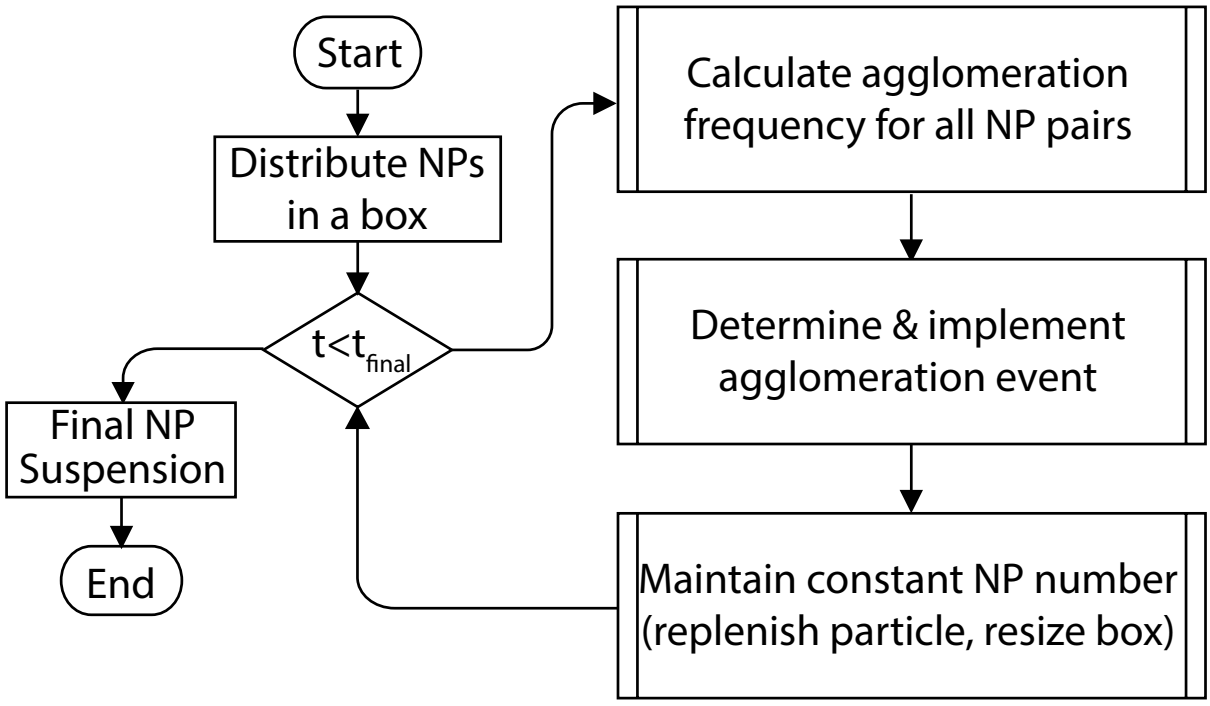

Figure 2-5. Illustration of simulation algorithm for event-driven constant-number DSMC simulation of particle agglomeration.

The typical simulation algorithm of an event-driven constant-number DSMC method is illustrated in Figure 2-5. The simulation is initiated with a set of randomly distributed particles (primary and agglomerates) in a simulation box. The pair-wise agglomeration frequencies between all particle pairs are then calculated. The agglomeration frequency is determined based on Brownian collision frequency and particle-particle interaction energies (e.g., as quantified by the classical DLVO theory [151] or suitable extensions [151]). A particle pair is selected for agglomeration, and the selection procedure is typically accomplished via an acceptance/rejection method, where a particle pair is selected at random, and is accepted for agglomeration if

$$R < \frac{k_{i,j}}{\max\{k_{i,j}\}} \qquad [2\text{-}25]$$

where R is a uniformly distributed random number between [0,1], and $k_{i,j}$ is the agglomeration frequency between particles i and j. A new particle pair is selected and tested if the previous pair was rejected, until the above condition is satisfied [147]. However, the acceptance/rejection method is not computationally efficient due to the large number of rejection. Alternatively, $k_{i,j} / \sum_i^N \sum_j^N k_{i,j}$ can be sequentially added, until the sum exceeds a uniformly distributed random number between [0,1] (Figure 2-6) [147]. Once the agglomeration pair is selected, the position and size of the resulting agglomerate is calculated, and the time required for this event is computed [147]. Subsequently, the constant particle number in the simulation box is maintained by either duplicating an existing particle from the simulation box, or by introducing a particle to the simulation box with its size sampled based on the distribution of the existing particles in the box. The above is repeated until the pre-specified final time is reached.

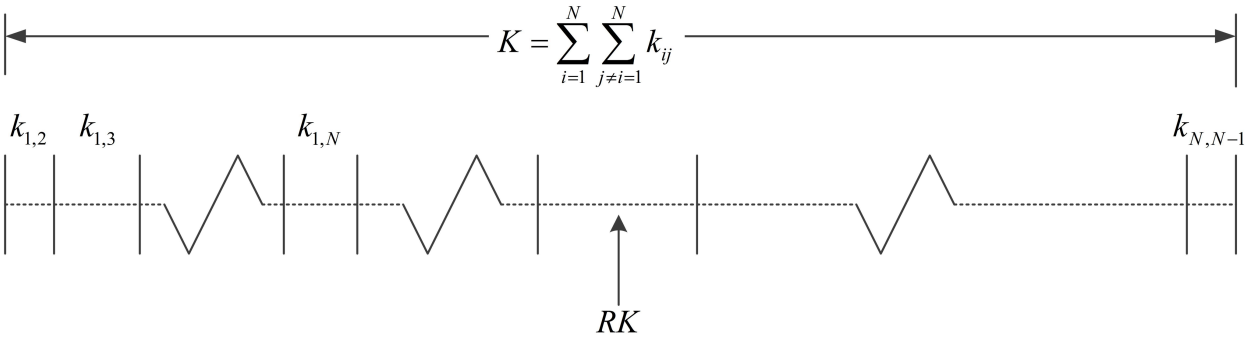

Figure 2-6. Illustration of the pair selection method. R is a uniformly distributed random number; and K is the sum of all possible aggregation frequency functions. Adapted from [49].

The BD and DSMC approaches typically utilize random sampling to represent stochastic mechanism of the agglomeration process. In contrast, in a recent study the ENM agglomeration process was modeled using an empirical analytical expression [152, 153]

$$r(t) = a \cdot \left\{1 + \frac{4k_B T n_0}{3\mu W} t\right\}^{1/d_F} \qquad [2\text{-}26]$$

where $r(t)$ is the agglomerate radius [nm] at time t (s), k_B [J K^{-1}] is the Boltzmann constant, T (K) is the absolute temperature, n_0 is the initial number concentration of primary particles, μ [Pa s] is the medium viscosity, W is the dimensionless stability ratio (i.e., inverse sticking coefficient), and d_F is the fractal dimension of the agglomerate. The inverse of stability ratio, also known as sticking coefficient, represents the probability of agglomeration given the occurrence of a collision event. Using the above approach, good agreement was reported between predicted and experimental DLS measurements of the average CeO_2 NP size at short agglomeration times (<90 min) times. However, it was noted in the above study [152] that the analytical expression (eq [2-26]), which invoked the approximation of a constant total particle-particle interaction energy, may only be valid when W does not change significantly as

agglomeration proceeds, such as in the case diffusion limited agglomeration [152], where essentially every particles collision results in agglomeration (i.e., $W \sim= 1$).

2.3.2 Limitations of Dynamic Light Scattering Measurements

In order to validate computational models for ENM agglomeration in aqueous suspensions, experimental techniques such as the dynamic light scattering (DLS) can be used to provide measurements of the particle size distributions. Although DLS is a rapid and convenient technique for particle size measurements, experimental variability can be encountered in reported DLS measurements of ENMs size [154, 155]. Such variability may be due to instrument limitations or use of DLS over a range of conditions where DLS has limited accuracy (i.e., high ionic strength). For example, in DLS one measures the time-dependent intensity of light scattered from particles in suspension in order to obtain intensity-weighted PSD (which is proportional to particle size to its sixth power). Therefore, even a few large particles (in a suspension with wide PSD) in the DLS crossbeam may significantly skew the measured hydrodynamic diameter toward larger particles [156-159]. DLS measurements also require sufficient concentration of particle suspensions (e.g., 1 mg L^{-1} for 100 nm polystyrene beads in 5 mW He-Ne laser DLS [160]) in order to ensure adequate photon detection [159], yet the suspensions should not be too concentrated to avoid multiple scattering [156]. Also, the appropriate concentration range is dependent on the material property (e.g., refractive index). For example, studies with polystyrene suspensions in water have shown that for He-Ne laser DLS (wavelength 633 nm), similar to that which was used in the present study, the best (i.e., lowest) minimum detection limit of 0.25 mg L^{-1} was reported for particle size of 280 nm [160]. Given the above, it is essential that the interpretation of DLS size measurements and comparison with model predictions consider factors such as sedimentation and suspension concentration.

Chapter 3. Analysis of Nanoparticle Agglomeration in Aqueous Suspensions via Constant- Number Monte Carlo Simulation

3.1 Introduction

Nanoparticles in aqueous suspensions, which are the focus of the present study, generally do not exist as stable suspensions of primary nanoparticles [54, 60-66]. This is particularly the case under environmental conditions where the ionic strength of natural water sources is sufficiently high and where adsorption of hydrophobic organics onto the nanoparticles [161, 162] can both promote rapid nanoparticle agglomeration [61-63, 65]. Indeed, the majority of studies on the environmental or toxic impact of NP have focused on qualitative interpretation of observed agglomeration behavior of nanoparticles via the classical DLVO theory [60-62, 64]. While there are factors (e.g., steric, geometric, hydrodynamic, hydration, magnetic) that can impact nanoparticle agglomeration that are not considered by the classical DLVO theory, it has been generally accepted, however, that the classical DLVO theory can provide a reasonable starting point for describing nanoparticle agglomeration in aquatic media under a wider range of environmental conditions [51, 54, 61, 70] and even for surface coated NP [70].

Quantitative simulation methods to describe agglomeration of nanoparticles can be implemented while accounting for particle–particle interactions [51, 135-138] as discussed in **§2.3.1**. The DSMC simulation approach [69, 136, 138, 144-148] is a particularly convenient method for describing particle agglomeration based on solving the population balance equations (PBEs) as described by the classical Smoluchowski coagulation equation [149, 150]. DSMC methods can be conveniently applied with moderate computational resources, in conjunction with the DLVO approach (or its extension) to quantitatively describe nanoparticle agglomeration

in aqueous suspensions. Additionally, most laboratory experiments dealing with the fate and transport [60, 63, 66, 68, 69] or toxicity [21, 55, 163] of nanoparticles in aqueous suspensions are typically conducted over extended periods of time (hours to days). Environmental time scales of interest are also of similar or longer magnitude. Therefore, model simulations need to consider the evolution of the particle size distribution (in aqueous suspension) to its steady-state (or stable) condition given the combined effects of agglomeration and sedimentation. Experimental studies have documented the sedimentation of agglomerated nanoparticles, based on UV–vis spectrometry [60, 63, 164, 165] and visual observations [166, 167] for measurement time scales on the order of hours [60, 63, 165] to days [164, 166, 167]. For example, studies with aqueous nanoparticle suspensions (~10–200 mg L^{-1}) have demonstrated significant concentration decrease (up to ~90% in some cases) for TiO_2 [60, 63] (21 nm) and iron-based [165] (50 nm) nanoparticles over a period of up to ~6 h.

In the present study, nanoparticle agglomeration was investigated within the context of the DLVO theory based on a computational constant-number DSMC approach [144, 145] of "particles in a box" considering Brownian motion and agglomerate sedimentation. In this approach, evolution of the particle size distribution is tracked to its steady state condition with model validation based on present experimental and literature reported dynamic light scattering (DLS) measurements of agglomerates sizes for TiO_2, CeO_2, and C_{60} nanoparticles in aqueous suspensions. A series of parametric simulations were also carried out in order to illustrate the influence of various model parameters (e.g., primary nanoparticle diameter, pH) on nanoparticle agglomeration behavior and thus suggest the potential use of the DSMC modeling approach and its potential extension (e.g., modified DLVO), as a useful tool for the study of nanoparticle agglomeration in aqueous suspensions.

3.2 Materials and Methods

The agglomerate size of nanoparticles in aqueous suspensions was evaluated via a constant-number DSMC approach [145] making use of the classical DLVO theory [150, 168] and accounting for agglomerate sedimentation. The modeling approach focused on enabling comparison of predicted and measured (via DLS) nanoparticle agglomerate sizes (in aqueous suspensions) over a period (24 h) typical in high throughput nanoparticle toxicity screening studies [60, 163].

3.2.1 Experimental

The agglomeration state of TiO_2 (Evonik Industries, Parsippany, NJ) and CeO_2 (Meliorum Technologies, Rochester, NY) nanoparticles (21 and 15 nm primary diameter, respectively) was quantified in aqueous suspensions over a pH range of 3–10 and ionic strength (IS) of 10^{-2}-1 mM. Aqueous suspensions of the commercial nanoparticles were prepared using 18 mΩ cm ultrapure D.I. water with pH adjustment using HCl, NaOH and $NaHCO_3$ and NaCl for ionic strength adjustment (ACS grade, Fisher Scientific, Waltham, MA).

Nanoparticle stock suspensions were first prepared at a concentration of 1000 mg L^{-1} by adding (over a ~5 s period) 10 mg of nanoparticles to a stirred 10 mL volume of water (in a 40 mL vial) previously adjusted to pH of 3 or 10; stirring was accomplished using a Teflon coated 15.8 mm (L) x 8 mm (D) magnetic stir bar and stirrer (Magnestir S8290, Scientific Products, McGaw Park, IL). The resulting suspension was immediately sonicated for 30 min at 23 ± 0.5 ^{o}C in a temperature controlled sonication bath (Bransonic 2510, Branson, Danbury, CT, 0.75 gallon, 130 W @ 40 Hz). The sonication bath temperature was maintained (±0.5 ^{o}C) by circulating water through a copper coil tube (0.635 cm inside diameter), submerged in the sonication bath, from a

constant temperature water circulator (NESLAB RTE-111, Thermo Scientific, Waltham, MA). Maintaining a constant temperature in the sonication bath was essential since, in the absence of temperature control, significant temperature rise was observed (up to ~20 °C over a 30 min period) as a consequence of the sonication process. It is noted that a sonication period longer than about 30 min did not improve nanoparticle dispersion. After sonication, 0.4 mL of the suspension was withdrawn and added to 19.6 mL of the same pH adjusted water in a 40 mL glass vial (resulting in 20 mg L^{-1} suspension) with additional 5 min sonication also at 23 ^{o}C. Nanoparticle suspensions at pH 8 were prepared by a similar procedure, but with 0.4 mL of a 1000 mg L^{-1} pH 10 stock suspension added to 19.6 mL of water at pH 8 and 2.4×10^{-4} M $NaHCO_3$. Immediately after 5 min sonication of the 20 mg L^{-1} (20 mL) suspension, 3 mL sample was transferred to a 4.5 mL cuvette for DLS analysis of the particle size distribution (PSD) measurements.

Particle size distributions for the different nanoparticle suspensions were quantified via DLS measurements (ZetaSizer Nano S90, Malvern Instruments, Worcestershire, UK) over a 24 h period. This DLS instrument utilizes a horizontal entry laser beam of ~40 μm in diameter, and detection angle of 90° with measurement reliability down to ~0.25 mg L^{-1}.[160] In the present study, the nanoparticle concentration decreased from its initial value of 20 mg L^{-1} to 1–17 mg L^{-1} (depending on the pH and ionic strength) and thus all DLS measurements were at concentrations above the minimum detection limit. The mass concentrations of the nanoparticles in the stock solutions and in samples used for DLS measurements were determined via elemental analysis of the suspension, by inductively coupled plasma mass spectrometry (ICP-MS) following a previously published protocol [169]. Finally, zeta potential for the nanoparticles was measured

(Brookhaven ZetaPALS, Brookhaven Instruments, Holtsville, NY) for the above nanoparticle suspensions at ionic strength of 0.1 mM.

3.2.2 Simulation Algorithm

A constant-number DSMC model of particles in a box [145] was developed to describe nanoparticle agglomeration in suspensions while accounting for agglomerate sedimentation. The accuracy of the DSMC simulations varies with the number of particles, N, in the simulation domain (i.e., box) with the error $\propto 1/\sqrt{N}$ [147]. Therefore, the number of particles was kept constant [145] and the nanoparticle mass concentration was preserved through simulation box expansion [144]. The simulation algorithm is described in Figure 3-1 with details of the working equations provided in Table 3-1.

The simulation approach (Figure 3-1) consists of initially distributing N NPs in a simulation box (Figure 3-2) of dimensions that are consistent with the desired nanoparticle mass concentration. The agglomeration frequencies for each of the N^2 pairs of particles are calculated following the approach of the Smoluchowski coagulation equation [168]. Subsequently, a pair of particles is selected for agglomeration based on a probability density function constructed from the agglomeration frequencies (Figure 2-6), and the size and position are then computed for the agglomerated particle pair. Only pairwise particle–particle interactions are considered [150, 168] and the agglomeration events are assumed to be irreversible [61, 161]. The time step for each consecutive agglomeration event is determined based on the inverse of agglomeration frequency (eq [3-10]) [138, 144, 145]. Each agglomeration event reduces the total number of particles (i.e., freely suspended primary particles and agglomerates) by one. Therefore, following each agglomeration event, a particle is added to the box in order to preserve the total number of

particles in the box. The added particle is selected by sampling from the particle size distribution of the particles in the simulation box. In order to preserve the mass concentration of nanoparticles, the simulation box is expanded to accommodate the added mass contributed by the above step of particle replenishment (Figure 3-2). Particles can exit the simulation box by gravitational settling and due to Brownian motion. Particles that have exited the bottom boundary of the simulation box are considered to be settled out of the box, and are replenished into the box by particles of size that is determined by random sampling of the PSD of previously settled particles. For particles that have exited the simulation box through the top or side boundaries (i.e., due to Brownian motion) a periodic boundary condition [170-172] is invoked to replace the particles, in which particles of the same size are reintroduced into the box from the opposite face (Figure 3-3).

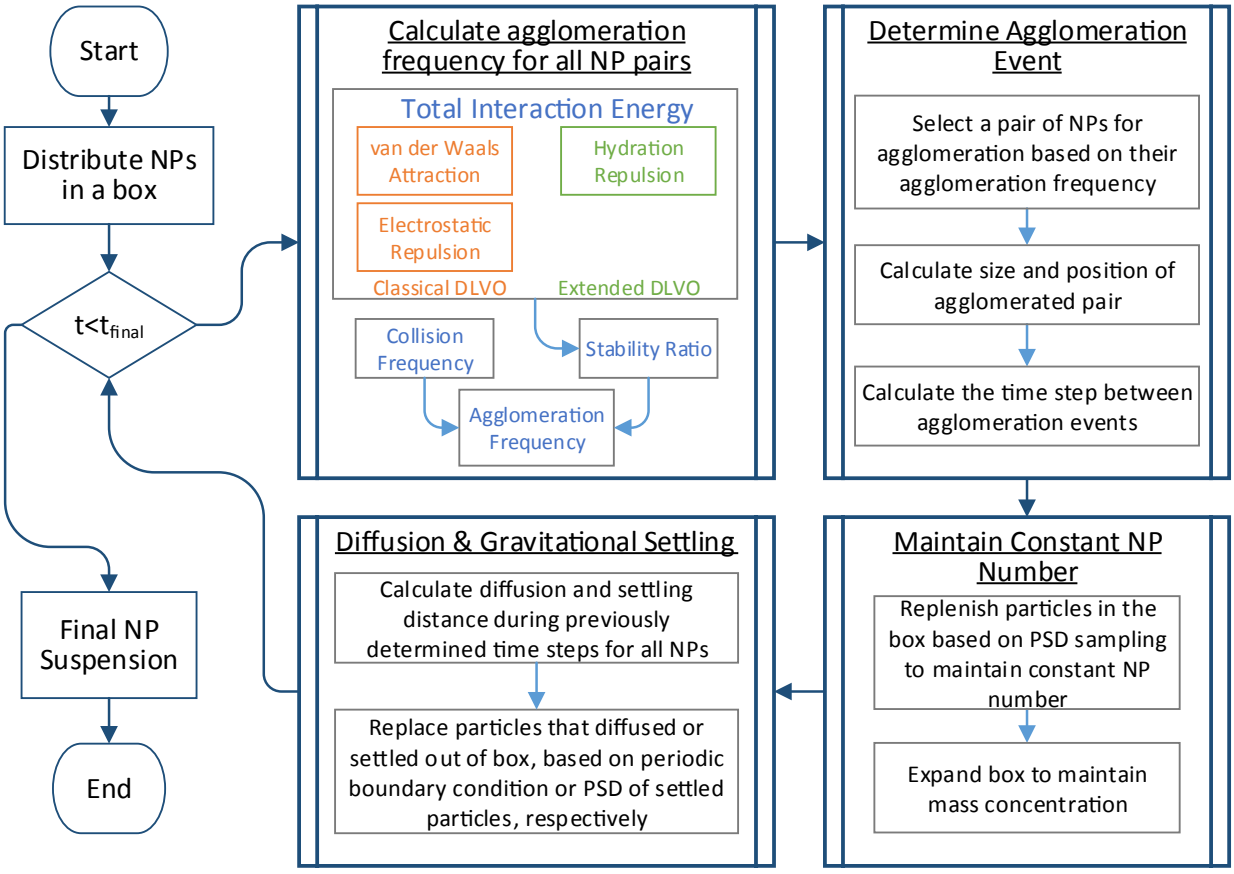

Figure 3-1. Overview of the DSMC particles in a box simulation

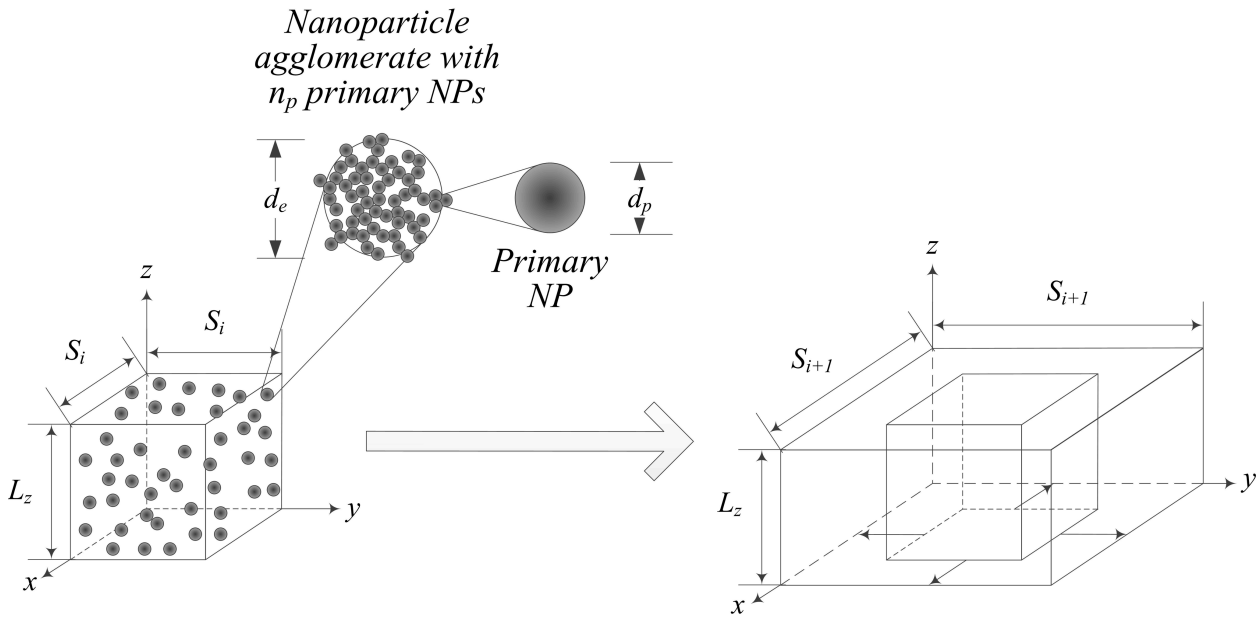

Figure 3-2. Schematic of the particle box and its expansion. Particle agglomerates are considered spherical with a diameter calculated based on a fractal dimension (eq [3-9]).

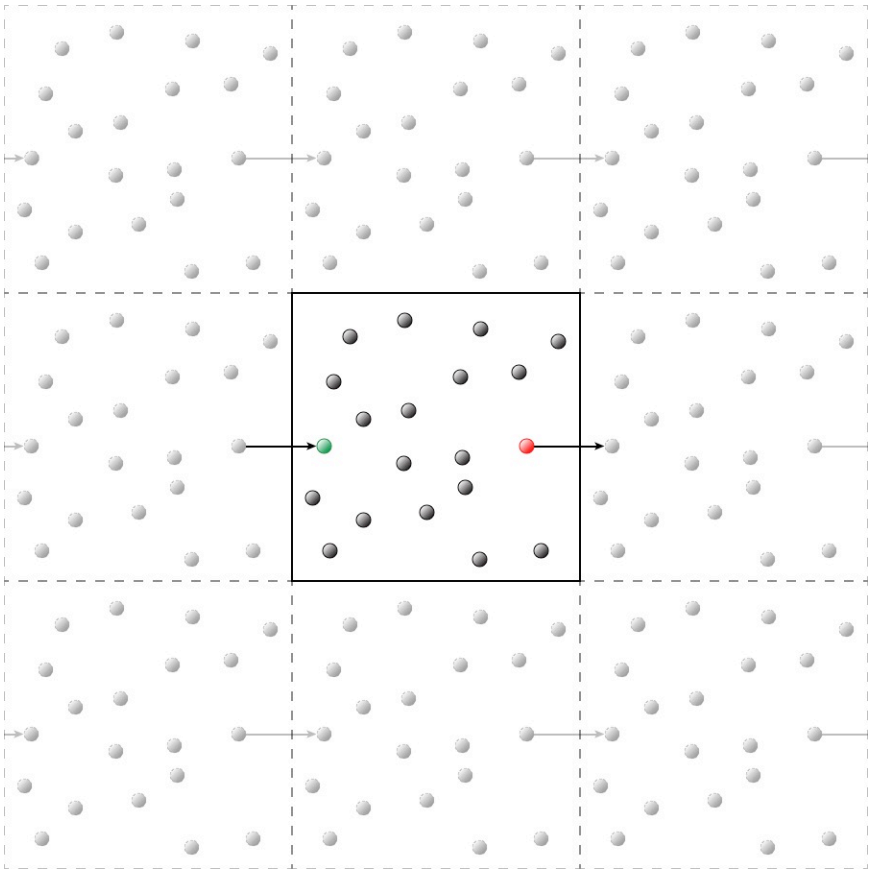

Figure 3-3. Schematic of the periodic boundary condition used for particle in a box simulation.

3.2.3 Model Equations

The simulation is initialized by first distributing N nanoparticles in a simulation box of volume V [m^3] satisfying the initial particle mass concentration, C_o [mg L^{-1}]:

$$V = \frac{\rho}{C} \cdot \sum_{i=1}^{N} \left(\frac{4}{3} \pi \cdot r_i^3 \right) \qquad [3\text{-}1]$$

where ρ [g m^{-3}] is the nanoparticle density, C is the mass concentration [mg L^{-1}], and r_i [m] is the radius of particle i. The initial nanoparticles in the simulation box (Figure 3-1) are positioned at

locations $(x_i,y_i,z_i) = (V)^{1/3}[P_x,P_y,P_z]$, where the random numbers P_x, P_y, and P_z are uniformly distributed in [0,1], while disallowing two particles to occupy the same space.

The agglomeration frequency N_{ij}, [no. of agglomeration events per m^3-s] between two particles *i* and *j* is determined based on the Smoluchowski coagulation theory where [149, 168, 173]

$$N_{ij} = k_{Ij} \cdot n_i \cdot n_j \quad [3\text{-}2]$$

where n_i and n_j are the number concentrations of particles *i* and *j*, respectively. The agglomeration frequency function, k_{ij}, is expressed as

$$k_{ij} = \frac{\beta_{ij}}{W_{ij}} \quad [3\text{-}3]$$

in which β_{ij} is the collision frequency function which arises due to Brownian motion [145, 150] given by

$$\beta_{ij} = \frac{2kT}{3\mu}(r_i + r_j)\left(\frac{1}{r_i} + \frac{1}{r_j}\right) \quad [3\text{-}4]$$

where r_i and r_j are the effective radii [m] (eq [3-9]) of particles *i* and *j*, respectively, *k* is Boltzmann's constant [k=1.38·10^{-23} J K^{-1}], *T* is temperature [K], and μ is the viscosity of the medium [Pa s]. The stability ratio, W_{ij} [dimensionless], is the inverse of the fraction of successful collisions for particle pair *i-j*, given as [150, 168]

$$W_{ij} = \frac{\#\ of\ collisions}{\#\ of\ collisions\ that\ result\ in\ agglomeration} = 2 \cdot \int_2^{\infty} \frac{\exp\left[\frac{\Phi_{T,ij}}{kT}\right]}{s^2} ds \quad [3\text{-}5]$$

in which $s = 2R/(r_i+r_j)$, where R is the distance between the center of the particles [m], and $\Phi_{T,ij}$ is the total interaction energy [J] between particle pair *i-j*. There are various approaches to quantifying $\Phi_{T,ij}$;[73, 168] however, the classical DLVO theory [150, 168, 173] (Table 3-1) can serve for a first order analysis, particularly given its success in describing surface interactions in colloidal systems [150, 168, 173]. According to the classical DLVO theory, the total interaction energy for a particle pair is the sum of the van der Waals attraction energy (as a function of the Hamaker constant A_H [J], particle sizes r_i and r_j [m], and separation distance between the particle pair R [m]) [150, 173] and the electrical double layer repulsion energy (being a function of the surface zeta potential of nanoparticles in solution ζ [V], solution ionic strength IS [M], r_i, r_j, and R) as summarized in Table 3-1. Other model parameters include the primary nanoparticle diameter d_p [m], initial nanoparticle concentration C_o [mg L^{-1}], agglomerate fractal dimension d_f [dimensionless] [149], and primary particle density ρ [g m^{-3}]. It is noted that for aqueous suspensions of high ionic strength (IS) and low absolute ζ-potential, hydration repulsion energy can significantly affect the agglomeration of ENMs as discussed in Chapter 4.

Table 3-1. Summary of DLVO working equations used in the present study.

Type of Interaction	Expression	Eq. #
vdW [150, 173]	$\Phi_{vdw,ij} = -\frac{A_H}{6}\left[\frac{2r_i r_j}{R^2-\left(r_i+r_j\right)^2}+\frac{2r_i r_j}{R^2-\left(r_i-r_j\right)^2}+\ln\left(\frac{R^2-\left(r_i+r_j\right)^2}{R^2-\left(r_i-r_j\right)^2}\right)\right]$	[3-6]
EDL κr>5 [150, 168]	$\Phi_{ele,ij} = 4\pi\varepsilon\varepsilon_o\psi_o^2\frac{r_i r_j}{r_i+r_j}\ln(1+\exp(-\kappa H))$	[3-7]
EDL κr<5 [168]	$\Phi_{ele,ij} = 4\pi\varepsilon\varepsilon_o r_i r_j Y_i Y_j\left(\frac{k_B T}{e}\right)^2\frac{\exp(-\kappa H)}{H+r_i+r_j}$	[3-8]

A_H is the Hamaker constant [J], R is the center-to-center particles separation distance [m]. κ is the inverse Debye length [m^{-1}], r is the particle radius [m]. ε is the dielectric constant of the medium [dimensionless], ε_o is the electric constant [$C^2\ N^{-1}\ m^{-2}$], ψ_o is the surface potential [V], estimated by the zeta potential [V] measurement ζ in the model and H is the surface to surface distance [m] between the two particles. Y_i is the dimensionless effective surface potential [174, 175].

Once the agglomeration frequency function is determined (eq [3-3]) for all particle pairs, a pair of nanoparticles (*i-j*) is selected to agglomerate, following the sampling approach proposed by Kruis *et al* [147], where the probability for the selected pair is taken to be proportional to the relative magnitude of its agglomeration frequency function (Figure 2-6). In this approach, the k_{ij} values are added sequentially for the list of all particle pairs until the k_{ij} sum exceeds the value of a sampled random number R in $\left[0, \sum_{i=1}^{N}\sum_{j=1}^{N} k_{ij}\right]$. When the above criterion is satisfied, the particle pair (*i-j*) corresponding to the last added k_{ij} is selected for agglomeration. The mass of this newly formed agglomerate, m_k, is the linear sum of the agglomerated particle pair, i.e., $m_k = m_i + m_j$. The effective diameter of this agglomerate, d_e, is calculated as [176]

$$d_e = d_p \cdot n_p^{\frac{1}{d_f}} \qquad [3\text{-}9]$$

where n_p is the number of primary particles in the agglomerate, and d_f is the fractal dimension for the specific agglomeration regime [149]. In order to maintain the total particle count in the simulation box, the lost particle (due to agglomeration) is replenished by sampling from the existing particle size distribution. The simulation box is then expanded to a new volume (eq [3-1]) in order to maintain the mass concentration. The box is expanded horizontally (in the *x,y* plane; Figure 3-2) in order to maintain consistency with experimental DLS measurements in which the thickness of the laser beam is fixed. Following box expansion (Figure 3-2), the time step [*s*] to the next agglomeration event is estimated based on the inverse of the average agglomeration frequency function $\langle k_{ij} \rangle$ over all N^2 particle pairs [145]

$$\Delta t = \frac{2}{C \cdot N \cdot \langle k_{ij} \rangle} \qquad [3\text{-}10]$$

Diffusion and settling distances due to Brownian diffusion and Stokes' sedimentation, respectively, are subsequently determined for the above time step (eq [3-10]) for all particles in the box. The vertical distance traveled by a particle *i* is estimated as:

$$\Delta z_i = z_{S,i} + z_{B,i} \qquad [3\text{-}11]$$

where $\Delta z<0$ represents net downward movement. The gravitational settling distance for particle *i* is given as $z_{S,i}=-v_{S,i} \cdot \Delta t$, where $v_{S,i}$ is its Stokes' settling velocity given by [50]

$$v_{S,i} = \frac{2(\rho_p - \rho_f) \cdot (1 - \phi_i) \cdot g \cdot r_i^2}{9 \cdot \mu} \qquad [3\text{-}12]$$

in which ρ_p is the particle density (g L^{-1}), ρ_f is the fluid density, g is the gravitational constant [m^3 kg^{-1} s^{-2}] and ϕ is the particle agglomerate porosity (i.e., $\phi = 1 - (r_m/r_e)^3$, where r_m is the mass equivalent radius of the particle ($r_m = \sqrt[3]{(3m_i)/(4\rho\pi)}$, [m]), and r_e is its effective radius

(eq [3-9]). The Brownian diffusion distance, $z_{B,i}$ (positive or negative for upward or downward movement, respectively) is estimated assuming that the distance traveled vertically is determined based on a random number sampled from a normal distribution with $\mu = 0$ and $\sigma = \sqrt{2 \cdot D_i \cdot \Delta t}$ [149, 168] such that

$$z_{B,i} \sim \mathcal{N}(0, 2 \cdot D_i \cdot \Delta t) \quad [3\text{-}13]$$

in which D_i is the Brownian diffusivity [$m^2 s^{-1}$] determined from [149, 168]

$$D_i = \frac{kT}{6\pi\mu r_i} \quad [3\text{-}14]$$

Following the above approach, particles for which $z_i + \Delta z_i \leq 0$ (where z_i is the particle vertical position at time t_i) are considered to have settled out of the box, thereby decreasing the number of particles in the box. This necessitates the introduction of new particles into the box in order to preserve the total particle count. The size of each replenishing particle is determined by sampling from the size distribution of the last N particles that have settled, given the expectation that particles can enter the box via its top face via sedimentation. The vertical positioning of each replenishing particle in the simulation box is assigned as $z_i = L_z + P_z \cdot \Delta z_i$, where L_z is the box height, and P_z is a uniformly distributed random number in [0,1]. Δz_i is the vertical distance that would be traveled due to the combined effect of sedimentation and Brownian motion, calculated as described above, for the same agglomeration time step (eq [3-10]). The above sampling is repeated until the condition, $0 < z_i \leq L_z$, for placing a particle inside the box is met and the mass concentration in the box is then recalculated. Finally, it is noted that particles can diffuse out of the vertical sides of the simulation box due to Brownian motion. However, in this case, one can invoke a periodic boundary condition specifying that a particle that diffuses out of a given

vertical face would be reintroduced from the opposite face. A similar reasoning is applied to particles that diffuse out of the box through the top (horizontal) face.

3.2.4 Simulations

Simulations were performed for TiO_2 and CeO_2 nanoparticles of 21 and 15 nm primary particle diameters, respectively, at initial concentration of 20 mg L^{-1}, matching the 24 h period of DLS measurements (Table A-1). Simulation conditions also matched the pH range of 3–10, and ionic strength of 0.02–0.4 mM at 23^{o}C for the present DLS measurements. For comparison with reported literature data for TiO_2 nanoparticle suspensions, additional simulations were also carried out for an initial concentration range of 40 mg L^{-1} – 50 mg L^{-1}, pH of 3–10.4 and IS of 0.01 mM – 12.5 mM [60, 64, 66]. Simulations were also carried for aqueous C_{60} nanoparticle suspensions (primary size of 80 and 168 nm [177, 178]), pH 5.5, 7 and ionic strength of 10–156 mM. The basic fundamental model parameters included: particle primary size, zeta potential, Hamaker constant, solution ionic strength and temperature. The first three parameters were obtained from either independent measurements or from reported literature data (Table A-1), while the latter two were the conditions as specified in the particular experiments. Therefore, all model simulations results that were compared with experimental data represent *a priori* predictions. Simulations were carried out with a number of particles in the box ranging from 500 up to 10,000. Different numbers of repeated simulations (for the same particle number) were carried out in order to evaluate the optimally reasonable number of particles needed to achieve convergence of the simulation results. Simulations were carried out on a cluster of 20 Intel Xeon Quad-Core processors at 2.2–3.0 GHz with 176 GB of total RAM. Simulation CPU times on this cluster ranged from as short as 100 s to as along as 15 days for 500 and 10,000 nanoparticles, respectively.

3.3 Results and Discussion

3.3.1 Convergence of Simulations

Simulations of nanoparticle agglomeration were first carried out to determine the number of particles necessary to achieve a convergent solution. A series of simulations with 500-10000 nanoparticles in the simulation box indicated, consistent with the existing DSMC literature, that the use of 5000 particles (e.g., Figure 3-4 and Figure 3-5) was sufficient for reaching accurate simulation results [136, 138]. However, given that the simulations were seeded with random numbers (Figure 3-1 and Figure 2-6), there were statistically measurable variations in the results for repeated simulations (e.g., Figure 3-6). It was found that above five replicate simulations and with 5000 (or more) particles in the simulation box, the change in the predicted average agglomerate size was less than 0.1% (e.g., Figure 3-6b) and the standard deviation of the predicted average agglomerate size over 10 replicate simulations was typically below 1% (Figure 3-4 and Figure 3-5). Accordingly, all results in the present work are presented as the average over 10 simulation replicates for 5000 particles in the simulation box.

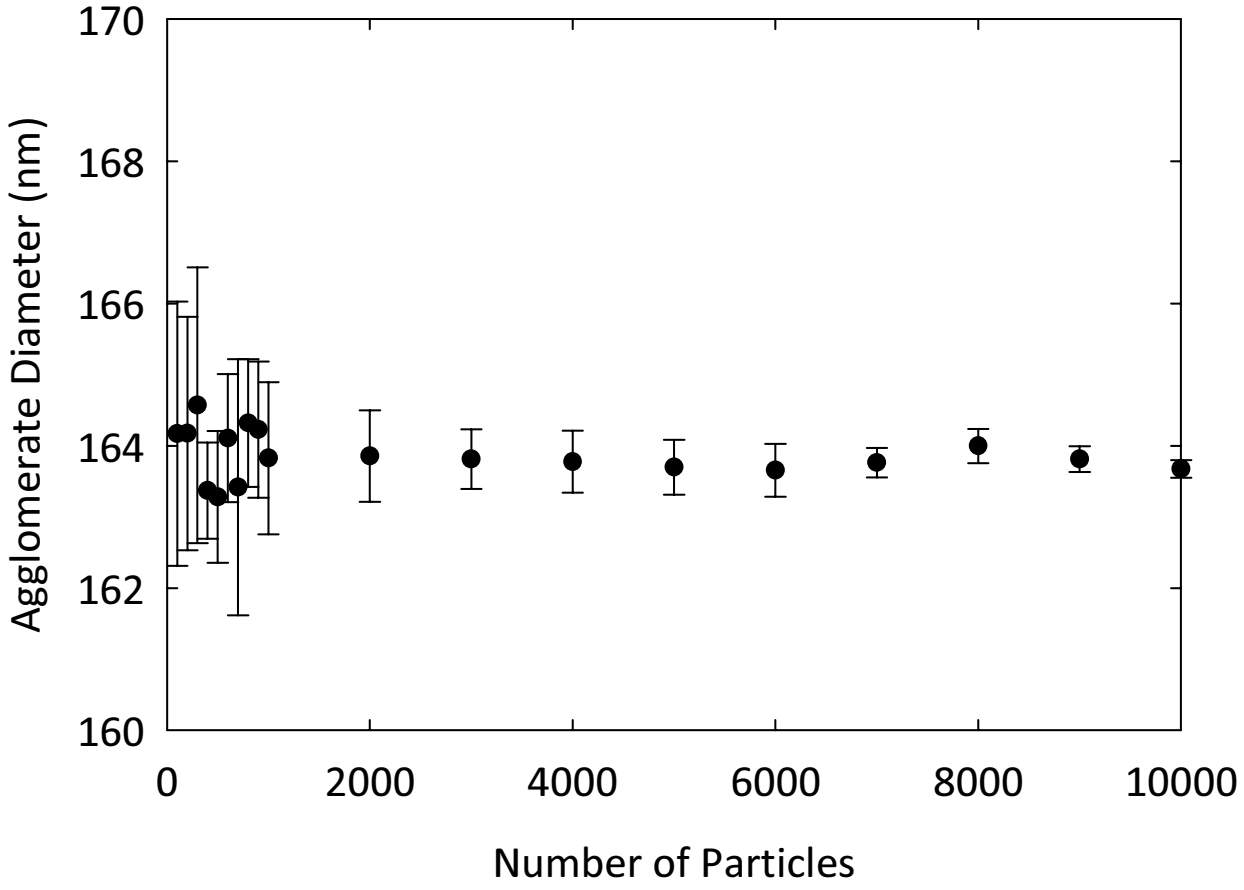

Figure 3-4**.** Mean agglomerate diameter based on the average of 10 simulations as a function of the number of particles in the simulation box. The vertical bars represent one standard deviation of the mean particle size over 10 simulation replicates. Simulation conditions: ζ = -40 mV, IS = 0.1 mM, d_p = 21 nm, A_H= 42 zJ.

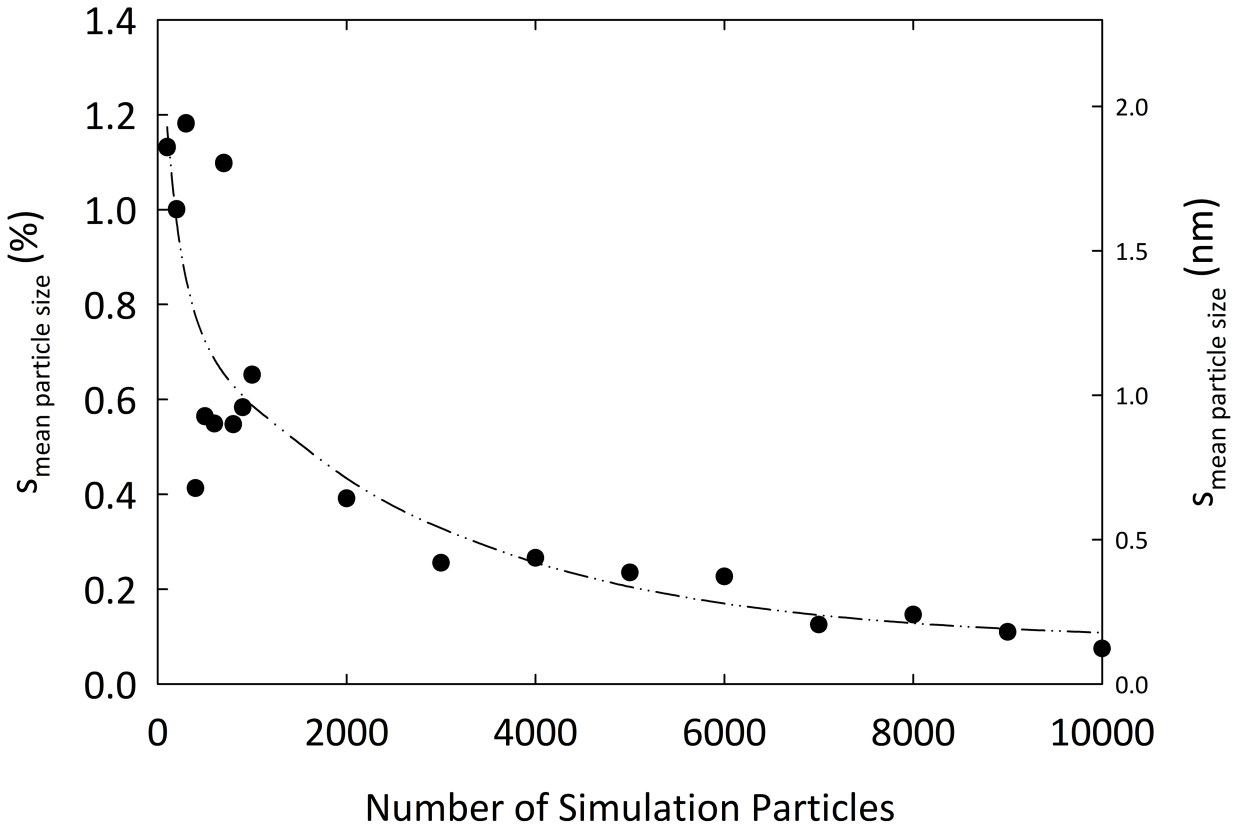

Figure 3-5**.** Effect of the number of particles in the simulation box on the standard deviation of mean particle agglomerate diameter over 10 simulations. Simulation conditions: ζ = -40 mV, IS = 0.1 mM, d_p = 21 nm, A_H= 42 zJ.

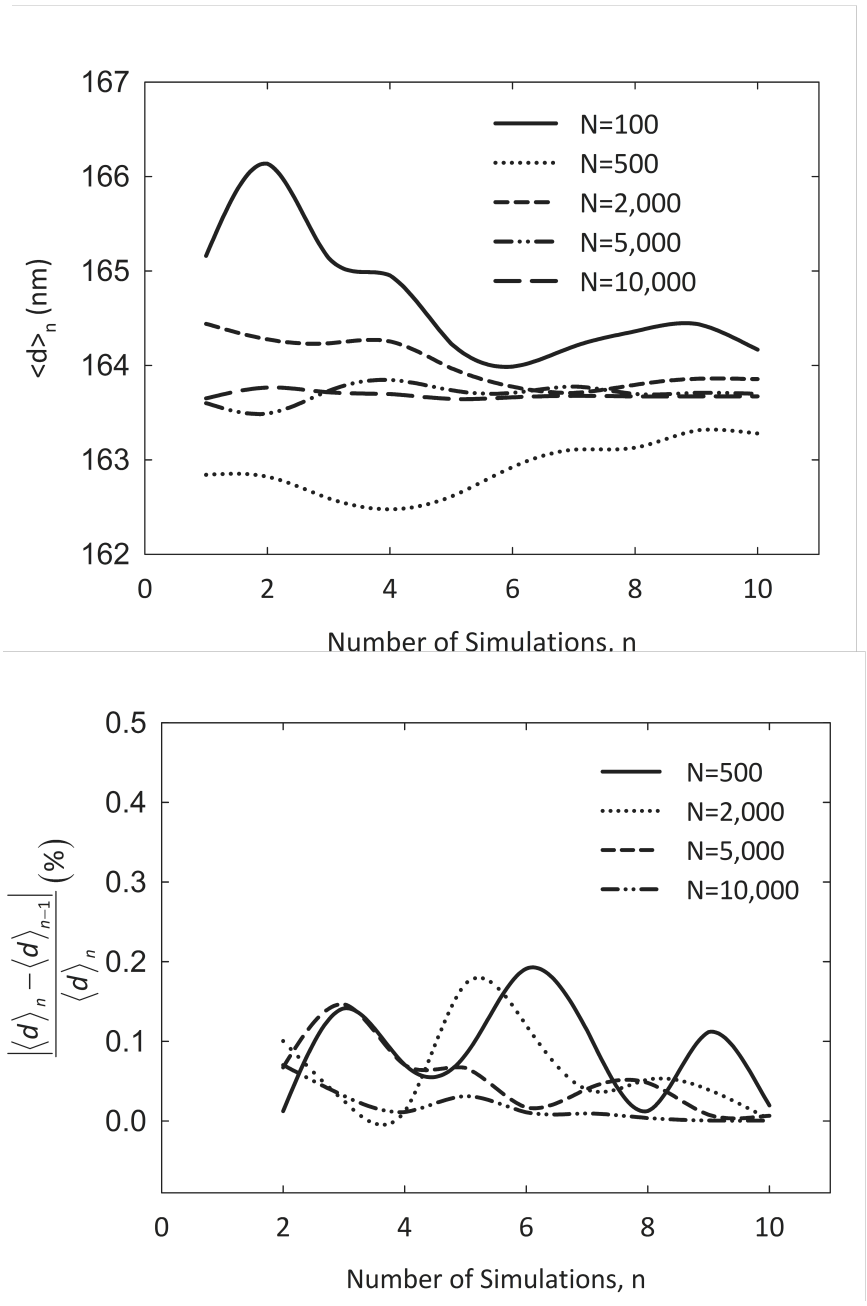

Figure 3-6**.** (a) Effect of the number of replicate simulations (n) on the average nanoparticle agglomerate diameter for different number of particles in the simulation box. (b) Variation of the predicted average agglomerate size due to incremental addition of replicate simulations. Note: $\langle d \rangle_n$ and $\langle d \rangle_{n-1}$ represent the average agglomerate size for *n* and *n-1* simulation replicates, respectively. Simulation conditions: ζ = -40 mV, *IS* = 0.1 mM, d_p = 21 nm, A_H= 42 zJ.

3.3.2 Nanoparticle Agglomeration

As nanoparticles agglomerate in aqueous suspensions, gravitational sedimentation can take place thereby altering the size distribution of the particles remaining in suspension. For example, impermeable nanoparticle agglomerates of size 100 nm and 250 nm can sediment a distance equivalent to a typical width of a DLS laser beam (~0.04 mm) in a period of 3 h and 1 h, respectively (Figure 3-7). Partially draining (i.e., permeable) nanoparticles can settle at an even faster rate (Chapter 5). Thus, if nanoparticle agglomerates reach the above size range or greater, settling due to gravity has to be considered, especially for applications and studies of extended duration. The occurrence of sedimentation can be inferred from a decrease in the photon count rate in DLS measurements. This is illustrated, for example, in Figure 3-8 revealing ~18% and ~30% photon count rate decrease in DLS measurements over a 24 h period for TiO_2 (pH 8 and 10, IS = 0.37 mM) and CeO_2 (pH 8, IS = 0.37 mM) nanoparticles, respectively. The simulations revealed a rapid rate of agglomeration with an agglomerate size that increases with time when sedimentation is not considered in the model. However, upon inclusion of sedimentation a "stable" (i.e., time independent) agglomerate size is reached (in suspension) after several hours. This behavior is illustrated in Figure 3-9 for CeO_2 and TiO_2 nanoparticles of 15 and 21 nm primary particle diameters, respectively, at pH 8 at low ionic strength of 0.065 mM. As a result of sedimentation, the mass concentration of the TiO_2 and CeO_2 nanoparticles in suspension decreased by 10–50% for the present range of simulation conditions (Table A-1) as was verified via ICP measurements; however the average particle size in suspension remained essentially at steady state (after ~15 h, Figure 3-9). Such behavior is reached once the rate of sedimentation is balanced by the rate of nanoparticle agglomeration.

The predicted average agglomerate size is in remarkable agreement with the present DLS measurements (Figure 3-9) with a prediction absolute error of 1% and 0.4% for TiO_2 and CeO_2 nanoparticles for the solution conditions indicated in Figure 3-9. However, it is noted that sonication of the suspensions, prepared from commercial nanoparticle powders, could only breakup the nanoparticle agglomerates to their "stable" suspension particle size. Therefore, the region of agglomerate evolution could not be traced via DLS and only the stable nanoparticle agglomerate size could be monitored (Figure 3-9).

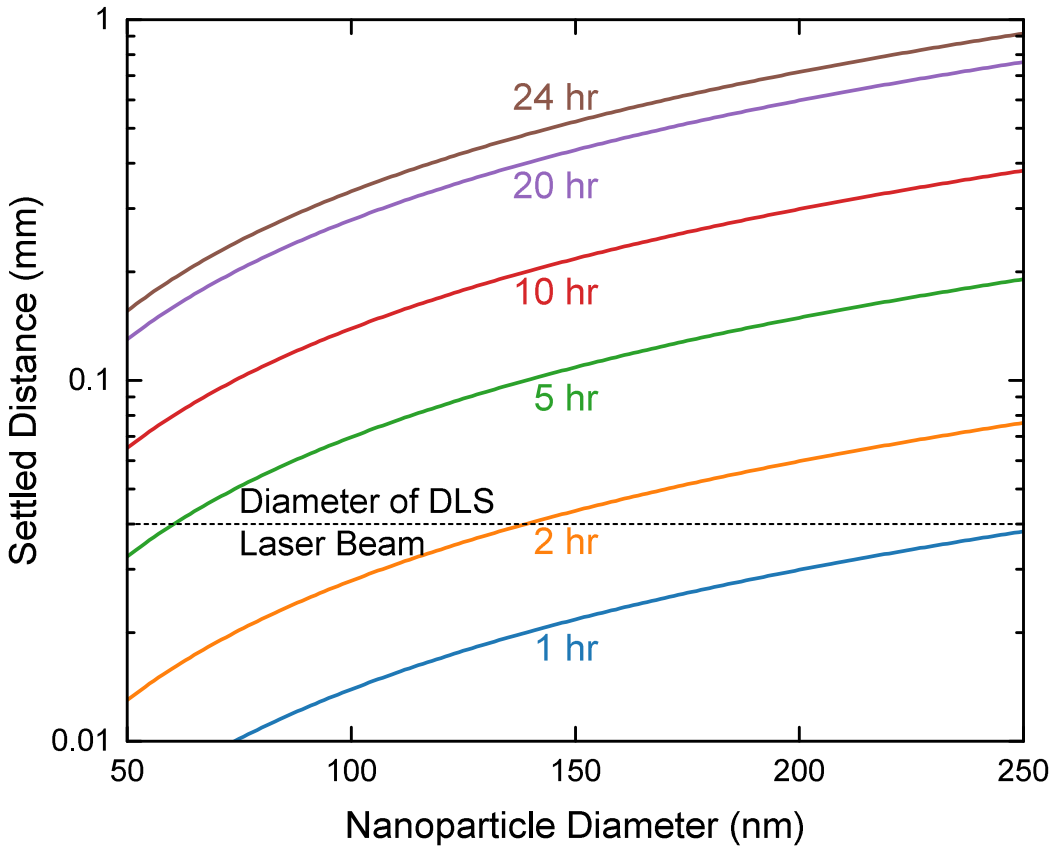

Figure 3-7. Settling distance for different times as a function of particle diameter, as calculated based on Stokes' settling (eq [3-12]) for impermeable particles. It is noted for partially draining particles, settling distance can be greater than shown in this figure (see Chapter 5).

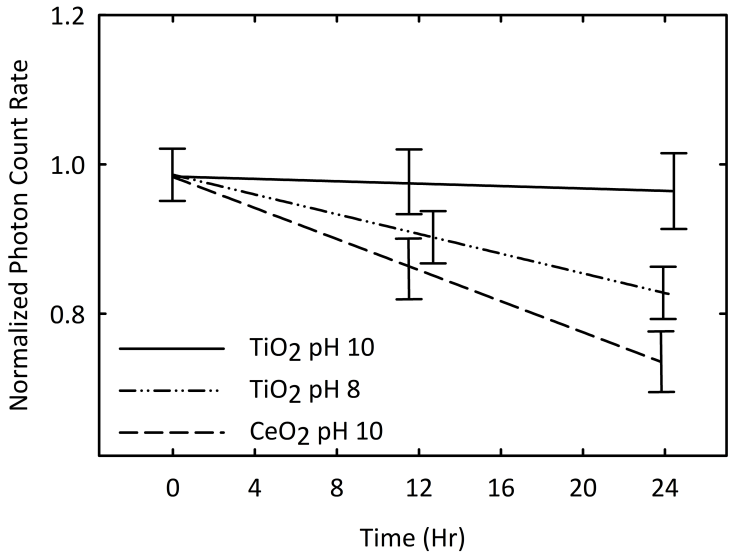

Figure 3-8. Examples of the normalized photon count rate (w.r.t. initial rate) for DLS measurements of TiO_2 and CeO_2 nanoparticles. Conditions: IS = 0.37 mM, d_p were 21nm and 15 nm for TiO_2 and CeO_2, respectively.

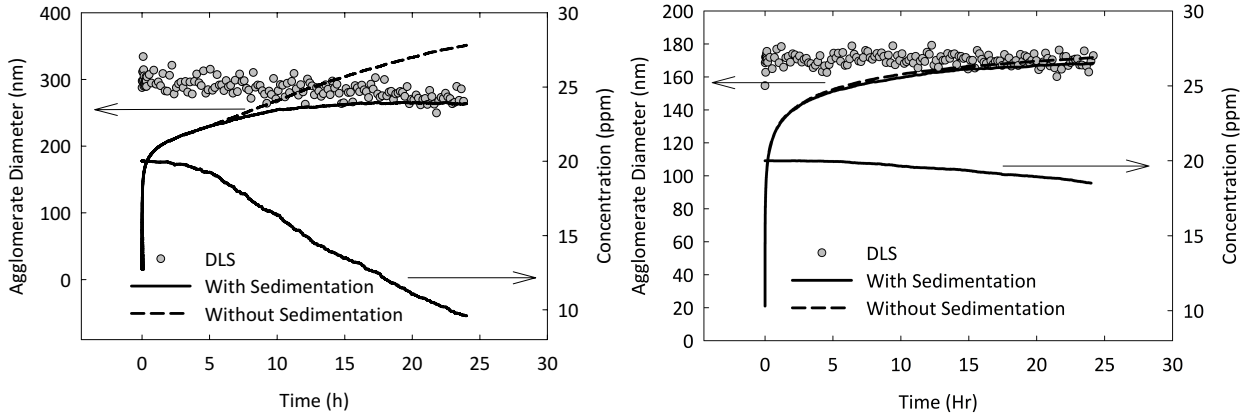

Figure 3-9. Evolution of CeO_2 (left) and TiO_2 (right) agglomerate diameter based on simulation with and without sedimentation, based on average of 10 simulation instances with 5000 particles in the simulation box. Simulation conditions: pH = 8, ζ_{CeO_2} = –24.5 mV, ζ_{TiO_2} = –29 mV, IS = 0.065 mM, $A_{H,\,CeO_2}$ = 21 zJ, $A_{H,\,TiO_2}$ = 42 zJ.

Comparison of DSMC model predictions of TiO_2 nanoparticle agglomerate size with the present series of DLS measurements and published literature data [60, 64, 66] along with comparisons of predictions with literature data for C_{60} nanoparticles [177, 178] are provided in Figure 3-10 and Table A-1. Only literature data for agglomerate sizes below 1 μm were considered as this size approaches the limitations of DLS measurements [160] as well as the DLVO theory [168]. Reasonable agreement of predictions with DLS data (present and literature data) were obtained with an absolute error in the range of 0.6%–25.3% and ~10.8% average absolute error for the 26 measurements depicted in Figure 3-10 (also Table A-1). Notwithstanding the success of the constant-number DSMC model predictions (Figure 3-9 and Figure 3-10; Table A-1) of nanoparticle agglomeration, broader assessment of the suitability of the present simulation approach for predicting short-time agglomeration kinetics would necessitate DLS measurements with aqueous suspensions in which the nanoparticles are initially near their primary diameter.

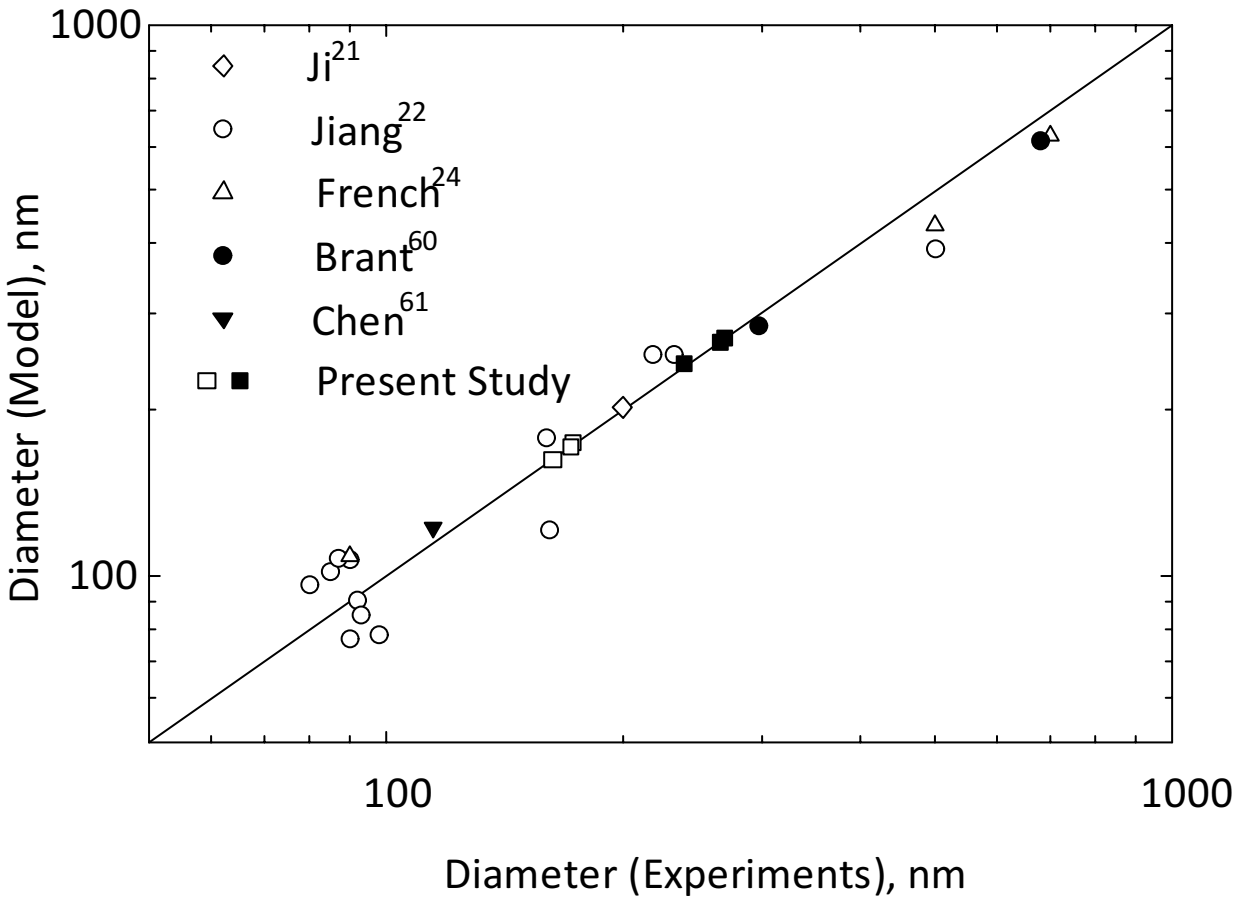

Figure 3-10. Comparison between simulation and experimental results for average agglomerate diameter for TiO_2 [60, 64, 66], CeO_2, and C_{60} [177, 178] nanoparticles. Primary NP diameters were: for TiO_2, 5 (Δ), 15 (O), and 21 (◊, □) nm; for CeO_2, 15 (■) nm; and for C_{60}, 80 (∇), 168 (•) nm. IS = 0.01 - 156 mM, pH = 3 - 10.4, ζ = -45 ~ 42 mV.

3.3.3 Dependence of Nanoparticle Agglomeration on Model Parameters (d_p, ζ, IS, A_H)

According to the DLVO theory [150, 168] nanoparticle agglomeration depends primarily on the nanoparticle primary diameter (d_p), Hamaker constant (A_H), ionic strength (IS), and surface electrical potential (estimated from the zeta potential, ζ). The zeta potential varies with solution pH and there is a pH at which the isoelectric point (IEP) is reached where the net surface charge

is zero (i.e., $\zeta = 0$) [151]. Particle agglomeration is expected to be most significant near the IEP as the electrical double layer diminishes and the attractive energy due to van der Waals forces becomes dominant. As the solution pH deviates away from the IEP, the electrical double layer thickness increases as does the surface charge (either positive or negative; Figure 3-11a) and thus greater particle repulsion and smaller agglomerates are expected. The above behavior is demonstrated in Figure 3-11a for simulations of TiO_2 nanoparticle agglomerates revealing agreement with measured DLS data within an absolute average error of 2.8%. The predictions are consistent with experimental observations of the maximum agglomerate particle size (400 nm) at the IEP and decreasing size away from the IEP (by about a factor of 3 for the measurements at the lowest and highest pH levels).

As shown in Figure 3-11b, nanoparticle agglomeration can also increase with increased ionic strength due to suppression of the electrical double layer. The typical reported dependence of particle agglomeration on ionic strength [64] is illustrated in the simulation results shown in Figure 3-11b for TiO_2 nanoparticles (d_p = 21 nm) at ζ = 20 mV and 40 mV. In this example, the critical coagulation concentrations at the above two conditions are estimated at ~0.08 mM and ~2.89 mM at which the agglomerate size is ~805 nm and ~563 nm, respectively. Although the predicted rise in agglomerate size at high ionic strength portrays the expected trend, the deviation of the calculated average agglomerate size from the mean is noteworthy. Considerably more than ten simulation instances with N > 5000 would have been necessary (at the expense of considerable CPU time of ~4 weeks) to achieve an accurate stationary solution, since the size fluctuation is large at high IS due to a significant degree of settling.

According to the DLVO theory, agglomerate sizes would also increase with increasing magnitude of the Hamaker constant, as this would imply increasing van der Waals attraction

energy (eq [3-6]). For the above TiO_2 example, the simulations revealed a linear dependence of agglomerate nanoparticle size on the Hamaker constant (A_H) demonstrating an agglomerate size increase from 110 to 550 nm with A_H increase from 10 to 90 zJ (Figure 3-12), corresponding to the range of literature reported values for the anatase [179, 180] and rutile [180, 181] forms of TiO_2.

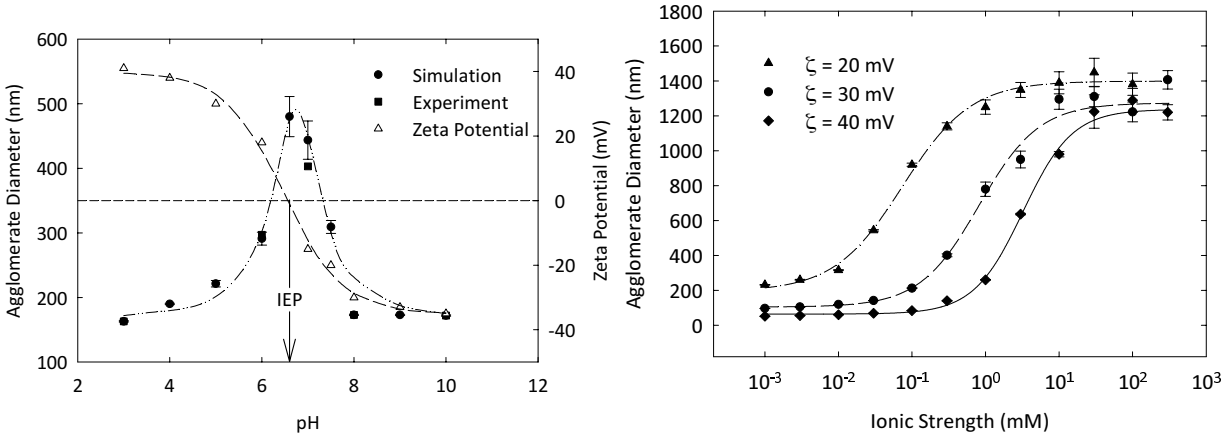

Figure 3-11. Average agglomerate diameter of nanoparticle aggregates after 24 hours as a function of (left) pH levels (at IS = 0.037 mM) and (right) ionic strength. Simulation conditions: A_H = 42 zJ, d_p = 21 nm, C_o = 20 mg L^{-1}, temperature = 23 °C. Note: the vertical bars represent one standard deviation over 10 simulation replicates.

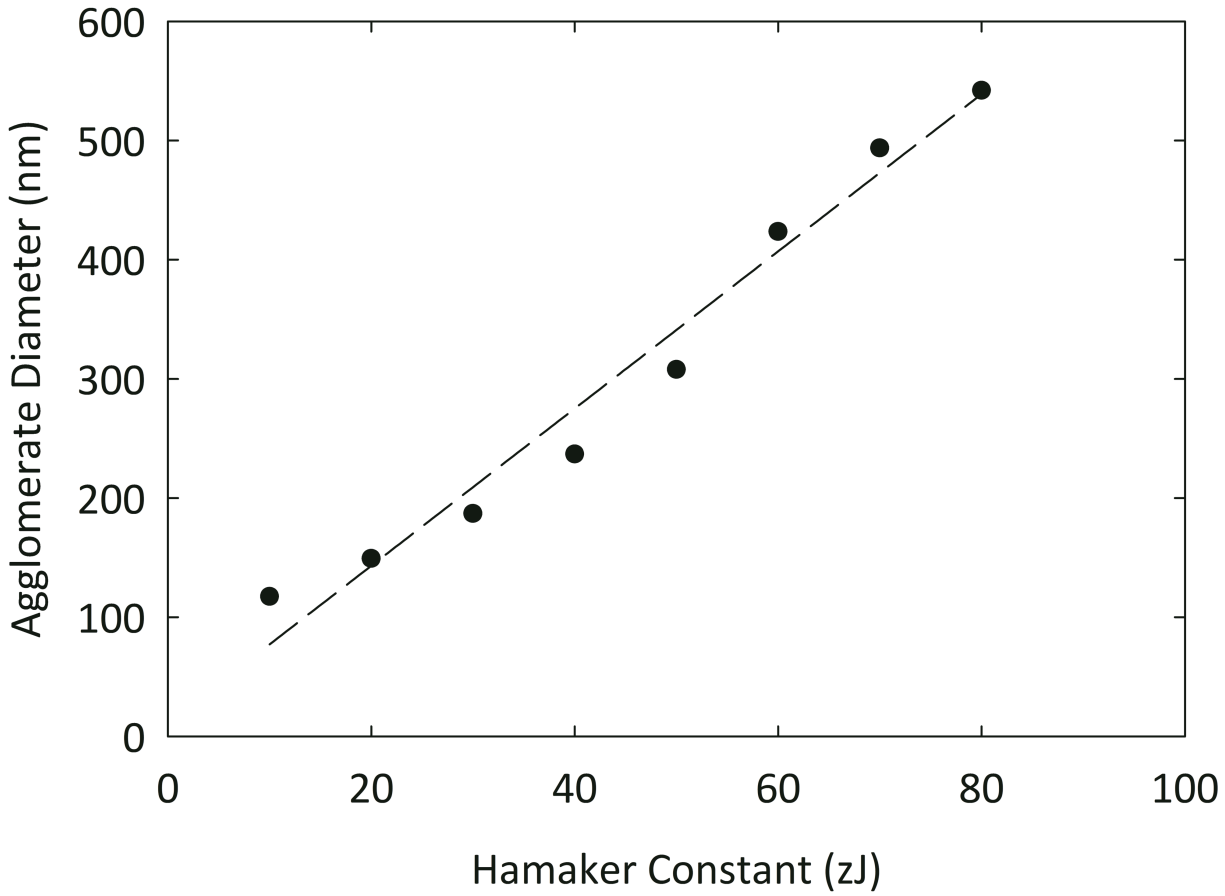

Figure 3-12. Dependence of average agglomerate diameter on the Hamaker Constant (A_H). Simulation conditions: ζ= -40mV, IS = 1 mM, d_p = 21 nm, C_o = 20 mg L^{-1}, T = 23 °C.

Simulations results demonstrated that the agglomerate size of nanoparticles in aqueous suspension increases with decreasing primary particle diameter (Figure 3-13). This result should not be surprising since van der Waals interactions increase with decreasing particle size ([3-6]), the collision frequency is more pronounced for smaller particles (eq [3-4]) and electrostatic repulsion increases with increased particle size (eqs [3-7] and [3-8]). As a result, smaller primary nanoparticles could form larger agglomerates. It is noted, however, that DLS measurements are only indicative of the size of particles remaining in suspensions and do not provide a measure of

the true distribution of all agglomerates that may have formed. Accordingly one would expect that, as a result of agglomeration and sedimentation, the nanoparticle size distribution in suspension (as determined by DLS) will reveal an increasing tail of smaller size agglomerates with increasing primary particle diameter (Figure 3-13). The above behavior should not be taken as a universal representation of nanoparticle agglomeration as one must be cautious with the limitation of the DLVO theory to nanoparticles with $\kappa r_i << 1$ (e.g. corresponding to $r_i << 10$nm at IS = 1mM; note κ is the inverse Debye length, Table 3-1). Moreover, it is also noted that the present application of the DLVO theory, as well as the simple application of gravitational settling, does not consider the impact of the details of agglomerate geometry and morphology. Nonetheless, the analysis suggests that interpretation of nanoparticle behavior in environmental aquatic media and potential toxic outcomes due to exposure to nanoparticles must carefully consider not only the particle size distribution but also the experimental protocols used to determine such size distributions.

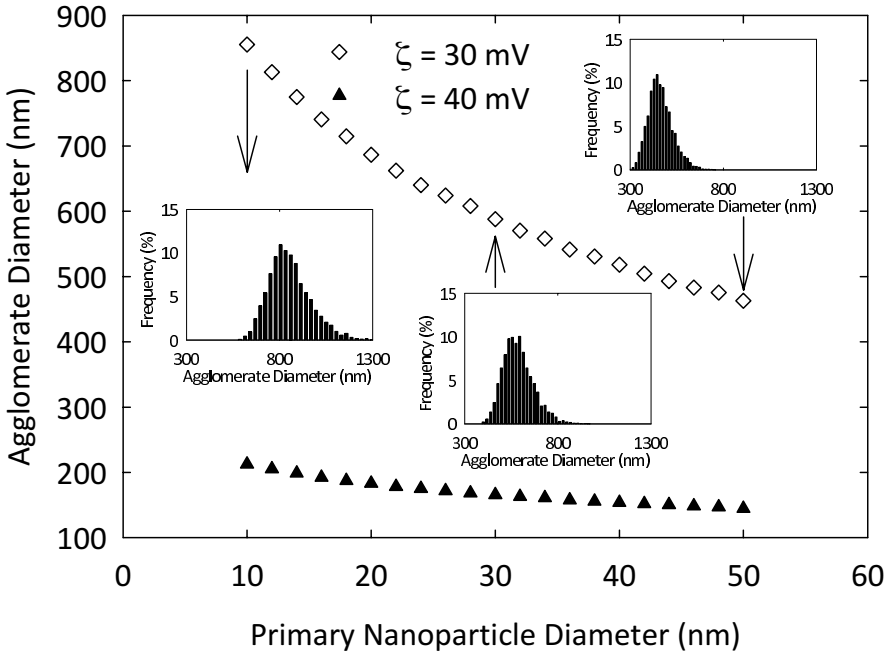

Figure 3-13. Dependence of average agglomerate diameter on the primary nanoparticle diameter. Simulation condition: IS = 0.5 mM, C_o= 20 mg L^{-1}, T = 23 °C.

In summary, the present constant-number DSMC approach of simulating nanoparticle agglomeration in aqueous suspensions demonstrated that classical DLVO theory can provide reasonably accurate predictions of the average nanoparticle agglomerate size as well as the particle size distribution over a wide range of solution pH (3-10) and ionic strength (0.01-12.5 mM; Table A-1). Extension of the present approach incorporating non-DLVO interaction is explored in Chapter 4 for a wide range of nanoparticle types and aqueous solution chemistries of environmental interest.

Chapter 4. Effect of Hydration Repulsion on Nanoparticle Agglomeration Evaluated via a Constant Number Monte Carlo Simulation

4.1 Introduction

The mechanistic model of NP agglomeration [49] presented in Chapter 3 was based on the classical DLVO theory and constant number Direct Simulation Monte Carlos (DSMC) solution of the Smoluchowski equation of particle agglomeration and considering Brownian diffusion and particle sedimentation. However, a number of studies have reported that the electrostatic repulsion energy contribution to the total repulsion energy between NPs decreases with increasing IS or decreasing |ζ-potential| [150, 151, 168, 173]. In fact, it has been argued that under the conditions of high IS or low |ζ-potential| hydration repulsion is dominant relative to electrostatic repulsion and thus should also be considered [73]. Indeed, it has been suggested that non-DLVO interaction such as hydration repulsion energy may be important for suspensions of high ionic strength (IS), whereby hydrated counter ions and surface bound water molecules create multiple hydration shells thereby leading to increased repulsion energy between the interacting (colliding) particles [151].

A simplified modeling approach to estimate the evolution of the average NPs size, accounting for the classical DLVO, along with hydration and steric repulsions, but without accounting for the complete PSD or gravitational settling, was recently advanced [152]. It was estimated that the hydration repulsion energy was a factor of ~10 higher than the electrostatic repulsion energy for an aqueous suspension of CeO_2 nanoparticles (primary size of 25 nm) in 2 mM $CaCl_2$ solution (IS = 8 mM). The approach invoked the approximation of a constant total particle-particle interaction energy that is independent of agglomerate size. Good agreement was

achieved between predicted and experimental DLS measurements of the average CeO_2 NP size in aqueous suspensions at short agglomeration times (<90 min) times. However, it should be recognized that agglomeration may continue for a significant period as has been reported in various studies [66, 182, 183]. For example, DLS measurements of aqueous (IS = 8.5 mM) TiO_2 NP (5 nm primary size) suspensions [66] demonstrated continued agglomerate size increase by a factor of ~2.5 over the period of 90 min to 100 hr. Another study reported that Ag NPs of primary size in the range of 20 – 80 nm in aqueous suspension (IS = 9.1 mM) continued to agglomerate after 90 min, and the agglomerate size increased by factors of ~3 - ~7 by 6 hr [183].

Agglomeration and sedimentation, in addition to the initial suspension concentration, can all impact the size distribution of the suspension over the course of DLS measurements [49, 63, 184]. For example, studies of metal oxide NP (e.g., TiO_2, ZnO, and CeO_2) suspension (with initial NP loading of up to 200 mg L^{-1}) in natural water (with IS up to 700 mM) have demonstrated NPs removal by up to 80% via sedimentation within a 6 hr period [63, 184]. Accounting for sedimentation, as well as both the evolution of NP agglomeration and the stable agglomerate size for a stable suspension (i.e., when the agglomerate size reaches a steady-state level), is of relevance in various studies (e.g., toxicity [185], environmental fate and transport studies [186], and NP removal from wastewater streams [187-189]) where the time period of interest may span many hours to days. In this regard, it is noted that recent simulations of CeO_2 agglomeration in aqueous suspension (IS=0.065 mM, 15 nm primary NP and ζ-potential= -24.5 mV), over a period of 24 hr, have shown that there may be up to ~25% overprediction of the average agglomerate diameter if sedimentation is neglected [49]. In the above study [49] hydration repulsion was not considered given the relatively low IS.

Given the existing body of evidence regarding the importance of hydration repulsion on NPs agglomeration in high IS and low |ζ-potential| suspensions (which can be encountered in environmental systems [63]), This Chapter presents an analysis of the impact of hydration repulsion via a fundamental model of NP agglomeration for high IS suspensions. The approach is based on a computational constant-number DSMC simulation [145, 147] to solving the Smoluchowski equation [149] (as presented in Chapter 3), but considering the addition of hydration repulsion[151] to the classical DLVO which also accounting for Brownian motion [149, 150] and sedimentation.

4.2 Materials and Methods

4.2.1 Compilation of Nanoparticle Size Data

DLS size measurements were compiled from the literature (Table A-2) for TiO_2 (primary size of 21 nm)[184], CeO_2 (primary size of 25 nm) [155], SiO_2 (primary size of 30 nm) [190], and α-Fe_2O_3 (hematite) (primary size of 12, 32, and 65 nm) [68] NPs for IS range of 2-900 mM (adjusted with NaCl, $CaCl_2$, NaCl, NaCl for the above four NPs, respectively) and |ζ-potential| range of 1.35-40 mV. The above data (12, 12, 9, and 6 different experimental conditions for TiO_2, CeO_2, SiO_2, and hematite, respectively) were supplemented in the present study (Table A-2) with experimental DLS measurements (36 different experimental conditions with respect to IS, pH and initial suspension concentration) for TiO_2 (Evonika Degussa Corporation, NJ; primary size of 21 nm), in aqueous suspensions for IS range of 1-31.6mM (adjusted with KCl) and |ζ-potential| range of 5.43 – 43.11 mV (corresponding to pH 3-9). Preparation of the suspensions and DLS measurements followed the protocol described in §3.2.1.

4.2.2 Modeling Approach

The agglomeration of NPs was described by the simulation of particles in a box (employing a constant number DSMC simulation to solve the Smoluchowski equation of particle agglomeration) as described in §3.2.2. The total particle-particle interaction energy is quantified by an extended-DLVO theory [151, 191] consisting of electrostatic (eqs [3-7],[3-8]) and hydration (eq [4-1]) repulsions and van der Waals attraction (eq [3-6]). It is well established that the classical DLVO theory is adequate for describing particle-particle interactions when long range van der Waals attraction and electrostatic repulsion energies are greater than their short range counterparts (e.g., hydration energy) [151]. However, hydration repulsion can be of greater significance relative to electrostatic repulsion, particularly at high IS and at short particle-particle-separation distances (~< 10 nm) [73, 192].

In the model formulation, the hydration repulsion energy, $\Phi_{hyd,ij}$ [J] between particles *i* and *j*, is expressed as [151, 193]:

$$\Phi_{hyd,ij} = \pi \left(\frac{r_i r_j}{r_i + r_j} \right) f_0 \cdot L \cdot e^{-\frac{H}{L}} \qquad [4\text{-}1]$$

where r_i and r_j [m] are the radii of particles *i* and *j*, and *H* [m] is the surface-to-surface separation distance between the two particles. The decay length of the media, *L* [m], has been reported to be in the range of 0.6 – 1.1 nm for aqueous suspensions with 1:1 electrolyte (e.g., NaCl, KCl, CsCl, or LiCl) solutions [151], and previous work with mica surfaces suggested a value of 1 nm as being reasonable [191, 194]. The surface energy density, f_0 [J m^{-2}], is typically reported to be in the range of 3 - 30 mJ m^{-2} [151] (and can be as low as 0.15 mJ m^{-2} [152]), and is a function of the surface type (e.g., NP type or surface functionalization) [151]. The value of f_0 for a specific NP

type and suspension conditions is commonly determined from matching agglomeration model predictions with reported DLS measurements [152, 195]. Accordingly, in the present work, a series of simulations were carried out to extract f_0 values based on best fits between model predictions and experimental data for the NP agglomerate size (Table A-2).

4.2.3 Simulations of NPs agglomeration

Simulations of NPs agglomeration were carried out over a wide range of suspension conditions (IS = 1 – 600 mM, |ζ-potential| = 5 – 50 mV) for TiO_2, CeO_2, SiO_2, and hematite particles of primary size in the range of 10 nm – 100 nm. Values of f_0 (eq [4-1]) were established from matching simulation predictions of agglomerate size with reported data (TiO_2, CeO_2, and SiO_2 of primary sizes of 21, 25, and 30 nm, respectively, and hematite of primary sizes of 12, 32, and 65 nm) within an error tolerance of ≤1% at which f_0 values changed by less than 0.1% upon further improvement in diameter prediction matching. In order to explore the effect of hydration repulsion energy on the NP agglomeration state, the magnitude of hydration repulsion energy (using the extracted f_0 values) was compared to the electrostatic repulsion energy at various IS and ζ-potential values. Additionally, NP agglomerate sizes were calculated from the PSD obtained from simulations with and without inclusion of the hydration repulsion energy in order to assess any deviations from the classical DLVO.

4.3 Results and Discussion

4.3.1 The Hydration Repulsion Surface Energy Density (f_0)

The best fit f_0 values for TiO_2, CeO_2, SiO_2, and hematite NPs suspensions were in the range of 3.01 – 3.35 mJ m^{-2} , 1.60 – 1.66 mJ m^{-2}, 0.80 – 1.52 mJ m^{-2}, and 2.85 – 2.91 mJ m^{-2}, respectively. The values for f_0 were extracted based on reported DLS NP size measurements. The

above ranges are within those reported for mica surfaces and for CeO_2 NPs [151, 152]. The f_0 values were essentially invariant with respect to IS and |ζ-potential| consistent with previous work [152]. However, it is important to note that the magnitude of f_0 can vary depending on the aquatic medium composition (e.g., presence of natural organic matter) and the NP surface chemistry. Given the above, it is reasonable to explore the effect of hydration repulsion energy on NP agglomeration based on average f_0 values (i.e., 3.13, 1.62, 1.23, and 2.88 mJ m^{-2} for TiO_2, CeO_2, SiO_2, and hematite, respectively). Agreement with reported experimental average agglomerate size and model predictions with the above f_0 values were with an average absolute relative error of 21% (corresponding to a correlation of pseudo R^2 of 0.87). Given the relatively large scatter in DLS measurements [154-160] (see §2.3.2) the above agreement is quite reasonable. For example, for the literature data used in the current work (Table A-2), standard deviations for repeated measurements of up to 24% and 50% have been reported for average agglomerate sizes of 21 nm and 25 nm primary sized TiO_2 [184] and CeO_2 [155] NPs, respectively. Similar behavior was observed in the present DLS measurements for TiO_2 NP suspensions for which the standard deviation was up to ~25.1% at high IS and low |ζ-potential| (Figure 4-1).

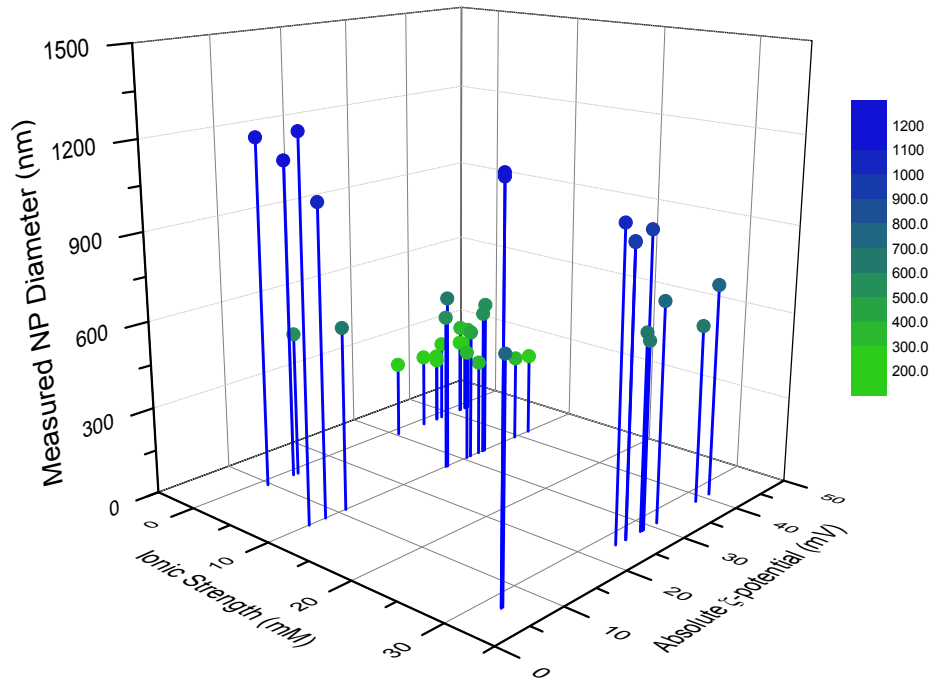

Figure 4-1. Average TiO_2 agglomerate diameter from present DLS measurements as a function of ζ-potential and IS. The standard deviation for triplicate measurements are 0.7-25.1%.

4.3.2 Effect of Hydration Repulsion on NP Agglomeration

The effect of hydration repulsion on NP agglomeration can be explored by noting the relative magnitudes of the different interaction energies as a function of particle-particle separation distances for different suspension conditions (i.e., IS and ζ-potential). Accordingly, an illustration is provided in Figure 4-2 showing the magnitudes of the different interaction energies for TiO_2, CeO_2, SiO_2, and hematite for a selected range of suspension conditions with respect to ζ-potential and IS. For the above three NPs, the electrostatic repulsion energy decreases by $\sigma(10^2)$ as the |ζ-potential| decreases from 40 mV to 5 mV (Figure 4-2). Similarly, as IS increases from 1 mM to 600 mM, the electrostatic repulsion energy decreases by $\sigma(10^1)$. The hydration repulsion energy increases with decreasing separation distance and depending on the suspension IS and |ζ-potential| can surpass the electrostatic potential. For example, for TiO_2 and

hematite at a relatively low IS of 1 mM and high |ξ-potential| of 40 mV, the hydration repulsion energy is a factor of ~22 and ~24, respectively, lower than the electrostatic repulsion energy at a particle-particle separation distance of 4 nm. As the separation distance decreases the hydration repulsion energy increases and at a separation distance of 0.1 nm, for example, it is a factor of 1.4 and 1.3 greater than the electrostatic repulsion energy, for TiO_2 and hematite, respectively (at the above IS and |ξ-potential| condition). For CeO_2 and SiO_2, at the above suspension conditions, the electrostatic repulsion energy is a factor of ~43 and ~56 greater than the hydration repulsion energy, respectively, at separation distance of 4 nm, but with corresponding factors of ~1.4 and ~1.8 greater as the separation distance decreases to 0.1 nm. As the IS increases from 1 mM to 600 mM and the |ξ-potential| decreases from 40 mV to 5 mV, the hydration repulsion energy for the above three NPs becomes much greater than the electrostatic repulsion energy. For example, for TiO_2, CeO_2, SiO_2, and hematite suspensions at IS = 600 mM and |ξ-potential| = 20 mV, the hydration repulsion energy is greater by at least a factor of 9, 5, 4, and 8 respectively, than the electrostatic repulsion energy. Overall, the illustration depicted in Figure 4-2 suggests that the significance of hydration repulsion (relative to electrostatic repulsion) increases with increasing IS and decreasing |ξ-potential|. Accordingly, for the above regime of suspension conditions, one would expect a greater effect of hydration repulsion on the resulting level of agglomeration.

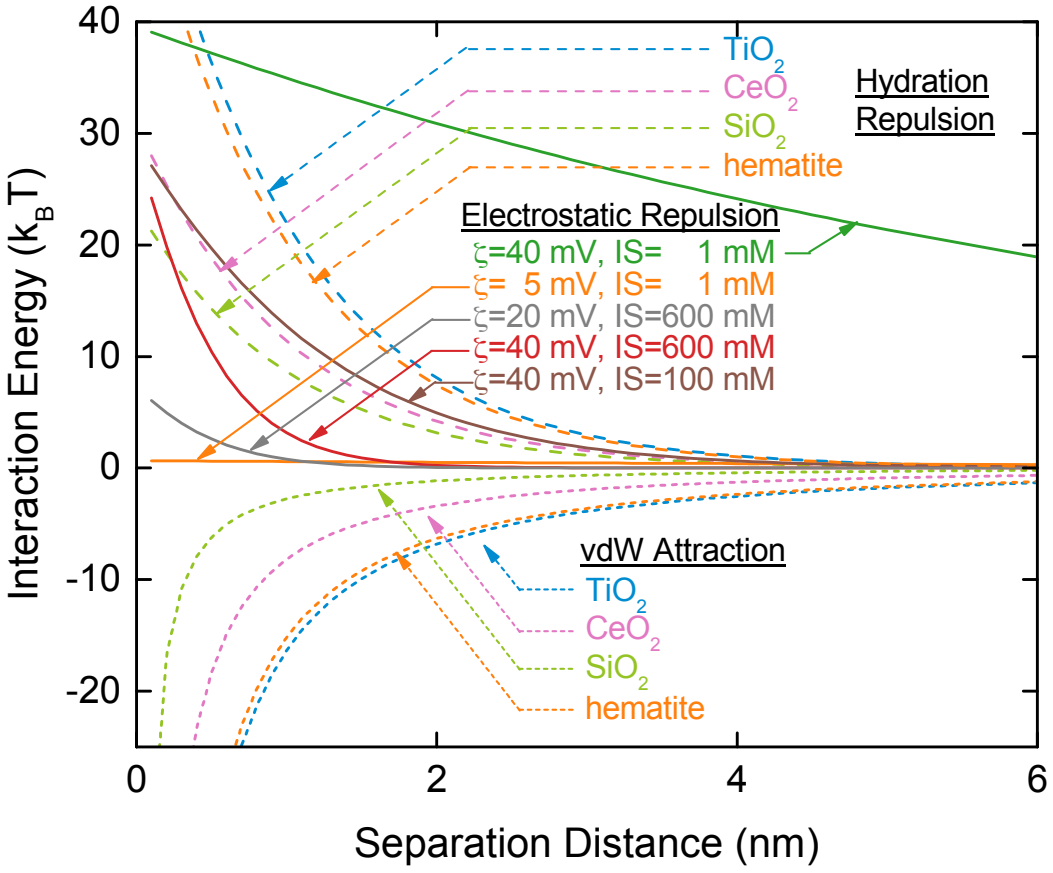

Figure 4-2. Comparison of the magnitude of particle-particle interaction energies for TiO2, CeO_2, SiO_2, and hematite. Conditions: d_p = 25 nm, A_H = 42 zJ (TiO_2), 21 zJ (CeO_2), 7.1 zJ (SiO_2), and 39 zJ (hematite), f_0 = 3.13 mJ m^{-2} (TiO_2), 1.62 mJ m^{-2} (CeO_2), 1.23 mJ m^{-2} (SiO_2), and 2.88 mJ m^{-2} (hematite).

Given the above analysis of the interaction energies, it is instructive to explore the impact of hydration repulsion on NP agglomerate diameter (Figure 4-3, Figure 4-6, and Figure 4-5) for a range of IS and |ξ-potential| conditions for the three NPs considered in this work. It is noted that in order to isolate the impact of hydration repulsion from that of primary NP diameter, the comparison is carried out for the same primary diameter of 25 nm. Hydration repulsion adds to the overall repulsion energy, thereby resulting in agglomerates that are of a smaller size than

would be predicted solely by the classical DLVO. For example, at |ζ-potential| of 5 mV the average NP agglomerate sizes for TiO_2, hematite, SiO_2, and CeO_2, NPs (Figure 4-3, Figure 4-4, Figure 4-5, and Figure 4-6) for IS range of 1 mM – 600 mM, are 1113 – 1186 nm, 1312 – 1431 nm, 436 – 520 nm, and 1198 – 1249 nm, respectively. However, if one adopts the classical DLVO without considerations of hydration repulsion, the predicted agglomerate diameters are higher by 57% – 93%, 26% – 72%, 119% – 138%, and 25% – 53%, for TiO_2, CeO_2, SiO_2, and hematite, respectively, at the above range of conditions.

As expected, the agglomerate size decreases with both increasing |ζ-potential| and decreasing IS, but the level of DLVO overprediction is most significant at high IS and low |ζ-potential|. For example, at the higher |ζ-potential| of 50 mV (for IS range of 1 mM – 600 mM), simulations with solely classical DLVO overpredict the agglomerate size of TiO_2, hematite, and CeO_2 by 5% – 85%, 3% – 38%, and 4% – 55%, respectively. For suspensions of low IS (1 mM), classical DLVO overpredicts agglomerate diameters by 5% – 120%, 3% – 82% and 2% – 57%, for TiO_2, hematite, and CeO_2, respectively, over the range of |ζ-potential| shown in Figure 4-3, Figure 4-4, and Figure 4-6, whereas in suspensions of high IS (600 mM), the corresponding overprediction is in the range of 85% – 93%, 38% – 53%, and 55% – 72%. It is noted that, predicted particle sizes with and without hydration repulsion energy appear to converge as IS reaches 1 mM and as |ζ-potential| exceeds 40 mV. This behavior is attributed to the electrostatic repulsion energy surpassing the hydration repulsion energy, the latter becoming negligible relative to the former at low IS and high |ζ-potential|.

It is noted that the TiO_2 NP agglomerate size is smaller by 3% – 37% than for CeO_2 over the range of conditions shown in Figure 4-3. This behavior is attributed to the higher hydration

repulsion energy (by a factor of 1.96, Figure 4-2) determined for TiO_2 relative to CeO_2. However, the classical DLVO predicts an opposite trend (i.e., greater agglomerate size for TiO_2 relative to CeO_2) since it neglects hydration repulsion, thereby resulting in larger predicted agglomerate sizes for TiO_2 given its larger van der Waals attraction energy relative to CeO_2 (by a factor of 2, Figure 4-2). For example, predicted agglomerate size based solely on classical DLVO is of 1748 – 1943 nm for CeO2 (primary size of 25 nm), for IS range of 10 – 120 mM and |ζ-potential| = 1.9 – 17 mV, which is about 23% - 98% higher than reported measurements [155] (Table A-2).

Although the effect of ζ-potential and IS on the predicted agglomerate diameter is quantitatively similar for TiO_2 (Figure 4-3), hematite (Figure 4-4), and CeO_2 (Figure 4-6), the agglomerate behavior of SiO_2 (Figure 4-5) is notably different. Over the IS range of 1-600 mV the agglomerate diameters, predicted both with and without accounting hydration repulsion energy, decrease rapidly with increasing |ζ-potential| and converge at large |ζ-potential| values (> 35 mV) toward the primary particle size (Figure 4-5). The above observed behavior for SiO_2 is attributed to the significantly greater electrostatic repulsion energy (even without the contribution of hydration repulsion) relative to the van der Waals attraction energy at sufficiently large |ζ-potential| (Figure 4-2), owing to the small Hamaker constant for SiO_2 (Hamaker constant of 7.1 zJ).

Finally, it is noted that for the range ζ-potential and suspension IS evaluated in the present work (§3.3.3 and present Chapter), the agglomerate diameter is predicted to decrease with increasing primary size (Figure 4-7). This behavior occurs both with and without the addition of hydration repulsion to the classical DLVO; however a more significant agglomerate size decrease (with increasing primary diameter) results when hydration repulsion is not considered

in the aggregation model. The decrease in agglomerate size with increasing NP primary size is consistent with previous studies that reported on the agglomeration of aqueous suspensions of TiO_2 (primary size 5 and 32 nm, IS = 20 mM [196]; primary size 5 nm – 100 nm, DI water [197]; primary size 10 – 50 nm, IS = 0.5 mM [49]), hematite (primary size 12 – 65 nm, IS = 1 – 100 mM [68]), Cu (primary size 40 – 80 nm, DI water [197]), and Au (10 and 30 nm, IS ~= 0.1 mM [198]) nanoparticles. The above behavior can be rationalized by noting that the net repulsion energy decreases (eqs [4-1], [3-6],[3-7], and [3-8]) while the collision frequency will increase (eq [3-4]) for agglomerating suspensions of smaller primary size NPs.

It is acknowledged, that the trend of increasing agglomerate size with increasing primary size, for a given NP type, can also be found in the literature as reported for example for TiO_2 (primary size 6 – 104 nm, DI water [199]; primary size 15 and 195 nm, DI water [64]), Al (primary size 50 – 120 nm, DI water [197]), and SiO_2 (primary size 5 and 25 nm, IS = 684 mM [200]). Providing a definitive conclusion based on reported literature data regarding the dependence of agglomerate size on primary size is a challenge given that various experimental factors can affect experimental DLS measurements including, but not limited to, the protocol for preparation of NP suspensions (e.g., sonication intensity and duration, suspension concentration and possible use of centrifugation for attaining a stable suspension) [64, 196], dependence of NP surface charge (and thus its isoelectric point) on primary size [199, 201], in addition to variability of structure and possibly chemistry of NP surfaces, on the synthesis method [199].

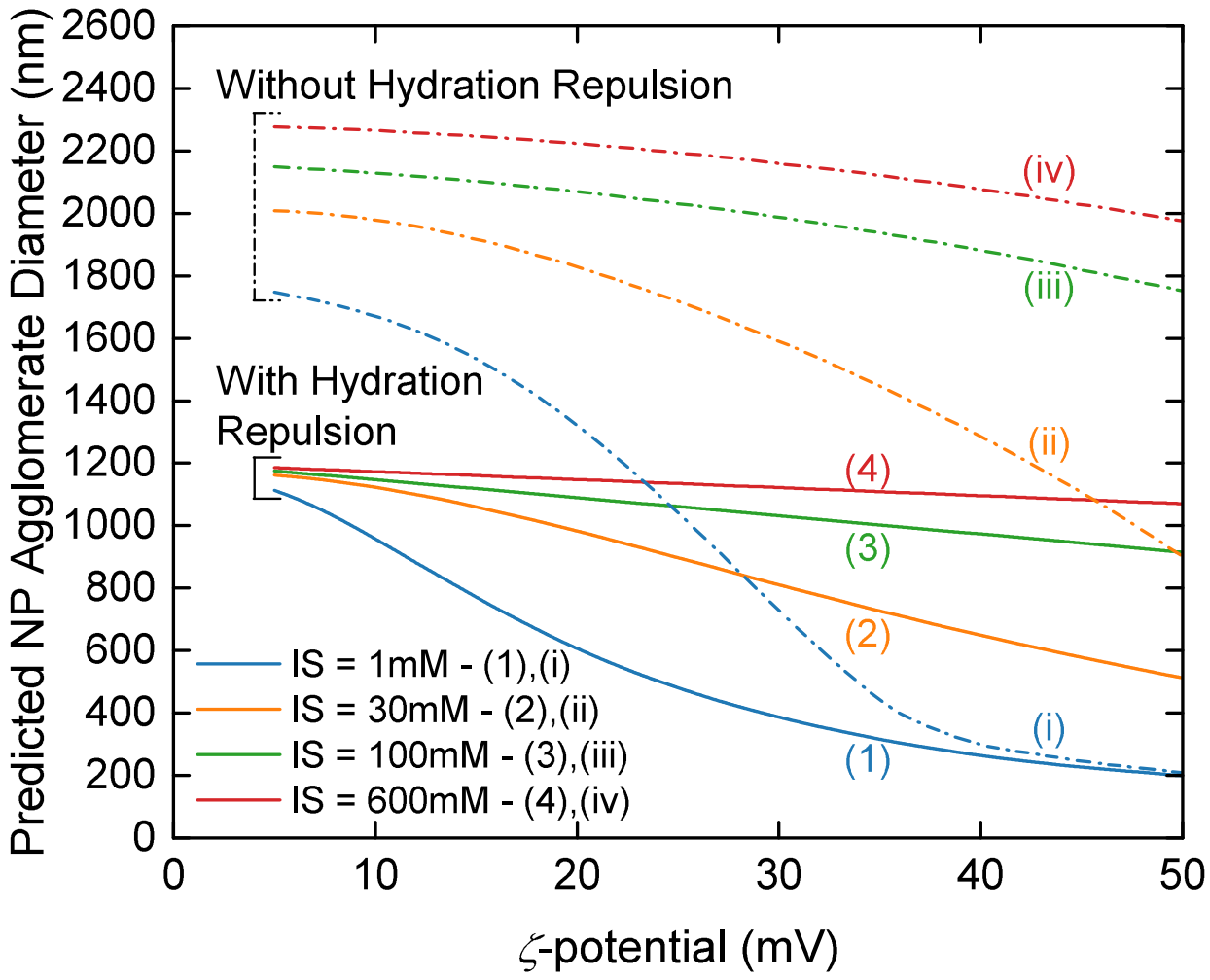

Figure 4-3. Predicted TiO_2 agglomerate diameter as a function of ξ-potential and IS. Simulation condition: $A_H = 42$ zJ, $f_0 = 3.13$ mJ m^{-2}, $d_p = 25$ nm.

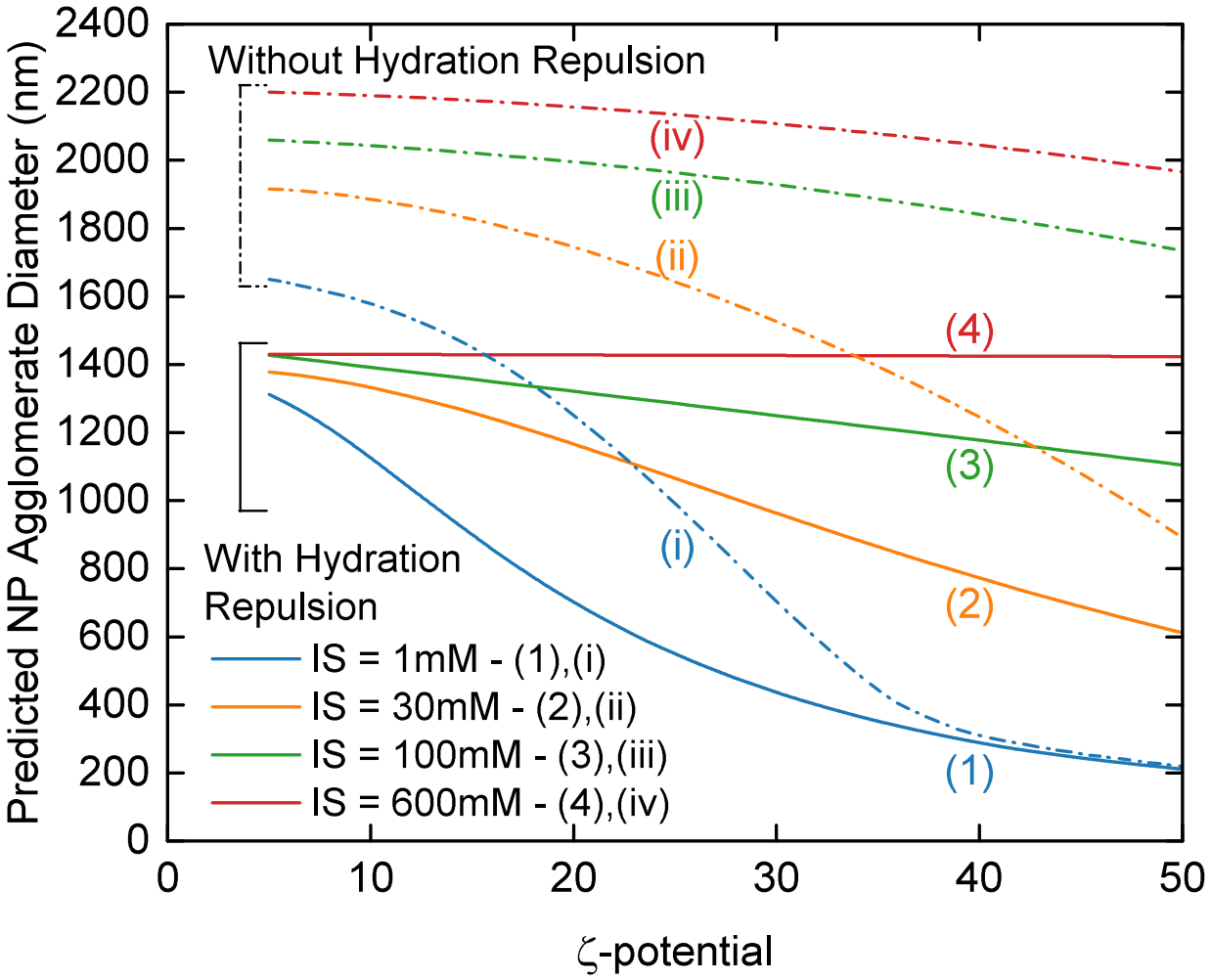

Figure 4-4. Predicted hematite agglomerate diameter as a function of ζ-potential and IS. Simulation condition: A_H= 39 zJ, f_0 = 2.88 mJ m^{-2}, d_p = 25 nm.

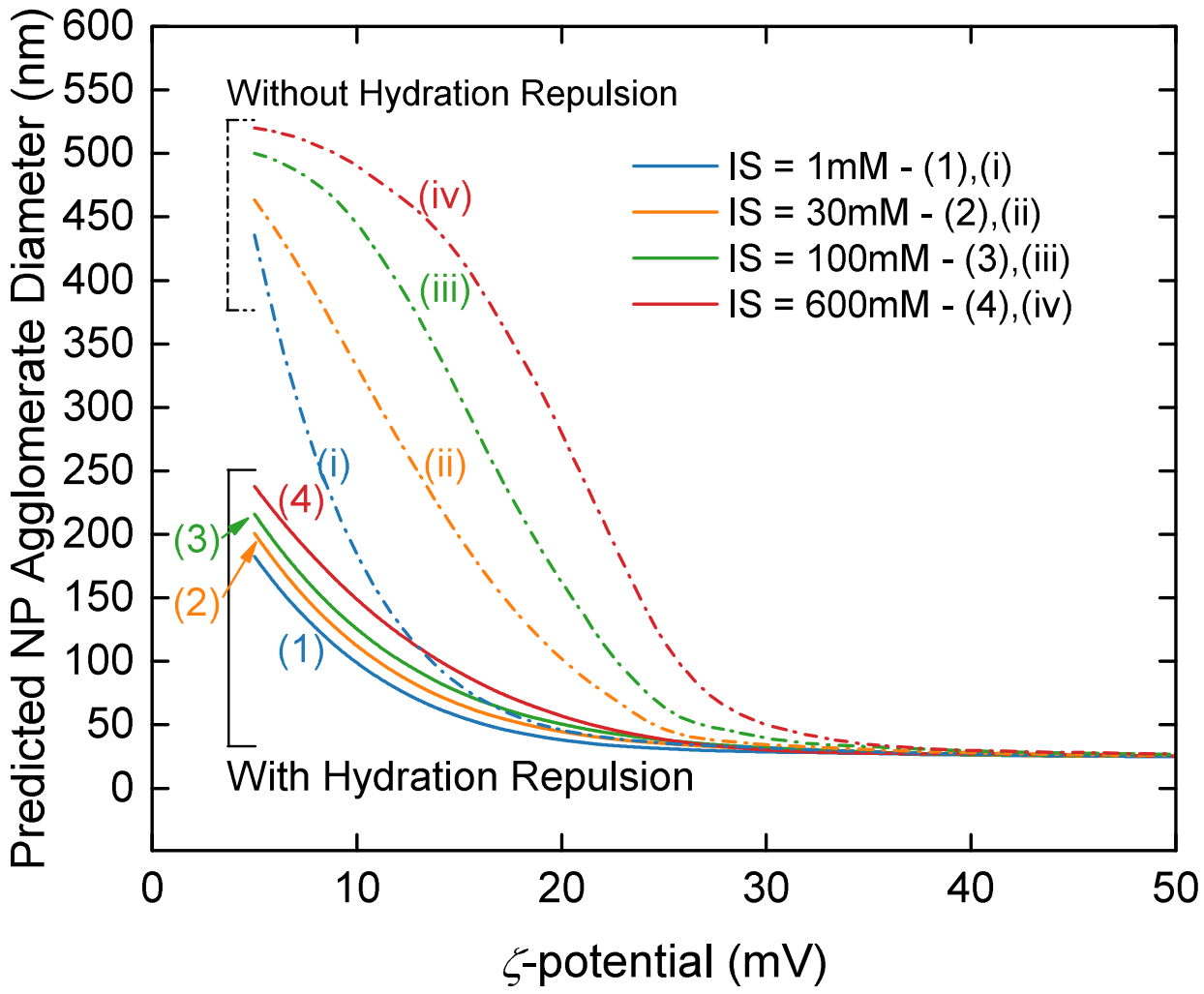

Figure 4-5. Predicted SiO_2 agglomerate diameter as a function of ζ-potential and IS. Simulation condition: $A_H = 21$ zJ, $f_0 = 1.23$ mJ m^{-2}, $d_p = 25$ nm.

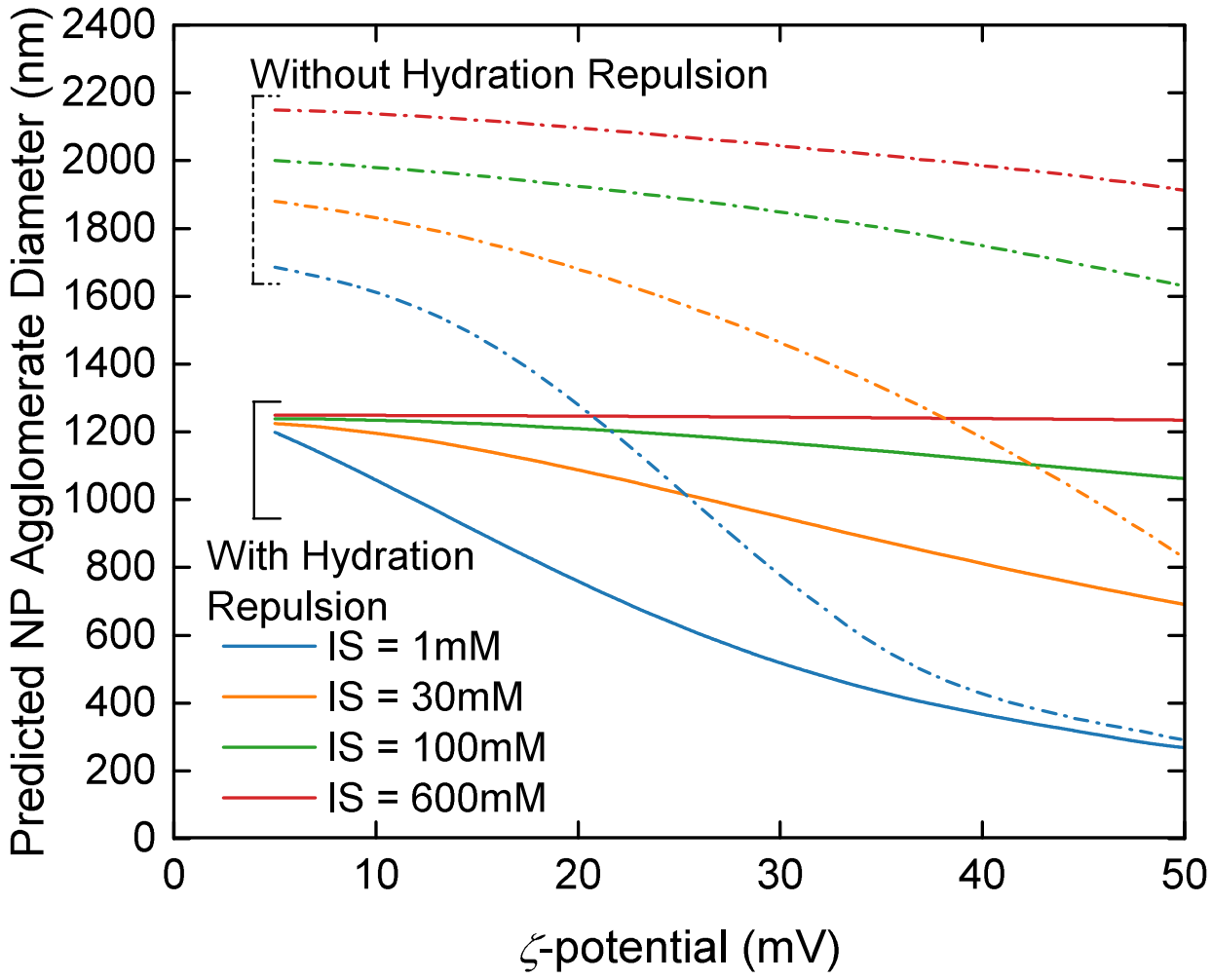

Figure 4-6. Predicted CeO_2 agglomerate diameter as a function of ζ-potential and IS. Simulation condition: A_H= 21 zJ, f_0 = 1.62 mJ m^{-2}, d_p = 25 nm.

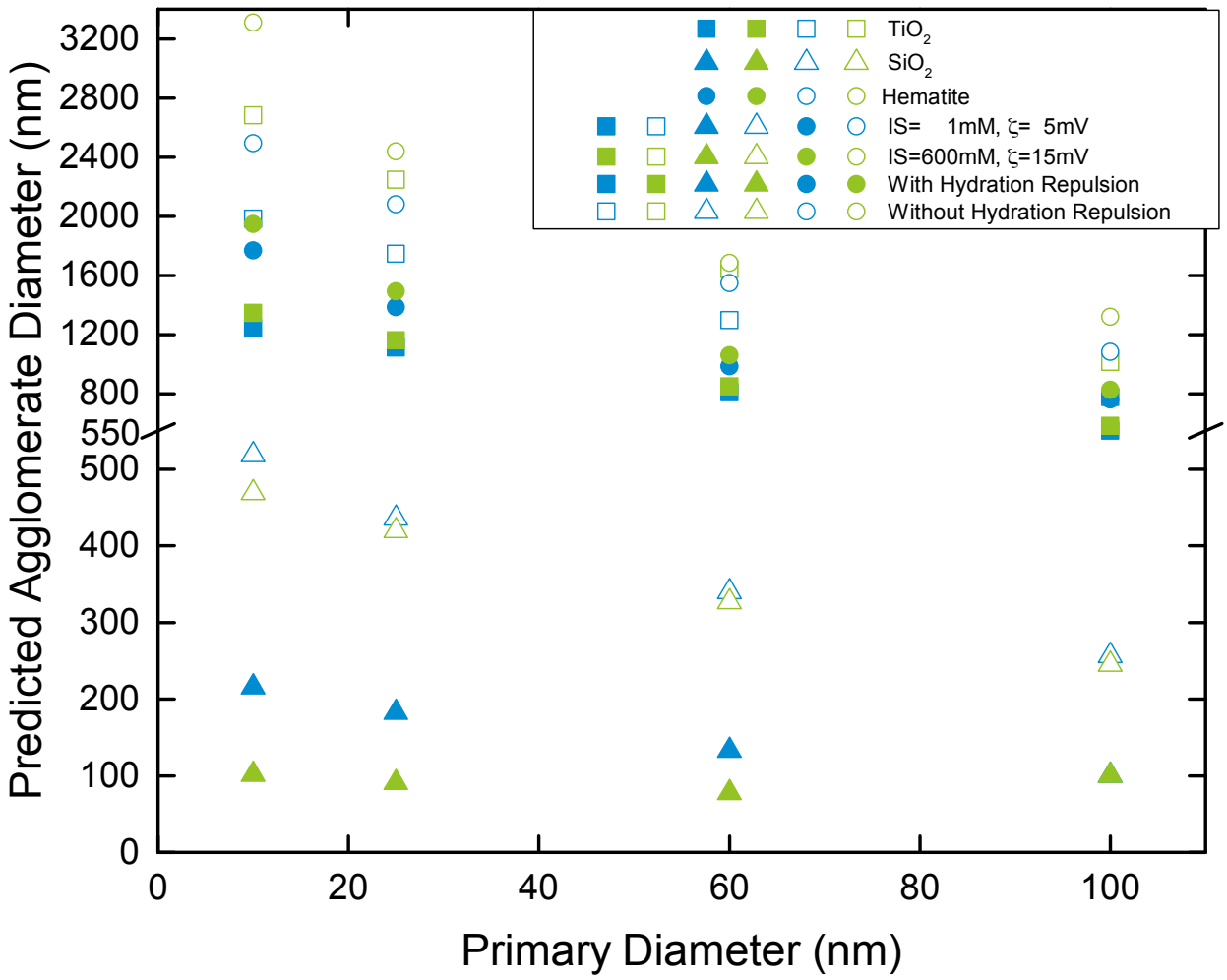

Figure 4-7. Predicted agglomerate diameter as a function of primary NP diameter over a primary diameter range of 10 – 100 nm, for TiO_2 (square), SiO_2 (triangle), and hematite (circle) at suspension conditions of: (a) IS=1 mM and for ζ-potential=5 mV (blue), and (b) IS=600 mM and ζ-potential=15 mV (green), in simulations with (filled) and without (empty) inclusion of hydration repulsion.

4.4 Conclusions

In summary, at the conditions of high IS and low |ζ-potential| the hydration repulsion energy can significantly surpass the electrostatic repulsion energy. Increased overall repulsion energy can then result in a significantly lower agglomerate diameter than predicted by the classical DLVO. While the classical DLVO theory is adequate for predicting NP agglomeration in suspensions of low IS (~< 1 mM) and high |ζ-potential| (~> 35 mV), it can significantly overpredict agglomerate sizes at high IS or low |ζ-potential|, e.g., by up to a factor 5 for the studied NPs (TiO_2, CeO_2, SiO_2, and hematite) over a primary size range of 10 – 100 nm.

Chapter 5. Dose Estimation for *in vitro* Toxicity Studies

5.1 Overview

There is a growing interest and efforts by the toxicology community to investigate whether toxicity determined in *in vitro* high throughput screening (HTS) experiments should be ascribed to delivered ENM dose (essentially ENM mass that sediments in HTS plate wells) or the conventional metric of administered concentration [56-59]. In such studies, cells in the HTS plate wells typically settle to the bottom, and ENMs, which are introduced into the wells as a suspension, may also settle to the bottom of the wells (i.e., on top of the cells) over the course of the experimental period. Experimental determination of the delivered dose for the wide range of ENMs, culture media, and HTS plate dimensions – all of which would affect ENM sedimentation – is a significant challenge. Therefore, in order to quantify the delivered dose, computational models have been developed to estimate the mass of ENMs that is likely to deposit to the bottom of *in vitro* plates [56, 58]. Previous studies [56, 58], which relied on analytical solution of the convection-diffusion equation to determine the delivered dose, have been able to reasonably predict (within ~9% average absolute relative error) the fraction of ENMs that settled for 3 CeO_2 suspensions (initial concentration of 12.5 $\mu g\ mL^{-1}$) in Dulbecco's Modified Eagle's Medium (DMEM) cell culture medium. However, those previous models utilized a single average particle size instead of the complete PSD in estimating the delivered dose [56, 58] while also not considering the permeability of ENMs fractal agglomerates. Such simplified models may result in unintended bias due to neglect of the tails of the PSD, which may have significant impact on toxicological response [163], as well as failing to consider the possible partial draining nature of the ENM agglomerates [202-204]. Accordingly, an improved

model was developed to estimate *in vitro* delivered dose while considering the full PSD, based on the particles in a box simulation approach, where the motion of the particle is given by Brownian diffusion and modified Stokes' settling.

The model developed in the present work to predict ENM sedimentation makes use of ENM properties (initial PSD, density, fractal dimension) and suspension properties (density, media depth, media viscosity, ENM concentration) as input to calculate, as a function of time: a) the fraction of the initial ENM mass (in the suspension) that would settle to the bottom (i.e., delivered dose) of *in vitro* HTS plate wells (typically ~3 mm), and b) the change in ENM PSD over time (i.e., due to sedimentation). The fraction of ENM mass that settles to the bottom of the HTS plate well at time t (f_t^s) is calculated from:

$$f_t^s = \frac{\sum_{i=1}^{S} m_i}{\sum_{j=1}^{N} m_i} \qquad [5\text{-}1]$$

where i=1…S denotes the ENM agglomerates that have settled, j=1…N represents the ENM agglomerates initially in the simulation box and m_i [kg] is the mass of ENM agglomerate i (i.e., $m_i = \rho_{e,i} \cdot \pi \cdot d_i^3/6$). The fraction of particles that settle from an initial suspension of a given PSD is determined via the simulation approach described in Section 5.2.

5.2 Simulation Approach

The modeling approach for particle sedimentation is based on a simulation of particles in a box containing randomly distributing N ENM particles (typically 10^5). The simulation starts with a set of N particles with diameters sampled following a specified PSD that may be obtained from experimental measurements of the ENMs PSDs in the liquid medium being evaluated. The above sampling can be accomplished, for PSDs that is in a functional distribution form (e.g., normal or

log-normal distribution), by generating N random numbers from the specified distribution. Alternatively, for PSDs that are in a discretized form (i.e., an array of size bins with corresponding frequencies (i.e., percent of total particles with sizes in a given size bin)), the sampling of ENM diameters can be carried out by first allocating m_l particles to each bin, l, based on the above specified frequencies, such that $m_l = N \cdot f_l^b / \sum_{l=1}^{M} f_l^b$, where f_l^b is the frequency for bin l, and l=1…M denotes the size bins. Subsequently, for each bin l, the particle sizes for each of the m_l particles are obtained by generating m_l uniformly distributed random numbers between the minimum and maximum particle sizes of the bin. The simulation divides a total simulation time of t_{final} [s] into n equal time steps (typically 100), whereby at each time step, the vertical positions of all ENM agglomerates in suspension are updated based on the particle displacement due to Brownian diffusion and gravitational settling. The vertical travel distance for particle i (Δz_i) is determined for each time step ($\Delta t\ [s] = t_{final}/n$) for all particles in the box according to:

$$\Delta z_i = \Delta z_{S,i} + \Delta z_{B,i} \qquad [3\text{-}11]$$

where $\Delta z_{S,i}$ and $\Delta z_{B,i}$ are the gravitational settling and diffusion travel distances in the vertical direction, respectively, of ENM agglomerate i (i.e., relative to their vertical position in the previous time step), as lateral particle movements (due to Brownian motion) do not contribute to vertical repositioning of particles. Therefore vertical particle travel distance attributed to Brownian diffusion, $\Delta z_{B,i}$, (positive or negative for upward or downward movement, respectively) is calculated by sampling a random number from a normal distribution with $\mu = 0$ and $\sigma = \sqrt{2 \cdot D_i \cdot \Delta t}$ [149, 168] such that

$$z_{B,i} \sim \mathcal{N}(0, 2 \cdot D_i \cdot \Delta t) \quad [3\text{-}13]$$

in which D_i is the Brownian diffusivity [$m^2 s^{-1}$] determined from [149, 168]

$$D_i = \frac{kT}{6\pi\mu r_i} \quad [3\text{-}14]$$

The gravitational sedimentation distance ($\Delta \mathbf{z}_{S,i}$, negative for downward movement) is estimated based on a modified Stokes' settling velocity ($v_{S,i}$) accounting for the porosity and permeability of the ENM agglomerate:

$$z_{S,i} = \Delta t \cdot v_{S,i} \quad [5\text{-}2]$$

At each time step (Δt), particles with vertical positions below the bottom boundary of the box (i.e., $z_{i,\tau} = z_{i,\tau-1} + \Delta z_i \leq 0$, where $z_{i,\tau}$ and $z_{i,\tau-1}$ are the particle vertical positions at time step τ and $(\tau - 1)$, respectively) are considered to have settled to the bottom of the box (i.e., the *in vitro* plate well) and thus no longer present as suspended particles (i.e., in the suspension).

ENMs that readily agglomerate in aqueous suspensions typically exist as a fractal structures (Figure 1-1). These fractal aggregates may be partially draining as has been discussed in a number of studies on gravitational settling of fractal agglomerates [202-204]. These studies have demonstrated that the assumption of impermeable agglomerates can lead to significant underestimation (by up to an order of magnitude and higher) of the agglomerate settling velocity. Accordingly, modifications to the classical Stokes' settling velocity have been proposed, whereby the correction factor takes the form [204]:

$$\Gamma = \frac{v_{s,i}^{permeable}}{v_{s,i}^{impermeable}} = \frac{\xi_i}{\xi_i - \tanh(\xi_i)} + \frac{3}{2\xi_i^2} \quad [5\text{-}3]$$

where $v_{s,i}^{permeable}$ and $v_{s,i}^{impermeable}$ are settling velocity of a permeable agglomerate and impermeable sphere of the same diameter , respectively. The dimensionless permeability of the fractal agglomerate i is designated by ξ_i, which is related to the permeability of the fractal agglomerate ($\kappa_{p,i}$) via $\xi_i = d_i/2\sqrt{\kappa_{p,i}}$ [203]. The Stokes' settling velocity for an impermeable sphere is expressed as:

$$v_{s,i}^{impermeable} = \frac{(\rho_{e,i} - \rho_f) \cdot g \cdot d_i^2}{18 \cdot \mu} \quad [5\text{-}4]$$

in which $\rho_{e,i}$ [g L^{-1}] and d_i [m] are the particle effective density and diameter, respectively, ρ_f is the fluid density, g is the gravitational constant [m^3 kg^{-1} s^{-2}], and μ is the medium viscosity [Pa s]. Since ENMs agglomerates have a fractal structure their effective density $\rho_{e,i}$, which is lower relative to that of a solid sphere of the same diameter, can be estimated as:

$$\rho_{e,i} = \rho_p \cdot (1 - \phi_i) + \rho_f \cdot \phi_i) \quad [5\text{-}5]$$

where ρ_p is the ENM material density, ϕ_i is the dimensionless ENM porosity related to the fractal dimension, d_f, by:

$$\phi_i = 1 - (d_i/d_p)^{d_f - 3} \quad [5\text{-}6]$$

in which d_p is the primary ENM diameter. It is noted that if an experimental measurement of the average effective density of the ENM agglomerates in suspension is available, the fractal dimension may be extracted by fitting eq [5-5] to experimental measurements of effective density [205].

Various expressions have been proposed for the permeability of a fractal agglomerate (e.g., Carman-Kozeny equation[206], Brinkman equation[207], Happel equation [208]). However, these permeability expressions are based on the assumption of primary particles and pores that are uniformly distributed; this simplification is unrealistic for fractal agglomerates, and results in significant underestimations (by up to a factor of 2) of the settling velocity [203, 209, 210]. In order to overcome the above limitation, modified permeability expressions were proposed [203], where an agglomerate is taken to be consist of a few ($\sigma(10^0)$) principle clusters (of primary particles) resulting in larger pores between principal clusters [203]. Among the various proposed modified permeability expressions, the Brinkman and the Happel equations were assessed to be most suitable for fractal agglomerates over a wide range of fractal dimension (d_f = 1.7 – 2.5) [203]. For example, the dimensionless permeability based on the modified Brinkman equation, which is used in the present analysis, is given as [203]

$$\xi_i = 4.2\left(\frac{n}{c}\right)^{\frac{1}{d_f}}\left[3+\frac{4}{c}\left(\frac{n}{c}\right)^{\frac{3-d_f}{d_f}}-3\sqrt{\frac{8}{c}\left(\frac{n}{c}\right)^{\frac{3-d_f}{d_f}}-3}\right]^{-\frac{1}{2}} \qquad [5\text{-}7]$$

in which n is the number of principal clusters (typically $n \geq 4$ [203]), c is a packing coefficient reported to be in the range of 0.15-0.25 [203]), and d_f is the fractal dimension. The above expression can then be used in eq [5-3] to calculate the settling velocity for the ENM aggregates.

5.3 Data Compilation

The ENM sedimentation model was validated using published data for sedimentation of CeO_2 (primary size of 20 nm) in deionized water (neutral pH) [211]. The above data were supplemented with a series of 1-day sedimentation experiments for CoO and Co_3O_4 whereby the suspension concentration in cell culture media (BEGM and DMEM) was determined (as was in

[211]) before and after sedimentation via ICP-OES (ICPE-9000, Shimadzu, Japan) following the approach described in [212]. Briefly, from the initial suspension and after allowing ENMs to settle for 24 hr, 0.9 mL of the "supernatant" was withdrawn and dissolved in 10 mL of concentrated nitric acid (HNO_3, 65-70%, Trace Metal Grade) for acid digestion in a HotBlock (SC100, Environmental Express) at 95°C, which is placed in the fume hood and the digested solution is air dried overnight. The dried sample was then extracted into a 8 mL of 2% diluted nitric acid and heated at 80°C for a period of 3 hrs. After cooling the sample to room temperature, additional 2% nitric acid was added to reach a total volume of 8 mL for ICP-OES analysis.

The initial PSDs for CoO, Co_3O_4, Cr_2O_3, CuO, Mn_2O_3, Ni_2O_3, TiO_2, ZnO were determined via DLS (ZetaPALS; Brookhaven Instruments, Holtsville, NY) analysis following the suspension preparation approach of [60]. Additionally, effective density measurements of CoO, Co_3O_4, Cr_2O_3, CuO, Mn_2O_3, Ni_2O_3, TiO_2, ZnO were obtained following the approach of [57]. Physicochemical properties of the settling systems are reported in Table 5-1. Finally, the PSD for CeO_2 in DI water was obtained from [211].

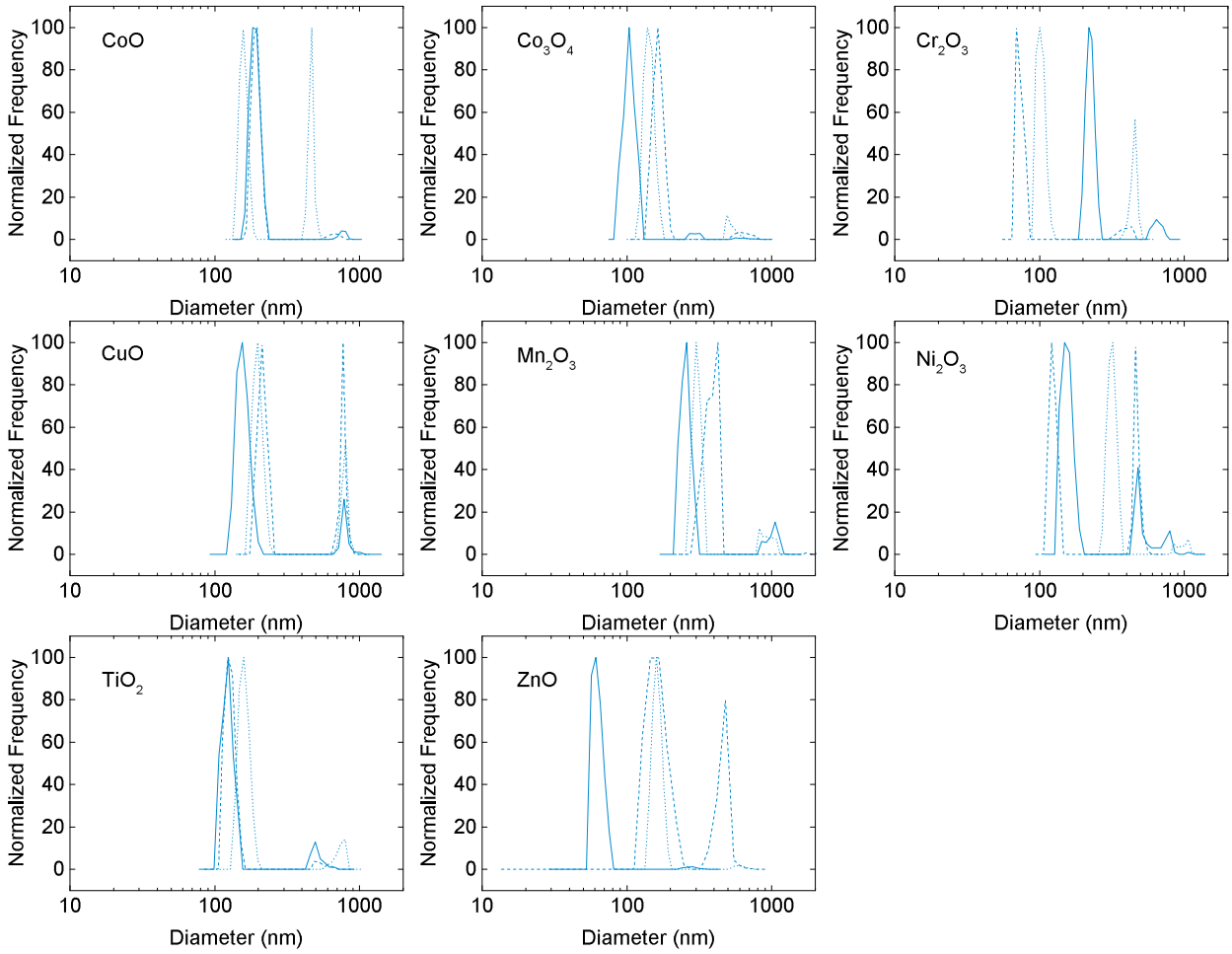

Figure 5-1. Particle size distribution of 8 metal oxide ENMs (CoO, Co_3O_4, Cr_2O_3, CuO, Mn_2O_3, Ni_2O_3, TiO_2, and ZnO) suspensions, obtained via DLS measurements in BEGM cell culture. The solid, dash, dotted lines in each sub-figure represent repeated measurements.

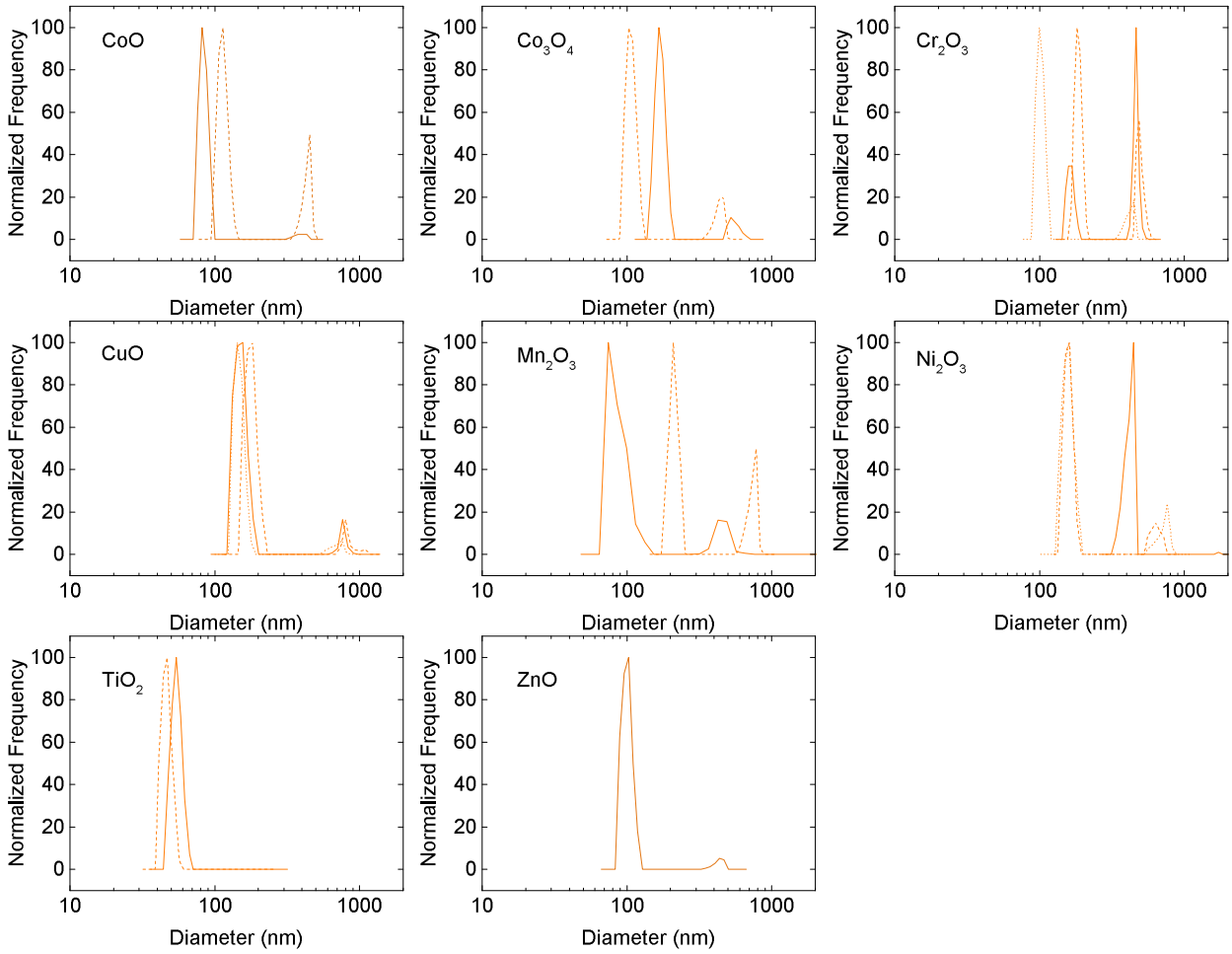

Figure 5-2. Particle size distribution for 8 metal oxide ENMs (CoO, Co_3O_4, Cr_2O_3, CuO, Mn_2O_3, Ni_2O_3, TiO_2, and ZnO) suspensions, obtained via DLS measurements in DMEM cell culture media. The solid, dash, dotted lines in each sub-figure represent repeated measurements.

Table 5-1. Summary of physicochemical properties of media and ENMs

Physicochemical Property	**Value**
Comparison with Quik, et al., 2010 [211]	
Water viscosity (μ), kg $m^{-1}s^{-1}$	0.000894 (25 °C)
Water density (ρ), g mL^{-1}	0.997
Media height (h), mm	22.5[a]
Fractal dimension (d_f)	2.45
Primary diameter (d_p), nm	20
ENM material density (ρ_p), g mL^{-1}	7.2
Initial ENM suspension concentration, mg L^{-1}	10
Present measurements	
Medium viscosity (μ), kg $m^{-1}s^{-1}$	0.00094 (BEGM [213]) and 0.00095 (DMEM [214])
Medium density (ρ), g mL^{-1}	0.984
Media depth (h), mm	22 [b] and 3.15[c]
Fractal dimension (d_f)	1.62–2.17[d]
Primary diameter (d_p), nm	71.8 (CoO), 10 (Co_3O_4), 193 (Cr_2O_3), 12.8 (CuO), 51.5 (Mn_2O_3), 140.6 (Ni_2O_3), 12.6 (TiO_2), 22.6 (ZnO) [215]
ENM material density (ρ_p), g mL^{-1}	6.44 (CoO), 6.11 (Co_3O_4), 5.22 (Cr_2O_3), 6.31 (CuO), 5 (Mn_2O_3), 4.84 (Ni_2O_3), 3.9 (TiO_2), 5.6 (ZnO)
Initial ENM suspension concentration, mg L^{-1}	100

[a] estimated based on 100 mL of solution in a 250 mL flask
[b] height of typical cuvette
[c] height of typical 384 well high throughput plate well
[d] extracted based on density measurements

5.4 Results and Discussion

Model predictions for the fractions of CeO_2 ENMs that settle over periods of 12, 24, 36, and 48 hrs (Figure 5-3) were compared with results from sedimentation experiments reported [211], for suspension in DI water (initial CeO_2 concentration of 10 g mL^{-1}). Excellent agreement between predictions and measurements of the fraction of ENMs that settled was obtained (average relative absolute error of 9.7%), demonstrating that the present model is suitable for quantitative prediction of sedimentation kinetic. Comparison was also made between model prediction and ICP measurements of the fraction of CoO and Co_3O_4 ENMs that settled in cell culture media (BEGM and DMEM) (Figure 5-2). Reasonable agreement was also obtained between predictions and experimental measurements (average relative absolute error of 14.8%) suggesting that the sedimentation model is of reasonable accuracy even for cell culture media.

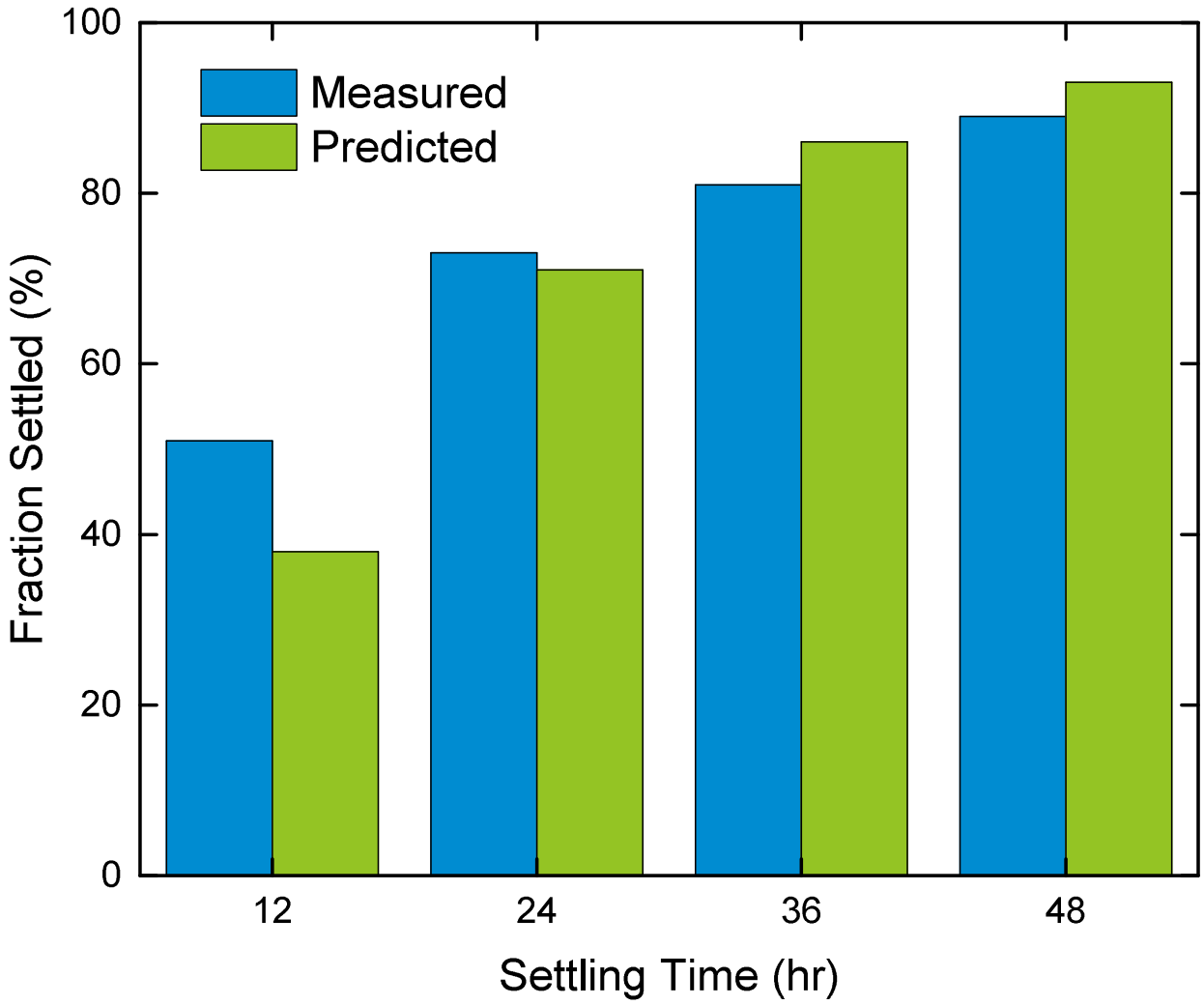

Figure 5-3. Comparison between measured and predicted mass fraction of CeO_2 that settled after 12, 24, 36, and 48 hrs in DI water. (Initial suspension concentration: 10 mg L^{-1}; primary ENM size: 20 nm; Table 5-1)

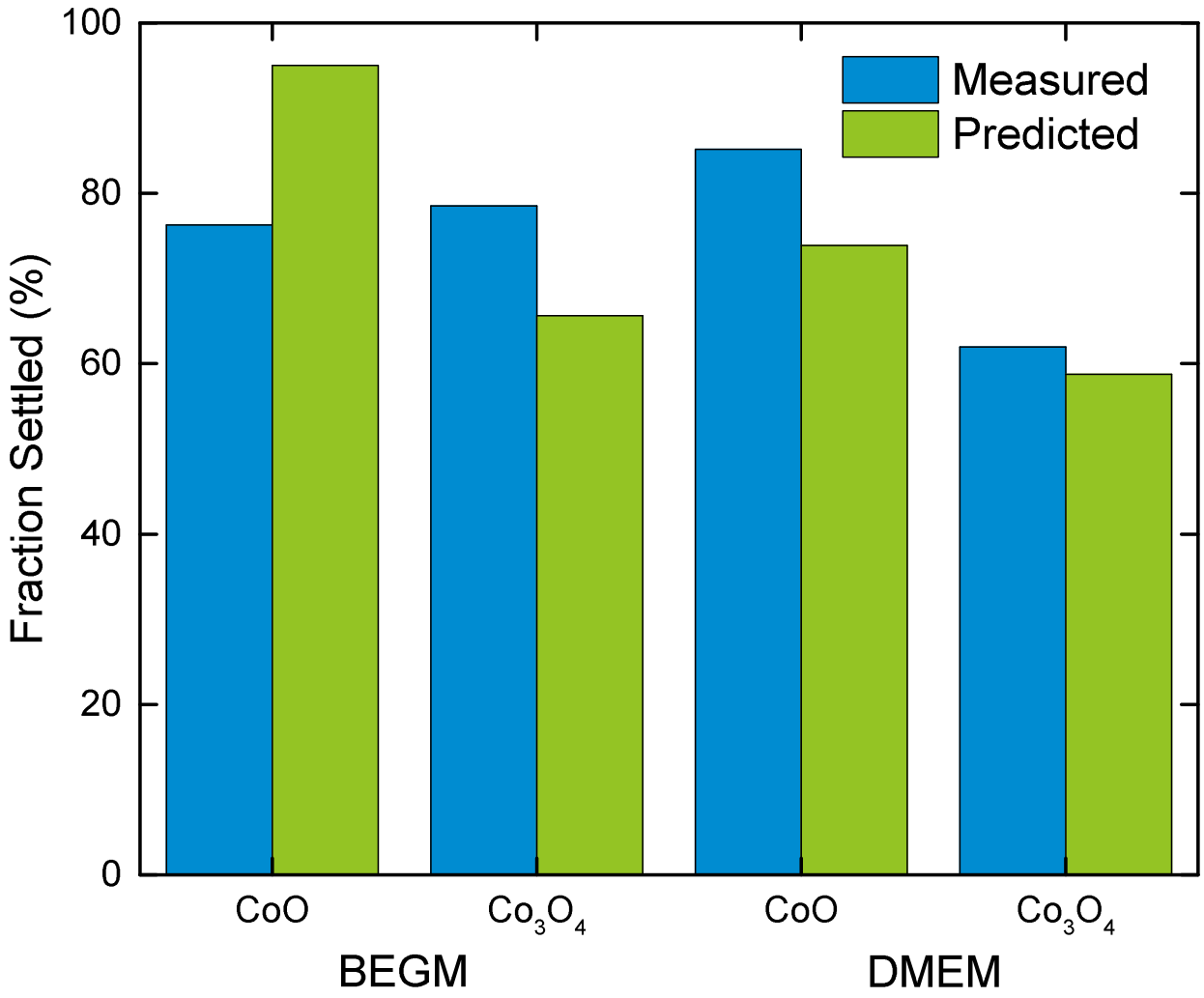

Figure 5-4. Predicted and measured mass fraction of ENMs that settled after 24 hrs for CoO and Co_3O_4, in two culture media. (Initial suspension concentration: 100 mg L^{-1}, primary ENM size: 71.8 nm (CoO) and 10 nm (Co_3O_4), media height (h) = 22 mm; Table 5-1).

In the above simulations, the number of principle clusters (n) was taken to be 4, consistent with the published literature [203]. However, in order to assess the sensitivity of the simulation results to the value of n, simulations were carried out, with varying n values (Figure 5-5). The results indicate that the fraction of ENMs settled decreased by 8.8% as n increased from 4 to 10. This behavior is expected since larger n would result in smaller pores for the media to permeate

(i.e., flow) through the fractal agglomerate. However, the relatively small change in the fraction of ENMs settled (8.8%) due to an increase of *n* by a factor of 2.5 (i.e., from 4 to 10) suggests little sensitivity to *n* over the above range of values.

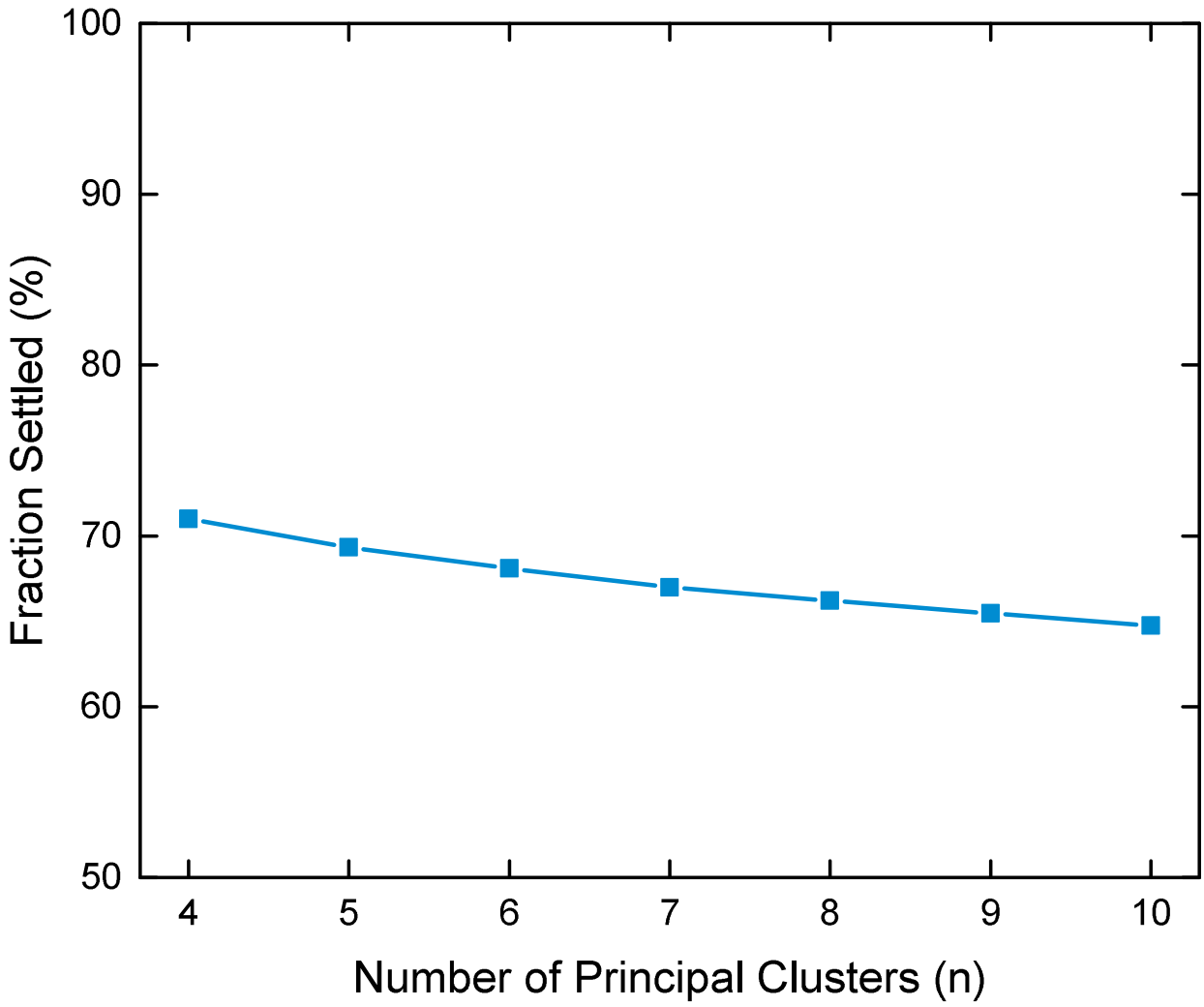

Figure 5-5. Effect of number of principals cluster on predicted fraction of ENMs settled (at the end of 24 hr period) for CeO_2 in DI water. (Simulation conditions were the same as those in Figure 5-3, initial suspension concentration: 10 mg L^{-1}; primary ENM size: 20 nm; Table 5-1).

Simulations were also carried out to quantify the effect of ENM permeability on the predicted fraction of ENMs that settled over a 24 hr period (Figure 5-6; using the test case of 100

mg L^{-1} TiO_2 ENM suspension of 12.6 nm primary diameter in DI water). Simulation results comparing the settling of permeable versus impermeable ENM agglomerates revealed that fraction of permeable ENM agglomerates that settled is greater than that of impermeable agglomerates by a factor of 1.46 – 1.93. The degree of underprediction of the fraction of ENM settled when assuming impermeable agglomerates increased with increasing ENM agglomerate diameter (from a factor of 1.46 to 1.93, over the range of ENM diameter in Figure 5-6, i.e., 200 – 1000 nm). The above correlation in the degree of underprediction with ENM agglomerate diameter is attributed to Brownian diffusivity, which is greater for smaller particles (eq [3-14]). Although sedimentation velocity correction factor (Γ) remains constant with respect to ENM agglomerate size, the fraction of ENM settled for smaller particles is more significantly dependent on the Brownian diffusivity, and to a lesser degree so on the settling velocity. Thus, for smaller ENM agglomerates, the increased settling velocity (due consideration of particle permeability) contributes less to the increase in fraction of ENM settled, relative to larger ENM agglomerates. Additionally, as ENM agglomerate diameter (d) increased by a factor of 5 (from 200 to 1000 nm), the fraction of ENM settled increased by factors of 3.79 and 5.01 for impermeable and permeable agglomerates, respectively. The above increase in fraction of ENM settled is significantly lower (by a factor of 5 – 6.6) than the value based on unmodified Stokes' settling (eq [5-4]), where settling velocity (and by extension fraction of ENMs settled) increases $\propto d^2$. The above behavior can be understood by noting that ENM porosity (ϕ) also increases with increasing d (eq [5-6]), thereby resulting in reduced effective density (see eq [5-5]) and thus lower settling velocity. Over the range of particle diameter shown in Figure 5-6 (i.e., 200 – 1000 nm), the increase in ϕ is from 91.6% to 98.0%.

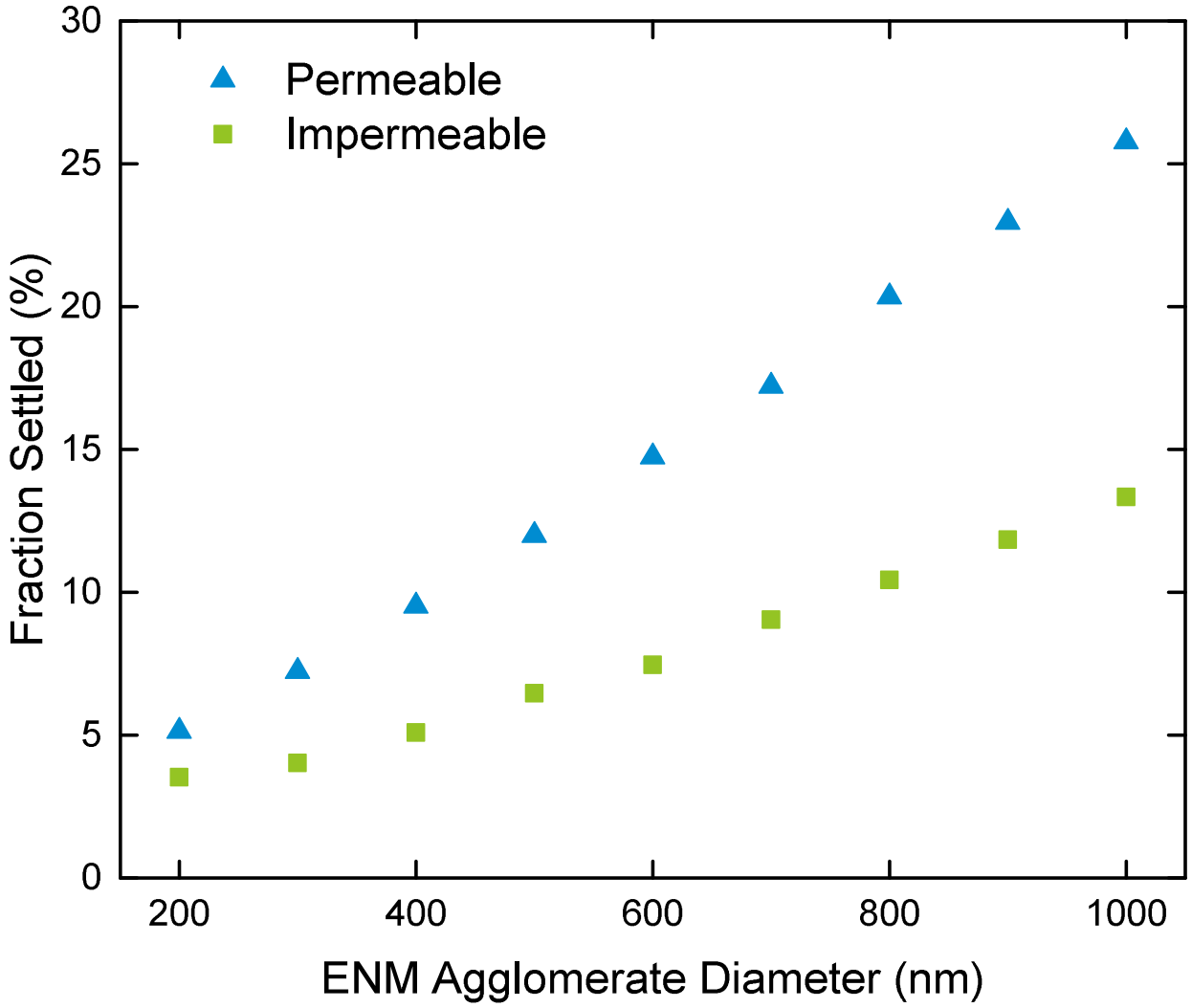

Figure 5-6. Effect of agglomerate permeability on the mass fraction of ENMs that settles over a period of 24 hr. The example is for TiO_2 ENM (ρ_p = 3.9 g mL^{-1}, primary size= 12.6 nm, d_f = 2.1). Simulation conditions are the same as those in Figure 5-3.

Lastly, in order to illustrate the application of the dosimetry model, simulations were carried out to determine the delivered dose of 8 metal oxide ENMs (CoO, Co_3O_4, Cr_2O_3, CuO, Mn_2O_3, Ni_2O_3, TiO_2, and ZnO) in BEGM and DMEM cell culture media (Figure 5-7). The results show complete sedimentation in the HTS well for CoO, Cr_2O_3, and Ni_2O_3, and over 95% of the suspended ENMs CuO and Mn_2O_3 settling over 24 hr period. In contrast, settling of Co_3O_4,

TiO_2, and ZnO were measurably less significant, where the fractions of ENMs settled are in the range of 71.5% – 87.3%, 47.7% – 54.0%, and 58.5% – 79.9%, respectively.

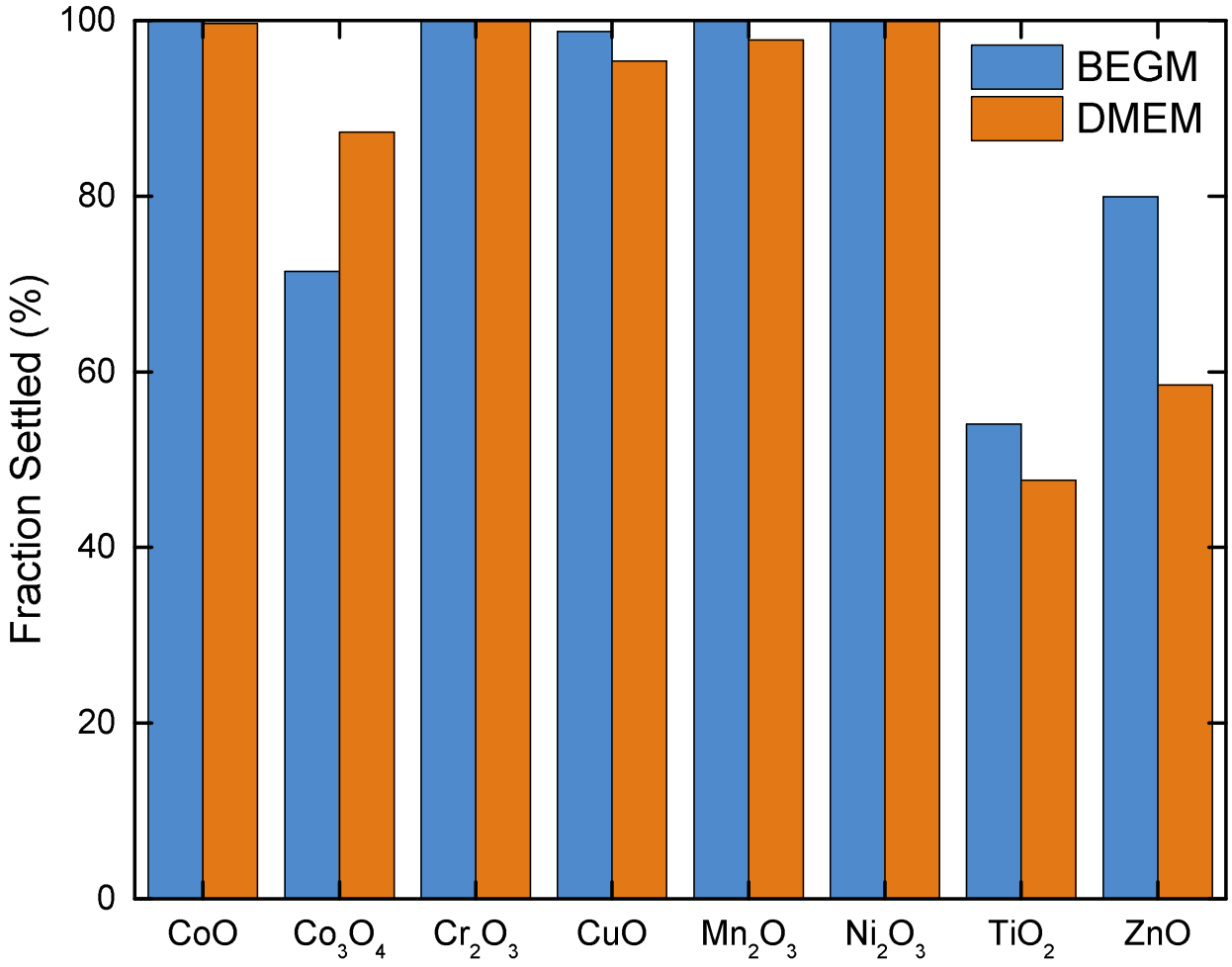

Figure 5-7. Predicted mass fraction of settled ENM for 8 metal oxide ENMs (CoO, Co_3O_4, Cr_2O_3, CuO, Mn_2O_3, Ni_2O_3, TiO_2, and ZnO) suspensions (100 mg L^{-1}) in BEGM and DMEM cell culture media at simulation time of 24 hr. Simulation conditions are reported in Table 5-1, media height (h) = 3.15 mm; ENM primary sizes are in the range of 10 – 193 nm (Table 5-1).

Chapter 6. Multimedia Environmental Distribution of Engineered Nanomaterials

6.1 Introduction

In order to assess the potential environmental ENM exposure levels, a generalized compartmental multimedia fate and transport modeling framework was developed with the capability for expansion as the knowledgebase regarding ENMs further develops. Following the above approach, a model for the multimedia environmental distribution of nanomaterials (MendNano) is presented that enables estimations of the dynamic mass distributions and exposure concentrations of ENMs within, and transport fluxes between various environmental media for a broad range of environmental scenarios of interest. A number of illustrative test cases are then discussed to elucidate the potential regional scale multimedia mass distribution, media concentrations, and significance of different transport pathways for selected ENMs.

6.2 Materials and Methods

6.2.1 Modeling approach

A multimedia compartmental modeling framework was developed for simulating the environmental distribution of ENMs. The present approach considers the environment as a collection of well-mixed compartments [44] each representing a specific medium (e.g., atmosphere, water, and top layer of soil and sediment) or biological entity (i.e., waterborne biota, vegetation), with intermedia mass transport between adjacent compartments (Figure 6-1). Multimedia compartmental models are suitable for a first tier assessment of potential environmental impact prior to engaging in more detailed and resource intensive use of spatial models or field monitoring [32].

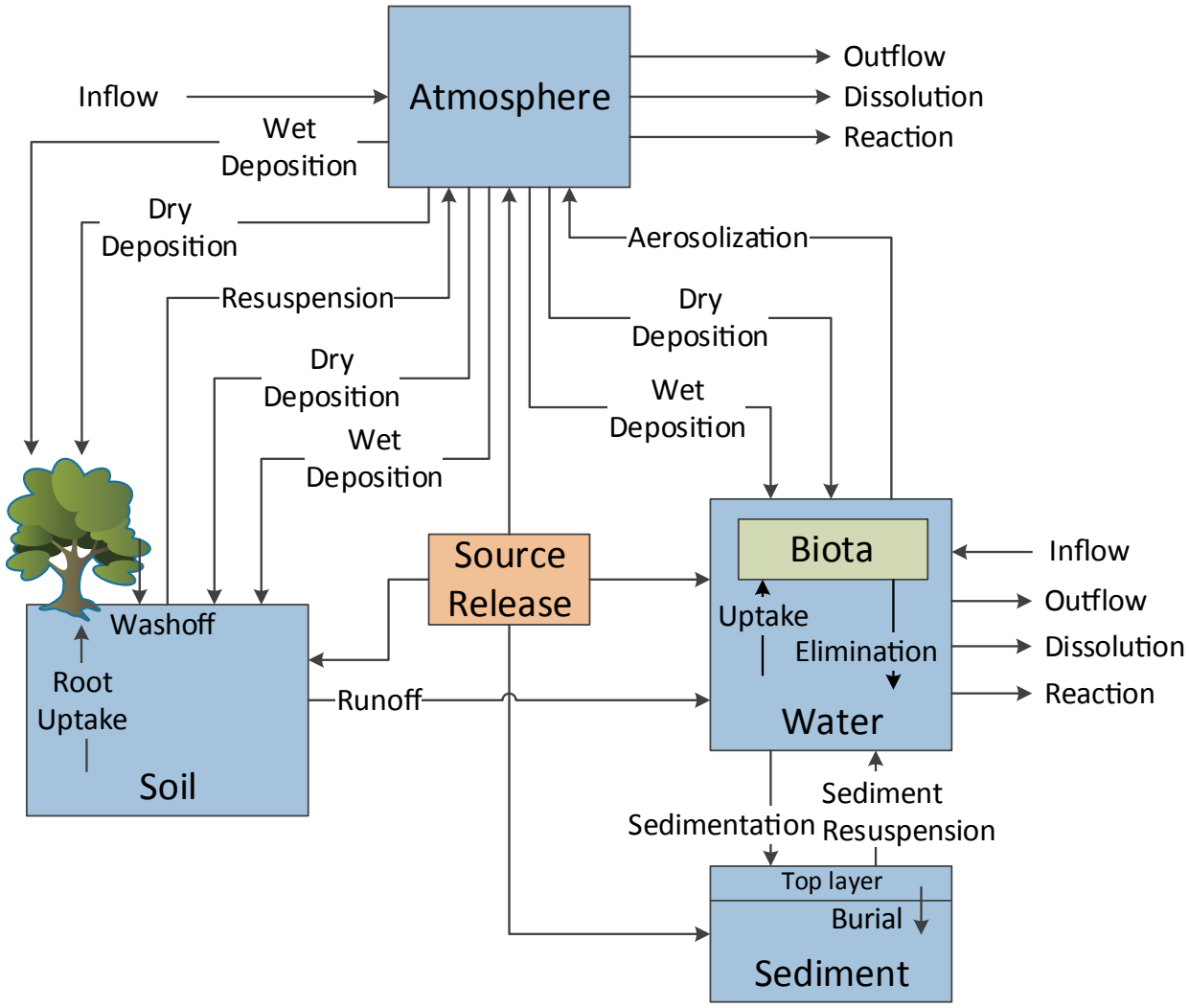

Figure 6-1. Environmental compartments and intermedia transport processes in a model multimedia environment.

6.2.2 Model Equations

In order to describe the environmental multimedia distribution of ENM, the particle size distribution is discretized into a number of size fractions. The dynamic mass balance for each particle size fraction, *k*, for a given compartment is then written in the following general form:

$$\frac{d}{dt}[V_i C_{i,k}] = \left(Q_i^{in} C_{i,k}^{in} - Q_i^{out} C_{i,k}\right) + \sum_{\substack{j=1 \\ j \neq i}}^{M} \sum_{l=1}^{P} I_{i,j,k}^{l} + \sum_{n=1}^{U} R_{i,k}^{n} + S_{i,k} \qquad \begin{matrix} k=1 \ldots N; \\ i = 1 \ldots T \end{matrix} \qquad [6\text{-}1]$$

where N is the number of particle size fractions, V_i [m^3] is the volume of compartment (or subcompartment) i and $C_{i,k}$ [g m^{-3}] is the compartmental ENM concentration associated with particles in size fraction k. The first bracketed term on the right-hand side (RHS) of eq [2-1] represents advective mass transport, whereby Q_i^{in} and Q_i^{out} are advective flow rates [m^3 s^{-1}] in and out of compartment i (note: advection is applicable only for the air and water compartments), and $C_{i,k}^{in}$ is the inflow ENM concentrations [g m^{-3}]. Intermedia transport rates between compartments i and j, via transport process l, are represented by $I_{i,j,k}^{l}$ [g s^{-1}] with the net intermedia transport exchange rate (the second term on the RHS of eq [2-1]) being the summed contributions of all processes (P) from all compartments (M) in contact (i.e., sharing a boundary) with compartment i. ENMs in the environment are subject to various transformation processes, such as dissolution, chemical reactions, and biological transformations [216] , whereby the rate of a given ENM transformation [g s^{-1}] n, in size fraction k in compartment i, is designated by $R_{i,k}^{n} = r_{i,k}^{n} V_i$, where $r_{i,k}^{n}$ is the volume specific ENM transformation rate [g m^{-3} s^{-1}]. For example, it has been reported that oxysulfidation of Ag [217], oxidation of Fe [218], and photodegradation of C_{60} [219] ENMs appear to follow first order reaction kinetics. Also, at the expected low environmental concentrations of ENM [42], a simple first order process may often suffice for first tier analysis, whereby the transformation rate can be expressed as $R_{i,k}^{r} = \zeta_i K_{i,k}^{r} C_{i,k} V_i$, where $K_{i,k}^{r}$ [s^{-1}] is the transformation rate constant, and ζ_i is set as -1 or +1 for a consumption or production transformation, respectively. The rate constant for ENM transformation can be a function of a range of variables including, but not limited to, temperature, solution chemistry

(e.g., pH, ionic species concentration, or presence of natural organic matter (NOM)), ENM chemistry and size. For physical transformation such as in the case of dissolution in the water compartment (i.e., *i*=*w*), for example, the rate of dissolution is given as $R_{w,k}^{diss} = K_{w,k}^{diss}\left(C_w^{(s)} - C_w^{(diss)}\right)A_{T,k}$, where $K_{w,k}^{diss}$ [m s^{-1}] is the ENM-environmental medium (e.g., water) mass transfer coefficient, which is a function of ENM size/geometry and chemistry, solution chemistry/composition, and flow hydrodynamics (§2.2.2.2); $C_w^{(s)}$ is the ENM solubility [kg m^{-3}] that can be affected by factors such as media pH, temperature, ENM surface chemistry, and the ambient concentration of various species; $C_w^{(diss)}$ [kg m^{-3}] is the background mass concentration of the ENM dissolved in water*;* and $A_{T,k}$ [m^2] is the surface area of particle size fraction *k* (§2.2.2.2). The mass transfer coefficient can be predicted based on classical dissolution models which in the present simulations focused on dissolving spherical particles [101]. If experimental dissolution data (i.e., dissolution kinetics) are available, then these can be used to extract the needed mass transfer coefficient. Finally, $S_{i,k}$ is the ENM source release rate [g s^{-1}] of particles of size fraction *k,* to compartment *i,* and may be either time-invariant (i.e., constant) or temporally variable (Figure 6-2). A convenient source release function that encompasses a wide range of possible release scenarios is as follows

$$S_{i,k}(t) = \begin{cases} \mathrm{A} \cdot \sin\left(t \cdot \dfrac{\tau}{\pi}\right) + r\,, & \left(t \bmod (\tau + g)\right) \le \tau \\ 0, & \left(t \bmod (\tau + g)\right) > \tau \end{cases} \qquad [6\text{-}2]$$

where $S_{i,k}(t)$ is the ENM release rate [kg s^{-1}] at t^{th} day, *A* [kg s^{-1}] is the amplitude of the sinusoid (Figure 6-2**d**), τ [day] is the cycle period, g [day] is the cycle gap period, and *r* [kg s^{-1}] is the average release rate. In eq [6-2], $t \bmod (\tau + g)$ represents the remainder of $t \,/\, (\tau + g)$.

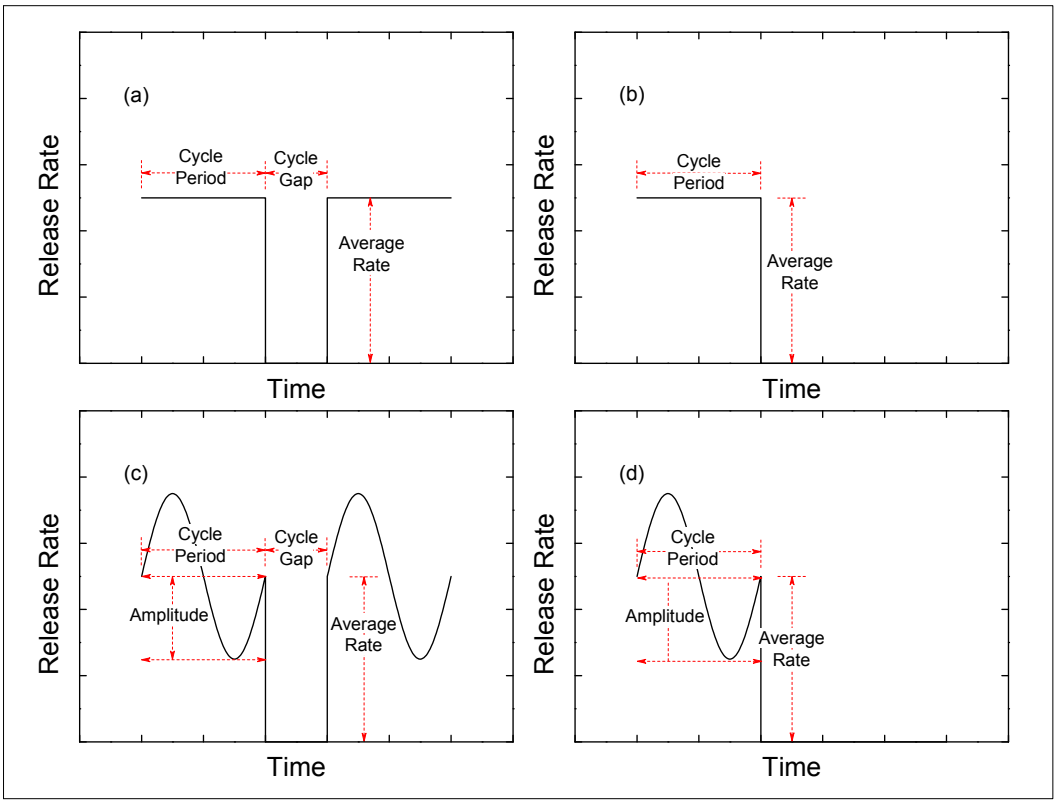

Figure 6-2. Source release scenarios are depicted for (a) repeating event of constant release rate, (b) single event of a constant release rate), (c) repeating cycles of a sinusoidal release rate, and (d) single event of sinusoidal release rate.

Ambient particles are present (in both air and water) at significantly higher number concentrations relative to those which may be expected based solely on potential releases of ENMs [38]. Therefore, ENMs are likely to be associated with ambient particulates (due to various surface–surface interactions [49]) given the high available surface area of ambient particles and tendency of most ENMs to agglomerate [54, 177, 220]. Thus, intermedia transport associated with both air and water will be impacted by the ambient PSDs in the above media. It is well known that ambient PSDs in air [123, 149, 221] and water [222, 223] are self-preserving (i.e., similar over time). The particle size of ambient aerosols typically ranges from 0.001 to 2 μm with PSDs typically described by a tri-modal log-normal size distribution [123]. Suspended

solids in natural water bodies are typically in the size range of 0.01–1 μm for lakes [224], 1–100 μm for oceans [225] and 30-150 μm for rivers [226] and log-normal size distributions have been often reported [38], with a concentration range that can vary significantly (30μg L^{-1} – 200 mg L^{-1}) [227, 228] depending on the specific water body. The attachment efficiency of ENMs to ambient particles is thus an important factor that is likely to dictate the distribution of ENMs throughout the particulate phase in various environmental media. The attachment efficiency (i.e., typically defined as fraction of collisions that result in attachment/agglomeration [38, 49]) is a complex parameter based on established theory of particle-particle interactions (e.g., the classical [168] and extended [51] DLVO theories, which describe particle-particle interactions due to attractive and repulsive interaction energies). However, fundamental predictions of ENM agglomeration (homogeneous and/or heterogeneous with ambient particles) based on the attachment efficiency (as predicted by DLVO/Extended DLVO) require solution of the Smoluchowski coagulation equation [38, 49], in which a single simulation instance may take many hours to days of CPU time [49]. Such complex Models are less practical for screening level multimedia assessment (where a single simulation instance takes only minutes to complete). It is noted that the Smoluchowski equation was used in recent work on environmental ENMs transport with assumed values for the attachment efficiency [38, 132]. Although the above did not provide *a priori* prediction of the agglomeration state based on predicted attachment efficiencies, reported simulation results suggest that, even with low attachment efficiency (0.01), essentially all ENMs would be attached to ambient particles [38]. In order to reduce the level of multimedia model complexity, yet retain a capability for exploring various levels of ENMs attachment to ambient particles, an "attachment factor" is introduced in the present work that is defined as the fraction of ENMs attached to ambient particles. ENMs are

therefore allowed to distribute throughout the ambient particulate phase based on a specified attachment factor that varies in the range of [0, 1] (i.e., no-attachment of ENMs to ambient particles to complete attachment), and may depend on water chemistry and ENM chemistry (for a given ENM and media conditions) as well as ENM and ambient particulate sizes.

Accordingly, the total ENM mass input rate, $\dot{m}_i$ [g s^{-1}], to compartment *i* (i.e., due to emission, discharge or convective mass input from an external adjacent compartment) is apportioned to ambient particles in the various size fractions such that the ENM mass input rate in for fraction *k*, $\dot{m}_{i,k}$ [g s^{-1}], is given by:

$$\dot{m}_{i,k} = \dot{m}_i \alpha(r_k, r_n) \frac{f(r_k) w(r_k)}{\int_0^\infty f(r) w(r)\, dr} \qquad [6\text{-}3]$$

where, and $\alpha(r_k, r_n)$ is the dimensionless attachment factor representing the fraction of total ENM mass of ENMs of size r_k (size fraction *k)* bound to ambient particles of size r_n (size fraction *n), f*(r_k) is the fraction of ambient particles in size fraction *k*, and *w*(r_k) is an attachment weighing factor (e.g., $w(r)=r^2$ would specify distribution of among ambient particulates according to surface area density of ambient particles in size fraction *k*. The mass input rate, $\dot{m}_{i,k}$, for the fraction of freely suspended ENM particles, $[1 - \alpha(r_k, r_n)]$, in size fraction *k* is given as:

$$\dot{m}_{i,k} = \dot{m}_i [1 - \alpha(r_k, r_n)] \frac{f(r_k)}{\int_0^\infty f(r)\, dr} \qquad [6\text{-}4]$$

which specifies the mass input rate (i.e., intermedia transport, advective input or source release rates) of an ENM into a given compartment *i*, whereby $\dot{m}_i$ designates the specific pathway for ENM input rate.

Transport rates of ENMs between compartments, $I_{i,j,k}^{l}$ (eq [6-1]), as depicted in Figure 6-1 can be described by various mechanistic intermedia transport process models as described in detail in the §2.2.2. Briefly, dry deposition rate was determined based on the air phase PSD and dry deposition velocity to water [90, 91], soil [90, 94], and vegetative canopy [90, 98]. The rate of precipitation scavenging (wet deposition) removal of particles from air[229] and required scavenging ratio were determined as a function of rainfall intensity and drop size distribution, while also accounting for the size distribution of airborne particles [92]. ENMs wash-off from foliage was determined based on water retention capacity of the vegetative foliage [32]. Wind resuspension rate was estimated by the Wind Erosion Equation(WEQ) [95] which accounts for soil properties; and soil loss due to runoff was estimated from the Revised Universal Soil Loss Equation based on soil erodibility and topographic factors [96]. Aerosolization (i.e., introduction of particles from water to air) was estimated with considerations of the effect of wind speed [93]. Sedimentation of particles suspended in water was determined by Stokes' settling while accounting for ENM agglomerates porosity [49]. It is noted that ENMs with fractal structures may have a higher settling velocity than predicted by Stokes' settling due to flow of water through the pores within the agglomerate (see Chapter 5). However, the fractal structure is likely to be negligible in natural water bodies, where ENMs are expected to attach to ambient suspended solids. In cases in which ENMs attachment to ambient suspended solids is not significant, or suspended solids contains fractal structures, the settling velocity may be corrected by accounting for permeability of the fractal structure. Resuspension of sedimented particles can be estimated from models that consider current stress at the sediment surface induced by waves [99, 109] or streamflow [100]. The rate of ENMs dissolution was estimated based on the classical diffusion model which in the present analysis focused on spherical particles [101] while

considering the size distribution and porosity of the suspended agglomerates. Finally, the capability of exploring ENMs uptake by biota and plant roots is provided via a simple uptake rate model (§2.2.2), requiring uptake and elimination rate constants (e.g., as may be determined from available experimental ENMs uptake data). The various intermedia transport equations along with the sources of parameters are provided in the Addendum to the dissertation.

The compartmental mass balance as given by eq [6-1] can be expressed in terms of the specific intermedia transport processes for the air (eq [6-5]) and water (eq [6-6]) compartments as:

$$\frac{d}{dt}\left[V_a C_{a,k}\right] = I_{s,a}^{resusp} + I_{w,a,k}^{aerosol} - \sum_j I_{a,j,k}^{dry} - \sum_j I_{a,j,k}^{wet} + \left(Q_a^{in} C_{a,k}^{in} - Q_a^{out} C_{a,k}\right) + R_{a,k} + S_{a,k} \qquad k=1\ldots N \quad [6\text{-}5]$$

$$\frac{d}{dt}\left[V_w C_{w,p}\right] = \sum_k I_{a,w,k}^{dry} + \sum_k I_{a,w,k}^{wet} + I_{sed,w}^{sed\ resusp} + I_{s,w}^{runoff} + I_b^{elim} - I_{w,sed}^{sed.} - I_{w,a,p}^{aerosol} - I_{w,b,p}^{uptake} + \left(Q_w^{in} C_{w,p}^{in} - Q_w^{out} C_{w,p}\right) + R_{w,p} - K_{i,k}^{diss}\left(C_w^{(s)} - C_w^{(diss)}\right) A_{T,k} + S_{w,p} \qquad p=1\ldots N \quad [6\text{-}6]$$

where the first four terms on the right hand side (RHS) of eq [6-5] represent (in order) the ENMs rates of wind soil resuspension, aerosolization (from water), and atmospheric dry and wet (rain scavenging) deposition. The first eight terms on the RHS of eq [6-6] represent (in order) ENMs rates of atmospheric dry and wet deposition to water, sediment resuspension, runoff (from soil to water), elimination from biota, sedimentation, aerosolization, and uptake by biota. In the above equations subscripts *a, b, s, w,* and *sed,* refer (in order) to air, biota, soil, water, and sediment and the indices *k* and *p* represent particle size fraction in air and water, respectively.

Retardation of ENMs infiltration in the soil matrix is enhanced when ENMs agglomerate, as expected under typical environmental conditions [230]. Consequently, ENMs are expected to accumulate primarily in the soil (and sediment) surface layer [32]. Studies have suggested that ENMs may penetrate only short distances into the soil column [230, 231], although detailed soil transport would clearly depend on specific soil conditions. Notwithstanding, for the purpose of estimating exposure concentrations, one may elect to calculate such concentrations based on a reasonable soil or sediment depth [232] over which the ENM mass is then assumed to distribute. Consistent with the above argument, ENM mass at the soil, m_s, and sediment, m_{sed}, surface layers are tracked via the following mass balances

$$\frac{d}{dt}m_s = \sum_k I_{a,s,k}^{dry} + \sum_k I_{a,s,k}^{wet} + I_{f,s}^{washoff} - I_{s,a}^{resusp} - I_{s,w}^{runoff} - I_s^{root} + R_s + S_s \qquad [6\text{-}7]$$

$$\frac{d}{dt}m_{sed} = I_{w,sed}^{sed.} - I_{sed,w}^{sed\ resusp} - I_{sed}^{burial} + R_{sed} + S_{sed} \qquad [6\text{-}8]$$

where the first six terms on the RHS of eq [6-7] represent (in order) ENMs input rates to soil by dry and wet deposition, washoff from foliage (designated by subscript *f*), and removal by wind resuspension, runoff, and removal via root uptake; the seventh and eighth terms represent ENMs transformation and source release rates, respectively. The five terms on the RHS of eq [6-8] represent, in order, the rates of ENMs sedimentation, resuspension from sediment, sediment burial, transformation and source release.

Within the multimedia compartmental modeling framework, ecological receptors (e.g., plant, biota) can be represented as additional compartments [32, 33, 44]. In such a formulation, rates of

accumulation of ENMs mass on vegetative foliage, m_f, and in root, m_{root}, can be represented by[32]

$$\frac{d}{dt}m_f = \sum_k I_{a,f,k}^{dry} + \sum_k I_{a,f,k}^{wet} - I_{f,s}^{washoff} \quad [6\text{-}9]$$

$$\frac{d}{dt}m_{root} = I_s^{root} \quad [6\text{-}10]$$

in which the terms on the RHS of eq [6-9] represent (in order) the rates of ENMs dry and wet deposition and washoff; and the term on the RHS of eq [6-10] represents ENMs removal from soil via root uptake. Efforts are currently underway to develop data and models of ENMs uptake via the root pathway [233, 234], and uptake rate constants need to be extracted from experimental data. In principle, one can also describe the accumulation of ENM mass, m_b, in biota via a compartmental mass balance

$$\frac{d}{dt}m_b = \sum_k I_{b,w,k}^{uptake} - I_b^{elim} \quad [6\text{-}11]$$

where the first and second terms on the RHS represent the rates of ENMs uptake and elimination by biota. Mechanistic models and/or experimental data for ENM accumulation in biota are in the developing stage, but nonetheless approximate treatment of uptake rate may be appropriate for a first tier analysis (§2.2.2). Alternatively, in the absence of uptake kinetics data, one may estimate the range of magnitude of concentrations in biota, using reported bioconcentration factors (BCFs; Table 2-2), in conjunction with model predictions of ENM concentrations in water.

Simulations of the multimedia distribution of ENMs require specification of ENM properties, environmental compartment properties, meteorological parameters (e.g., monthly average

temperature, wind speed, relative humidity and rainfall data; Table 6-1), intermedia transport process parameters, and source emission scenarios which can be set as temporally variable (Figure 6-2). The modeled region is described by its dimensions and other geographical parameters. The volume of atmosphere compartment is set as $(A_{as} + A_{aw})H_{mix}$, where H_{mix} [m] is the atmospheric mixing height [235]. The mixing height can vary seasonally and diurnally, but an average monthly or annual mixing height is often suitable for first tier analysis [44]. Note that it is reasonable to set $Q_i^{in} = Q_i^{out}$ and thus advective volumetric flow rates Q_i^c into the atmospheric and water compartments are expressed as $Q_i^c = V_i/\tau_{i_{res}}$, where V_i is the compartmental volume and $\tau_{i_{res}}$ [s] is the advective residence time. In the absence of information regarding $\tau_{i_{res}}$, one can set $Q_i^c = v_i^c \cdot A_i^c$, where v_i^c is the wind or current speed, and A_i^c is the cross-sectional compartmental area perpendicular to the prevailing wind or current direction. Finally, surface area of the foliage compartment is expressed as $A_{as} \cdot \phi_{veg} \cdot F_f$ where ϕ_{veg} is the fraction of soil area, A_{as}, covered by vegetation, and F_f [m^2_{foliar} m^{-2}_{soil}] is the foliage area per unit area of soil [236, 237].

Table 6-1. Basic intermedia transfer factors

NP Physicochemical Properties	Particle size distribution (ENMs in air and water, ambient particles in air and water)	
	Aqueous solubility	
	Reaction rate constant	
	Attachment factor (to ambient particles)	
	Density	
Intermedia transport parameters	*Process*	*Major factors*
	Dry Deposition	Temperature, wind speed, atmospheric stability, humidity, surface characteristics, ambient aerosols PSD
	Precipitation scavenging	Precipitation intensity, cloud base height, ambient aerosols PSD
	Aerosolization	Wind speed
	Soil wind resuspension	Wind speed, atmospheric stability, soil surface characteristics
	Soil runoff	Precipitation intensity, soil surface characteristics, ground incline degree
	Foliage washoff	Precipitation, foliage properties (e.g., water holding capacity), foliage coverage
	Sedimentation	PSD and density of suspended solids
	Sediment resuspension	Water bottom current velocity, sediment type and roughness, wind speed, depth of water body

6.2.3 Model Structure

MendNano includes modules for: a) mechanistic sub-models for rates of intermedia transport processes [44, 131]; b) dynamic compartmental mass balance equations consisting of a set of 50 – 204 (depending on user specified scenario) ordinary differential equations (ODEs); c) event tracker (for episodic events, e.g., precipitation, wind resuspension); and d) ODE solver (Figure 6-3). Required model input includes ENM and ambient particle properties, geographical parameters, meteorological parameters, and source release rates. Once a multimedia scenario is established the set of model ordinary differential mass balance equations (eqs [2-1]-[6-11]) are solved along with the various intermedia transport sub-models (§2.2.2 and Table 2-1). The compartmental mass balance ODEs (eq [6-1]) are solved via the Adams-Bashforth-Moulton predictor-corrector method [238], with time steps selected dynamically with the numerical solution error (in terms of compartmental ENM mass) set with 0.1% relative error tolerance (defined as percent change in two consecutive solutions). At each time step, the rates of advective (i.e., via air and water flow) and intermedia transport, reactions, and source release are computed based on the temporally varying parameters (wind speed, temperature, biological organism mass, ENM release rates). Model simulations were carried out on Linux based server (Intel Xeon 8-Core processors at 2.66GHz, 64GB RAM), with a typical ~3 min CPU time for a 1-year simulation.

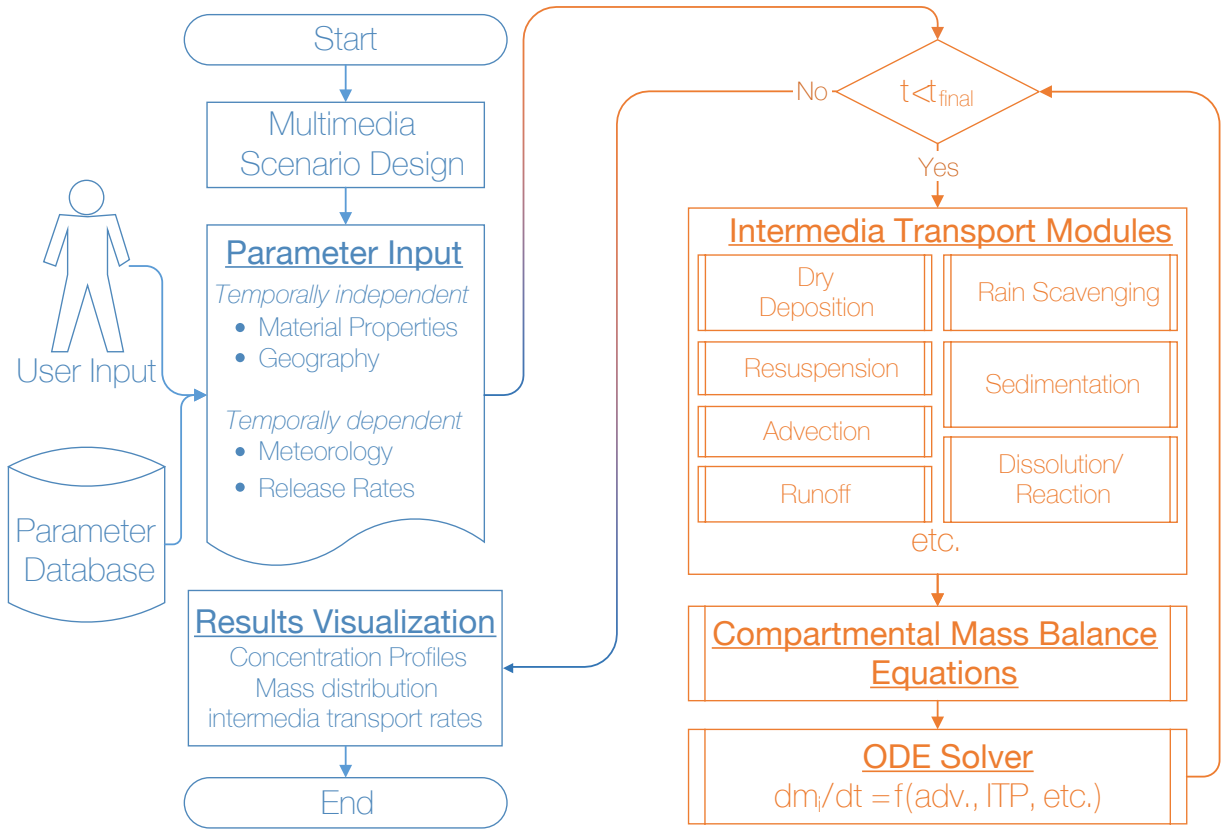

Figure 6-3. Overview of the MendNano modeling platform.

6.2.4 Assessment of Modeling Approach Based on Simulations of the Multimedia Distribution of Particulate Matter

In order to assess the suitability of the present modeling approach for describing the dynamic multimedia distribution of particulate matter, simulations were first carried out for low volatility [77, 78] and essentially water insoluble (solubility 0.26-2.7 μg L^{-1}) [79] polycyclic aromatic hydrocarbons (PAHs) (e.g., benzo[a]pyrene (B[a]P), benzo[ghi]perylene (B[ghi]P), dibenz[a,h]anthracene (DBA)), which strongly adsorb onto particulate matter [239, 240]. MendNano simulations for B[a]P, B[ghi]P, and DBA for the Southeast Ohio (US), Los Angeles(CA, US), and Birmingham (UK) regions, for which monitoring data were provided,

demonstrated agreement with field data, to within a factor of 2 or better, at the acceptable level for compartmental models (§C.1) [241-243].

6.2.5 Model Applicability

Overall, Multimedia compartmental modeling (MCM) is typically applicable for a region of minimum area of about 1 km^2 [44]. The MCM approach does not provide spatial resolution since each compartment is taken to be well-mixed. The MCM approach is accepted as suitable for screening level analysis and has been adopted in regulatory applications by various Federal [244-246] and State Agencies [247]. Although first tier compartmental models do not provide spatial resolution, spatial resolution can be increased via the use of nested or sub-compartments and integration of spatial and compartmental description of the pertinent environmental media [32]. Description of the environmental multimedia partitioning of chemicals or particulate matter via spatial level models increases the required model parameters, increases the computational burden and required user expertise for using such models. Therefore, it is typically recommended that first tier screening level models be used first with the aim of determining the significance of various transport pathways and range of expected chronic exposure concentrations subject to various release and environmental scenarios. Accordingly, the present multimedia compartmental model was formulated with intermedia transport processes that are specific for particulate matter as well as for pollutants that exist primarily in the particle-bound form (e.g., non-volatile or semi-volatile organics); the latter can be handled by MendNano via the use of the attachment factor (§6.2.2; eqs [6-3], [6-4]). The various intermedia transport sub-models **(§2.2.2)** have been shown in various previous studies to be valid for particles in the size range of ~1 nm - 100 μm [44]. It is also important to note that the present approach is suitable for assessing average multimedia distributions of ENMs over the region of interest. Therefore, the modeling

approach is most suitable for dealing with distributed sources (including point sources that are distributed throughout the region of interest); use of singular point sources in the present model would likely result in underestimation of the magnitude of local exposure concentrations.

6.2.6 Test Cases of Multimedia Distributions of ENMs

MendNano simulations of the multimedia distribution of ENMs were carried out for selected ENMs including metal oxide (Al_2O_3, CeO_2, CuO, Fe_3O_4, TiO_2, ZnO), silver (Ag), nanoclays, silica (SiO_2) and carbon nanotubes (CNT) ENMs. The analyses included both multimedia distributions of the above ENMs on a country scale for U.S. and Switzerland as well as for a regional scale of the characteristics of Los Angeles County. ENM, regional and meteorological parameters used in the simulations [248, 249] are reported in §A.3. All simulations were carried out for a period of at least one year.

Emission release rates for the ENMs of the present test cases were reported in the literature [42, 43] based on life cycle inventory assessment (LCIA) study [10] for the global release rates of Ag, Al_2O_3, CeO_2, CNT, Cu-based ENMs, Fe-based ENMs, nanoclay, SiO_2, TiO_2, and ZnO (Table A-5), which were reported based on estimated global production rates and expressed as percentages of the total production rates of the ENMs [10], consistent with those reported elsewhere [42]. A recent study [250] suggested that regional release rates of ENMs can be estimated by scaling global ENM release rates on the basis of population and economic indicators if such are available. Accordingly, the above approach was utilized, in illustrative test case simulations for the Los Angeles region (Table A-3), to estimate media-specific ENM releases (Table A-5). Estimates of ENM release rates depend on various assumptions regarding production rates, ENM manufacturing, and use and disposal; thus, it is not surprising that a significant range of release estimates have been reported [250-252]. Nonetheless, LCIA

estimates of ENM release rates are useful for first tier analysis of the multimedia distribution of ENMs. In this regard, it is noted that ENMs release to soil is often reported as the sum of two contributions: (1) releases from wastewater treatment plants (WWTP), and (2) "direct releases" (mostly during the "use" stage of the ENM life cycle) [10]. ENMs release to soil by "direct release" was reported to account for about 8% [42] to 71% [10] of the total release to soil. However, it is unclear from published LCIA studies if "direct release" to soil is localized or represents ENM release that is regionally distributed. Additionally, it has been reported that in certain countries residuals from WWTP are not released to soil [42], while in the US biosolids (i.e., WWTP sludge) are applied to less than 1% of the country's agricultural land [253]. Clearly, there is uncertainty as to the apportionment of local versus regional (if any) ENMs release to soil. At the same time, one should recognize the possibility of hot-spots that can result in elevated ENM concentrations in soil. While some MFA studies have assumed scenarios in which total ENMs releases to soil (including those from WWTP) are distributed over the entire soil in the region [19, 41-43], the validity of such an assumed scenario is questionable. Nonetheless, in the present study, the impacts of the above soil release scenarios with and without ENM release from WWTP (Figure C-2**)** and with and without "direct release" to soil (Figure 6-5**,** Figure 6-7**,** Table 6-2) were explored via MendNano simulations.

6.3 Results And Discussion

6.3.1 Significance of Intermedia Transport Pathways and Source Apportionment on Multimedia Distribution of ENMs

An illustration of the impact of regional meteorology and relative release rates of ENMs on their environmental distribution is provided in Figure 6-4 and Figure 6-5, based on simulations

for selected metal and metal oxide, CNTs and nanoclay ENMs, focusing on the Los Angeles region as an illustrative case. As expected, ranking of ENM concentrations in air follows (as expected) the order of increasing concentrations correlating with increased source release rates (Table A-5). Similarly, ranking of ENMs concentrations in water follows the order of release rates to water (Table A-5), with exception of the sparingly soluble ENMs (Fe (Fe oxide), ZnO, Ag, Cu (Cu Oxide)). The above behavior is attributed to the fact that ENMs release rate to water dominates any input from intermedia transport (i.e., atmospheric deposition and runoff) (Figure 6-6, Figure 6-7, and Figure 6-8).

In the absence of direct ENMs release to soil, atmospheric deposition is the sole contributor to the mass of ENMs in soil, with percent ENM mass (relative to the total ENM mass in the environment) being in the range of 2.53–96.05% for the set of ENMs considered in the present study (Table 6-2). The mass distribution of ENMs as shown in the example of Figure 6-6 for TiO_2 indicates only 2.53% of the total environmental mass of this ENM in soil with atmospheric wet deposition being the major ENM input to this compartment. When direct release to soil is considered, the percent mass of ENM in the soil can increase significantly (77.01–99.90%; Table 6-2). Similarly, in the absence of direct ENM release to water, one would expect ranking of ENMs concentrations in water to also follow the ranking of release rates to air, given that ENMs input to water would also be primarily due to atmospheric deposition (Figure 6-6). With direct release to soil, compartmental concentrations (relative to the absence of direct ENM release to soil) would increase by factors of up to 3 and 106 in air and soil, respectively, and by up to 6% and 0.2% in water and sediment, respectively. At the same time, higher ENMs soil concentrations would result in correspondingly higher ENMs input rate to air by wind resuspension as depicted for the example of TiO_2 distribution (Figure 6-7) and also evident in the

mass distribution of the various evaluated ENMs (Table 6-2). It is also noted, as shown in the Los Angeles example, simulations for TiO_2 (Figure 6-9) as the fraction of total ENM release to soil, which is apportioned for regional distribution (i.e., over the soil), is increased from zero (i.e., equivalent to the case of confined local release) to 100% (i.e., complete regional distribution); TiO_2 concentrations in air and soil increase by factors of 5.8 and 236, respectively. Clearly, the multimedia mass distribution of ENMs can be significantly impacted by the apportionment of the total estimated release rates among the different media. For example, simulation of TiO_2 distribution for the Los Angeles test case (Figure 6-10) indicates percent of total regional ENM mass in water and sediment that decreased significantly from 0.66% to 0.01% and from 49.25% to 2.06%, respectively, as the ratio of ENM release to air relative to water decreased from 4:1 to 1:0 (i.e., 100% release to air).

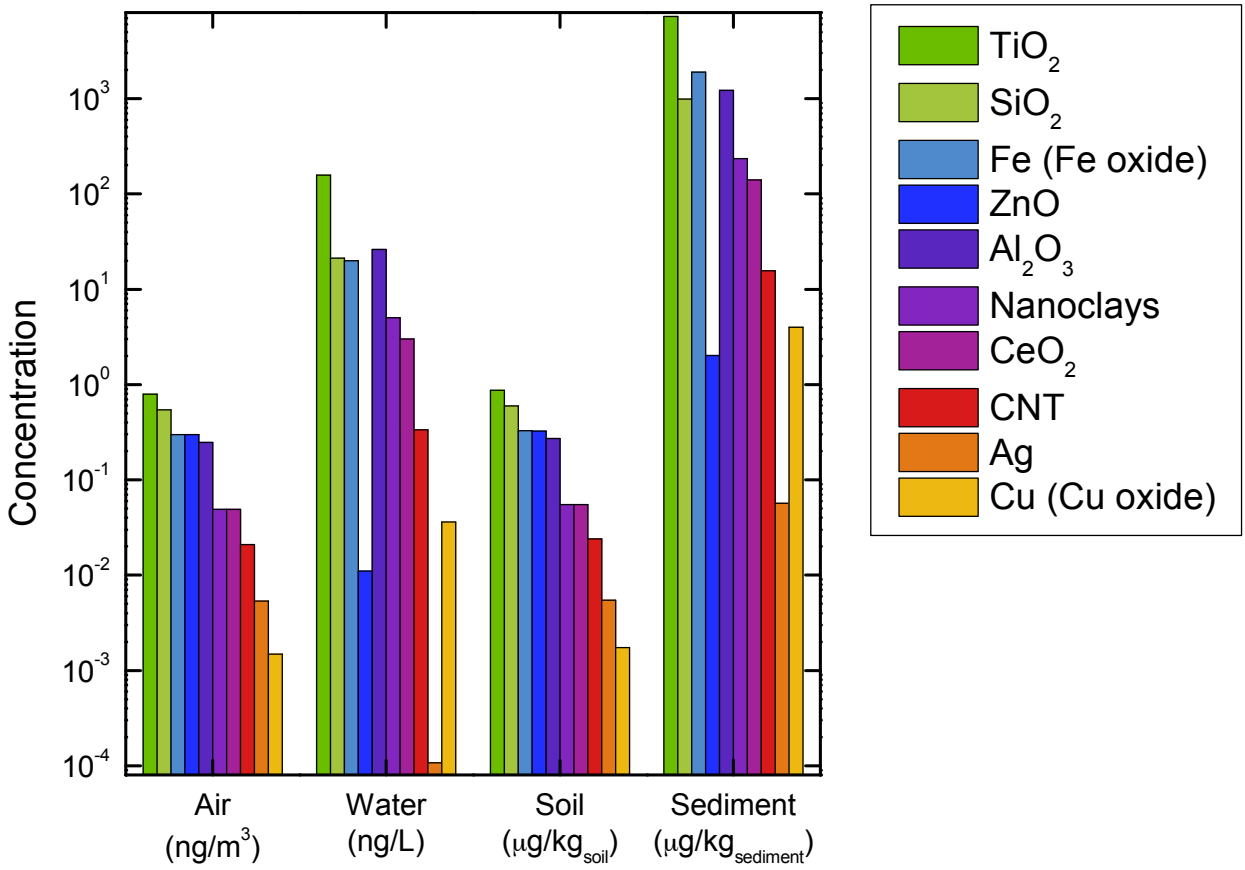

Figure 6-4. Predicted compartmental concentrations of Ag, Al_2O_3, CeO_2, CNT, Cu-based ENMs (metal and metal oxides), Fe-based ENMs (metal and metal oxides), nanoclays, SiO_2, TiO_2, and ZnO in the Los Angeles region at the end of 1-year simulation. ENM releases are to air and water only, and the release rates (to air and water) were estimated following the proposed regional scaling from published [10] estimates of global media-specific ENMs release rates (Table A-5) to the Los Angeles region and assuming no regional distribution of ENM releases to soil. (Note: Fe (Fe oxide), ZnO, Ag, and Cu (Cu oxide) solubilities are 0.001, 4.45, 1.9, and 0.002 mg L^{-1}, respectively; Table A-4).

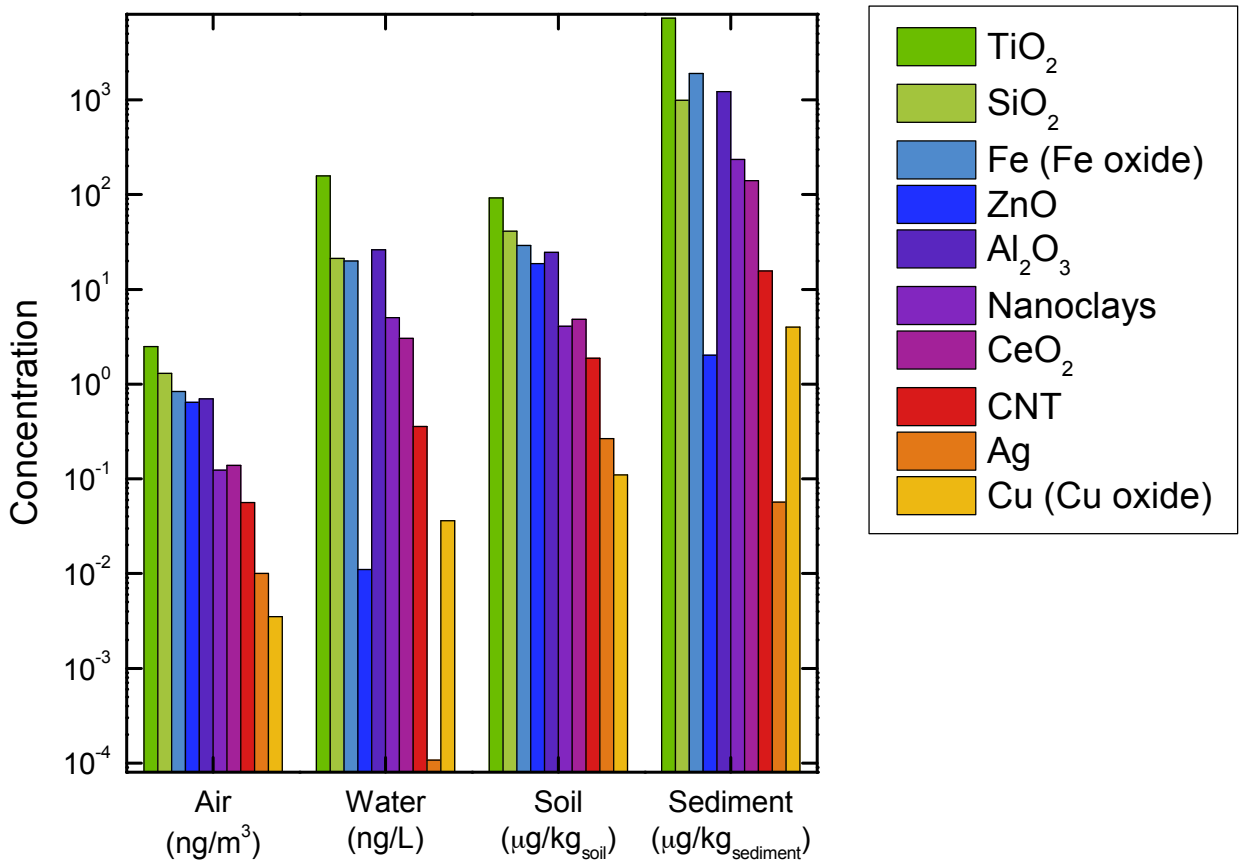

Figure 6-5. Predicted compartmental concentrations of Ag, Al_2O_3, CeO_2, CNT, Cu-based ENMs (metal and metal oxides), Fe-based ENMs (metal and metal oxides), nanoclays, SiO_2, TiO_2, and ZnO in the Los Angeles region at the end of 1-year simulation. ENMs releases are to air, water, and soil, and release rates were estimated by population-based scaling of global media-specific ENMs release rates estimates[10] (see Table A-5) for the simulation conditions listed in Table A-3. Note: a) only the "direct release" portion of the release to soil is considered to be regionally distributed (see Table A-5); b) Fe (Fe oxide), ZnO, Ag, and Cu (Cu oxide) solubilities are 0.001, 4.45, 1.9, 0.002 mg L^{-1}, respectively; (Table A-4).

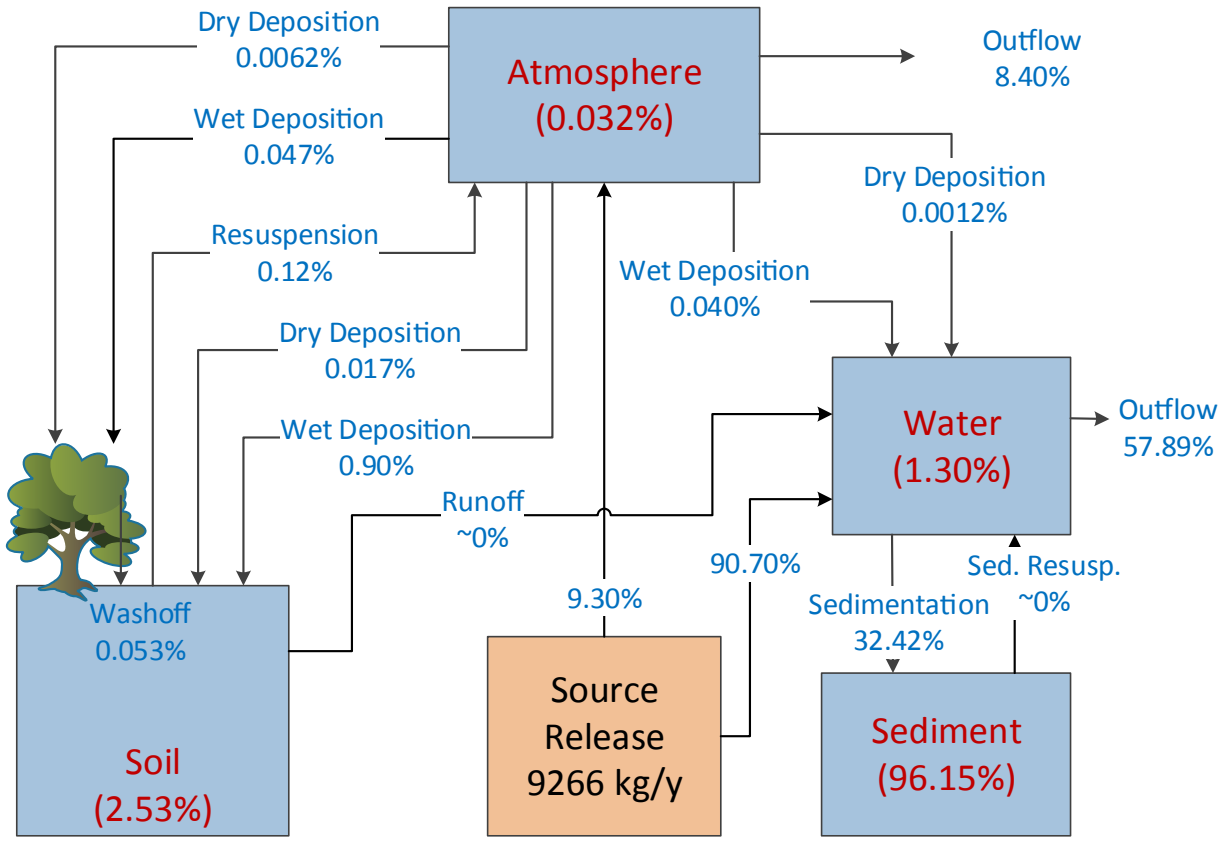

Figure 6-6. Intermedia transport rates of TiO_2 and mass distribution among the various compartments at the end of 1-year simulation for the Los Angeles test case. Simulation conditions (including release rates of TiO_2) are the same as in Figure 6-4. ENM intermedia transport rates are reported as percent (in blue font) of the total ENM source release rate (note: runoff and sediment resuspension are of the order of 10^{-6} % and 10^{-5} %, respectively). The percent of the total ENM mass in the multimedia system is also reported for each compartment (in red font within the parentheses).

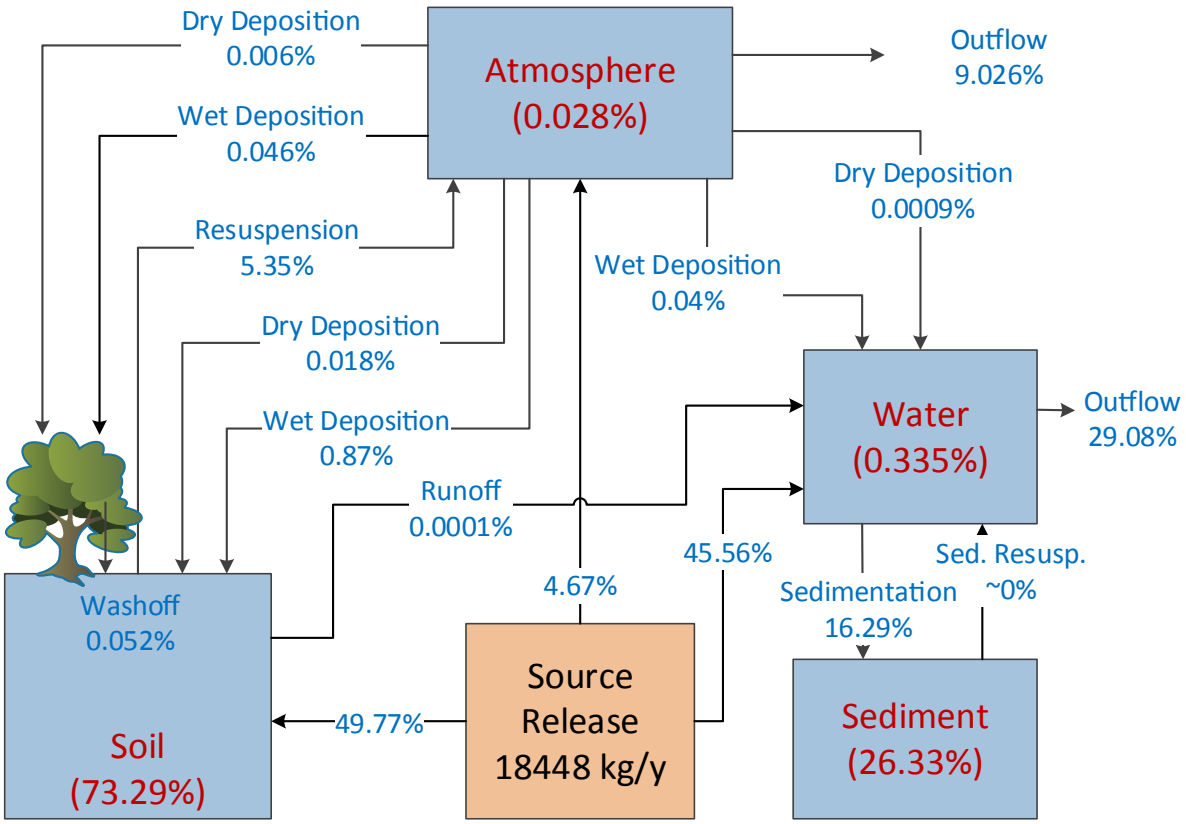

Figure 6-7. Intermedia transport rates of TiO_2 and mass distribution among the various compartments at the end of 1-year simulation for the Los Angeles simulation conditions of Figure 6-4. Simulation conditions (including release rates of TiO_2) are same as in Figure 6-5. Note that only the "direct release" portion of total ENM release to soil is considered to be regionally distributed. ENM intermedia transport rates are reported as percent (in blue font) of the total ENM source release rate (note: sediment resuspension is of the order of 10^{-5} %). The percent of the total ENM mass in the multimedia system is also reported for each compartment (in red font within the parentheses).

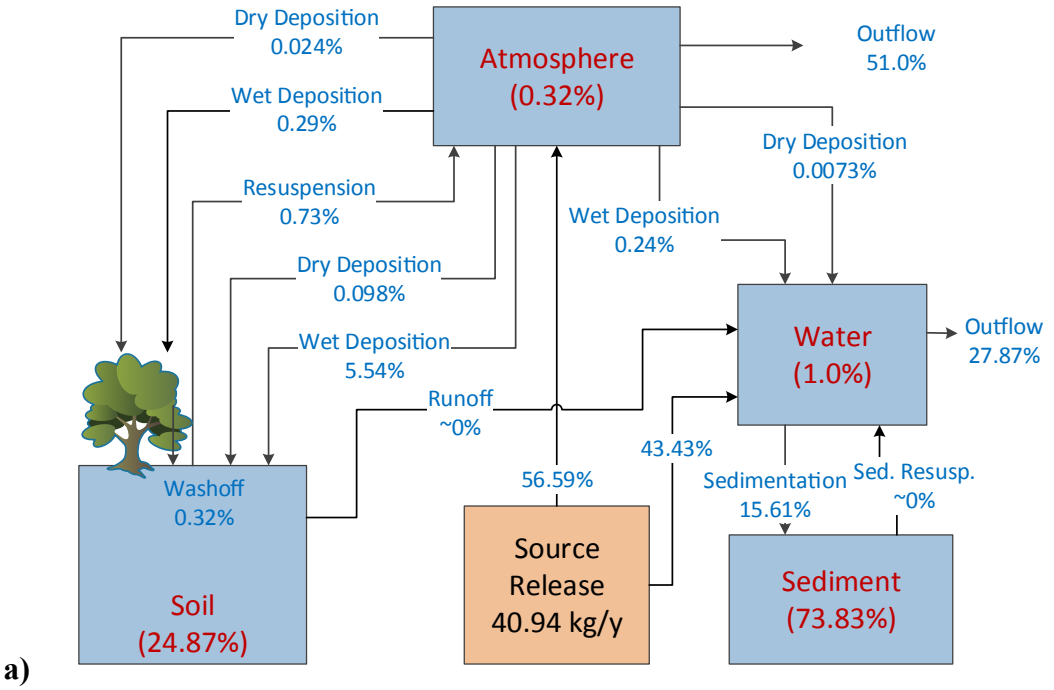

a)

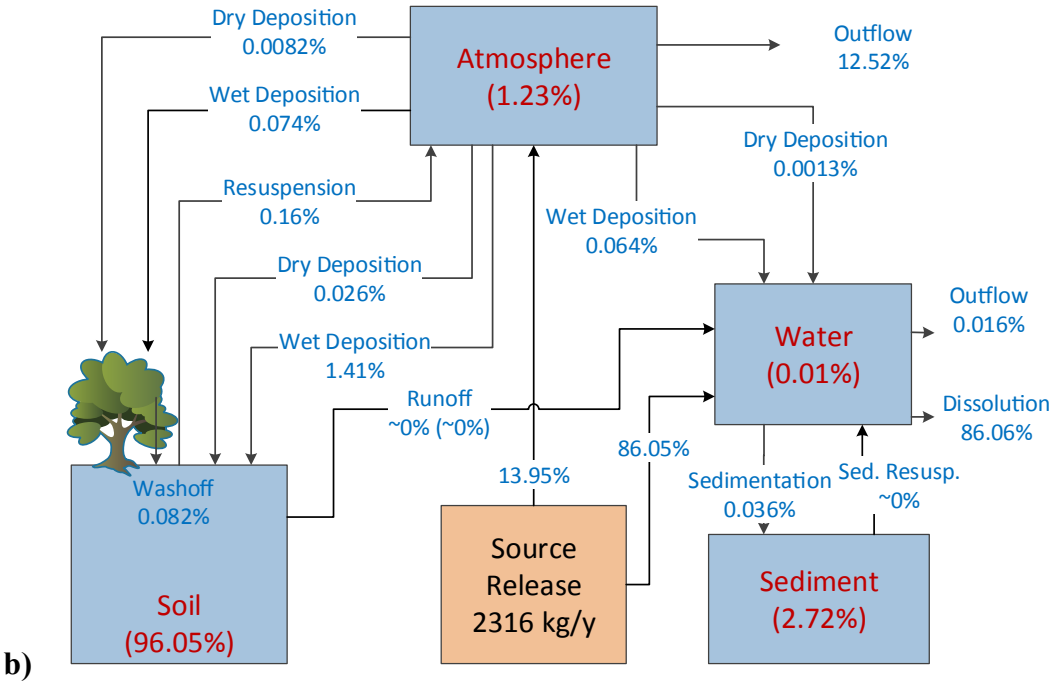

b)

Figure 6-8. Intermedia transport rates of a) CNT and b) ZnO and their mass distribution among the various compartments at the end of 1-year simulation for the Los Angeles test case (Table A-3). Simulation conditions (including release rates of CNT and ZnO) are same as in Figure 6-4. ENMs releases in the simulation were taken to be to air and water only with the total

release estimated by population-based scaling, to the Los Angeles region, of reported global media-specific ENMs release rates (Table A-5) [10]. ENM intermedia transport rates are reported as percent (in blue font) of the total ENM source release rate (note: runoff and sediment resuspension are of the order of 10^{-6} % and 10^{-5} %, respectively). The percent of the total ENM mass in the multimedia system is also reported for each compartment (in red font within the parentheses).

Table 6-2. Compartmental mass distribution of Ag, Al_2O_3, CeO_2, CNT, Cu-based ENMs (metal and metal oxides), Fe-based ENMs (metal and metal oxides), nanoclays, SiO_2, TiO_2, and ZnO in the Los Angeles region at the end of 1-year simulation.

	Air	**Water**	**Soil**	**Sediment**
Ag	1.23% (0.053%)	0.0048% (0.00011%)	94.65% (99.85%)	4.11% (0.097%)
Al_2O_3	0.060% (0.033%)	1.27% (0.25%)	4.64% (81.41%)	94.03% (18.31%)
CeO_2	0.099% (0.036%)	1.22% (0.158%)	7.85% (88.09%)	90.82% (11.71%)
CNT	0.32% (0.041%)	1.00% (0.052%)	24.87% (96.26%)	73.61% (3.64%)
Cu (Cu oxide)	0.106% (0.039%)	0.51% (0.080%)	8.69% (85.80%)	90.69% (14.08%)
Fe (Fe oxide)	0.047% (0.031%)	0.63% (0.15%)	3.63% (77.01%)	95.69% (22.81%)
Nanoclays	0.061% (0.034%)	1.26% (0.28%)	4.87% (79.00%)	93.81% (20.69%)
SiO_2	0.15% (0.04%)	1.17% (0.13%)	11.67% (90.00%)	87.00% (9.83%)
TiO_2	0.032% (0.028%)	1.23% (0.355%)	2.53% (73.29%)	96.15% (26.33%)
ZnO	1.23% (0.048%)	0.0093% (0.00017%)	96.05% (99.90%)	2.72% (0.049%)

Note: % in the parentheses indicate mass distribution for scenarios in which there is direct release to soil. ENMs releases are to air, water, and soil, and release rates were estimated by population-based scaling of global media-specific ENMs release rates estimates[10] (see Table A-5) for the simulation conditions listed in Table A-3. Note: a) only the "direct release" portion of the release to soil is considered to be regionally distributed (see Table A-5); b) Fe (Fe oxide), ZnO, Ag, and Cu (Cu oxide) solubilities are 0.001, 4.45, 1.9, 0.002 mg L^{-1}, respectively; Table A-4).

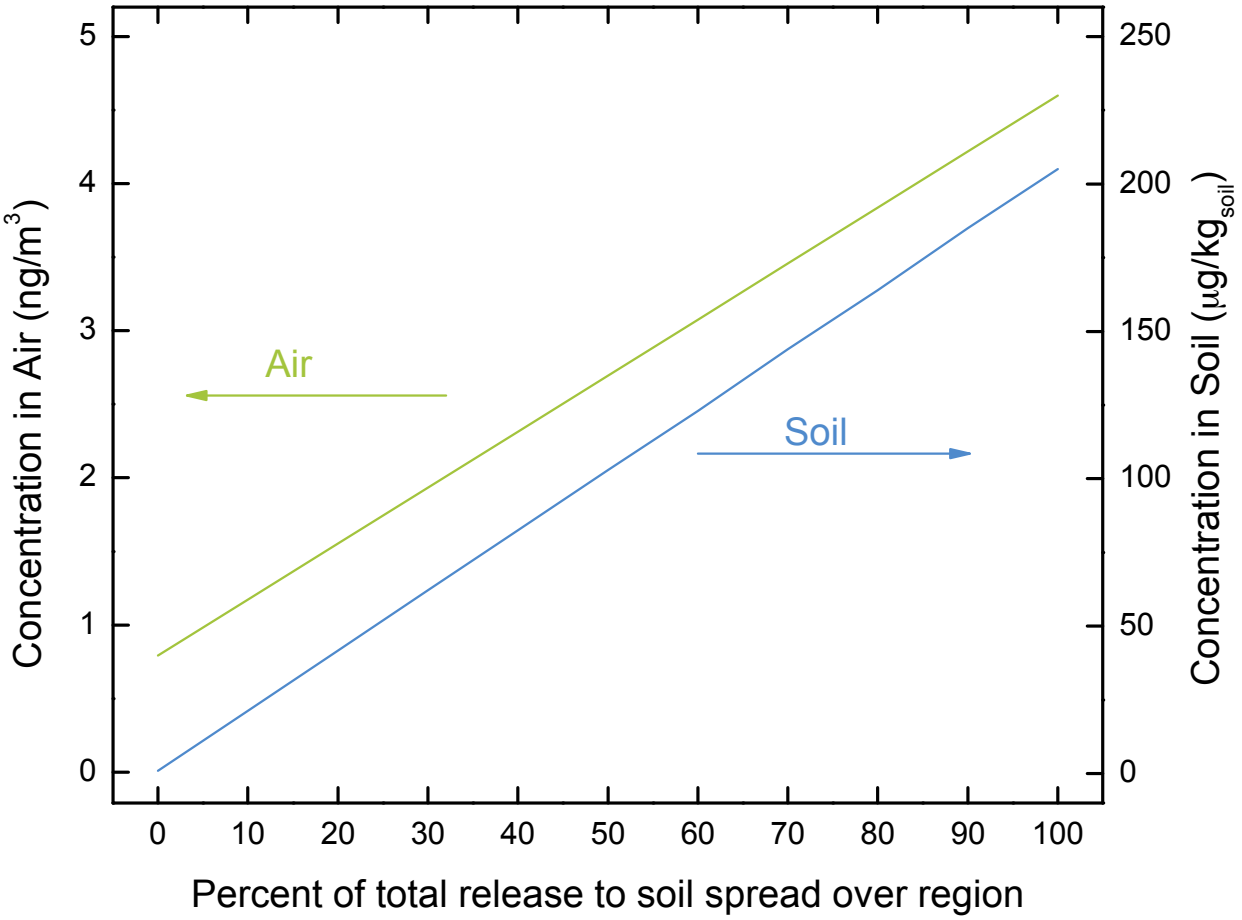

Figure 6-9. Effect of the apportionment of TiO_2 ENM release to soil as being regionally distributed over the simulation region (i.e., the remainder is not considered to be released to the environment). ENM's concentrations in air and soil are for the Los Angeles region at the end of 1-year simulation. Geographical, meteorological parameters and total release rate are the same as for the simulation of Figure 6-4.

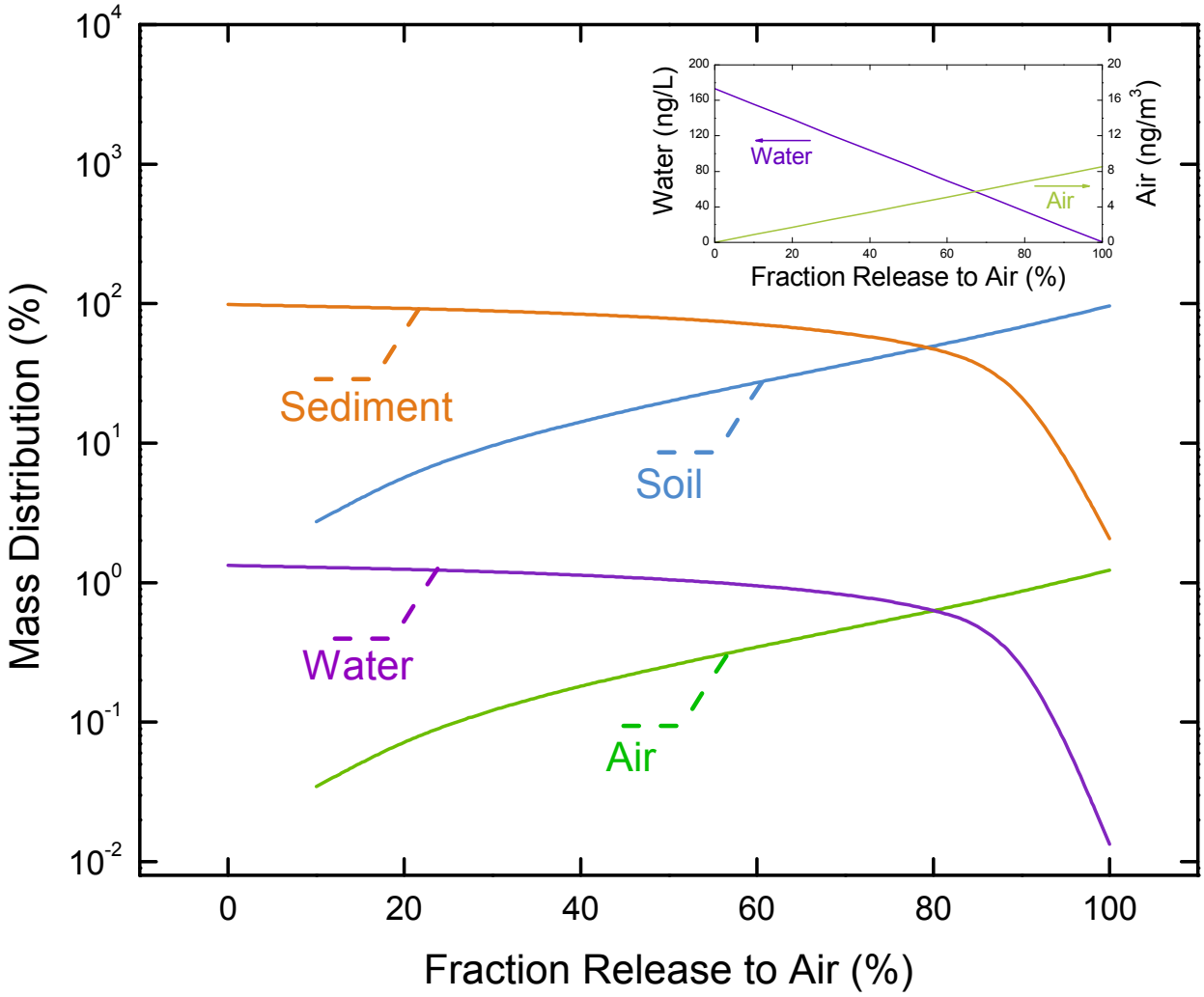

Figure 6-10. Simulated TiO_2 mass distribution of ENM in air, water, soil, and sediment (and concentrations in air and water in inset) as a function of the fraction of total ENM release (total of release to air and water) that is emitted to air, for the Los Angeles region at the end of 1-year simulation. ENM release is taken to be only to air and water. Geographical, meteorological parameters and total release rate are the same as in Figure 6-4.

Dynamic evolution of the compartmental concentrations (and thus mass distribution) is illustrated in the example of Figure 6-11 for an ENM with a size distribution patterned after TiO_2 but with release rate only to air and water. It is apparent that ENM concentrations in air and

water approach steady state behavior over short periods of 72 h and 8 days, respectively. ENM concentrations in air fluctuate markedly with rain events during which there is rapid reduction in the atmospheric ENM concentrations, followed by a rise to steady-state value after each event. In contrast, ENM concentrations in soil increases continually with each rain event adding to the total ENMs mass accumulation in the soil. For example, for the simulation that starts on January 1st, the ENM concentration in soil rapidly rises within about 4 months and subsequently increases slowly over time with continuing input of ENMs to soil from wet scavenging as well as dry deposition (inset in Figure 6-11); in the above specific simulation steady state would not be expected to occur until after about 10 years. Input of ENMs to sediment also continues to increase over time (Figure 6-11). In the absence of direct release to water, one would expect episodic inputs from wet scavenging to lead to periodic increases in the ENM water concentration that would subside after rain events (primarily due to advection from the water compartment).

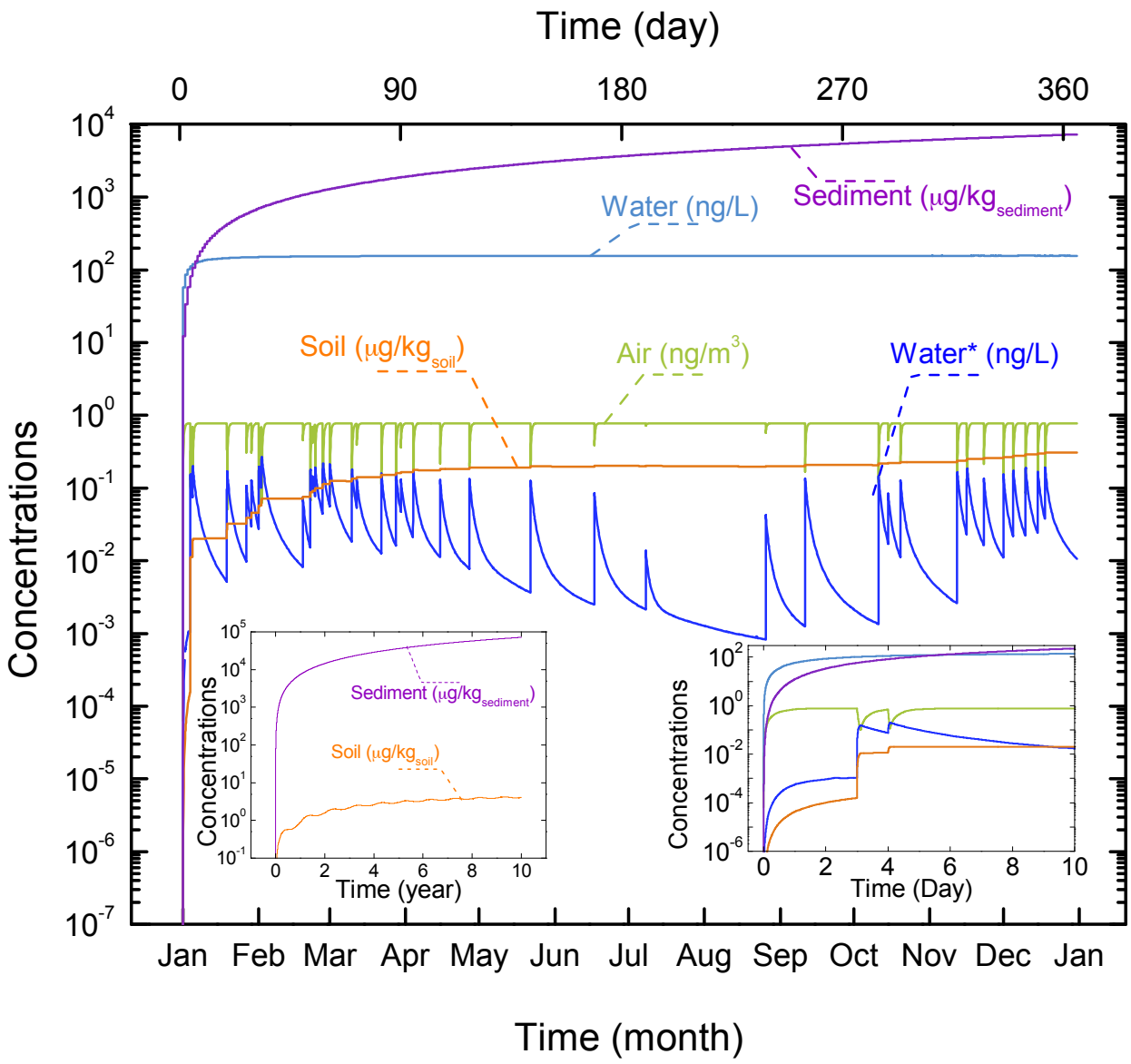

Figure 6-11. Temporal concentration profiles of TiO_2 in Los Angeles. Simulation conditions (including release rates of TiO_2) are the same as in Figure 6-4. Also reported is TiO_2 concentration profile in water for a scenario without direct release to water, denoted by the asterisk (*) and the corresponding curve. Inset figures: (left) concentration profiles for soil and sediment for 10 years and (right) concentration profiles for the first 10 days (day 0 to day 10).

6.3.2 Effect of Nanomaterial Attachment to Ambient Particulates

Although there have been numerous studies on the attachment efficiency of ENMs associated with ambient aerosols [54], data and predictive models of ENMs association with ambient particles (in air and in water) under environmental conditions are lacking [38, 220]. Therefore, in the present modeling approach, ENM association with ambient particles was incorporated via an attachment factor (as defined per eq [6-3]). An illustration of the attachment factor impact on ENM concentration in water and sediment is provided in Figure 6-12 (also for the Los Angeles Region) for ENM of properties and emission rates patterned based on TiO_2 as in the simulation of Figure 6-11. It is apparent that once the attachment factor increases to above ~0.7, predicted ENM concentration in water decreases rapidly, while correspondingly ENM concentration in sediment increases. Over the attachment factor range of [0:1] predicted ENM concentrations increase in water and decrease in sediment by factors of 1.5 and 69, respectively. The above behavior is due to the greater effect of sedimentation on ENM removal from the water column with increased ENMs attachment to larger ambient suspended solids. ENMs removal from the water compartment via advection (i.e., currents, tidal flow) is influenced by partitioning of ENMs to suspended ambient particles. This behavior is illustrated in the inset in Figure 6-12, which demonstrates that as the attachment factor increases the percent of ENMs removal (relative to the total input) via advection decreases, given the lower concentration in water due to increased ENMs removal by sedimentation. Overall, however, advective ENM removal from water column is ~2-200 times greater than removal by sedimentation. ENMs association with ambient atmospheric aerosols can also impact the dynamic multimedia distribution of ENMs. For example, for the same conditions as in Figure 6-11, simulations over a range of values of the attachment factor for ENMs in the air phase (Figure 6-13) from 0 (i.e., no attachment to ambient

aerosols) to unity, revealed decreased dry and wet deposition rates by 52%, and 10%, respectively, with little effect on the atmospheric concentration given the dominance of advective transport as a mechanism for ENM removal from the modeled region (see Figure 6-6).

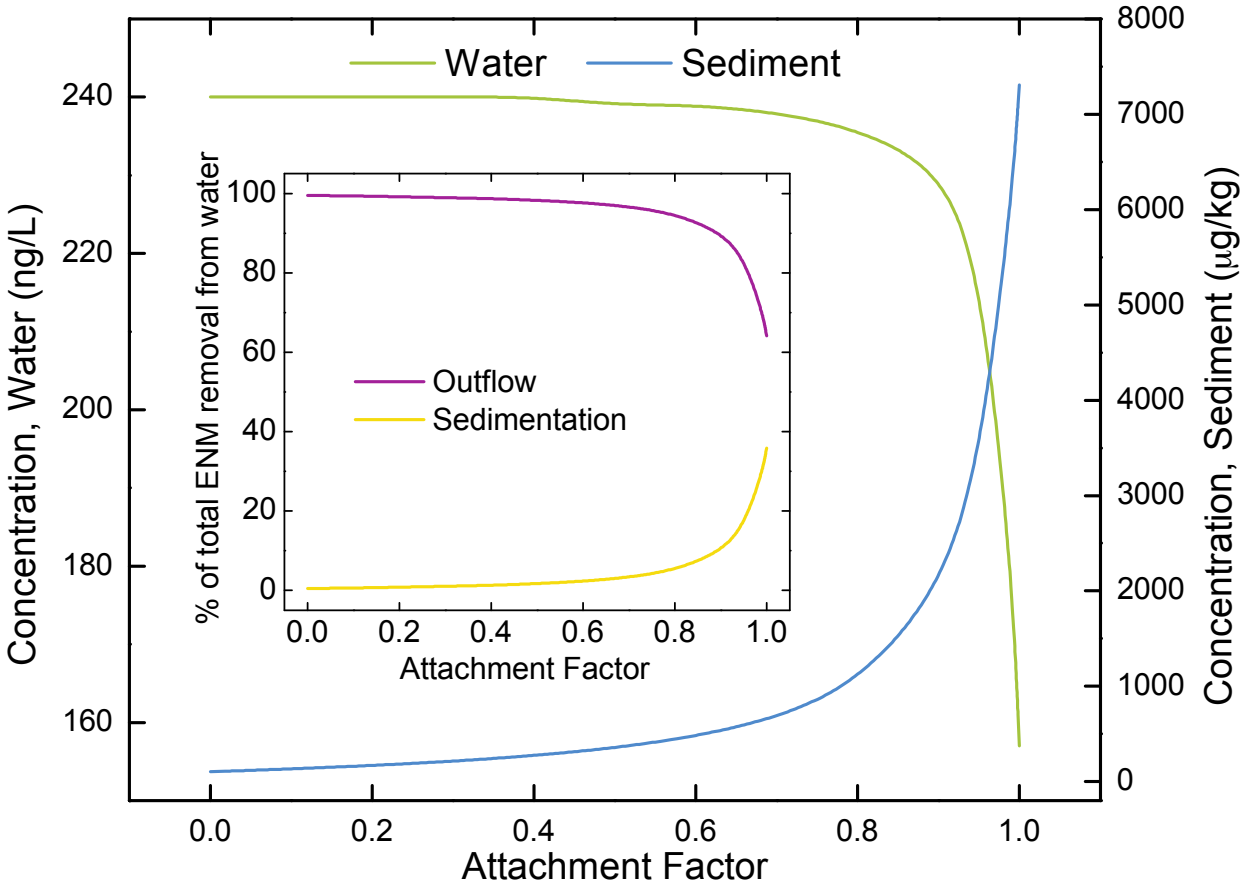

Figure 6-12. Impact of TiO_2 ENM attachment to suspended solids (in water) on ENM concentrations in water and sediment at the end of 1-year simulation. Inset: Percent ENM removal from water compartment due to advection and sedimentation. Geographical and meteorological conditions, and release rates of TiO_2 are same as in Figure 6-4. The initial log–normal PSD parameters for suspended ENMs: μ_{ln}=5.7 nm, σ_{ln}=0.4 nm.

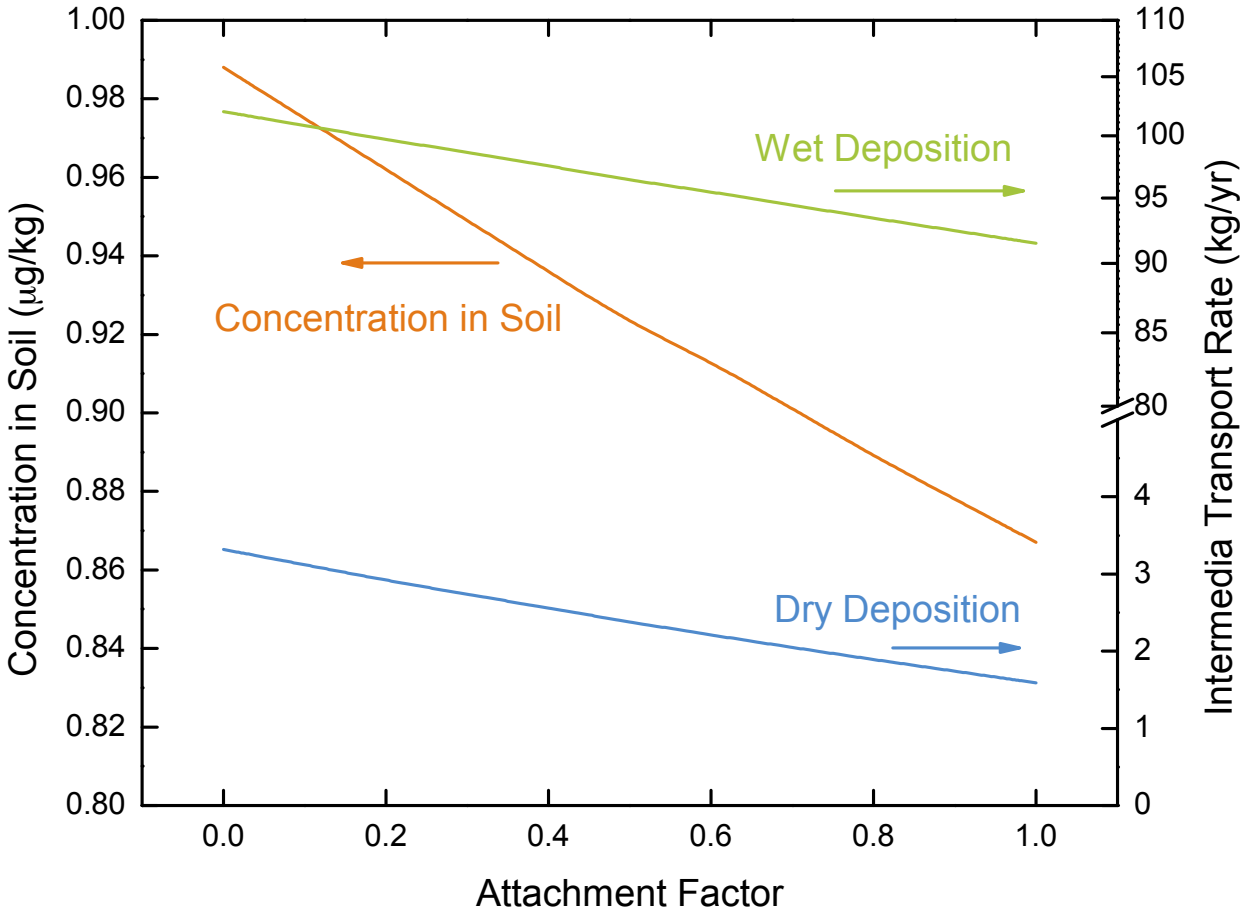

Figure 6-13. Impact of ENM attachment to ambient aerosol (in air) on ENM concentration in soil, and on the dry/wet deposition rate at the end of 1-yr simulation. Simulations are patterned after TiO_2 for the Los Angeles region (Table A-3) with ENM release rate being to air and water as for the simulation of Figure 6-4. The initial lognormal particle size distribution parameters for suspended ENMs: μ_{ln}=5.7nm, σ_{ln}=0.4nm.

6.3.3 Effect of Nanomaterial Dissolution on Environmental Distribution of ENMs

Nanomaterials are generally regarded as being water insoluble, however certain ENMs can exhibit significant aqueous solubility (e.g., ZnO, Ag, CuO, Fe_3O_4) [117, 119-121, 254], which can enhance their loss (transformation) as suspended ENMs in water leading to lower

concentration of these suspended ENMs in the water and sediment (Figure 6-14). An illustration of the impact of dissolution on ENM loss (from the water column) is shown in Figure 6-15 for the same conditions as for the ZnO example in Figure 6-4, and with the ENM solubility as a simulation variable. Dissolution has a low impact on the ENMs loss from the water column (≤5%) when the ENM solubility is below ~5×10^{-5} mg L^{-1}. The concentration of suspended ENMs in water decreases with increased ENM solubility, and for the present example, this concentration would decrease by ~3 orders of magnitude (from 37.3 ng L^{-1} to 0.011 ng L^{-1}) as one progresses away from the condition of essentially insoluble ENMs (i.e., solubility ≤ 10^{-6} mg L^{-1}) to sparingly soluble ENMs such as ZnO (aqueous solubility ~4.45 mg L^{-1} at ~pH 8) [120]. For the case of ZnO, the driving force for dissolution is sufficiently large (given that the background zinc ion concentration in natural water bodies is a few orders of magnitudes lower than ZnO solubility) [255], which is expected to result in essentially total dissolution of this ENM. In general, increased ENM dissolution will correspondingly reduce the accumulation of ENMs onto the sediment (Figure 6-15). When the ENMs are freely suspended in the water compartment (i.e., not attached to suspended ambient suspended solids) one should expect a higher ENM particle loss (due to increased dissolution) for the smaller ENM particles (given that particle area/volume ratio ∝ 1/diameter; also eq [2-16]). However, accumulation of ENM particles on the sediment will be affected to a greater degree by a higher settling rate of larger freely suspended particles.

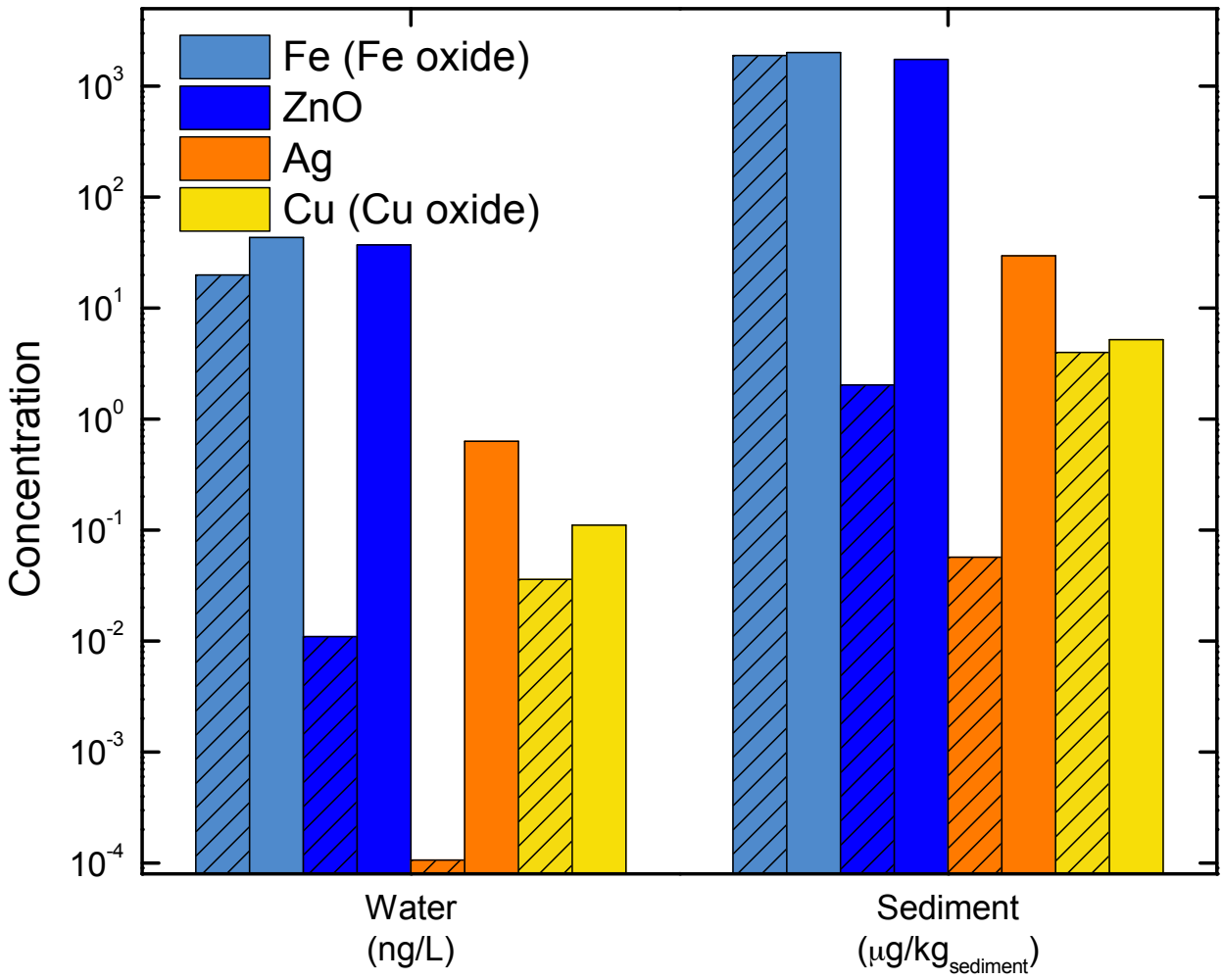

Figure 6-14. Impact of ENM dissolution ENM concentration in water and sediment at the end of 1-yr simulation. Patterned and non-patterned bars represent simulations with and without ENM dissolution, respectively. Simulations are for the Los Angeles region (Table A-3) with ENM release rate being to air and water as for the simulation of Figure 6-4. The aqueous solubilities of Fe (Fe oxide), ZnO, Ag, and Cu (Cu oxide) are 0.001, 4.45, 1.9, 0.002 mg L^{-1}, respectively (Table A-4).

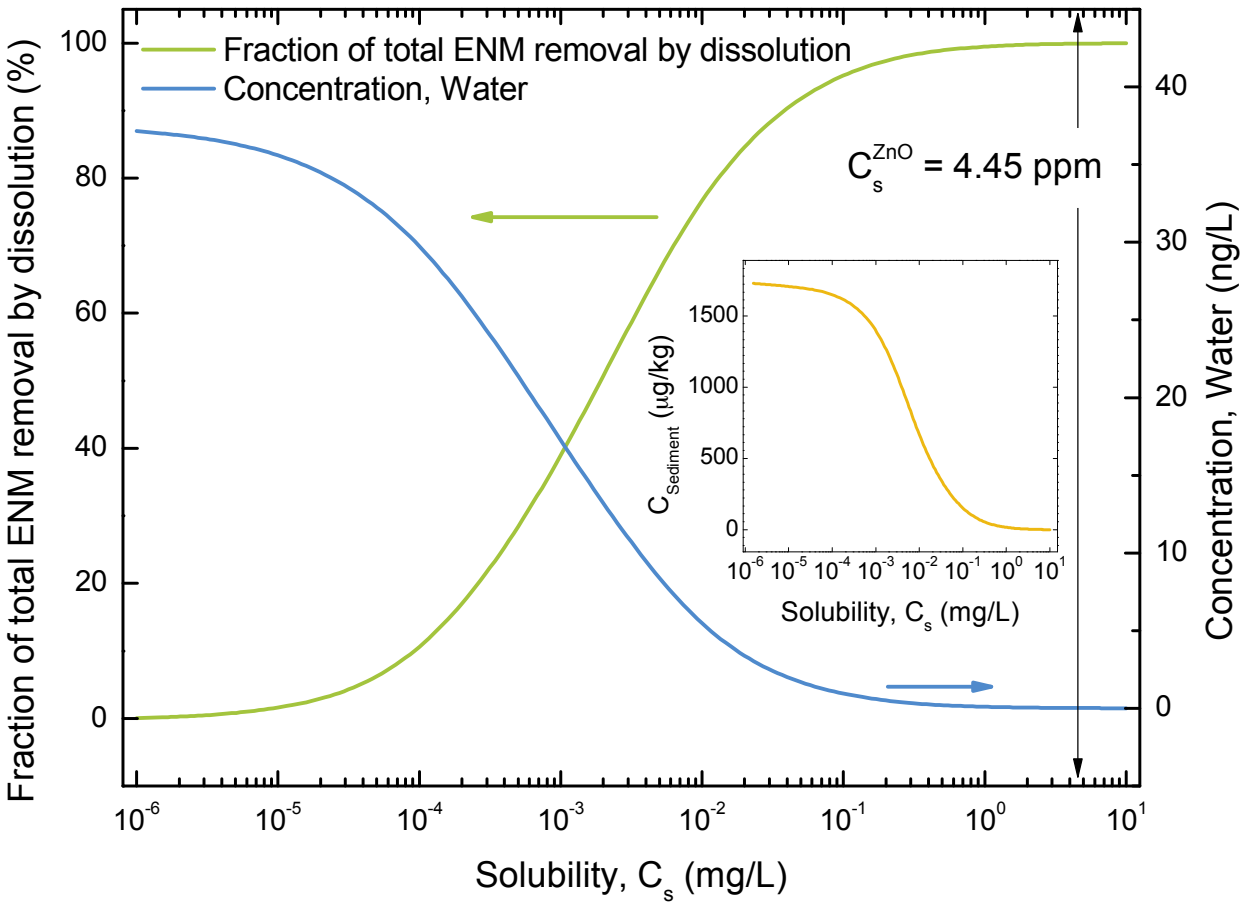

Figure 6-15. Contribution (%) of dissolution to total ENM removal and ENM concentrations in water and sediment (inset) as functions of solubility at the end of 1-year simulation. Simulation conditions (with release rates of ZnO, ambient PSD, and regional parameters) are same as in Figure 6-4. The ionic diffusivity of 6.7×10^{-10} m^2 s^{-1} is used, which is a typical value for a range of metallic ions, including Zn^{2+} [121].

In summary, model simulations for various environmental scenarios indicated that ENM accumulation in the sediment increased significantly with increased ENMs attachment to suspended solids in water. Atmospheric dry and wet depositions can be important pathways for ENMs input to the terrestrial environment in the absence of direct and distributed ENM release

to soil. Increased ENM concentration in water due to atmospheric deposition (wet and dry) is expected as direct ENM release to water diminishes. However, for soluble ENMs dissolution can be the dominant pathway for suspended ENM removal from water even compared to advective transport. Mass accumulation in the multimedia environment for the evaluated ENMs (metal, metal oxides, carbon nanotubes (CNT), nanoclays) was mostly in the soil and sediment.

Chapter 7. Regional multimedia distribution of nanomaterials and associated exposures: A software platform

7.1 Introduction

In Chapter 6 a compartmental multimedia model (MendNano) was developed [131] and its validation was demonstrated based on environmental monitoring data for semi-volatile organics, thus illustrating that compartmental models can be useful in providing a first-tier analysis for estimating the magnitudes of potential ENM exposure concentrations. However, in order to support timely decision analysis regarding the potential environmental impact of ENMs, it is imperative to make available integrated tools that enable rapid analysis. Accordingly, an integrated simulation tool was developed for estimating potential releases and environmental distribution of nanomaterials (RedNano), which interfaces MendNano [131] with a LCIA based model for estimating ENM release rate [10, 80]. The integrated simulation tool, implemented as a web application, was developed as a modular system and its structure and utility are demonstrated in this chapter with a number of illustrative use cases.

7.2 Integrated Simulation Tool for Assessing the Release and Environmental Distribution of Nanomaterials (RedNano)

7.2.1 Overview of RedNano simulation tool

RedNano consists of four main elements (Figure 7-1): 1) user interface for scenario design and results visualization, 2) MendNano (Chapter 6), 3) Lifecycle Environmental Assessment for Release of Nanomaterial (LearNano) model for estimating ENM release rates, 4) a parameter database, and 5) a repository for building a library of scenarios and simulation cases. The

RedNano graphical user interface (GUI) provides guidance for scenario design and parameters specification; the latter may be obtained from an integrated the parameter database, input manually, or calculated by various sub-models. Based on the designed scenario, MendNano computes the multimedia mass distribution of ENMs given a rate of release and/or initial concentration of the selected ENM in one or more of the environmental compartments. Simulation results are then graphically represented via visualization modules as well as provided in standard numerical formats. The RedNano integrated simulation tool was designed as a client-server web application using standard web development environment (i.e., HTML, PHP, JavaScript, MySQL).

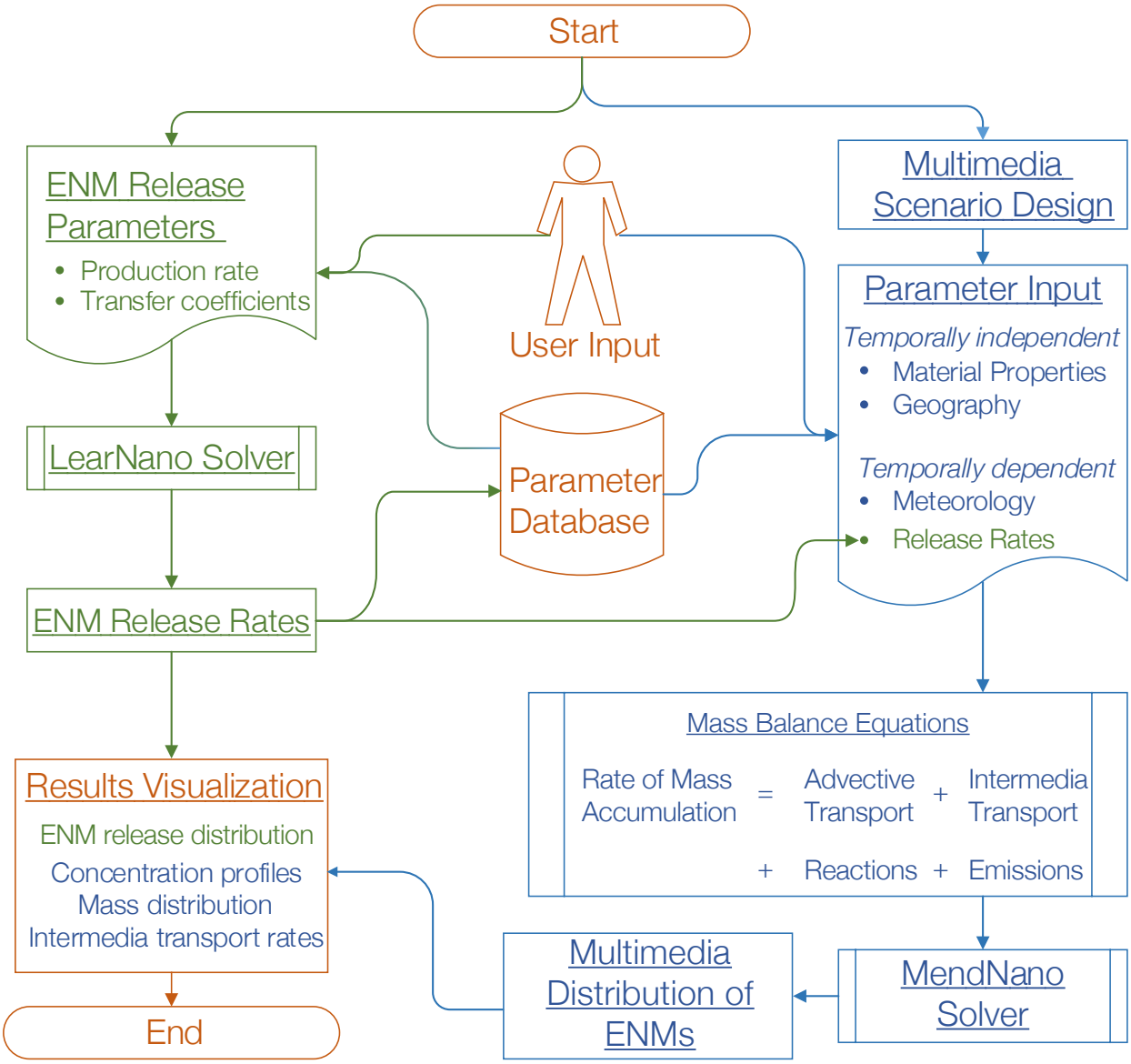

Figure 7-1. Overview of the simulation tool, for assessing the release and environmental distribution of nanomaterials.

7.2.2 LearNano

Estimation of ENM release rates can be accomplished by the LCIA modeling approach as described in detail elsewhere [10, 42]. Briefly, in LCIA based models, reported ENM mass production rates [9] are allocated to the various ENM applications (e.g., paints, cosmetics,

electronics, catalysts), waste processing facilities (i.e., technical compartments), and eventually environmental compartments (Figure 7-2) [10, 42]. Transfer coefficients, which are dependent on the ENM type, ENM application, and region under consideration [10, 42], then serve to quantify the fractions of ENMs entering the "source" compartments that are subsequently transferred to the "target" compartment (Figure 7-2). Accordingly, a series of algebraic mass balance equations that describe ENM mass release rates to the various environmental compartments [10, 42] are incorporated in LearNano:

$$M_A = \text{mass release rate to air} = M_{prod}\left[F_{m,a}\sum_i\left(F_{u,a,i}+F_{d,a,i}\right) + F_{d,I}\times T_{I,air} + F_t\times T_{t,b}\times T_{b,I}\times T_{I,air}\right] \quad [7\text{-}1]$$

$$M_W = \text{mass release rate to water} = M_{prod}\left[T_{t,e}\times\left(F_{m,t}+\sum_i\left(F_{u,t,i}+F_{d,t,i}\right)\right)+F_{u,w}\right] \quad [7\text{-}2]$$

$$M_S = \text{mass release rate to soil} = M_{prod}\left[\sum_i F_{u,s,i} + F_t\times T_{t,b}\times T_{b,s}\right] \quad [7\text{-}3]$$

where M_{prod} is the total mass production rate, and *F* and *T* are transfer coefficients [10]. The lifecycle stages *manufacturing, use,* and *disposal* are represented by subscript *m*, *u*, and *d*. The technical compartments refers to *waste incineration plant (WIP), wastewater treatment plant (WWTP),* and *biosolids*, and are denoted by subscripts *I, t,* and *b*, respectively. The environmental compartments *air, water,* and *soil* are denoted by *a, w, and s.* The subscript *i* represents various ENM applications (e.g., cosmetic, coating/paints/pigments, electronics/optics).

Implementation of the LearNano model includes user guidance and visualization tools for input data and results, model solver, and a parameter database. The analysis scenario (i.e., a given combination of ENM, region, and application(s)) is constructed within the GUI, which also captures ENM production rates and the various transfer coefficients between adjoining compartments (both technical and environmental). ENM production rates and transfer coefficients can be obtained from a parameter database by specifying the ENM(s), application(s), and region(s) of interest (see section *Databases*). The mass balance equations (eqs [7-1]–[7-3]) are then solved to determine the average ENM release rates to the environmental compartments (i.e., air, water, and soil). The mass "flows" of ENMs among the various compartments can be visualized using a dynamic and interactive Sankey diagram (Figure 7-3). Also, the global distribution of ENM releases (to various environmental compartments) in different countries can be represented on a world map (Figure 7-4). It is noted that, while the present version of LearNano computes ENM release rates on a country level, estimates of regional ENM release rates may be obtained by scaling country level release rates on the basis of population, area, or economic indicators [10, 42].

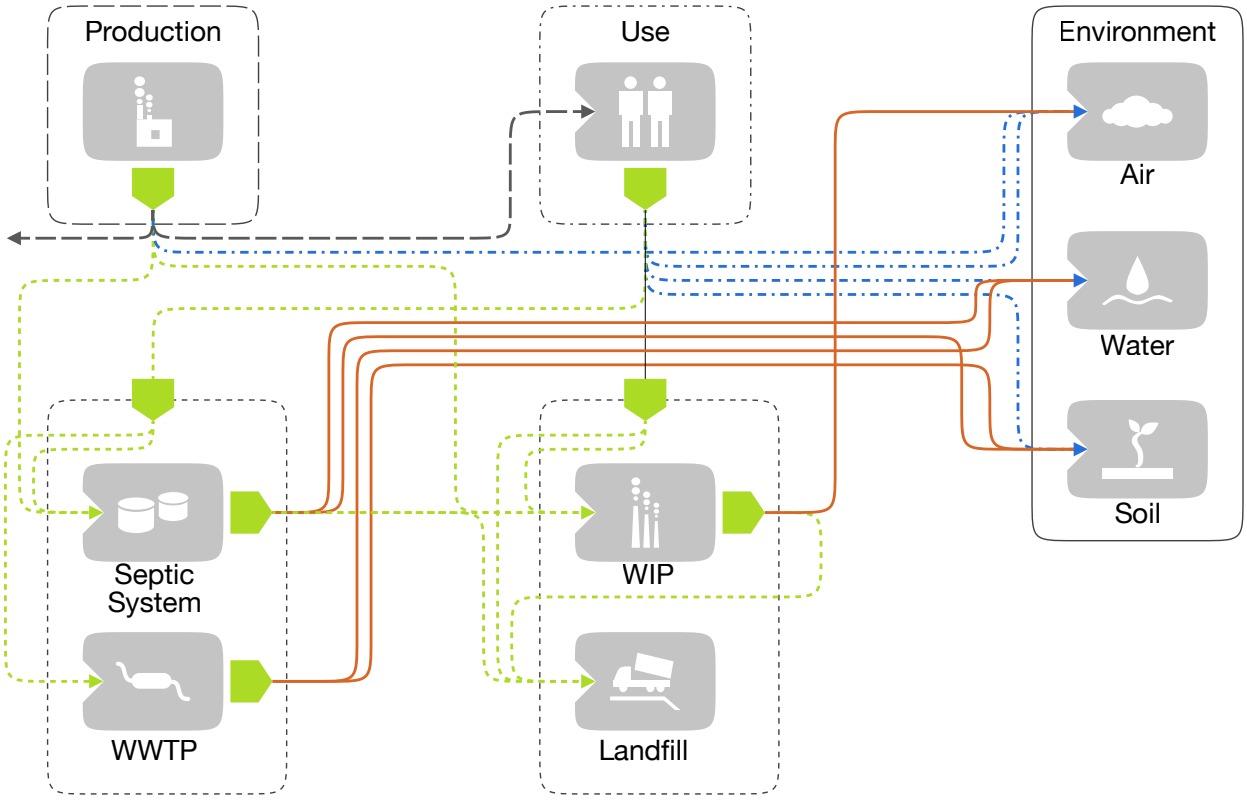

Figure 7-2. Lifecycle tracking of ENMs. The various lines represent the paths for which transfer coefficients quantify the portion of ENMs transferred from the source to the target compartments. Blue lines represent direct release to environmental compartments from production and use, green lines represent ENM transfer from production and use to waste processing facilities, orange lines represent indirect release to environmental compartments from waste processing facilities, and gray lines represent import/export and ENM transfer from production to phase.

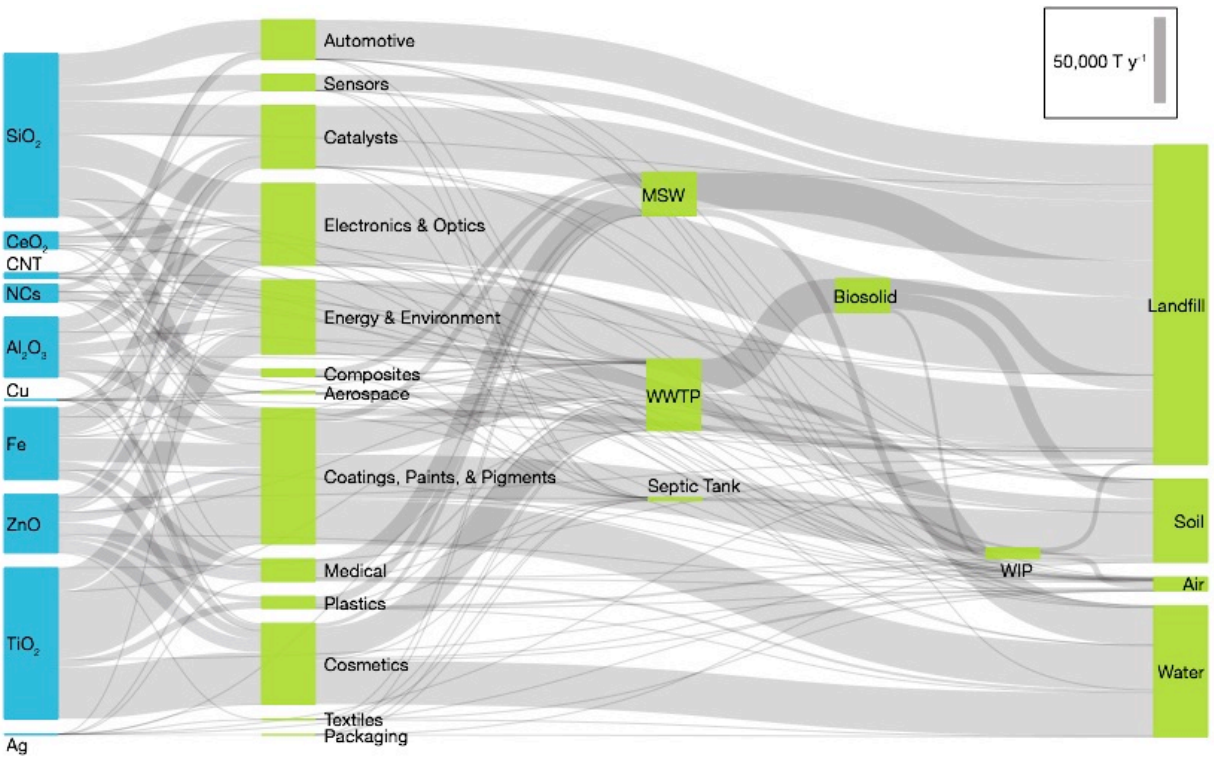

Figure 7-3. Example Sankey diagram to visualize ENM lifecycle flow (for different ENMs) from production and use, through technical compartments, to disposal and release to the environment. The vertical size of the bars and thickness of the links represent the magnitude of the ENM mass transfer rate.

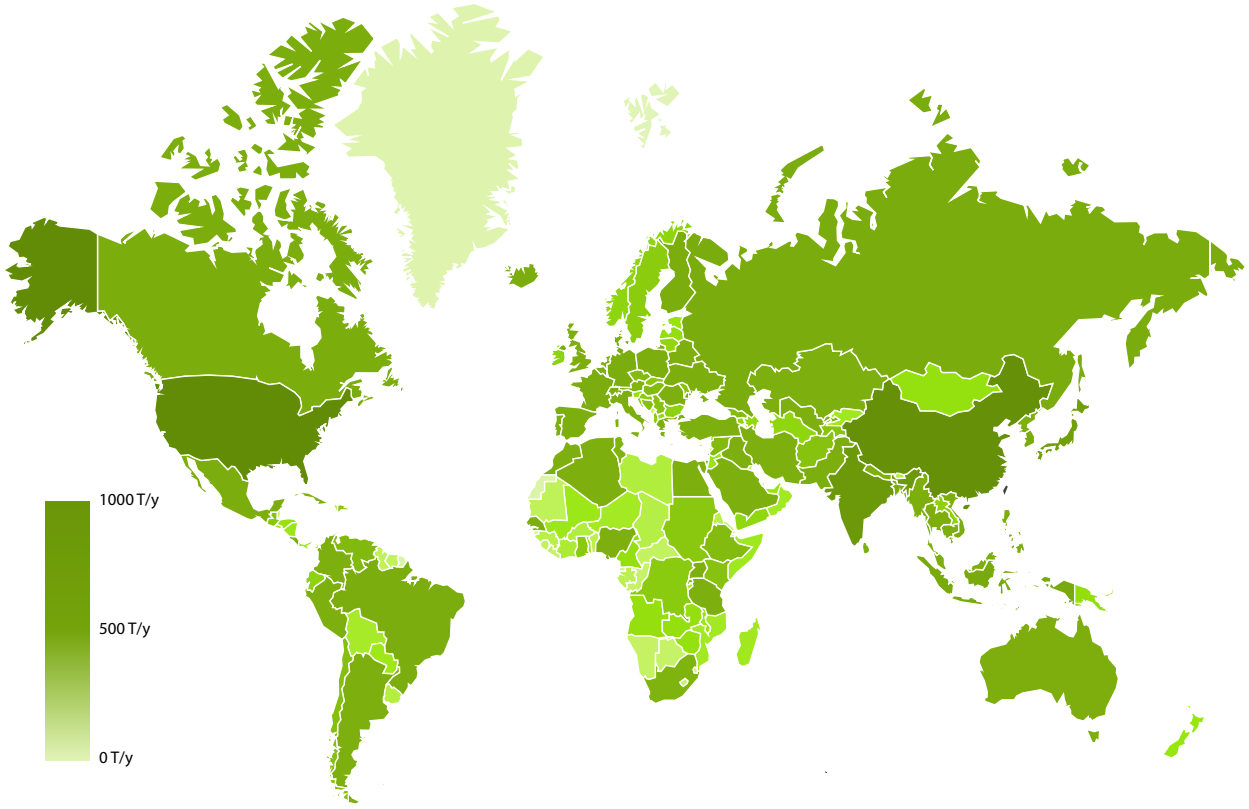

Figure 7-4. Example of the global distribution of the release rates of TiO_2 to water.

7.2.3 Graphical user interface (GUI)

The web-based GUI for RedNano enables building multimedia scenarios, initiating model execution, as well as visualization of simulation results. A multimedia scenario refers to the specification of a model environment (i.e., geographical region and its meteorology), the target ENM, and its release rates. A multimedia scenario is built by specifying or selecting the needed parameters from modules that include: a) geography, b) meteorology, c) material properties, and d) source release (Figure 6-2).

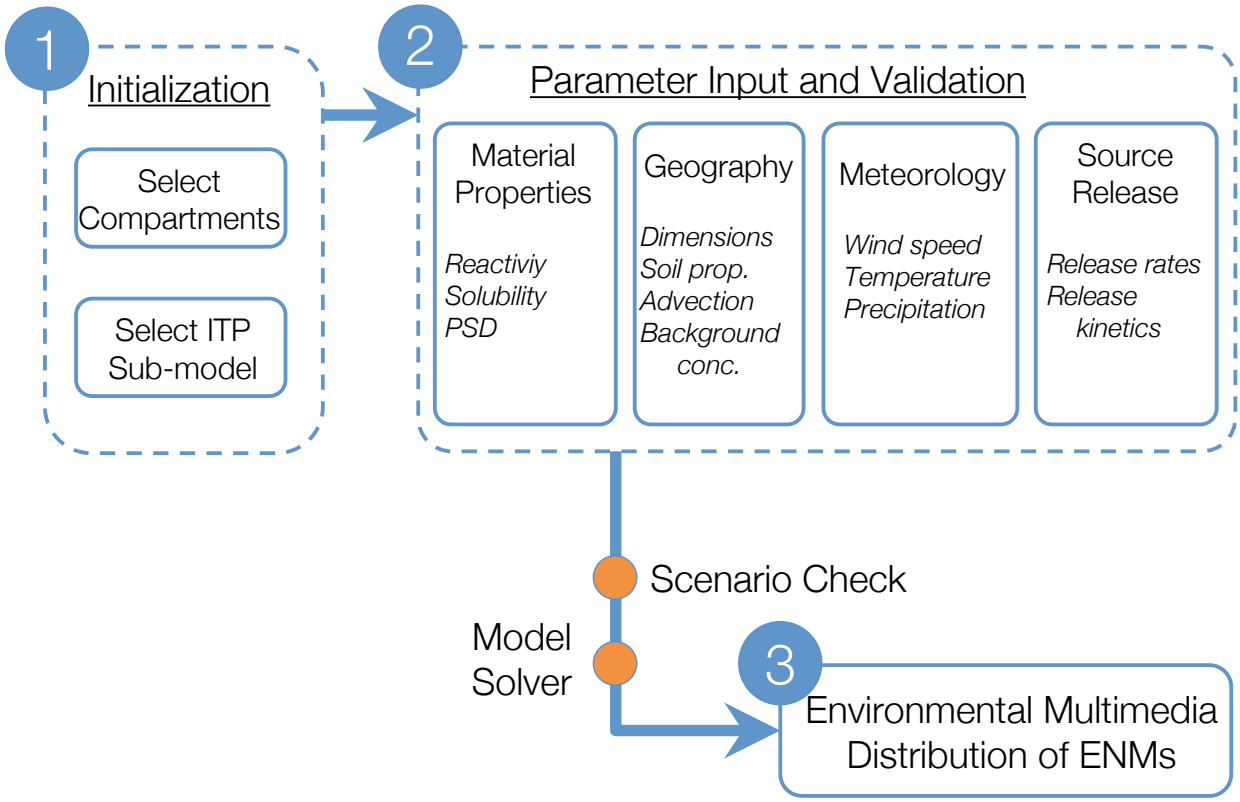

Figure 7-5. Workflow for assessing the environmental distribution of ENM. ITP: intermedia transport processes, PSD: particle size distribution.

Scenario design is initiated by selecting the environmental compartments (e.g., air, water, soil, sediment, vegetation canopy, biota) and ITPs (e.g., dry/wet deposition, resuspension, sedimentation, dissolution) of interest for the desired simulation period (typically ~1 yr) and the target ENM and its properties (Figure 7-5). Subsequently, sub-models are selected for the specified ITPs (Figure 2-3) and the regional geographical and meteorological parameters are specified for the selected region (Figure 7-5). The values for the above parameters may be obtained from the system's parameter database, or be provided by the user. ENM release rates to the various compartments are also required and these can be obtained from LearNano by selecting target ENM, region, and applications of interest, or specified directly by the user

(Figure 7-5). The temporal profile of the ENM release rates kinetic can be specified as constant or periodic sinusoidal (e.g., to mimic seasonal and diurnal variability).

The specification of the needed parameter values is accomplished in a series pages (or views; Figure 7-6) within the GUI corresponding to the modules shown in (Figure 7-5). The parameters input is validated, prior to model execution, to ensure that specified values are within reasonable range and/or constrains (e.g., minimum regional area, maximum rainfall intensity). Additional simulation scenario validation is also conducted to ensure that scenarios are not ill-defined (e.g., simulation with neither source release nor initial compartmental concentration). Upon completion of a simulation scenario, model execution is initiated (a unique Simulation ID is assigned for compilation of a scenario library) and the results can be visualized via a series of graphical representations. The dynamic multimedia ENM distributions can be represented as: a) ENM temporal concentration (or mass) profiles in various compartments (Figure 7-7); b) intermedia mass transport rates or fluxes; c) ENM mass distribution (percent) among the various compartments (Figure 7-7); d) ENM apportionment throughout the ambient particle size distribution (Figure 7-7); and e) the magnitude of intermedia transport rates, as fraction of the ENM release rates, that allows assessment of the relative significance of the various intermedia transport processes (Figure 7-8). For example, in the illustration of Figure 7-7, ENM concentrations in air and water (left upper plot) rapidly reach pseudo steady state, except during episodic rain events, in which a sharp decrease in ENM concentration in air is observed, followed by a rapid increase after the rain event. In contrast, ENM concentrations in soil and sediment continue to increase, since ENM removal rates from soil and sediment are significantly lower than the rate of ENM entering the soil and sediment. Given the above and that ENM release rate to water was greater relative to air (Figure 7-8, Table A-8), the majority of ENM

mass accumulated in the sediment (right upper subplot). ENM mass distribution in air among the particle sizes fractions of ambient aerosol is shown to follow the expected tri-modal distribution (lower subplot).

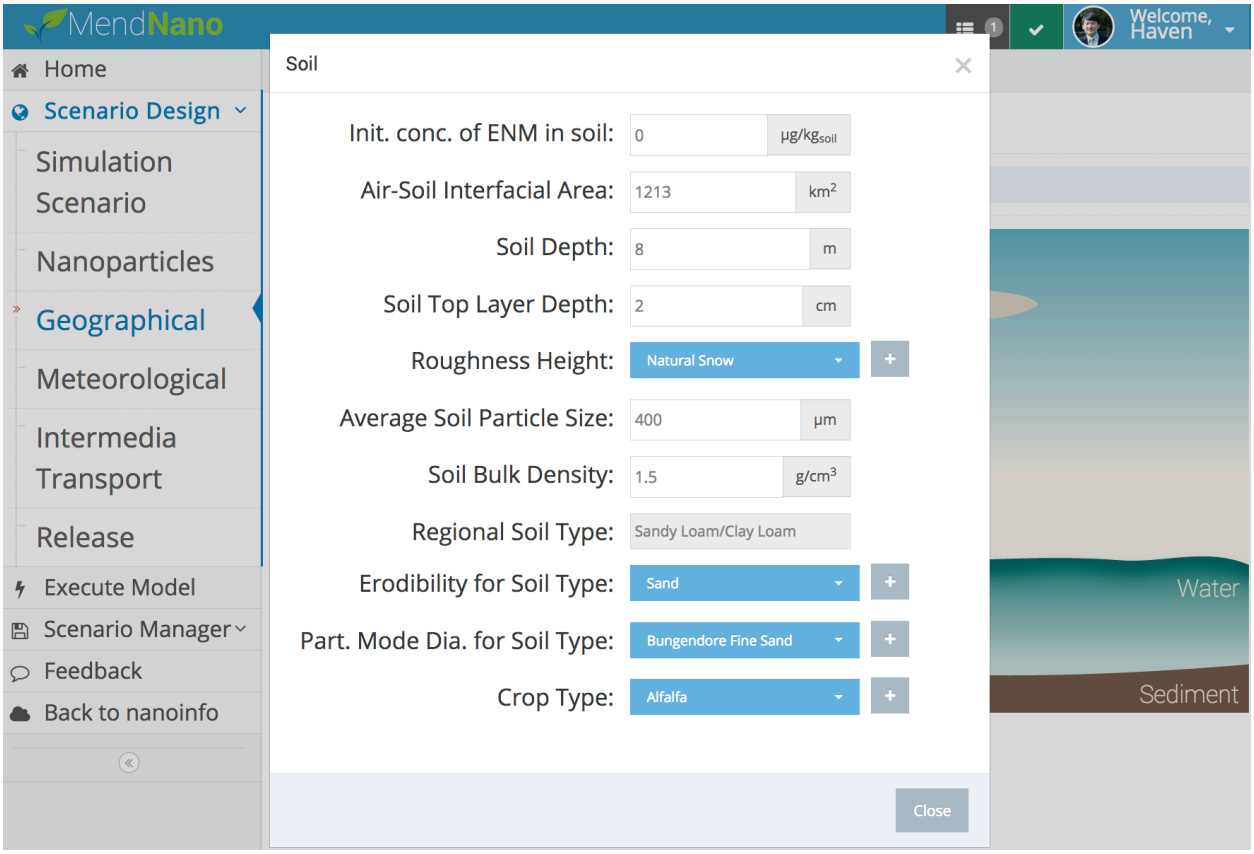

Figure 7-6. Examples of MendNano web-based graphical user interface for scenario building showing inputs of soil parameters.

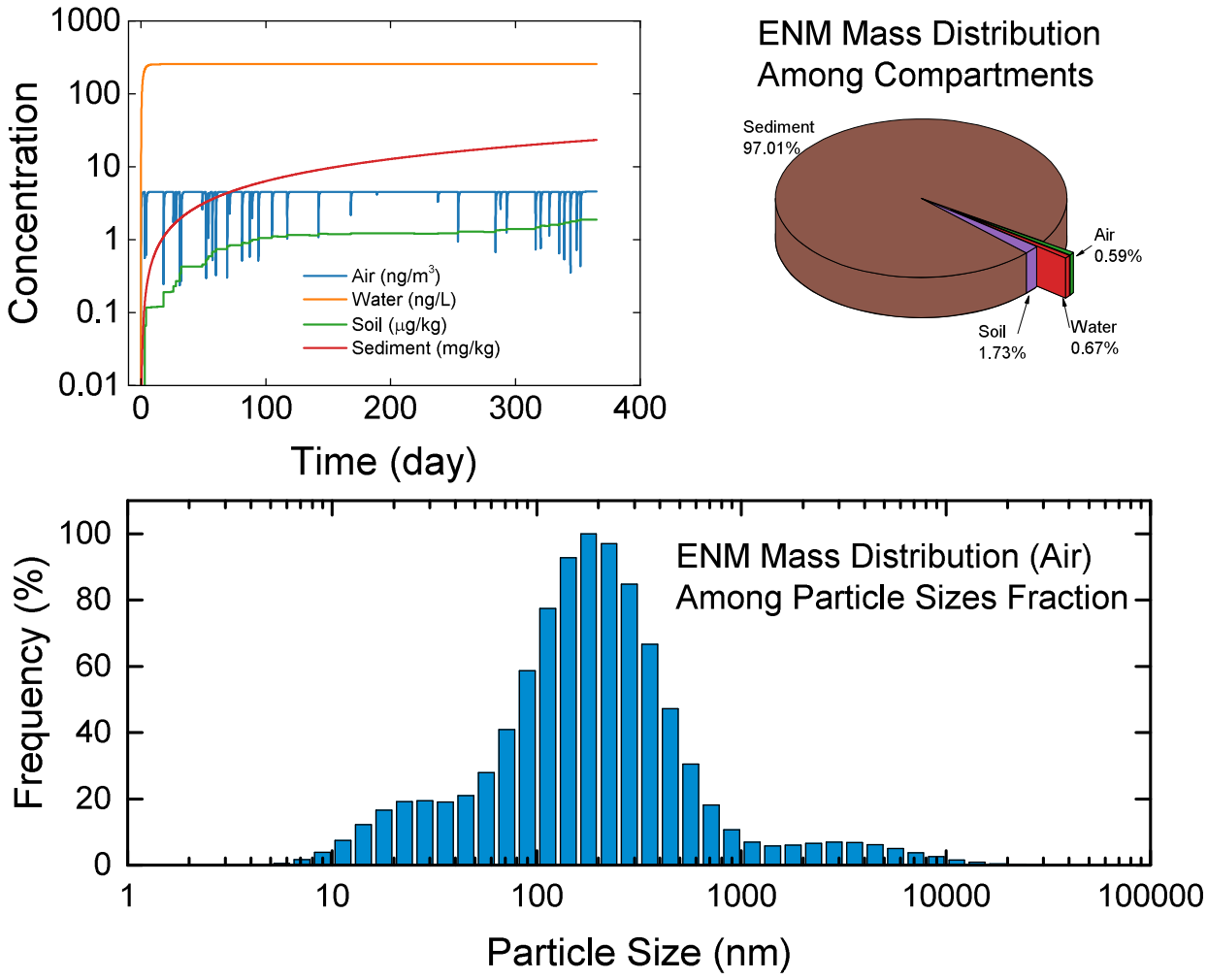

Figure 7-7. Examples of graphical presentations of MendNano simulation depicting concentration profiles and mass distributions of TiO_2 in the Los Angeles region among the various compartments and among the ambient size distribution. Releases of TiO_2 in the above example are to air (5,000 kg yr^{-1}) and water (19,381 kg yr^{-1}).

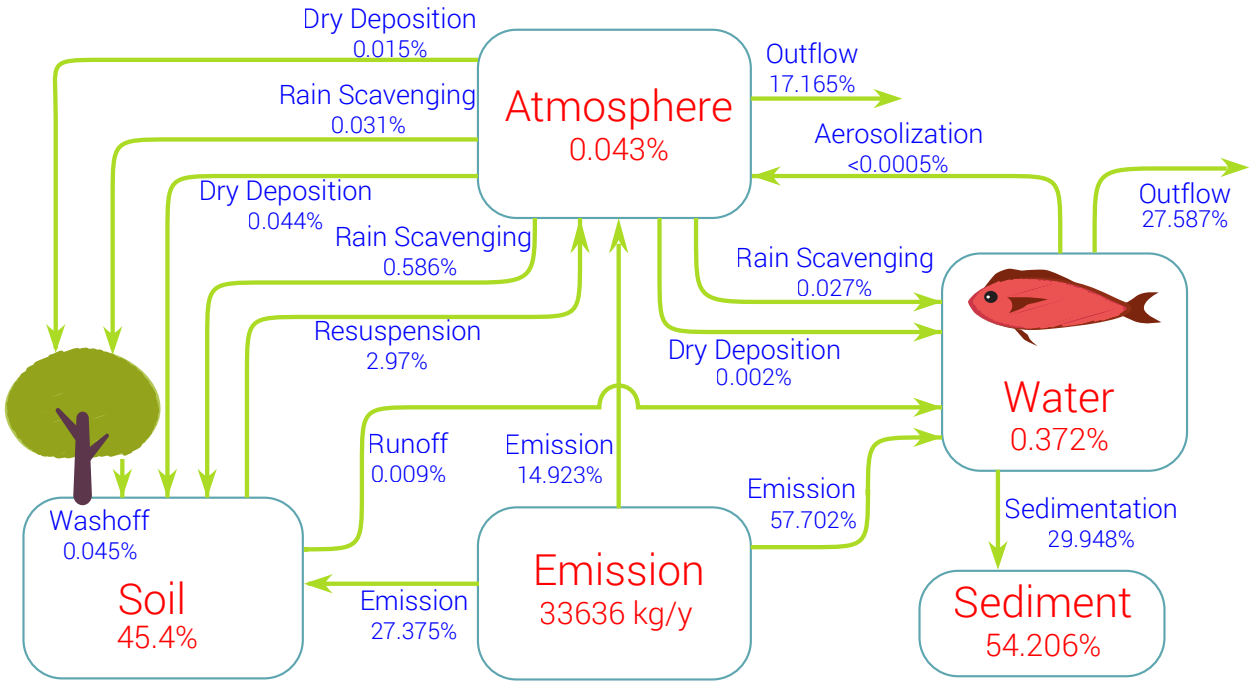

Figure 7-8. Intermedia transport rates of TiO_2 and mass distribution among the various compartments at the end of 1-year simulation for the Los Angeles test case. TiO_2 release rates are reported in Table A-8, and regional geographical and meteorological parameters are reported in Table A-7. Intermedia transport rates (in blue font) are reported as percent of total ENM release rate, and the mass distribution of ENM for each compartment is reported as percent of total ENM mass in the environment (in red font).

7.2.4 Databases

The parameter database contains material properties, geographical, and meteorological parameter values (Table 7-1), which are compiled from various literature and database sources [123, 248, 256, 257]. The parameter database also includes a library of ENM production rates and transfer coefficients corresponding to specific ENMs, applications, for different geographic regions (Table), compiled from various published studies [42], public databases [258], market research [9], and estimated based on economic indicators [259]).

Table 7-1. Parameters database.

Category	Sub-category	Property
Material properties		PSD (ENM and aerosol)
Geographical parameters	Physical description	Interfacial Area (air-water, air-soil) Mixing height Water depth Water flow rate Average suspend solids diameter Sediment depth Soil depth
	Dry deposition to vegetation	Roughness factor Characteristic field length Crop vegetation factor
	Dry deposition to soil Wind resuspension of soil	Roughness height Soil erodibility
Meteorological parameters		Monthly Temperature (air, water) Wind speed (monthly, annual average, max) Rainfall rate (monthly)
LearNano parameters		ENM Global production rate Transfer coefficients (ENM specific) Transfer coefficients (application specific) Transfer coefficients (region specific)

* Additional parameters, including those calculated internally by the model, are provided in Table 6-1.

7.3 Use Cases for Assessing Multimedia Distribution of ENMs

The integrated RedNano simulation tool is suitable for a variety of assessments regarding the environmental distribution of ENMs and their fate and transport behavior. These assessments can be classified into use cases that include, but not limited to, the following:

1. Environmental ENM concentrations and mass distribution based on a specified multimedia scenario;
2. Dynamic response of the environmental system to temporally varying ENM release rates;

3. Impact of specific intermedia transport processes on the temporal dynamics of ENM distribution in the environment;
4. Comparison of estimated environmental ENM concentrations in various regions;
5. Contribution by ENM applications (or use) to the overall ENM releases and exposure concentrations in the various environmental compartments;
6. Estimation of source release rates, based on matching of model estimates and reported environmental concentrations.

In order to demonstrate the above use cases, illustrative simulations were conducted to estimate the environmental distributions of TiO_2, CeO_2, SiO_2, and CNT in selected regions.

7.3.1 Use case 1. Environmental ENM concentrations and mass distribution

The typical use case of the RedNano integrated simulation tool is to estimate environmental ENM concentrations and mass distributions based on a specified scenario as per the workflow described in the Graphical User Interface section (Figure 7-7). It is noted that the parameter input does not need to follow a specific order. Also, the scenario design is checked internally at the GUI level prior to execution to ensure that the scenario is properly conceived (e.g., parameter values are within reasonable constrains, source release or initial compartmental concentration are non-zero). The simulation results can then be explored via the data visualization modules accessible via the GUI (Figure 7-1).

7.3.2 Use case 2. Dynamic response of environmental system to temporally varying ENM release rates

ENM release rates are recognized as one of the most important parameters in environmental multimedia assessment [131]. The case of a constant (i.e., time-invariant) release rate, for estimation of steady state concentrations in the various environmental media, is the commonly used scenario [38, 42, 131, 132]. However, time-dependent release rates may also be of interest. For example, ENM releases from sunscreens to water bodies in coastal cities may follow a sinusoidal function, where the releases in the summer may be significantly higher than those in the winter. Similarly, releases of ENMs due to vehicular traffic (either from automobile exhaust or due to release of carbon from wear of tires) may follow a periodic function with release rates during the day being greater than night. Additionally, the time required for the environment to recover (i.e., for ENMs to be removed from the environment via various transport processes) after the cessation of source release (e.g., after incidental spill) may also be of interest. Accordingly, within RedNano, simulations can be carried out to evaluate ENM distributions with different ENM release kinetics. The source release can be simulated as a single or repeating release events, and the release rate of the events can be either a constant rate or given by sinusoidal functions (Figure 6-2), where the cycle period, cycle gap (for repeating events), and amplitude (for sinusoidal releases) can be specified.

The multimedia distribution of ENMs (use case #1) and the dynamic response of an environmental system to temporal variations of ENM release rate (use case #2) are illustrated for TiO_2 in Los Angeles. Due to lack of transfer coefficients specific to Los Angeles, TiO_2 release rates for Los Angeles were estimated by scaling from US release rates on the basis of a population ratio. TiO_2 release rates to air and water were taken to follow a sinusoidal release

function with a cycle period of 100 days, where the release rates fluctuated between 0 to 27.4 and 0 to 106.2 kg day^{-1}, for releases to air and water, respectively, and were terminated thereafter. The results as shown in Figure 7-9 indicate that TiO_2 concentrations in air and water that fluctuate between 3.3 – 4.4 ng m^{-3} and 195 – 267 ng L^{-1}, respectively, represent ~±15% deviation (in both media) from the time averaged concentration in the respective compartments. Following cessation of source releases to air and water (at t = 100 day), TiO_2 concentration in both compartments decreased rapidly (Figure 7-9), to 90% of the levels just prior to the termination of the release in ~1 and ~4 days, respectively. TiO_2 concentrations continue to decrease until pseudo steady state is reached in air and water, within ~4 and ~38 days, respectively. Although ENM releases to air and water ceased after 100 days, ENM concentrations in air and water did not vanish since ENMs in soil (accumulated during in the first 100 days) continued to be transported to air via soil wind resuspension, and subsequently deposited to the water compartment via dry and wet depositions.

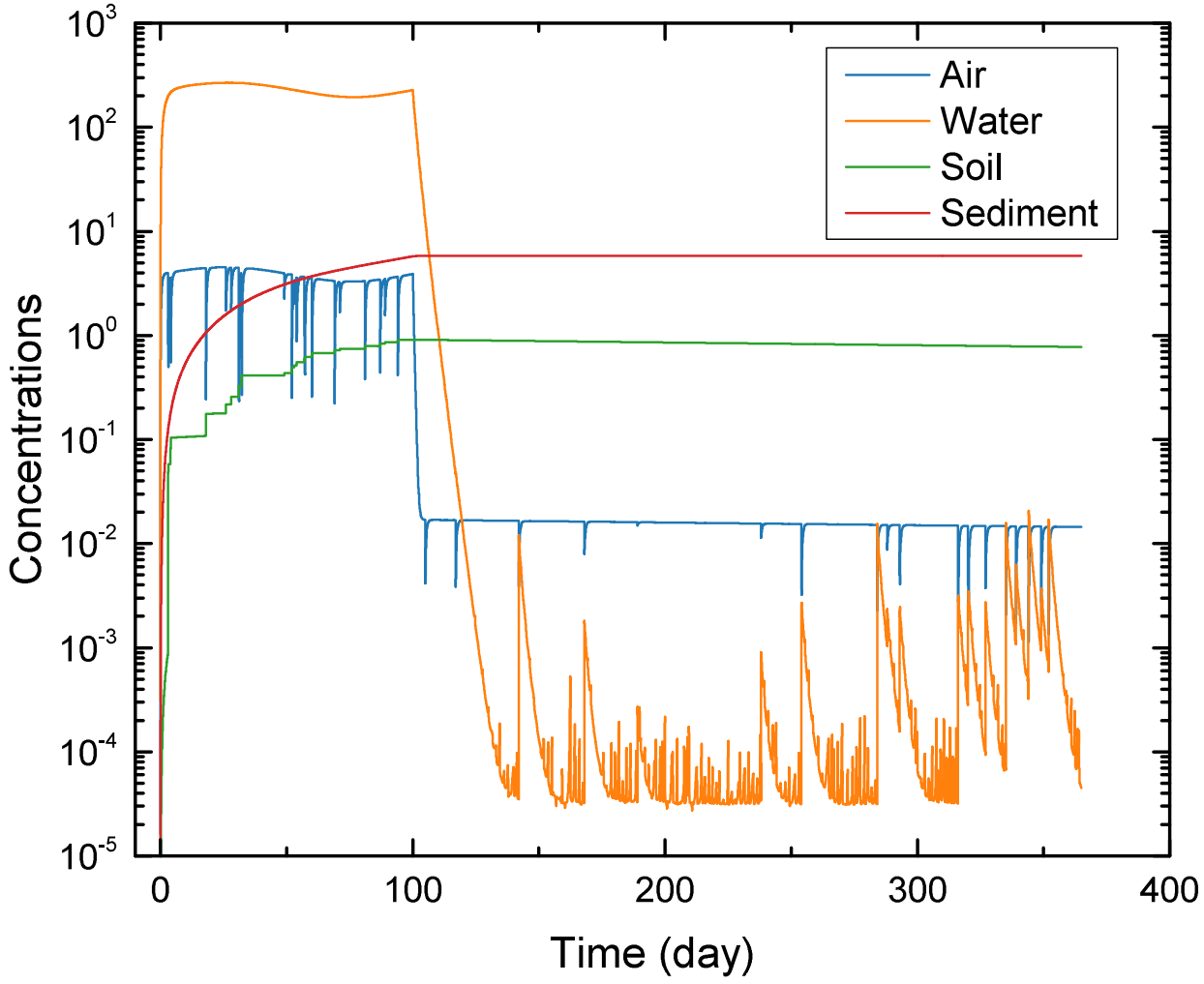

Figure 7-9. Effect of release scenario on temporal dynamics of TiO_2 media concentrations in Los Angeles. TiO_2 release rates to air and water were obtained from LearNano (Table A-8). The ENM release rates (to air and water) followed a sinusoidal function for the first 100 days (cycle period of 100 days, amplitude of 13.7 and 53.1 kg day^{-1}, for releases to air and water, respectively), after which the source releases are terminated. Regional geographical parameters are reported in Table A-7.

7.3.3 Use case 3. Impact of specific intermedia transport processes on the temporal dynamics of ENM distribution in the environment

To examine the impact of intermedia transport on ENM environmental distribution and to assess the effect of specific transport processes individually, one can construct scenarios that consider select intermedia transport process(es) independently from each other, and from source release. The above may be accomplished by setting a non-zero initial ENM media concentration and setting the source release rate to zero. Additionally, one may carry out a series of simulations with varying meteorological and geographical parameters, and thus varying intermedia transport rates, to evaluate the quantitative dependency of multimedia distribution on specific parameters. Examples demonstrating the above was provided in the main text for dry deposition and rain scavenging. An additional illustrative example is provided below for wind dilution.

Impact of specific intermedia transport processes on the temporal dynamics of ENM distribution in the environment (use case #3) is highlighted via a series of simulations for TiO_2 in Los Angeles focusing on intermedia transport via dry deposition, rain scavenging, and wind dilution. In these scenarios, the initial TiO_2 concentration in air is taken to be the steady state TiO_2 concentration reached after 1 yr with all other compartments being initially free of TiO_2.

Dry deposition is a process in which particles (including ENMs) are collected onto terrestrial (e.g., soil, vegetative canopy) and aquatic surfaces due to Brownian diffusion, impaction, and interception [90]. The intermedia transport rate due to dry deposition is a function of wind speed (among other parameters, e.g., surface roughness). The average wind speed is typically 3.3±0.95 m s^{-1} (1 standard deviation, 1996-2006) [260], with maximum ~10 m s^{-1}, in the Los Angeles region (LAX station). Increases in wind speed would lead to increases in the rates of collection by impaction and interception [90], and thus increases in the overall rate of dry deposition. The

predicted temporal ENM concentrations profiles in air and soil (Figure 7-10) reveal that the time to remove 90% of TiO_2 by dry deposition alone is ~100 – 230 days for wind speed in the range of 2.7 – 10 m s^{-1}, respectively. Additionally, at the end of a 1 yr simulation, 0.1 – 3.4% of the initial ENM mass in air remains in the air compartment for the above wind speed range.

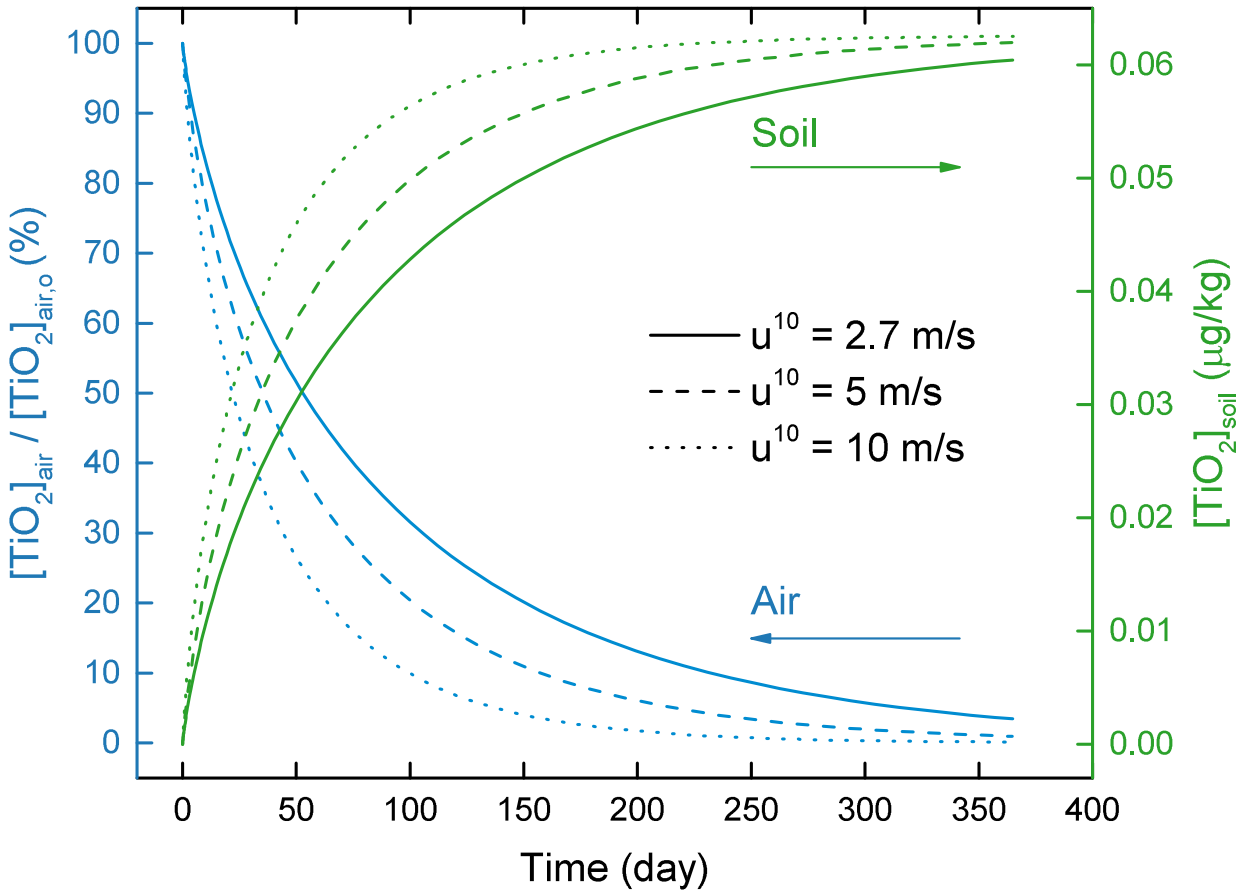

Figure 7-10. Effect of dry deposition on reduction of TiO_2 concentration in air and soil (post cessation of all ENM releases) in Los Angeles as a function of wind speed (range of 2.7 – 10 m s^{-1}). Regional geographical parameters are reported in Table A-7.

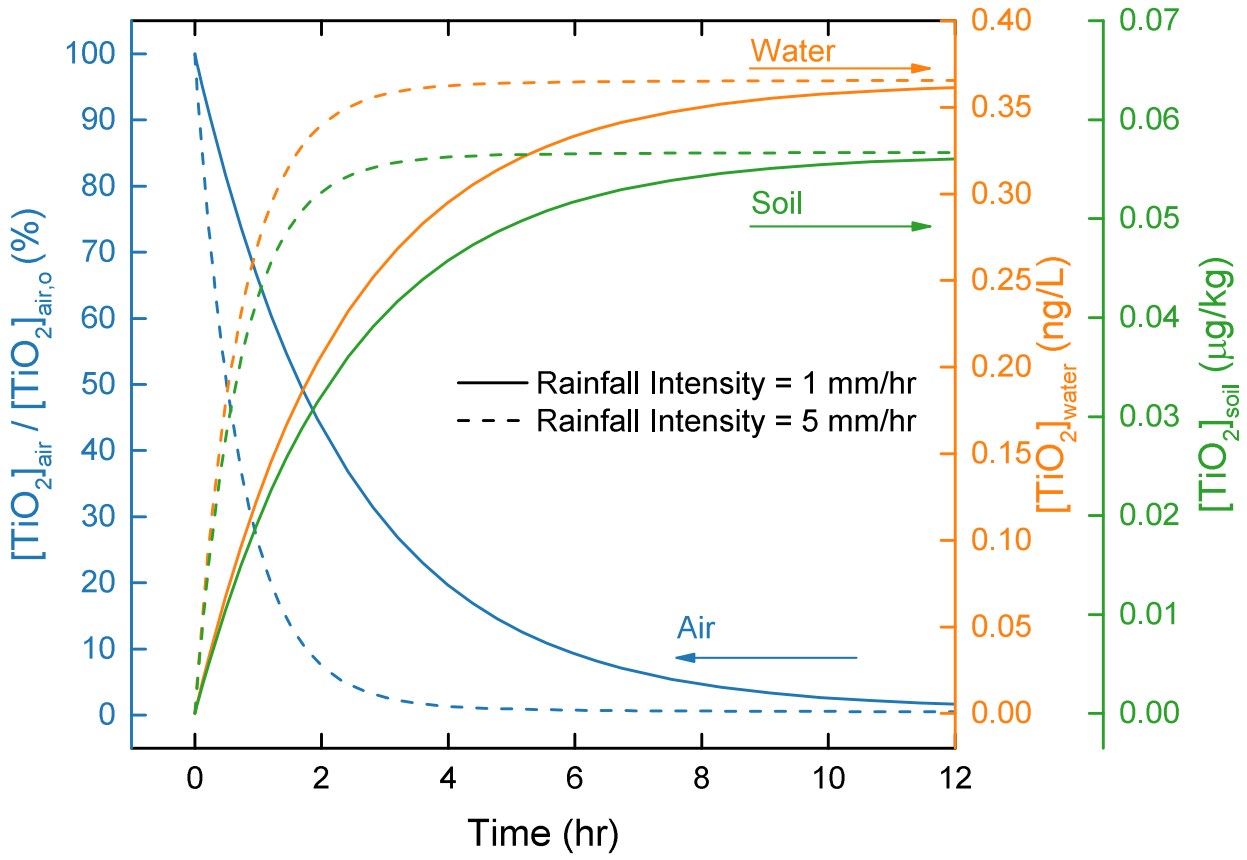

Figure 7-11. Effect of rain scavenging on TiO_2 concentration in air, water, and soil in Los Angeles as a function of rainfall intensity (1 – 5 mm hr^{-1}). All ENM releases are terminated at the start of a long rain event, which was taken to last for 12 hrs. Regional geographical parameters are reported in Table A-7.

Rain scavenging of particulate matter (including ENMs) by raindrops results in removal of particulate matter from the atmosphere and its deposition onto terrestrial and aquatic surfaces. ENM removal rate by rain scavenging is governed by rainfall intensity (typically in the range of 1 – 10 mm hr^{-1} for light to moderate rain [261], and can exceed 50 mm hr^{-1} for intense storms [262]). Rain scavenging can typically remove atmospheric particles at a faster rate relative to dry deposition. As illustrated in Figure 7-11, even with mild rainfall intensity of 1 – 5 mm hr^{-1}, 90% of TiO_2 can be removed in ~ 6 – 2 hr, respectively, compared to many days for removal by dry

deposition (Figure 7-10). Since rain scavenging is an episodic process (in contrast to the continuous dry deposition), the annually averaged ENM removal rate by rain scavenging is expected to be lower than the instantaneous removal rate during rainfall events as shown in Figure 7-11. Nonetheless, the averaged transport rate by rain scavenging can exceed that by dry deposition. For example, in Los Angeles, the estimated annually averaged TiO_2 removal by rain scavenging is a factor of ~10 greater than by dry deposition (Figure 7-8), indicating that rain scavenging has a more significant impact on environmental ENM distribution relative to dry deposition.

ENMs can be removed from the modeled atmospheric airshed (to neighboring airsheds) by the outflowing wind, via the wind dilution process, which occurs when the ENM concentration in the inflow wind is lower than that in the outflow wind. The rate of ENM removal by wind dilution is typically characterized by the convective residence time (or retention time) of the airshed, which is typically ~10 hr for an urban region such as Los Angeles. Under ideal conditions (i.e., with perfect mixing), the residence time [hr] can be estimated via $\tau = V/Q$, where V [m^3] is the volume of the airshed, and Q [m^3 hr^{-1}] is the volumetric flow of the wind [263]. However, flow recirculation and shortcuts in the region can cause non-ideal mixing, and can result in increases or decreases in the effective (or apparent) convective residence time [263]. In such case a correction factor, which may be obtained from tracer studies or determined via dispersion models, can be applied to correct the residence time [131]. The illustrative case of TiO_2 removal by wind dilution in Los Angeles is depicted in Figure 7-12, in which the time to remove 90% of ENMs from the airshed with convective residence time in the range of 5 – 20 hr is ~0.5 – 2 day, respectively. Although time scale for ENM removal via wind dilution is typical longer than that of instantaneous rain scavenging removal of ENM from the atmospheric airshed,

wind dilution may be more significant in removing ENM when averaged over long periods of time (e.g., years) due to the episodic nature of rain scavenging. For example, in Los Angeles, the mass of ENM removed in 1 yr via wind dilution is a factor of ~27 greater than via rain scavenging (to vegetative canopy, soil, and water surfaces) **(**Figure 7-9**)**.

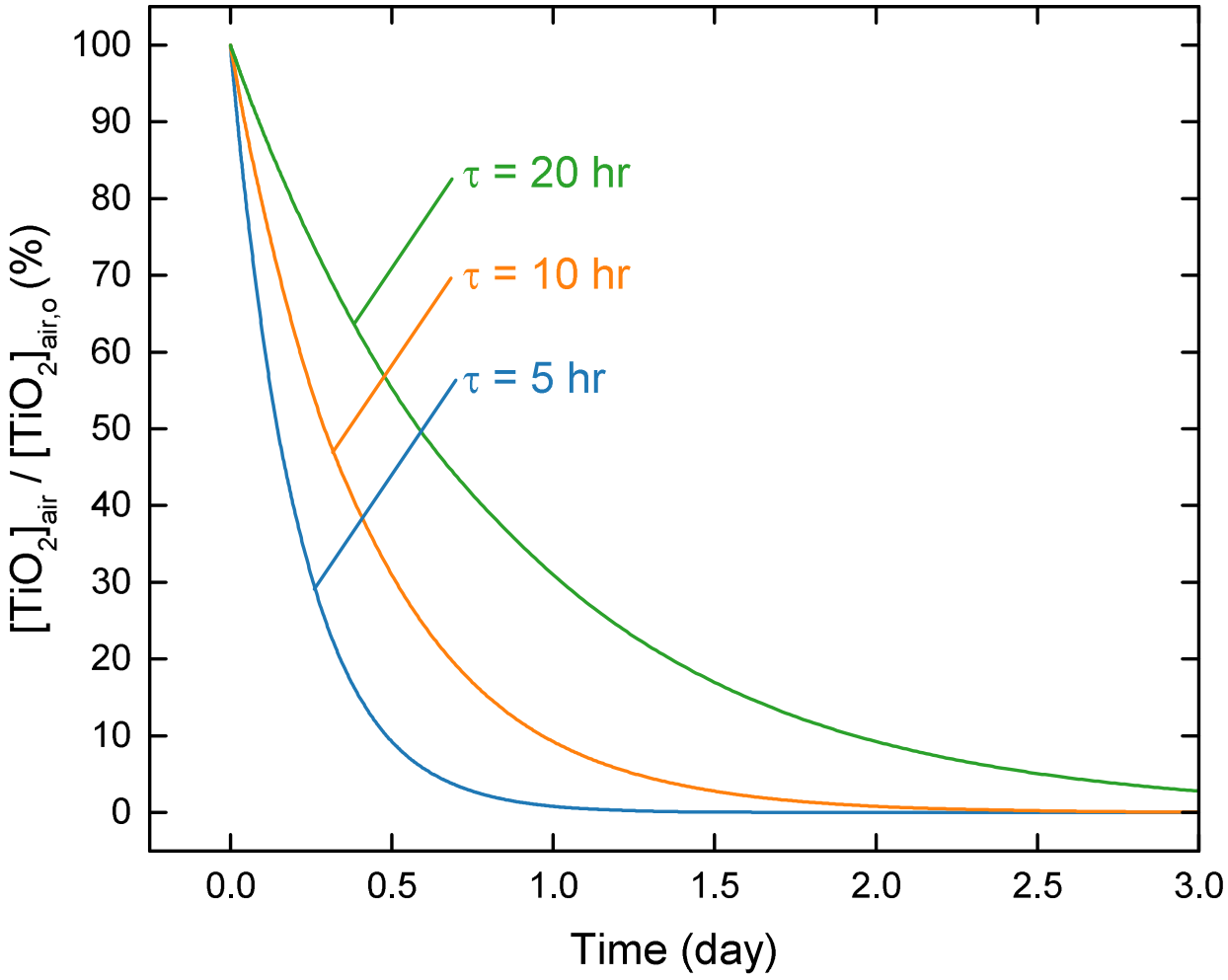

Figure 7-12. Effect of wind dilution on dynamics of TiO_2 concentration in air in Los Angeles as a function of convective residence time (τ) over the range of 5 – 20 hr. TiO_2 concentration in air is reported as percent of its initial concentration, which is the predicted steady state concentration for TiO_2 in Los Angeles, and the source release is taken to be zero for all compartments. Regional geographical parameters are reported in Table A-7.

7.3.4 Use case 4. Comparison of estimated environmental ENM concentrations in various regions

In order to evaluate the overall impact of ENMs on the environment, it is of interest to estimate the environmental distribution of ENMs in different regions (e.g., countries), by performing a series of simulations using geographical parameters, meteorological conditions, and source release rates specific to the regions under consideration. In this regard, it is noted that the parameter database in the present modeling platform contains a library of regionally specific geographical, meteorological parameters, and transfer coefficients for estimating ENM releases.

Comparative analysis of the potential environmental ENM concentrations in various countries (use case #4) is given by the example of CeO_2 ENMs, whereby release rates were estimated via LearNano for 12 selected countries. These countries were selected to represent the high ENM producing (and high emission) regions. Estimated CeO_2 release rates (high estimate) of the 12 countries spans over the range of 7.2 T yr^{-1} to 486 T yr^{-1} for Chile and China, respectively (Figure 7-13). The high estimates of the release rates for the 12 countries are, on average, a factor of ~12 greater than the low estimates, with the highest difference up to a factor of 86 (e.g., for release to water in the Switzerland). Release rates to air, water, and soil represent, on average for the different countries, 10% (3% - 40%), 38% (33% - 46%), and 52% (24% - 60%) of the total release rates, respectively (Figure 7-14). The above analysis suggests that, while some differences exist in apportionment of total release to various compartments between countries, the majority of ENM releases are to water, followed by soil and air. It should be noted that among the total ENM release to soil, only the direct release portion (~79%; i.e., excluding release from WWTP biosolids) may be considered to be distributed over the entire soil area in the region. The distinction between direct releases to soil and those from WWTP biosolids is

important. Although biosolids are applied to some agricultural lands in the USA, the USEPA estimates that <1% of agricultural lands receive biosolids [253], which suggests that the application of biosolids to soil does not represent a wide spread release in the USA. Similarly, it has been reported that in Switzerland, biosolids are not applied to soil, and are instead processed in waste incineration plants [42].

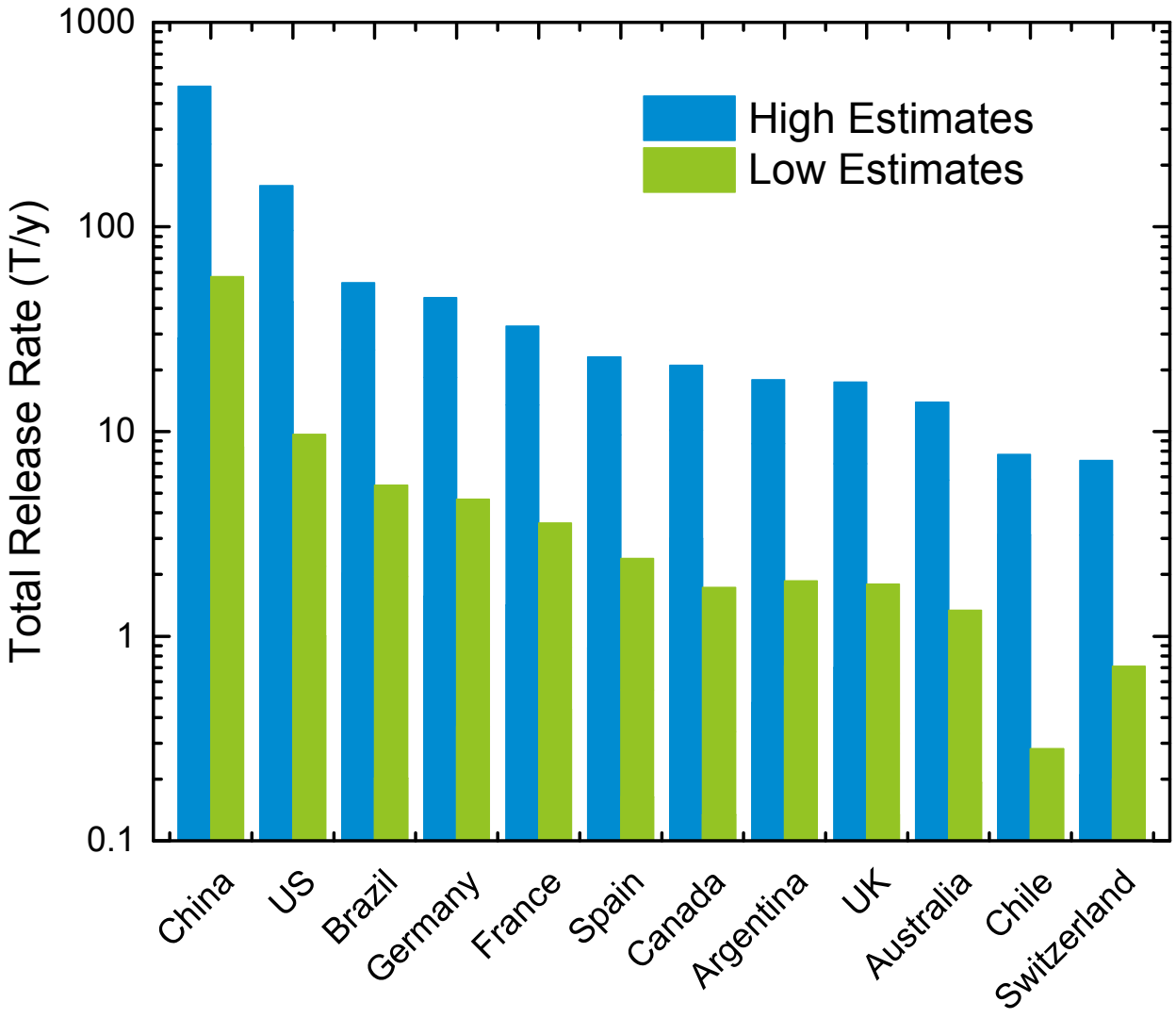

Figure 7-13. Estimated CeO_2 release rates for the 12 selected countries.

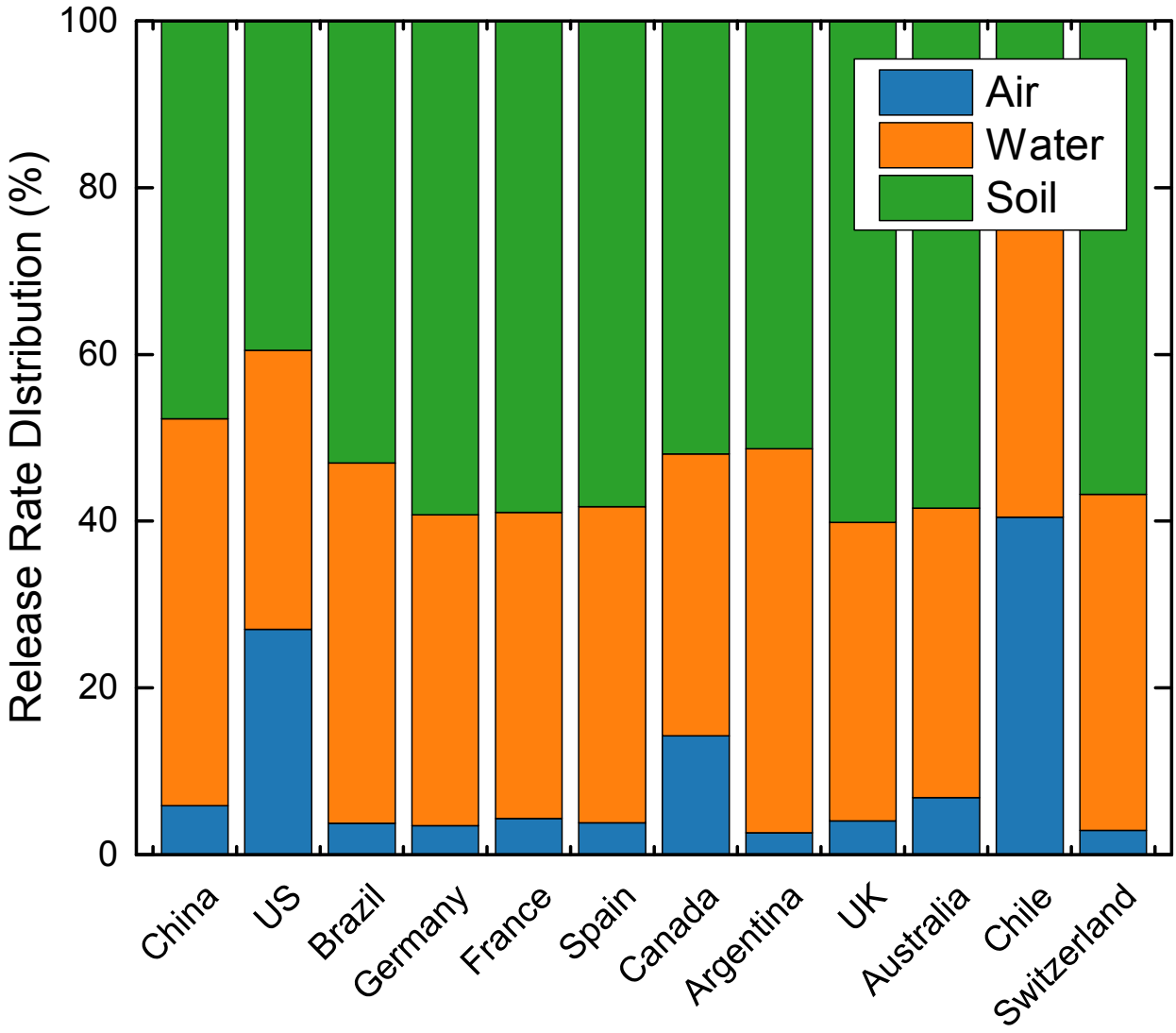

Figure 7-14. CeO_2 Release rate distribution (between air, water, and soil) for 12 selected countries. High estimate of the release rates are depicted.

Compartmental concentrations of CeO_2 for the 12 countries were estimated via MendNano using the release rate estimates shown in Figure 7-15, as well as country specific geographical and meteorological conditions (Table A-6). The simulations were carried out assuming that only direct release to soil is regionally distributed. Overall, the predicted CeO_2 concentrations (using the high release rates estimates) are in the range of 0.0003–0.097 ng m^{-3}, 0.0058–2.7 ng L^{-1},

0.0095–0.74 μg kg^{-1}, and 0.0054–0.25 mg kg^{-1} for air, water, soil, and sediment respectively (Figure 7-15). Relative to the above predictions, CeO_2 concentrations predicted using the low release rates estimates are a factor of ~5–1243 lower (Figure 7-16). Clearly, there is a large uncertainty in estimated media concentrations due to uncertainties in ENM release estimates. Nonetheless, it is noted that the above predicted CeO_2 concentration range is significantly below concentrations typically used in experimental toxicity studies [264].

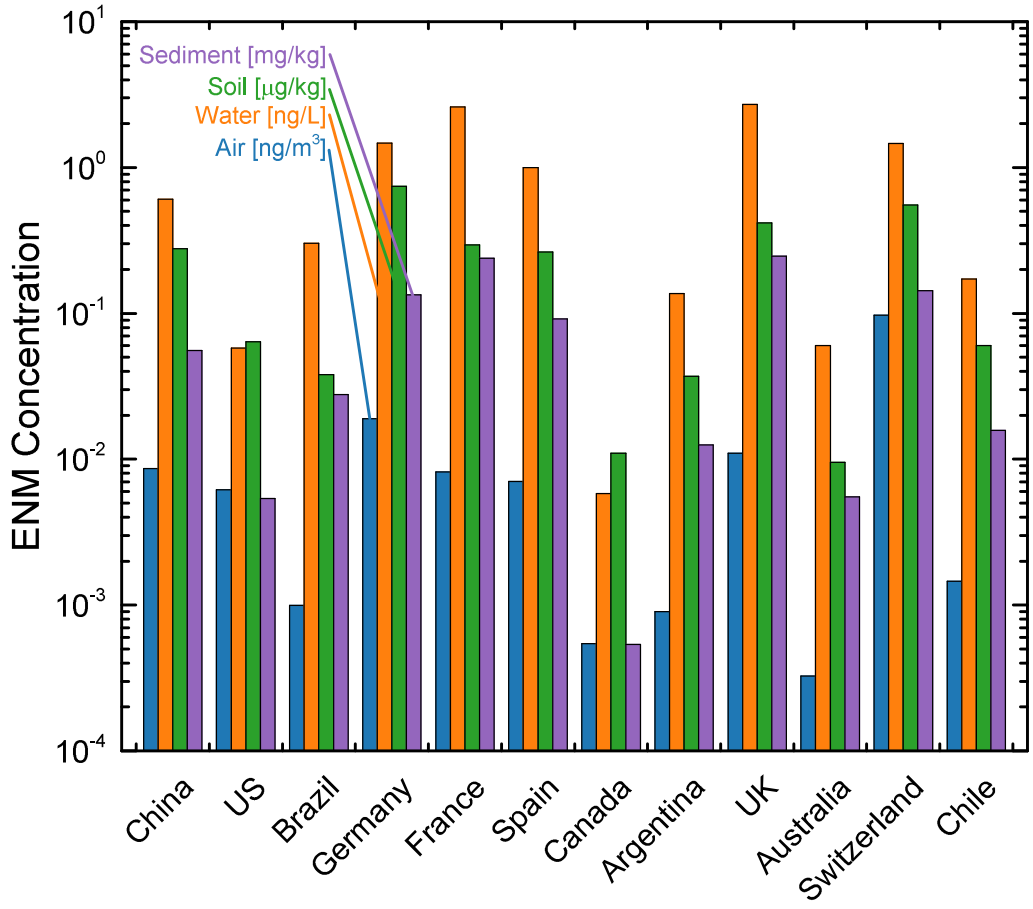

Figure 7-15. Predicted compartmental concentrations for CeO_2 in 12 selected countries at the end of 1 year simulation for the ENM release rates are reported in Figure 7-13. Regional geographical and meteorological parameters are reported in Table A-6.

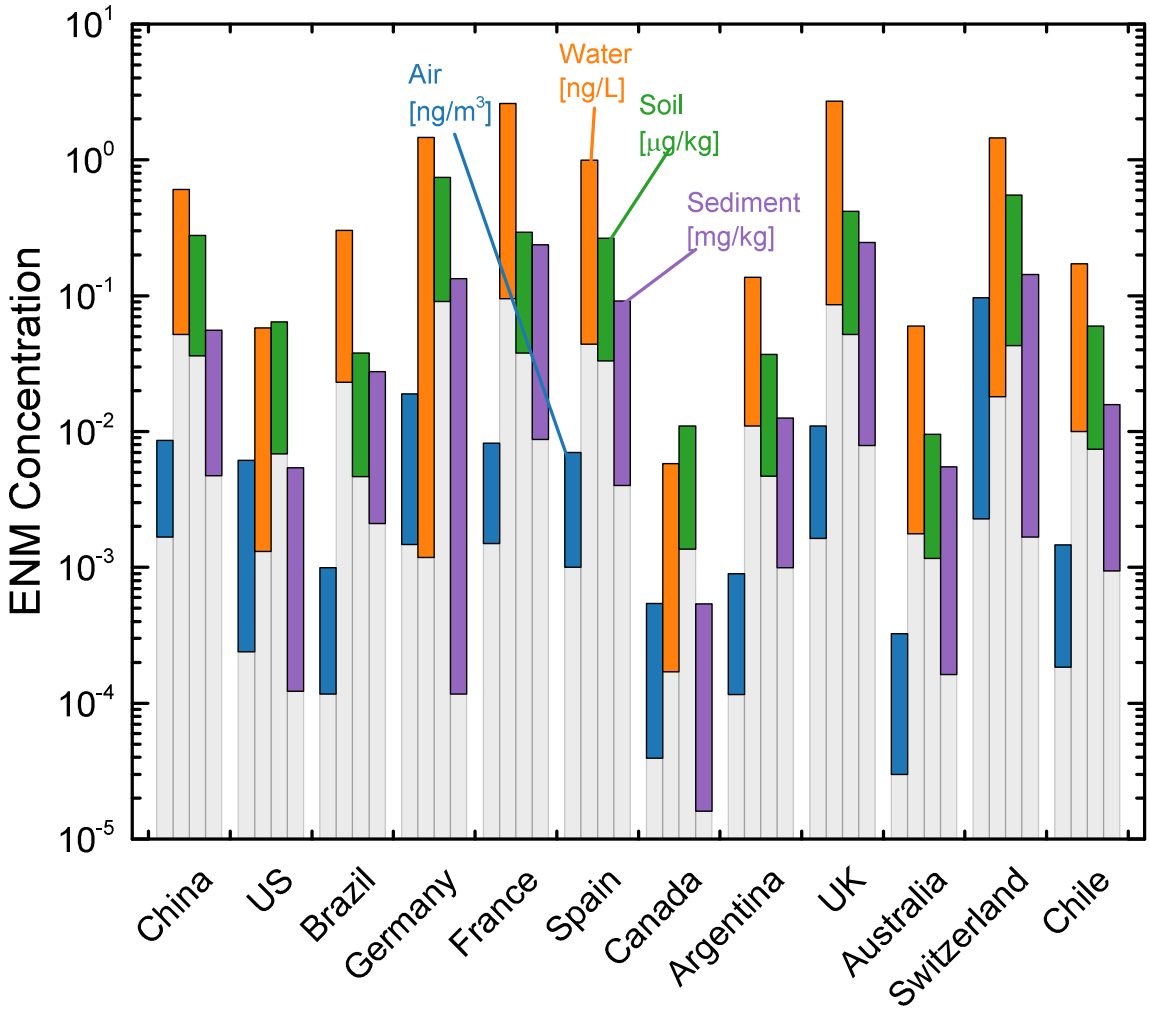

Figure 7-16. Estimated range of regional average CeO_2 compartmental concentrations for 12 selected countries at the end of 1-year simulation.

It is interesting to note that while the USA ranks second highest in terms of release rates (for all compartments), it ranks 7th (out of 12) in terms of CeO_2 concentration in air and soil, and 11th based on concentration in water and sediment. In contrast, while UK and Switzerland rank 9th and 11th with respect to total release rates, respectively, Switzerland and UK rank first (i.e., highest) in terms of the compartmental concentrations in air and water, respectively. Additionally, the environmental concentrations in the European countries are all significantly

higher than that in the US (by factors of 1.4 – 15) despite having total release rates that are lower than for the USA (by factors of 3.5 – 20). The apparent resulting discrepancy between release and environmental concentrations is attributed to differences in geography and meteorology. For example, Figure 7-17 shows that the release rate to air per unit area (combined soil and water) in Switzerland is a factor of 17 greater than in the US; similarly, release rates to water per unit area in UK is a factor of 46 greater than in the US.

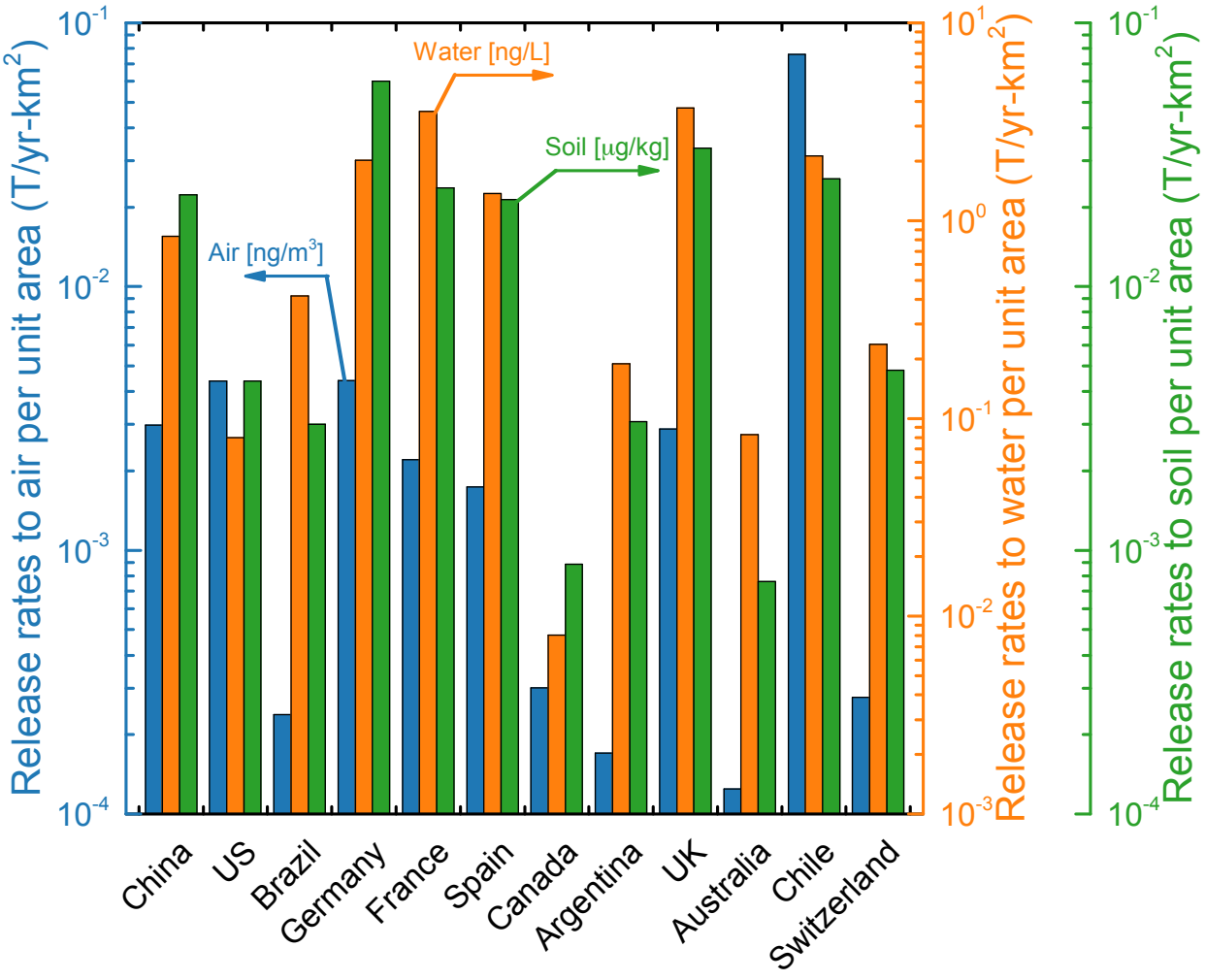

Figure 7-17. CeO_2 release rates (high estimate) per unit area for 12 selected countries. The air-soil and air-water interfacial areas are listed in Table A-6.

7.3.5 Use case 5. Contribution by application to ENM environmental distribution

Contribution of the application to ENM release and environmental distribution may provide useful information to researchers as well as assist the regulatory community, since ENMs may undergo transformation (e.g., surface functionalization) specific to an application [265] throughout their life cycle. The above can be accomplished with the present modeling platform, by estimating release rate of a given ENM associated with a specific application via LearNano, and evaluate the associated multimedia distribution with MendNano.

The contribution of ENM releases by various ENM applications (or use) to the overall ENM releases and exposure concentrations in the various environmental compartments (use case #5) is illustrated in the example of Figure 7-18 and Figure 7-19. Accordingly, simulations were carried out for Los Angeles with TiO_2 and SiO_2 selected since these are produced in the largest quantity [10] and CNT due to its diverse applications [10]. TiO_2 release rates attributed to coatings, paints, and pigments applications are the primary contributors of the release of this ENM to air (~45%) and soil (~77%). In water and sediment, TiO_2 releases associated with cosmetic applications represent the largest fraction (~53%), while those associated with coatings, paints, pigments represent ~44% with remainder due to energy (e.g., photovoltaic, energy storage [10]), environmental (e.g., remediation [10]), and plastic applications. The above results are consistent with reported TiO_2 use in coatings, paints, and pigments and associated releases to the environment due to weathering [266] while TiO_2 used in cosmetics is primarily released during washing [81] to water. SiO_2 releases to air (Figure 7-18) associated with energy and environmental applications is the largest fraction (~21%), while other applications (i.e., automotive, catalysis, coatings/paints/pigments, electronics/optics, and sensors) contribute less but still significant amounts (9.5% - 19.6%). In contrast, SiO_2 releases to soil are dominated by

energy and environmental applications, and the group of coating, paints, pigment applications (46% and 40%, respectively), while other applications collectively contributes less than 14% of the total SiO_2 releases to soil. The most significant contribution to SiO_2 mass released to the water and sediment is also associated with coating, paints, and pigments applications (~41%). Finally, the largest contributions to CNT releases to air, water, and soil are associated with composite (~28%), coating, paints, pigments (~43%), and energy and environmental applications (~40%), respectively.

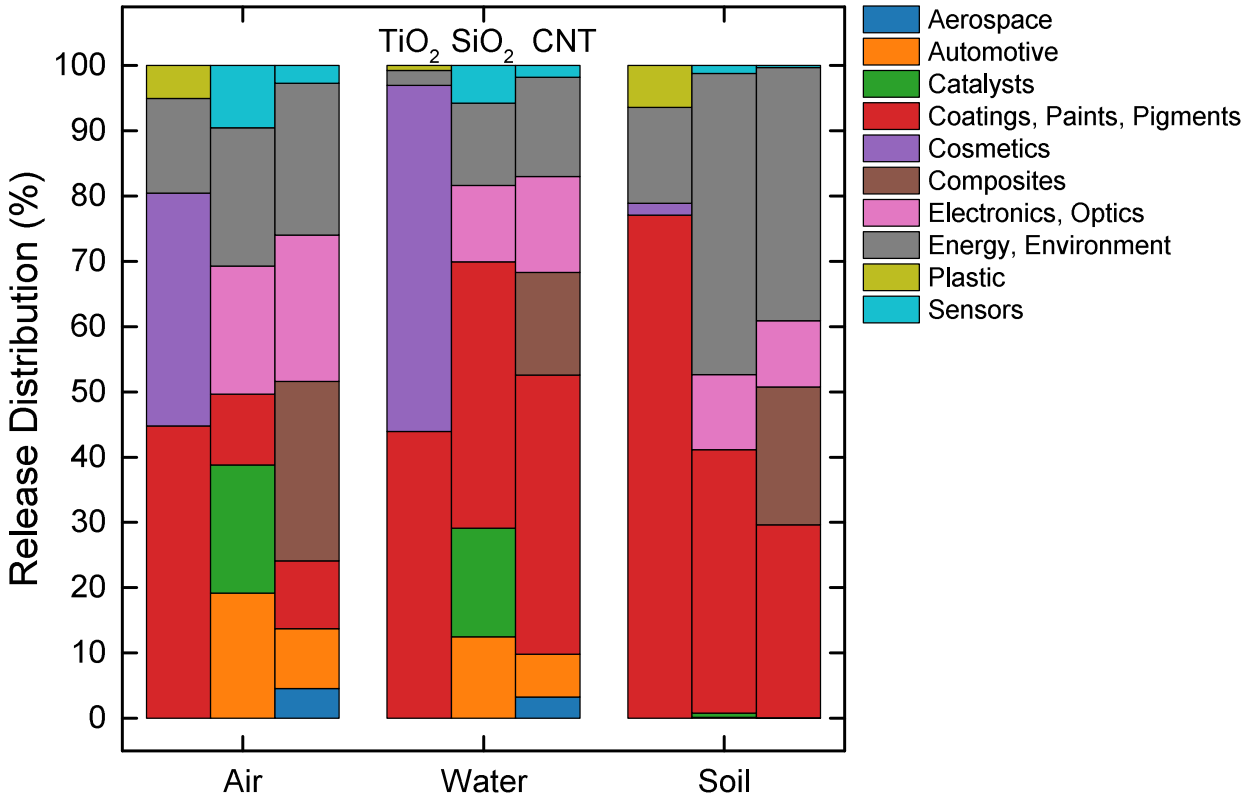

Figure 7-18. Environmental distribution of ENMs apportioned to release rates from different ENM applications.

The contributions of the various ENM applications to compartmental concentrations (Figure 7-19) are, as expected, typically qualitatively similar to their contributions to the ENM release

rates shown in Figure 7-18. However, noticeable differences can be observed in some cases due to intermedia transport of these ENMs from soil to air. For example, ENM associated with a given ENM application can be transported to the air compartment via soil wind resuspension in larger portion relative to other applications; thus, increased ENM concentration in air may occur for that application. Such a behavior can be expected when an ENM application contributes to the ENM release to soil in larger proportion relative to its contribution to ENM release to air. The above behavior is demonstrated in Figure 7-19 for TiO_2, for which releases associated with coating, paints, pigments contribute ~45% to the total TiO_2 release to air while contributing ~77% of total TiO_2 release to soil (Figure 7-18). As a result, ~54% of TiO_2 mass concentration in air is attributed to releases associated with coatings, paints, and pigments. In contrast, when 36% of total TiO_2 release to air is associated with cosmetics applications, and only 1.8% of total TiO_2 release to soil is associated with cosmetics, less than 28% of TiO_2 mass concentration in air is related to this category of ENM application. Therefore, since wind resuspension from soil may be a significant transport pathway of ENMs into the air compartment, the apportionment of total ENM release to soil associated with the various applications may have a notable impact on the contribution of ENM application to its concentrations in air.

7.3.6 Use case 6. Estimation of source release rates, based on matching of model estimates and reported environmental concentrations

ENM release rates can be estimated by iteratively executing simulations with varying ENM release rates to match the measured ENM concentrations. Using a Newton-Raphson's iteration, one can achieve rapid matching between estimated and reported concentrations. This approach is useful, for example, for retrospective estimates of ENM release rates of ENMs. The above use

case can also be utilized to check for consistency between reported ENM release rate, and measured ENM concentrations.

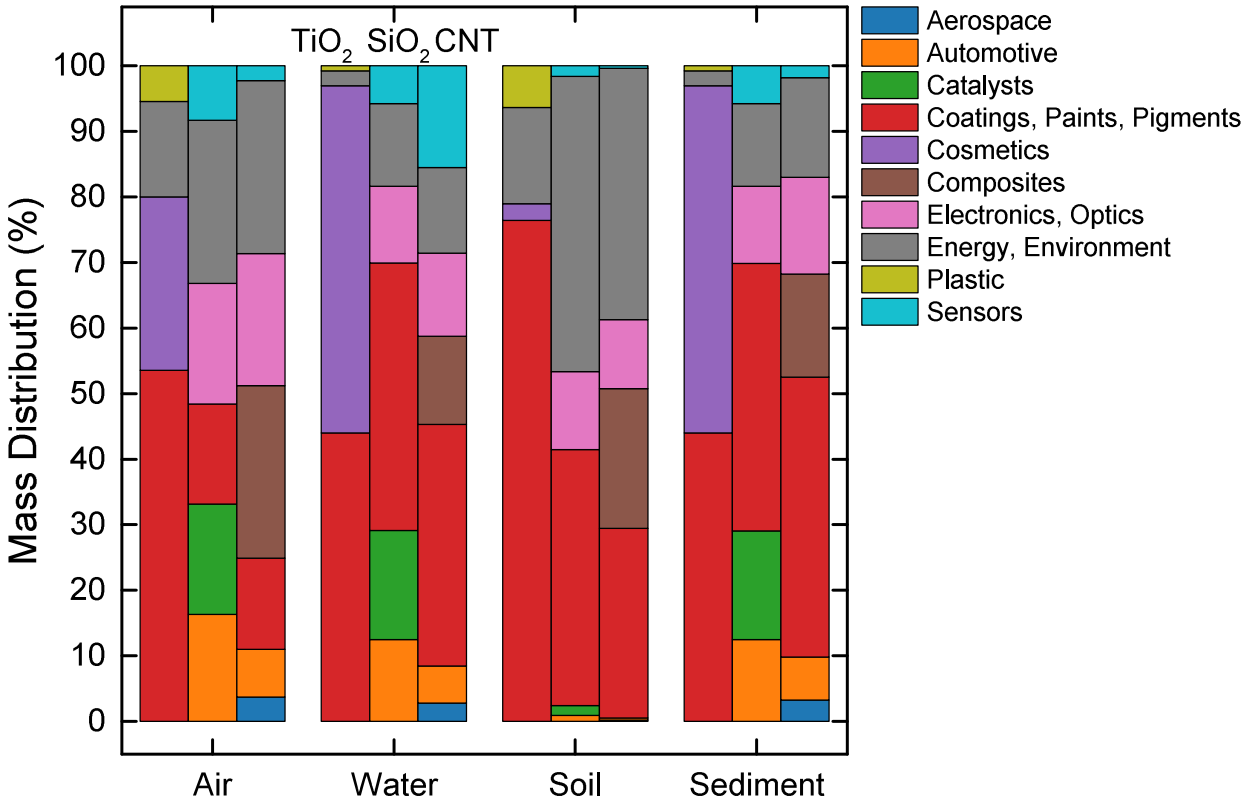

Figure 7-19. Contribution of various applications to the compartmental mass distribution of TiO_2, SiO_2, and CNT at the end of 1-year simulation for the Los Angeles test case. ENM release rates and regional geographical and meteorological parameters are reported in Table A-8 and Table A-7, respectively.

Estimation of ENM release rates, based on reported environmental ENM concentrations (use case #6), can be accomplished as described in the example of simulations of CeO_2 environmental distribution in Newcastle (UK). In this example, the release rate of CeO_2 ENM from fuel additive in Newcastle was estimated based on matching reported atmospheric concentrations before and after the introduction of the fuel additive with MendNano simulation results.

Monitoring results showed following the introduction of Envirox, a CeO_2 ENM based diesel fuel combustion catalyst, to a bus fleet in the Newcastle area, the ambient CeO_2 concentration increased by a factor of ~4.2 (0.574 ng m^{-3}; i.e., from 0.145 to 0.612 ng m^{-3}) [267]. MendNano simulations carried out considering geographical and meteorological scenario setup for the Newcastle region revealed that CeO_2 release rate of 43.96 kg yr^{-1} would result in the reported increased CeO_2 concentration (i.e., due to release from diesel fuel additive). MendNano estimate of CeO_2 release rate is consistent with the release rates estimated based on: a) vehicle-miles-travelled (VMT) and b) diesel fuel consumption rate in the region of Northumberland, which is in proximity to Newcastle and of similar population (§A.4.1). Estimated CeO_2 release rates for the above two cases were determined to be 21.48 and 44.82 kg yr^{-1}, respectively.

7.4 Conclusions

In summary, an integrated release and environmental distribution of nanomaterial (RedNano) simulation tool was developed, and implemented as a web-based application to enable rapid "what-if?" scenario analysis. The use cases described in this Chapter demonstrates (for TiO_2 in Los Angeles) that after cessation of source release, ENM concentrations would rapidly decrease, to 90% of the concentration just prior to termination of release in ~1 and ~4 days. Additionally, simulation results revealed precipitation scavenging removes ENMs in the atmospheric airshed at the highest rate during rain events (i.e., instantaneous removal rate), while wind dilution removes significantly more (by more than a order of magnitude in simulation for Los Angeles) over long periods (e.g., 1 yr). In contrast, dry deposition removes ENMs from the atmosphere at a much lower rate compared to rain scavenging and wind dilution.

Chapter 8. Conclusions and Recommendations

A modeling platform was developed for predicting ENM agglomeration in aqueous suspensions and the environmental distribution of ENMs, based on fundamental mechanistic description of ENM fate and transport. The current modeling approach, which incorporates a life-cycle analysis based estimation of ENMs releases to the environment, is aimed at the critical goal for assessing the exposure concentrations of ENMs.

The first phase of the modeling platform consists of a numerical constant number Direct Simulation Monte Carlo (DSMC) model for quantitative *a priori* prediction of ENM agglomeration in aqueous suspensions based on the classical DLVO theory. Model predictions were excellent agreement with experimental measurements of particle size distributions over a wide range of suspension conditions. Simulations results demonstrated, in quantitative agreement with DLS measurements, that NP agglomerate size increased with increasing ionic strength (IS), and decreasing |ζ-potential|. Also, simulation results indicated that NP agglomerate size increased with decreasing primary particle size, consistent with experimental findings in the literature. Particle-particle interactions in addition to those described in the classical DLVO theory may be important under certain environmental relevant conditions. Accordingly, the DSMC modeling approach, which was used to explore the significance of one of the most important non-DLVO interaction, the hydration repulsion interaction, over a wide range of environmentally relevant conditions and material properties. Simulation results revealed quantitatively that hydration repulsion energy is greater than the repulsion energy provided by the classical DLVO theory (i.e., electrostatic repulsion) by over an order of magnitude in high ionic strength or low |ζ-potential| conditions, and simulations in the above conditions may

overpredict agglomerate size by up to a factor of 5 if hydration repulsion is neglected. In contrast, in low ionic strength and high |ζ-potential| suspensions, the hydration repulsion may have a negligible impact on the predicted agglomerate size.

Given information regarding particle size distribution, simulations with the MendNano model enabled predictions of environmental ENM concentrations. MendNano, which was validated using reported concentration measurements of semi-volatile organic compounds (SVOCs), was then used to evaluate the environmental distribution of various ENMs (metal, metal oxide, CNT, nanoclays). Simulation results indicated that ENMs are generally expected to accumulate in the terrestrial environment (i.e., soil) and sediment. Additionally, evaluation of the effect of transport processes on the multimedia distribution of ENMs revealed that for certain ENMs (e.g., ZnO, CuO) dissolution may be a significant removal mechanism of suspended ENM. Simulation results also indicate that environmental ENM concentrations in air and water reach steady-state rapidly (within days) after introduction and termination of source releases, whereas ENM concentration in soil and sediment steadily increases over longer period (~years). Analysis of the impact of intermedia transport processes revealed that rain scavenging can be an important mechanism for removal of ENMs from the atmosphere and their deposition onto soil. Additionally, analysis of the regional multimedia distribution of ENM indicated that in various European countries (e.g., Germany, France, Spain, UK, and Switzerland) ENMs multimedia exposure concentrations are significantly higher than in the U.S., primarily due to the lower area-specific release rates in the U.S.

In summary, the present modeling approach, in its web-based implementation, provides a capability for rapid “what-if?” analysis of the releases, agglomeration, multimedia environmental mass distribution and potential exposure concentrations of ENMs.

Appendix A Summary of experiment conditions and simulation parameters

A.1 Data and parameters for Chapter 3

Table A-1. Summary of experimental and simulation conditions

	ENP	ζ [mV] (pH)	IS [mM]	d_p[nm]	d_{exp} [nm]	d_{sim} [nm]	% abs. error[(a)]
Jiang, *et al.,* [64]	TiO_2	38 (3.3)	1	15	80	96[(c)]	20.0%
	TiO_2	36 (3.8)	1	15	85	102[(c)]	20.0%
	TiO_2	34 (4.45)	1	15	87	108[(c)]	24.1%
	TiO_2	28.5 (5.3)	1	15	233	252[(c)]	8.2%
	TiO_2	-30 (7.8)	1	15	218	251[(c)]	15.1%
	TiO_2	-38 (8.2)	1	15	162	121[(c)]	25.3%
	TiO_2	-43 (8.7)	1	15	92	90[(c)]	2.2%
	TiO_2	-47.5 (9.65)	1	15	93	85[(c)]	8.6%
	TiO_2	-45 (10.4)	1	15	98	78[(c)]	20.4%
	TiO_2	36 (4.6)	0.01	15	90	77[(c)]	14.4%
	TiO_2	42 (4.6)	1	15	90	107[(c)]	18.9%
	TiO_2	40 (4.6)	5	15	160	178[(c)]	11.3%
	TiO_2	36 (4.6)	10	15	500	392[(c)]	21.6%
French, *et al.,* [66]	TiO_2	35 (4.5)	4.5	5	90	109[(c)]	21.1%
	TiO_2	35 (4.5)	8.5	5	500	432[(c)]	13.6%
	TiO_2	35 (4.5)	12.5	5	700	628[(d)]	10.3%
Ji, *et al.,* [60]	TiO_2	30.2 (6.1)	1	21	200	202[(c)]	1.0%
Brant, *et al.*, [177]	C_{60}	-32 (7)	10	168[(b)]	298	284[(c)]	4.7%
	C_{60}	-25 (7)	100	168[(b)]	680	615[(c)]	9.6%
Chen, *et al.,* [178]	C_{60}	-35(5.5)	156	83	115	122[(d)]	6.1%
Present Study	TiO_2	41 (3)	0.37	21	163	162[(e)]	0.6%
	TiO_2	-30 (8)	0.027	21	173	175[(e)]	1.2%
	TiO_2	-35 (10)	0.12	21	172	171[(e)]	0.6%
	CeO_2	32 (3)	0.37	15	271	269[(e)]	0.7%
	CeO_2	-23.5 (8)	0.027	15	266	264[(e)]	0.8%
	CeO_2	-30 (-30)	0.12	15	240	243[(e)]	1.3%

[(a)] % abs. error = $(|d_{exp}-d_{sim}|/d_{exp})\cdot 100\%$; [(b)] Reported initial particle size;
Model is carried out until steady state was reached[(c)], or for simulation time of [(d)]35 min and [(e)]24 h.

A.2 Data and parameters for Chapter 4

Table A-2. Summary of experimental and simulation conditions

	ζ [mV]	IS [mM]	d_{exp} [nm]
Present Study	37.3	1	233.31
(TiO_2)	30.5	1	268.21
d_p = 21 nm	-14.1	1	504.21
	-38.2	1	289.13
	33.4	10	514.09
	27.0	10	544.79
	-11.0	10	621.22
	-30.5	10	392.03
	31.1	31.6	742.40
	28.1	31.6	661.47
	-6.0	31.6	760.78
	-28.7	31.6	630.86
	41.6	1	270.85
	35.0	1	262.45
	-13.3	1	1103.18
	-43.1	1	312.00
	41.9	10	294.09
	33.8	10	544.89
	-8.0	10	1044.43
	-31.2	10	462.04
	38.5	31.6	608.74
	23.8	31.6	1030.90
	-5.8	31.6	1252.95
	-25.5	31.6	965.49
	42.5	1	260.59
	37.3	1	249.27
	-9.6	1	1194.95
	-41.8	1	329.90
	39.3	10	304.77
	14.8	10	611.45
	-5.7	10	1271.86
	-32.6	10	339.19
	41.1	31.6	728.60
	28.5	31.6	985.20
	-5.8	31.6	1263.63
	-25.6	31.6	962.00
Röhder, *et al*. [155]	-1.9	10	1420
(CeO_2)	-3.1	20	1031
d_p = 25 nm	-9.4	30	883

	ζ [*mV*]	IS [*mM*]	d_{exp} [*nm*]
	-13.4	40	1409
	-11.2	50	1009
	-13.9	60	1197
	-2.7	70	1203
	-1.4	80	1077
	2.7	90	1260
	11.6	100	1214
	12.0	110	900
	16.7	120	1357
Brunelli, *et al.* [184]	32	16.7	290
(TiO_2)	35	2.0	220
d_p = 21 nm	30	9.8	207
	23	630.0	381
	32	690.0	225
	35	2.0	607
	30	9.8	799
	23	630.0	466
	32	690.0	627
	35	2.0	226
	30	9.8	531
	23	630.0	883
Orts-Gil, *et al.* [190]	28.2	100	39.62
(SiO_2)	23.3	200	42.59
d_p = 30 nm	18.7	300	49.03
	14.2	400	57.45
	10.7	500	66.37
	7.2	600	108.96
	6.3	700	174.34
	5.2	800	288.25
	6.2	900	424.95
He, *et al.[68]*	21.4[a]	70	880
α-Fe_2O_3 (hematite)*	21.7[b]	54	1020
	25.6[c]	63	1100
	-9.6[a]	1	870
	-8.4[b]	1	950
	-15.2[c]	1	1280

* hematite NP primary sizes (d_p) are: a) 65 nm, b) 32 nm, and c) 12 nm.

A.3 Data and parameters for Chapter 5

Table A-3. Parameters for simulations of ENMs distribution for the Los Angeles Region

Parameter	Parameter Value	
Air-soil interface area[249]	1,213	km^2
Air-water interface area[249]	52.7	km^2
Atmospheric mixing height	1,000	m
Depth of Soil	0.05	m
Depth of Water	4.9	m
Depth of Sediment	0.03	m
Atmospheric convective residence time	10	hr
Water convective residence time	65	hr
Annual rainfall rate[248]	326	$mm\ yr^{-1}$
Average wind speed[248]	2.7	$m\ s^{-1}$
Dry soil density	1,500	$kg\ m^{-3}$
Dry sediment density	260	$kg\ m^{-3}$
Ambient aerosol PSD (Table 8.3 in Seinfeld and Pandis)[123]	Urban	
Ambient aerosol density	1,500	$kg\ m^{-3}$
Parameters of lognormal size distribution of suspended solids in water compartment		
Mode	5	μm
μ_{ln}	8.5	nm
σ_{ln}	0.6	nm
Ambient suspended solids density	1,500	$kg\ m^{-3}$
Parameters of lognormal size distribution of TiO_2		
μ_{ln}	5.7	nm
σ_{ln}	0.4	nm
Fractal dimension	2.09	
TiO_2 density	5,000	$kg\ m^{-3}$
TiO_2 surface charge	20	mV
Attachment factor [a]	1	
Initial and inflow concentration of ENMs in air and water	0	$ng\ m^{-3}$
Foliage area per unit soil area (leaf area index)[237]	2.87	$m^2_{foliar}\ m^{-2}_{soil}$
Fraction of soil covered by vegetation[268]	0.5	

Table A-4. Solubility and ionic diffusivity of select ENMs

	Solubility ($mg\ L^{-1}$)
Ag[117]	1.9
Cu, Cu oxide[118]	0.002
Fe, Fe oxide[119]	0.001
ZnO[120]	4.45
Dissolved species diffusivity[121]	$6.7x10^{-10}\ m^2\ s^{-1}$

Table A-5. Global production and media-specific release rates of ENMs

ENM	Release [a] (metric ton yr^{-1}) [10]				Production (metric ton yr^{-1})
	Air	Water	Soil[b]	Soil[c]	
Ag	11 (2.6%)	63 (14.9%)	150 (35.4%)	49 (11.4%)	424
Al_2O_3	500 (1.4%)	2,600 (7.5%)	8,200 (23.5%)	4,535 (13.0%)	34,900
CeO_2	100 (1.0%)	300 (3.0%)	1,400 (14.0%)	887 (8.9%)	10,000
CNT	43 (1.3%)	33 (1.0%)	500 (15.3%)	344 (10.5%)	3,276
Cu [d]	3 (1.5%)	11 (5.5%)	36 (18.0%)	20 (10.0%)	200
Fe [d]	600 (1.4%)	4,300 (10.3%)	11,300 (27.0%)	5,362 (12.8%)	41,900
NCs [e]	100 (1.0%)	500 (4.8%)	1,400 (13.5%)	748 (7.2%)	10,400
SiO_2	1,100 (1.2%)	2100 (2.2%)	10,600 (11.2%)	7,531 (7.9%)	95,000
TiO_2	1,600 (1.8%)	15,600 (17.7%)	38,200 (43.4%)	17,044 (19.4%)	88,000
ZnO	600 (1.8%)	3,700 (10.9%)	8,700 (25.5%)	3,452 (10.1%)	34,100

[a] Values in parentheses represent the indicated release rates (outside the parentheses) as percent of total production rate for the specified ENM (i.e., last column) calculated from data provided in [10]. [b] Total release to soil compartment via the sum of direct release and release associated with WWTP sludge. [c] Direct release to soil compartment. [d] Include associated metal oxide species. [e] NCs: Nanoclays

A.4 Data and parameters for Chapter 6

Table A-6. Parameters for simulation of ENM distributions in various countries

Country	Soil Area (km^2)[256]	Water Area (km^2) [256]	Annual rain fall (mm) [256]
Argentina	27,36,690	43,710	591
Australia	76,33,565	58,459	534
Brazil	84,60,415	55,352	1,782
Canada	90,93,507	891,163	537
Chile	7,43,812	12,290	1,522
China	93,26,410	270,550	645
France	6,40,427	3,374	867
Germany	3,48,672	8,350	700
Spain	4,98,980	6,390	636
Switzerland	39,997	1,280	1,537
UK	2,41,930	1,680	1,220
US	91,61,966	664,709	715

Common Parameter	Parameter Value	
Atmospheric mixing height[42]	1000	m
Depth of soil[42]	0.1	m
Depth of water[42]	3	m
Depth of sediment[42]	0.03	m
Average wind speed	3	$m\ s^{-1}$
Dry soil density[42]	1,500	$kg\ m^{-3}$
Dry sediment density[42]	260	$kg\ m^{-3}$
Ambient aerosol PSD (Table 8.3 in Seinfeld and Pandis)[123]	Rural	
Ambient aerosol density	1,500	$kg\ m^{-3}$
Parameters of lognormal size distribution of Suspended Solids in water compartment		
Mode	5	μm
μ_{ln}	8.5	nm
σ_{ln}	0.6	nm
Ambient suspended solids density	1,500	$kg\ m^{-3}$
Initial and inflow concentration of ENMs in air and water	0	$ng\ m^{-3}$
Attachment factor	1	

Table A-7. Parameters for simulation of ENM distributions in Los Angeles

Parameter	Parameter Value	
Air-soil interface area[249]	1,213	km^2
Air-water interface area[249]	52.7	km^2
Atmospheric mixing height	1,000	m
Depth of Soil	0.05	m
Depth of Water	4.9	m
Depth of Sediment	0.03	m
Atmospheric convective residence time	10	hr
Water convective residence time	65	hr
Annual rainfall rate [248]	326	$mm\ yr^{-1}$
Average wind speed [248]	2.7	$m\ s^{-1}$
Dry soil density	1,500	$kg\ m^{-3}$
Dry sediment density	260	$kg\ m^{-3}$
Ambient aerosol PSD (Table 8.3 in Seinfeld and Pandis) [123]	Urban	
Ambient aerosol density	1,500	$kg\ m^{-3}$
Parameters of lognormal size distribution of suspended solids in water compartment		
Mode	5	μm
μ_{ln}	8.5	nm
σ_{ln}	0.6	nm
Ambient suspended solids density	1,500	$kg\ m^{-3}$
Attachment factor [a]	1	
Initial and inflow concentration of ENMs in air and water	0	$ng\ m^{-3}$
Foliage area per unit soil area (leaf area index)[237]	2.87	$m^2_{foliar}\ kg^{-1}_{plant}$
Fraction of soil covered by vegetation[268]	0.5	

Table A-8. Release rates of TiO_2, SiO_2, and CNT in Los Angeles

ENM and Application	Release [a] (kg yr^{-1})			
	Air	Water	Soil[b]	Soil[c]
TiO_2				
Coatings, Paints, Pigments	2249 (5.2%)	8528 (19.9%)	7100 (16.5%)	11248 (26.2%)
Cosmetics	1789 (4.2%)	10293 (24.0%)	167 (0.4%)	5107 (11.9%)
Energy, Environment	729 (1.7%)	438 (1.0%)	1352 (3.2%)	1499 (3.5%)
Plastic	253 (0.6%)	149 (0.4%)	589 (1.4%)	639 (1.5%)
SiO_2				
Automotive	947 (5.9%)	625 (3.9%)	5 (0.03%)	213 (1.3%)
Catalysts	971 (6.0%)	833 (5.2%)	27 (0.2%)	355 (2.2%)
Coatings, Paints, Pigments	539 (3.3%)	2046 (12.6%)	1703 (10.5%)	2698 (16.7%)
Electronics, Optics	968 (6.0%)	587 (3.6%)	487 (3.0%)	672 (4.2%)
Energy, Environment	1050 (6.5%)	631 (3.9%)	1947 (12.0%)	2157 (13.3%)
Sensors	470 (2.9%)	288 (1.8%)	51 (0.3%)	141 (0.9%)
CNT				
Aerospace	8 (1.3%)	5.3 (0.9%)	0.05 (0.01%)	1.8 (0.3%)
Automotive	15.9 (2.79%)	10.5 (1.8%)	0.1 (0.02%)	3.6 (0.6%)
Coatings, Paints, Pigments	18.2 (3.1%)	68.9 (11.6%)	57.4 (9.7%)	90.9 (15.3%)
Composites	48.1 (8.1%)	25.3 (4.3%)	41 (6.9%)	49.1 (8.3%)
Electronics, Optics	39.1 (6.6%)	23.7 (4.0%)	19.7 (3.3%)	27.2 (4.6%)
Energy, Environment	40.7 (6.9%)	24.4 (4.1%)	75.4 (12.7%)	83.6 (14.1%)
Sensors	4.8 (0.8%)	2.9 (0.5%)	0.5 (0.1%)	1.4 (0.4%)

[a] Values in parentheses represent the indicated release rates (outside of the parentheses) as percent of total release rate to the environmental compartments for the specified ENM (i.e., release to air, water, and soil).
[b] Direct release to soil compartment (i.e., not including release from WWTP)
[c] Total release to soil compartment via the sum of direct release and release associated with WWTP sludge

A.4.1 Estimation of CeO_2 Release Rates in Newcastle UK

Estimated CeO_2 release rate based on Vehicle Miles Travelled (VMT)

Since VMT for buses was not reported specifically for Newcastle, the estimated VMT for England [269] was used, and scaled to Newcastle on the basis of population ratio. The CeO_2 release rate was subsequently estimated using typical diesel bus fuel efficiency [270] and CeO_2 concentration [267] in the fuel additive.

Table A-9. Parameters for estimating CeO_2 release rates

Parameter	Value	Unit	Ref
Diesel bus fuel efficiency (*f*)	2.55	km L^{-1}	[270]
VMT, England	1,298,000,000	miles yr^{-1}	[269]
Population, England	53.5	million people	[271]
Population, Newcastle, UK	280,200	people	[272]
CeO_2 concentration in diesel fuel additive	5	mg L^{-1}	[267]

$$Release = \left(\frac{280200}{53.5\times10^6}\right)\cdot 1298\times10^6\,\frac{mile}{yr}\cdot\left(1.609\,\frac{km}{mile}\right)\cdot\left(\frac{L}{2.55\,km}\right)\cdot\left(5\,\frac{mg}{L}\right)\cdot\left(\frac{kg}{10^6\,mg}\right)$$

$$= 21.48\ kg/yr$$

Estimated CeO_2 release rate based on Fuel Consumption

The release rate of CeO_2 from diesel fuel additive was also estimated based on reported fuel consumption data for a town (Northumberland) in the same region (Northeast UK) with similar population (316,028). Total fuel consumption by buses for the above city was reported to be 7.7 KTonne yr^{-1}[273], which was then scaled to Newcastle on a population basis. The density of diesel fuel is taken to be 0.832 kg L^{-1}.

$$Release = \left(\frac{280200}{316028}\right)\cdot\left(7700\,\frac{tonne}{yr}\right)\cdot\left(1000\,\frac{kg}{tonne}\right)\cdot\left(\frac{L}{0.745}\right)\cdot\left(5\,\frac{mg}{L}\right)\cdot\left(\frac{kg}{10^6\,mg}\right)$$

$$= 45.82\ kg/yr$$

Appendix B Rain Event Generator

Conducting highly detailed rainfall simulation requires considerable rainfall data. In the present implementation of the modeling approach, rain events are generated based on user input at various tiers of detail. In the low detail tier (i.e., least amount of user input), the only required parameters are the average monthly rainfall rates (R, mm mo^{-1}) for each month. In this tier, uniform random number sampling is used to determine the days of the month in which there is rainfall, rainfall event duration (t_i, h, between 1 h and 24 h) and intensity (I_i, mm h^{-1}, between 1 mm h^{-1} and 60 mm h^{-1}) for each rainy day i. The total generated rainfall rate is scaled to equal to the user specified rainfall rate by adjusting the rainfall intensities, such that the adjusted rainfall intensities ($I_{i,adj}$) is:

$$I_{i,adj} = I_i \cdot \frac{R}{\sum_i t_i \cdot I_i} \qquad \text{[B-1]}$$

In the high detail tier (i.e., more user input), the user can specify the number of rainfall events of a given intensity (I_j) and corresponding duration (t_j) and the number of such rainfall events (n_j) in each month. In this tier of rainfall simulation, the total monthly rainfall, R, is therefore:

$$R = \sum_j n_j \cdot t_j \cdot I_j \qquad \text{[B-2]}$$

Appendix C MendNano Validation and Comparison with Existing Models.

C.1 Assessment of Multimedia Compartmental Modeling Approach

Particulate transport processes govern the fate and transport (F&T) of nanomaterials, and hence, the present approach to modeling the multimedia distribution of particulate matter was first evaluated with respect to the transport of semi-volatile polycyclic aromatic hydrocarbons (PAHs; e.g., benzo[a]pyrene (B[a]P), benzo[ghi]perylene (B[ghi]P), dibenz[a,h]anthracene (DBA)) and PCBs that are present mostly in the particle-bound form. Previous studies have estimated that under typical environmental conditions, up to 94% of B[a]P [239, 240], 91% of B[ghi]P [240], 88% of DBA [240] partition to the particle phase. Therefore, it is reasonable to assert that transport behavior of the above particle-bound organics is governed primarily by particle transport mechanism. Simulations were first carried out for the multimedia concentrations of B[a]P in Southeast Ohio [241] (Table C-1) and in California South Coast Air Basin (SoCAB) [242] (Table C-2), with simulation results compared to available environmental monitoring data [241, 274] and previous modeling results [241, 242]. Simulations results for an additional test case were for B[a]P, B[ghi]P, and DBA in Birmingham, UK region (Table C-3) for which predicted PAHs concentrations in air based on vehicular emission of PAHs were compared with reported data [243]. Since approximately ~88% of PAHs emission was reported as from vehicular sources in Birmingham, UK, emission rate of PAHs was estimated based on product of Vehicle Miles Travelled (VMT) [km] [275] and PAH specific emission factor ranges [μg PAH emission km^{-1}][276]. Finally, simulations were also carried out for PCBs in Lake Michigan region (Table C-4) for which predicted intermedia transport fluxes were compared with reported data [277, 278].

Table C-1. Parameters for simulation of benzo[a]pyrene distribution in Southeast Ohio Region

Parameter	Parameter Value	
Air-soil interface area[241]	368	km^2
Air-water interface area[241]	32	km^2
Atmospheric mixing height	1,000	m
Depth of Soil[241]	0.05	m
Depth of Water[241]	7.5	m
Average wind speed[241]	5	$m\ s^{-1}$
Atmospheric convective residence time[241]	50	hr
Average flow rate in water[241]	$1.1x10^7$	$m^3\ hr^{-1}$
Water convective residence time[241]	22	hr
Ambient aerosol PSD (Table 8.3 in Seinfeld and Pandis)[123]	Remote Continental	
Ambient aerosol density	1,500	$kg\ m^{-3}$
Parameters of lognormal size distribution of suspended solids in water compartment		
Mode	8	μm
μ_{ln}	9	nm
σ_{ln}	0.6	nm
Ambient suspended solids density	1,500	$kg\ m^{-3}$
B[a]P concentration in inflow air[241]	0.50	$ng\ m^{-3}$
B[a]P concentration in inflow water[241]	10.09	$ng\ L^{-1}$
Release rate of B[a]P in Air[241]	3,647	$kg\ yr^{-1}$
Release rate of B[a]P in Water[241]	332	$kg\ yr^{-1}$
Attachment factor	1	

Table C-2. Parameters for simulation of benzo[a]pyrene distribution in South Coast Air Basin

Parameter	Parameter Value	
Air-soil interface area[242]	16,900	km^2
Air-water interface area	52.7	km^2
Atmospheric mixing height	400	m
Depth of Soil	0.05	m
Depth of Water	4.9	m
Average wind speed[248]	2.7	$m\ s^{-1}$
Atmospheric convective residence time	20	hr
Water convective residence time	65	hr
Ambient aerosol PSD (Table 8.3 in Seinfeld and Pandis)[123]	Urban	
Ambient aerosol density	1,500	$kg\ m^{-3}$
Parameters of lognormal size distribution of suspended solids in water compartment		
Mode	5	μm
μ_{ln}	8.5	nm
σ_{ln}	0.6	nm
Ambient suspended solids density	1,500	$kg\ m^{-3}$
Initial and inflow concentration of B[a]P in air and water	0	$ng\ m^{-3}$
Release rate of B[a]P in Air[242]	1,105	$kg\ yr^{-1}$
Attachment factor	1	

Table C-3. Parameters for simulation of PAHs transport in Birmingham, UK

Parameter	Parameter Value	
Air-soil interface area	268	km^2
Atmospheric mixing height	1,000	m
Depth of Soil	0.05	m
Average wind speed	4	$m\ s^{-1}$
Atmospheric convective residence time	10	hr
Ambient aerosol PSD (Table 8.3 in Seinfeld and Pandis)[123]	Urban	
Ambient aerosol density	1,500	$kg\ m^{-3}$
Initial and inflow concentration of PAHs in air and water	0	$ng\ m^{-3}$
Release rate of B[a]P in Air[a]	76-118	$kg\ yr^{-1}$
Release rate of B[ghi]P in Air	252-394	$kg\ yr^{-1}$
Release rate of DBA in Air	15-23	$kg\ yr^{-1}$
Attachment factor	1	

[a] Release rates calculated based on product of Vehicle Miles Travelled (VMT) [km][275] and PAH specific emission factor [μg PAH / km][276]. Range of emissions were based on the estimate that 50% - 80% of vehicles are not equipped with catalytic converters (in 1996, UK); the above was estimated based on the fraction of vehicles on the road manufactured prior to 1993 (i.e., when the requirement of catalytic converters was enacted in UK).

Table C-4. Parameters for simulation of PCBs intermedia transport in Lake Michigan

Parameter	Parameter Value	
Air-soil interface area[33]	57,800	km^2
Air-water interface area[33]	82	km^2
Depth of sediment[33]	0.01	m
Average wind speed[33]	5.5	$m\ s^{-1}$
Water convective residence time	99	yr
Ambient aerosol PSD (Table 8.3 in Seinfeld and Pandis)[123]	Remote Continental	
Ambient aerosol density	1,500	$kg\ m^{-3}$
Parameters of lognormal size distribution of suspended solids in water compartment		
Mode	400	nm
μ_{ln}	6	nm
σ_{ln}	0.6	nm
Ambient suspended solids density	1,500	$kg\ m^{-3}$
Particle-bound PCBs concentration in air[33],[a]	0.12	$ng\ m^{-3}$
Release rate of PCBs in Water[33]	650	$kg\ yr^{-1}$
Attachment factor	1	

[a] Particle-bound PCBs concentration is taken to be 10% of total air compartment PCBs concentration, based on reported gas/particle partitioning of PCBs.[78]

Simulations for the test case of B[a]P in the Southeast Ohio resulted in predicted B[a]P concentrations within the range of reported measurement for the air and water compartments. Although the predicted soil concentrations are consistent with previous multimedia model predictions (Figure C-1) for particle-bound organics [241], they are significantly lower than the reported near road-side field concentrations, which are expected to be higher than regional average due to vehicular emissions [241]. Predicted multimedia distribution of B[a]P in SoCAB agreed well (well within a factor of 2) with previous modeling results, as well as measured concentrations in two cities within the SoCAB [274]. The measured air compartment concentrations of all three PAHs (i.e., B[a]P, B[ghi]P, DBA) in Birmingham UK are also within ranges of the predicted concentrations.

In addition to the above demonstration of MendNano performance, predicted PCBs sedimentation flux was within the reported range for PCBs flux of sedimentation (Figure C-1), with dry deposition velocities being within a factor of 1.8 lower than reported measurements, but clearly within the order of magnitude accuracy expected for screening level analysis. It is noted that the above predictions of PCB fluxes are within a similar range predicted in a previous modeling study [33]. Overall, the above test cases indicate that the present modeling approach can provide a reasonable representation of intermedia transport of particulate matter of which nanomaterials are a subset whose F&T behavior is governed by their size distribution [49, 82] and association with ambient particles.

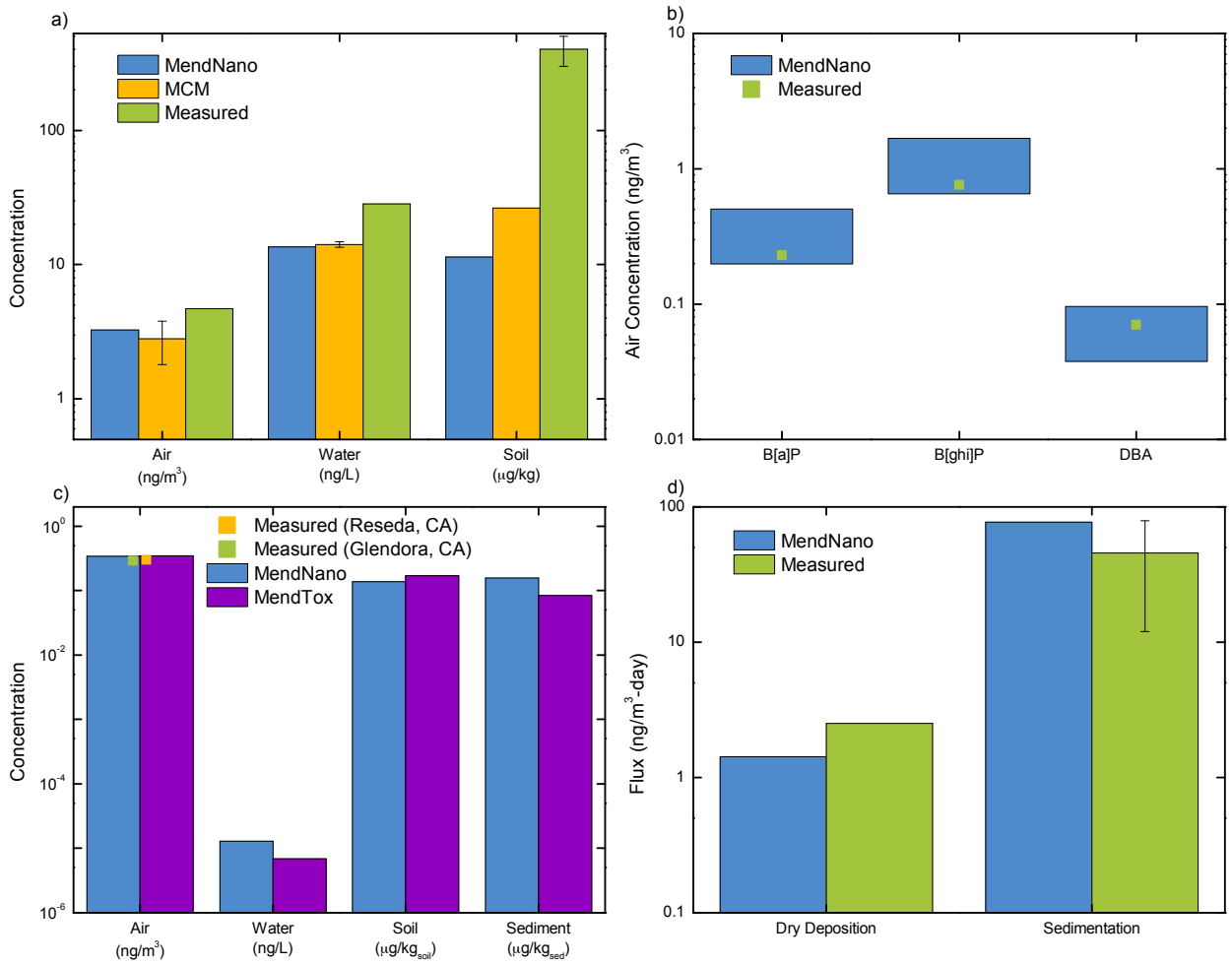

Figure C-1. a) Comparison of MendNano simulation results, previously published model predictions [241], and reported concentrations of particle-bound B[a]P in Southeast Ohio; b) Predicted and reported historical (1996) air compartment concentrations for selected particle-bound PAHs in Birmingham, UK; c) Comparison of predicted multimedia concentrations of particle-bound B[a]P in California South Coast Air Basin (SoCAB) by MendNano and Previously published model predictions [242], as well as air monitoring data reported for two California SoCAB cities (i.e., Reseda, CA and Glendora, CA) [241, 274]; and d) Predicted and reported [277, 278] historical (1984-1991) intermedia transport fluxes for particle-bound PCBs in Lake Michigan.

C.2 Multimedia Distribution of ENMs and Relation to Material Flow Analysis

A number of recent studies have provided approximate account of the global and regional environmental multimedia distribution of ENMs based on material flow analysis (MFA) [42, 43]. Estimated ENMs release rates (to the various media) from such studies for the US were then utilized to simulate the multimedia distributions of TiO_2, ZnO, Ag and CNT. The present model predicted media concentrations for TiO_2, Zn, Ag and CNT with those reported in MFA for the US [42], at the end of 1 year simulation, were obtained for the same ENMs releases to air, water and soil as reported in the MFA study [42]. In the above comparative analysis the same ENM emission rates were used as reported in the MFA study [42], where it was assumed that the total ENM release to soil (including those from wastewater treatment plants (WWTP)) are applied to the entire soil; it is noted that such a scenario may be viewed as unlikely given the release from WWTP are more likely to be localized. Therefore, additional simulations were carried out where only "direct releases" to soil were included (as reported by the MFA study [42]) to be regionally distributed, while considering releases from WWTP to be localized and thus not contributing to the soil concentration on a regional scale.

A comparison of the predicted media concentrations for the above scenarios is provided in Figure C-2. Predicted ENMs concentrations in all compartments (ZnO and Ag in water in sediment being the exception) were at most within a factor of two of the approximate values reported based on MFA (Figure C-2). It is also noted that concentrations in air for TiO_2 and ZnO were only reported in the MFA study [42] as being <0.5 ng m^{-3} which is consistent with MendNano predictions for TiO_2 and ZnO of 0.12 and 0.024 ng m^{-3}, respectively. Clearly, with the assumption in the MFA study [42] that the total ENM release is regionally distributed to soil, there is a close agreement with predictions for the soil compartment since the concentration in

soil would then be dominated by the direct release to soil. However, if one accepts the more realistic scenario, whereby only "direct releases" to soil are regionally distributed (while releases from WWTP are localized and thus not distributed regionally), the MFA predicted concentrations in air and soil are about factors of 1.1-3.6 and 2.7-39.6 overestimated relative to predictions of the current compartmental mass balance approach. Additionally, MFA concentration estimates for ZnO and Ag in water and sediment are greater relative to present model results for water and sediment by factors of 4-6 and 2-4, respectively. (It is noted that the above behavior is essentially independent of the assumed release to soil given the small impact of soil runoff and wind erosion on the average concentrations in the water and sediment compartments). The above deviation is possibly due to the assumptions (rather than calculations based on consistent transport mechanisms) invoked in MFA with respect to the percentage of material that would settle (i.e., deposited) from the water compartment. For example, the MFA analysis [42] assumed, for the above US test case, that the following percentages (or percent ranges) of ENM input to water will settle: 0% to 100% for Ag, 29% to 100% for TiO_2, 6% to 74% for ZnO, and 79% to 99.9% for CNT; following Monte Carlo simulations for MFA and making use of the ranges, it was reported that the mode value for the fraction of ENMs inputs to water which settled were 99%, 20%, 50%, 98% for TiO_2, ZnO, Ag, and CNT, respectively. The difficulty with the above approach is that the assumed deposited percentages are not bounded by fundamental mechanistic parameters and approximations based on laboratory beaker experiments are not necessarily reflective of environmental behavior. Moreover, ENMs in the aquatic environment are likely to be associated (e.g., attach) with suspended solids [38, 220] and thus their deposition will be dictated by the size distribution of the ambient suspended particulates. In fact, the fraction of ENM that settles onto the sediment, calculated based on

mechanistic sedimentation rate expressions (eqs [2-7] and [3-12]), for the above US scenario is about 92% of all the ENMs entering the water compartment.

A second test case for the distribution of ENMs in Switzerland, for which release rates were reported for TiO_2, CNT, and Ag was also carried out. Simulations of the multimedia distribution for the above ENMs also showed a similar deviation of MFA estimation of media concentrations (Figure C-3). Particularly noteworthy is that MFA reported steady-state analysis results for the atmospheric compartment appear to be based on the assumption of complete atmospheric deposition of all ENMS input, with reported air concentration in the range of 0.006 - 3 ng m^{-3} for the above three ENMs. In contrast, MendNano simulations revealed steady state concentrations in air of 0.2 - 1.2 ng m^{-3}, 0.002 – 0.007 ng m^{-3} and 0.004 – 0.03 ng m^{-3} for TiO_2, CNT, and Ag, respectively. It is unclear if previously reported MFA estimations of media concentrations considered advective dilution in the atmospheric compartment [43]; neglect of advection would clearly lead to overestimation of ENM concentrations in the atmospheric compartment. It is also noted that, contrary to reported MFA estimates [43] of total ENM removal from the atmosphere by dry and wet deposition, the present analysis reveals that dry and wet deposition account for about 37-85% of the ENM release rate to the atmosphere.

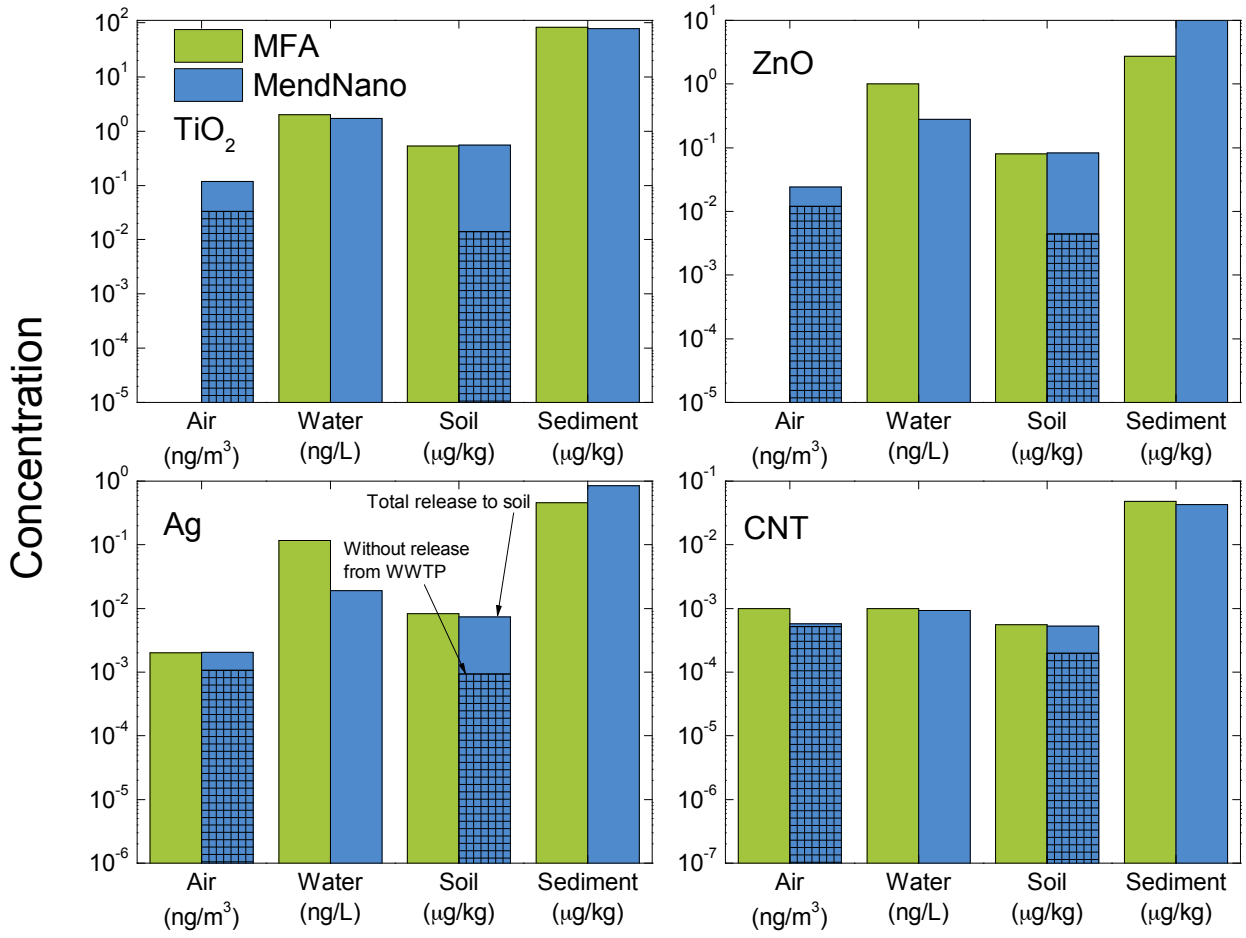

Figure C-2. MendNano and MFA [42] predictions of concentrations of TiO_2, ZnO, Ag, and CNT in the US based on ENM release rates reported in the MFA study (Table C-5) [42] for the regional parameters listed in Table C-6. ENM releases to soil are considered for two scenarios: 1) total ENM releases to soil (including those from WWTP) are applied to the entire soil (as performed by MFA [42]), and 2) only "direct release" to soil are spread over the entire soil (patterned portion). Concentrations in water and sediment are negligibly affected by the above two scenarios of release to soil. Note: (i) Concentrations of TiO_2 and ZnO in the atmospheric compartment in the MFA study [42] were reported as being <0.5 ng m^{-3} (for both ENMs); (ii) The resulting ENM concentrations in sediment for TiO_2 ZnO, and Ag at the end of 1 year (based on the reported ENM concentration increment for sediment in the MFA study [42]), were found to be inconsistent with the specified total ENM net input to sediment and the

reported sediment volume in the region (19.94 m^3). Specifically, for TiO_2 ZnO, and Ag, the ENM net input to sediment were reported to be 427.5, 14.1, and 2.4 metric tons/year, for which the estimated concentration in sediment at the end of 1 year would be 82.45, 2.72, and 0.46 μg/kg, respectively, and not 53, 0.51, and 0.195 μg/kg as deduced from the concentration increments reported in a published MFA study [42]. Therefore, in comparing the MFA estimates with the present model simulations, the concentrations resulting from the MFA analysis [42] were calculated based on the reported sediment volume and reported ENM net input to sediment; and (iii) ENM release to soil based on the assumption in the MFA study[35] of regional ENM distribution to soil from either the sum of ENM "direct release" and from WWTP sludge and additionally considering only "direct release".

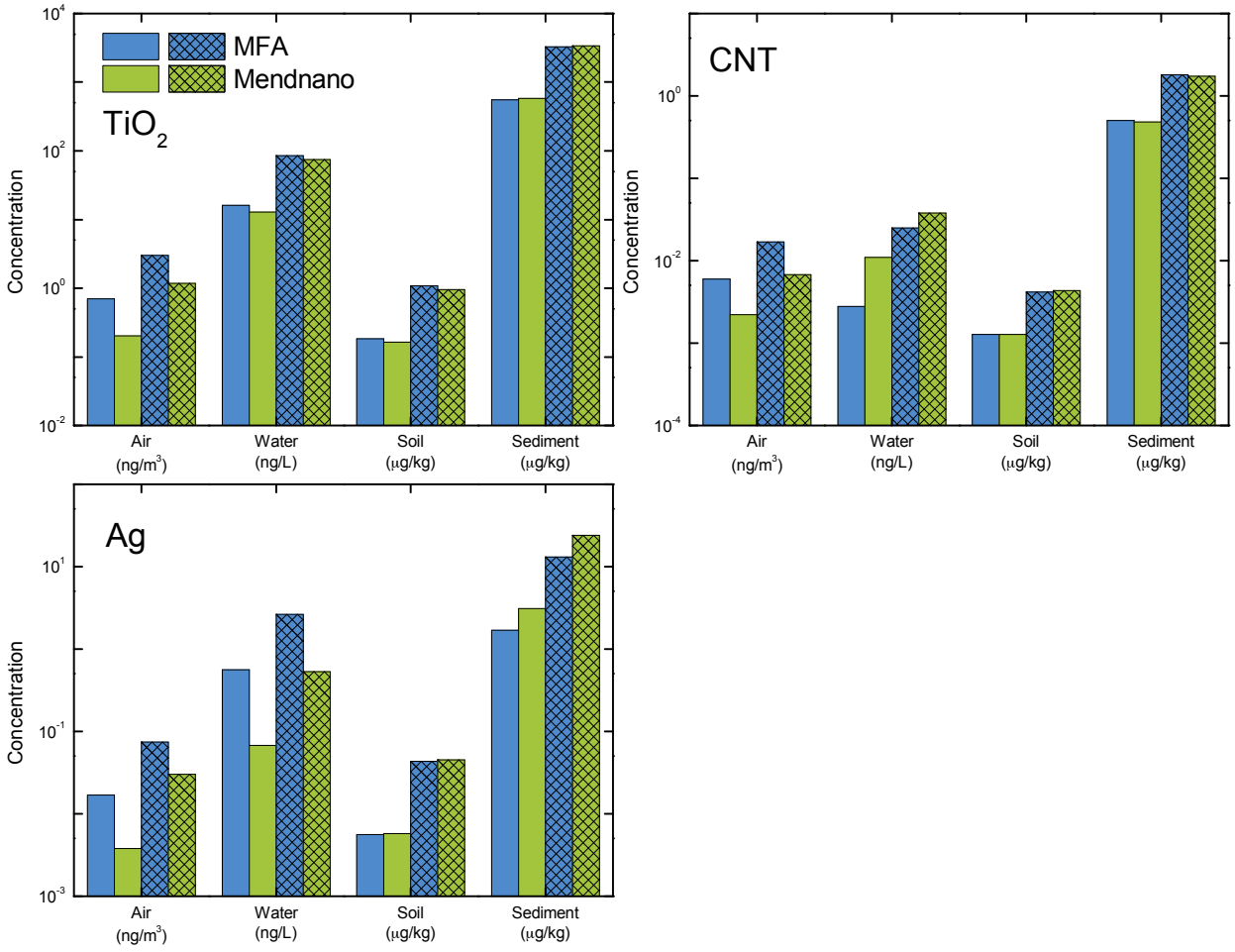

Figure C-3. MendNano and MFA [43] predictions of multimedia concentrations of TiO_2, CNT, and Ag in Switzerland. The release rates are those reported in [43] (Table C-7) and the regional parameters are listed in Table C-8. Non-patterned and patterned bars represent the lower and upper quantile values in reported MFA [43] predicted concentrations. Note: (a) Soil and sediment concentrations estimated from MFA analysis [43] were determined on the basis of the ENM net input to soil and sediment reported by the MFA study [43] as per the details provided in the caption of Figure C-2; (b) ENM release to soil based on the assumption in the MFA study of Gottschalk et al. [43] of regional ENM distribution of soil from the sum of ENM "direct release" and from WWTP sludge.

Table C-5. Production and release rates of TiO_2, ZnO, Ag, CNT ENMs in the U.S.

ENM	Release [a] (metric ton yr^{-1}) [42]				Total Production
	Air	Water	Soil[b]	Soil[c]	(metric ton yr^{-1})
TiO_2	30.7 (1.0%)	428.7 (14.4%)	762 (25.6%)	2.5 (0.1%)	2981.3
ZnO	10.7 (2.1%)	69.8 (13.6%)	110.1 (21.5%)	0 (0%)	512.95
Ag	0.9 (2.7%)	4.7 (14.1%)	9.8 (29.3 %)	2.8 (8%)	33.4
CNT	0.5 (0.6%)	0.22 (0.3%)	0.47 (0.6%)	0 (0%)	74.9

[a] Values in parentheses represent the indicated release rates (outside of the parentheses) as percent of total production rate for the specified ENM (i.e., last column) calculated from the data in [42].
[b] Total release to soil compartment via the sum of direct release and release associated with WWTP sludge
[c] Direct release to soil compartment (i.e., not including release from WWTP)

Table C-6. Parameters for simulation of environmental distribution of ENMs in the U.S.

Parameter	Parameter Value	
Air-soil interface area[42]	9,161,966	km^2
Air-water interface area[42]	664,709	km^2
Atmospheric mixing height[42]	1000	m
Depth of soil[42]	0.1	m
Depth of water[42]	3	m
Depth of sediment[42]	0.03	m
Average wind speed	3	$m\ s^{-1}$
Atmospheric convective residence time[42]	10	day
Water convective residence time[42]	40	day
Annual rainfall rate [279]	715	$mm\ yr^{-1}$
Dry soil density[42]	1,500	$kg\ m^{-3}$
Dry sediment density[42]	260	$kg\ m^{-3}$
Ambient aerosol PSD (Table 8.3 in Seinfeld and Pandis)[123]	Rural	
Ambient aerosol density	1,500	$kg\ m^{-3}$
Parameters of lognormal size distribution of Suspended Solids in water compartment		
Mode	5	μm
μ_{ln}	8.5	nm
σ_{ln}	0.6	nm
Ambient suspended solids density	1,500	$kg\ m^{-3}$
Initial and inflow concentration of ENMs in air and water	0	$ng\ m^{-3}$
Attachment factor	1	

Note: Foliage compartment was not included in the above simulation. Therefore, predicted ENM concentrations in soil with the above parameters represent upper limit estimates.

Table C-7. Production and release rates of TiO_2, Ag, CNT ENMs in Switzerland

ENM	Release [a] (metric ton yr^{-1}) [43]			Total Production
	Air	Water	Soil[b]	(metric ton yr^{-1})
TiO_2	0.85 – 4.96	6.24 – 36.57	0.34 – 1.98	70 – 410
Ag	0.015 – 0.118	0.033 – 0.256	0.02 – 0.157	0.386 – 3
CNT	0.008 – 0.027	0.005 – 0.018	0	1.2 – 4

[a] Value ranges represent the range of lower and upper quantiles reported in [43].
[b] Total release to soil compartment via the sum of direct release and release associated with WWTP sludge

Table C-8. Parameters for simulation of environmental distribution of ENMs in Switzerland

Parameter	Parameter Value	
Air-soil interface area[256]	39,997	km^2
Air-water interface area[256]	1,280	km^2
Atmospheric mixing height	1,000	m
Depth of soil[42]	0.1	m
Depth of water[42]	3	m
Depth of sediment[42]	0.03	m
Average wind speed	3	$m\ s^{-1}$
Atmospheric convective residence time[42]	10	day
Water convective residence time[42]	40	day
Annual rainfall rate[279]	1,537	$mm\ yr^{-1}$
Dry soil density[42]	1,500	$kg\ m^{-3}$
Dry sediment density[42]	260	$kg\ m^{-3}$
Ambient aerosol PSD (Table 8.3 in Seinfeld and Pandis)[123]	Rural	
Ambient aerosol density	1,500	$kg\ m^{-3}$
Parameters of lognormal size distribution of Suspended Solids in water compartment		
Mode	5	μm
μ_{ln}	8.5	nm
σ_{ln}	0.6	nm
Initial and inflow concentration of ENMs in air and water	0	$ng\ m^{-3}$
Ambient suspended solids density	1,500	$kg\ m^{-3}$
Attachment factor	1	

Note: Foliage compartment was not included in the above simulation. Therefore, predicted ENM concentrations in soil with the above parameters will be upper limit estimates.

Appendix D Environmental Impact Ranking.

Environmental Impact Assessment (EIA) for ENMs can benefit from ranking of their potential environmental impact in different geographical regions. Such ranking can achieved on the basis of potential environmental exposure levels weighted with respect to a suitable toxicity metric [82]. Suitable toxicity metrics may consist, for example, of slopes of dose-response curves [82], specific exposure levels at which specific effect levels are either observed (e.g., EC_{50}, IC_{50}) or not observed (e.g., No-Effect level or NOEL [280]). At present, however, ENMs dose-response data based on animal studies are scarce, while toxicity data based on high throughput screening (HTS) toxicity assays for various cell lines and bacterial have been rapidly developing [281]. In this regard, recent studies have shown, based on HTS toxicity data for various cell lines, that it is feasible to quantify the probability, P_i, of a given ENM i as being toxic (or non-toxic) given its fundamental physicochemical properties [281]. Accordingly, it is possible to arrive at an "environmental impact" *EI* index for ranking ENMs (for a given environmental compartment) within a given set of ENMs. The EI index for a given ENM can be defined as the normalized product of its potential compartmental (exposure) concentration, C_i, and the probability the ENM being toxic (i.e., $\beta_i = C_i \cdot P_i$), given by:

$$EI_i = \frac{\beta_i}{\max(\beta)} \qquad \text{[D-1]}$$

The value of *EI* is in the range of [0,1] and thus all the ENMs in the set are ranked relative to the ENM of highest potential impact. An illustration of a possible ranking on the basis of eq [D-1] is provided in Figure D-1 focusing on the resulting concentrations in water for the Los Angeles test case (Figure 6-4). The result demonstrate that ranking on the basis of decreasing

exposure concentrations is of the order TiO_2 > ZnO > Al_2O_3 > SiO_2 > CeO_2. However, ranking on the basis of decreasing environmental impact index (*EI*) is of the order ZnO > TiO_2 > CeO_2 > Al_2O_3 > SiO_2. Although the exposure concentration for ZnO is lower than for TiO_2, it has the highest *EI* given the significant weigh of it toxicity probability (inset in Figure D-1). It is also noted that although the concentration of CeO_2 in water is lower than that of Al_2O_3 and SiO_2 by factors of 8.7 and 7.0, respectively, its *EI* value greater by corresponding factors of 31 and 385 relative to the above two ENMs. Given the range of concentrations expected for the different ENMs, ranking on the basis of concentration of either no-effect level or level of acceptable exposure level would clearly be an advantage over the use of a toxicity probability function. Nonetheless, it is emphasized that given estimated exposure concentrations, even the above simple ranking can provide information that may be useful for prioritization of regulatory and research efforts.

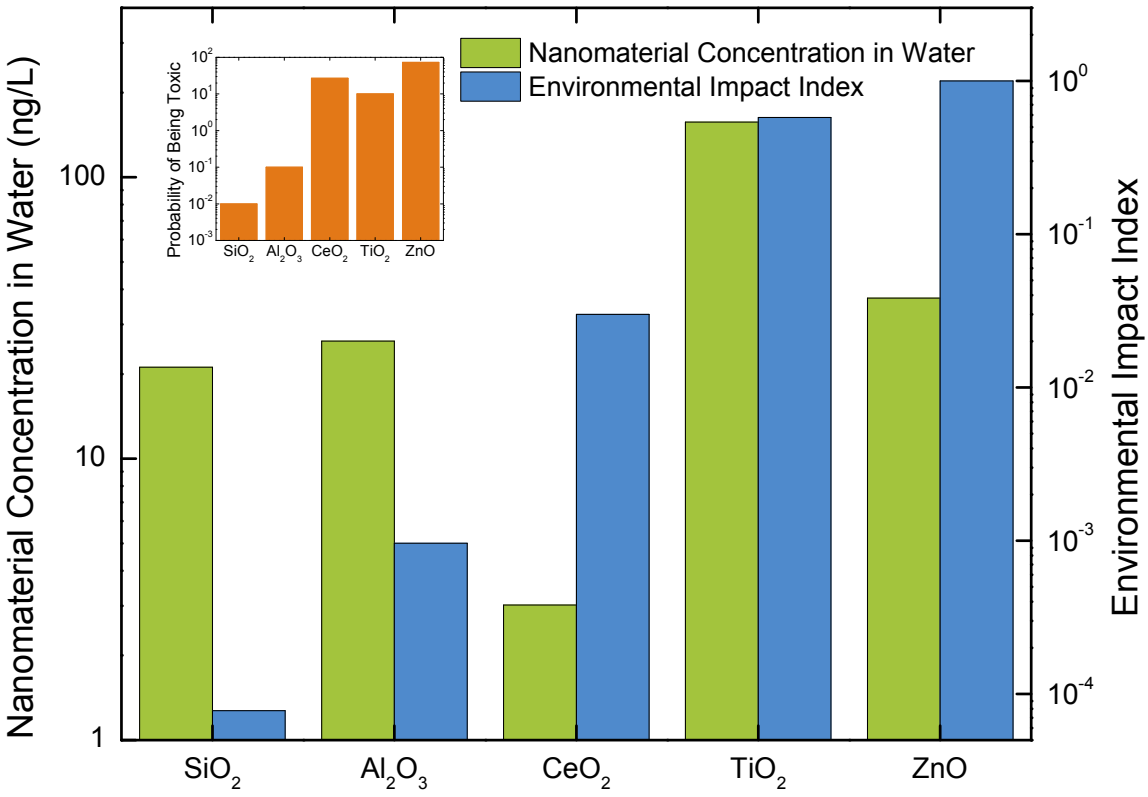

Figure D-1. Ranking of 5 ENMs based on an environmental impact index (eq [D-1]) and exposure concentrations in water based on simulations results for the Los Angeles test case of Figure 6-4.

References

1. International Organization for Standardization, *ISO/TS 27687:2008: Nanotechnologies -- Terminology and definitions for nano-objects -- Nanoparticle, nanofibre and nanoplate*. 2008.
2. Biswas, P. and C.Y. Wu, *Critical Review: Nanoparticles and the environment*. Journal of the Air & Waste Management Association, 2005. **55**(6): p. 708-746.
3. Esquivel, E.V. and L.E. Murr, *A TEM analysis of nanoparticulates in a Polar ice core*. Materials Characterization, 2004. **52**(1): p. 15-25.
4. Guo, Z. and L. Tan, *Fundamentals and Applications of Nanomaterials*. 1st ed. 2009: Artech House Publishers.
5. Klaine, S.J., P.J.J. Alvarez, G.E. Batley, T.F. Fernandes, R.D. Handy, D.Y. Lyon, S. Mahendra, M.J. McLaughlin, and J.R. Lead, *Nanomaterials in the environment: Behavior, fate, bioavailability, and effects*. Env. Tox. & Chem., 2008. **27**(9): p. 1825-1851.
6. Handy, R.D., R. Owen, and E. Valsami-Jones, *The ecotoxicology of nanoparticles and nanomaterials: current status, knowledge gaps, challenges, and future needs*. Ecotoxicology, 2008. **17**(5): p. 315-325.
7. Wiesner, M.R., G.V. Lowry, P. Alvarez, D. Dionysiou, and P. Biswas, *Assessing the risks of manufactured nanomaterials*. Env. Sci. & Tech., 2006. **40**(14): p. 4336-4345.
8. *The Project on Emerging Nanotechnologies: Consumer Products Inventory (Woodrow Wilson International Center)*. 2010 09/22/2011]; Available from: http://www.nanotechproject.org/inventories/consumer/.
9. Future Markets, *The global market for nanomaterials 2002-2006: production volumes, revenues, and end use markets*., 2012, Future Markets Inc.,.
10. Keller, A., S. McFerran, A. Lazareva, and S. Suh, *Global life cycle releases of engineered nanomaterials*. Journal of Nanoparticle Research, 2013. **15**(6): p. 1-17.
11. Becheri, A., M. Dürr, P. Lo Nostro, and P. Baglioni, *Synthesis and characterization of zinc oxide nanoparticles: application to textiles as UV-absorbers*. Journal of Nanoparticle Research, 2008. **10**(4): p. 679-689.
12. Lee, J., S. Mahendra, and P.J.J. Alvarez, *Nanomaterials in the Construction Industry: A Review of Their Applications and Environmental Health and Safety Considerations*. Acs Nano, 2010. **4**(7): p. 3580-3590.
13. Serrano, E., G. Rus, and J. García-Martínez, *Nanotechnology for sustainable energy*. Renewable and Sustainable Energy Reviews, 2009. **13**(9): p. 2373-2384.

14. Farré, M., K. Gajda-Schrantz, L. Kantiani, and D. Barceló, *Ecotoxicity and analysis of nanomaterials in the aquatic environment*. Analytical and Bioanalytical Chemistry, 2009. **393**(1): p. 81-95.

15. Savage, N. and M.S. Diallo, *Nanomaterials and Water Purification: Opportunities and Challenges*. Journal of Nanoparticle Research, 2005. **7**(4): p. 331-342.

16. Badireddy, A.R., E.M. Hotze, S. Chellam, P. Alvarez, and M.R. Wiesner, *Inactivation of Bacteriophages via Photosensitization of Fullerol Nanoparticles*. Env. Sci. & Tech., 2007. **41**(18): p. 6627-6632.

17. Wang, L., W. Chen, D. Xu, B.S. Shim, Y. Zhu, F. Sun, L. Liu, C. Peng, Z. Jin, C. Xu, and N.A. Kotov, *Simple, Rapid, Sensitive, and Versatile SWNT–Paper Sensor for Environmental Toxin Detection Competitive with ELISA*. Nano Letters, 2009. **9**(12): p. 4147-4152.

18. Scholars, W.W.I.C.f., *Project on Emerging Nanotechnologies: A Nanotechnology Consumer Products Inventory*.

19. Mueller, N.C. and B. Nowack, *Exposure modeling of engineered nanoparticles in the environment*. Env. Sci. & Tech., 2008. **42**(12): p. 4447-4453.

20. Boxall, A.B.A., Q. Chaudhry, C. Sinclair, A. Jones, R. Aitken, B. Jefferson, and C. Watts, *Current and Future Predicted Environmental Exposure to Engineered Nanoparticles*. Central Science Laboratory, 2007.

21. Rallo, R., B. France, R. Liu, S. Nair, S. George, R. Damoiseaux, F. Giralt, A. Nel, K. Bradley, and Y. Cohen, *Self-Organizing Map Analysis of Toxicity-Related Cell Signaling Pathways for Metal and Metal Oxide Nanoparticles*. Env. Sci. & Tech., 2011. **45**(4): p. 1695-1702.

22. Pietroiusti, A., *Health implications of engineered nanomaterials*. Nanoscale, 2012. **4**(4): p. 1231-1247.

23. Oberdoester, G., *Nanotoxicology: An Emerging Discipline Evolving from Studies of Ultrafine Particles (vol 113, pg 823, 2005)*. Environmental Health Perspectives, 2010. **118**(9): p. A380-A380.

24. Chae, S.-R., S. Wang, Z.D. Hendren, M.R. Wiesner, Y. Watanabe, and C.K. Gunsch, *Effects of fullerene nanoparticles on Escherichia coli K12 respiratory activity in aqueous suspension and potential use for membrane biofouling control*. Journal of Membrane Science, 2009. **329**(1-2): p. 68-74.

25. Lyon, D.Y., L.K. Adams, J.C. Falkner, and P.J.J. Alvarez, *Antibacterial activity of fullerene water suspensions: Effects of preparation method and particle size*. Env. Sci. & Tech., 2006. **40**(14): p. 4360-4366.

26. Wiesner, M.R., G.V. Lowry, K.L. Jones, M.F. Hochella, R.T. Di Giulio, E. Casman, and E.S. Bernhardt, *Decreasing Uncertainties in Assessing Environmental Exposure, Risk, and Ecological Implications of Nanomaterials*. Env. Sci. & Tech., 2009. **43**(17): p. 6458-6462.

27. Limbach, L.K., P. Wick, P. Manser, R.N. Grass, A. Bruinink, and W.J. Stark, *Exposure of engineered nanoparticles to human lung epithelial cells: Influence of chemical composition and catalytic activity on oxidative stress*. Env. Sci. & Tech., 2007. **41**(11): p. 4158-4163.

28. Gao, J., J.-C.J. Bonzongo, G. Bitton, Y. Li, and C.-Y. Wu, *Nanowastes and the environment: Using mercury as an example pollutant to assess the environmental fate of chemicals adsorbed onto manufactured nanomaterials*. Env. Tox. & Chem., 2008. **27**(4): p. 808-810.

29. Barnard, A.S., *Computational strategies for predicting the potential risks associated with nanotechnology*. Nanoscale, 2009. **1**(1): p. 89-95.

30. Stone, V., B. Nowack, A. Baun, N. van den Brink, F. von der Kammer, M. Dusinska, R. Handy, S. Hankin, M. Hassellöv, E. Joner, and T.F. Fernandes, *Nanomaterials for environmental studies: Classification, reference material issues, and strategies for physico-chemical characterisation*. Science of the Total Environment, 2010. **408**(7): p. 1745-1754.

31. Kahru, A. and H.-C. Dubourguier, *From ecotoxicology to nanoecotoxicology*. Toxicology, 2010. **269**(2-3): p. 105-119.

32. Cohen, Y. and E.J. Cooter, *Multimedia Environmental Distribution of Toxics (Mend-Tox). I: Hybrid Compartmental-Spatial Modeling Framework*. Practice Periodical of Hazardous, Toxic, and Radioactive Waste Management, 2002. **6**(2): p. 70-86.

33. Cohen, Y. and E.J. Cooter, *Multimedia Environmental Distribution of Toxics (Mend-Tox). II: Software Implementation and Case Studies*. Practice Periodical of Hazardous, Toxic, and Radioactive Waste Management, 2002. **6**(2): p. 87-101.

34. Colvin, V.L., *The potential environmental impact of engineered nanomaterials*. Nature Biotechnology, 2003. **21**(10): p. 1166-1170.

35. von der Kammer, F., P.L. Ferguson, P.A. Holden, A. Masion, K.R. Rogers, S.J. Klaine, A.A. Koelmans, N. Horne, and J.M. Unrine, *Analysis of engineered nanomaterials in complex matrices (environment and biota): General considerations and conceptual case studies*. Env. Tox. & Chem., 2012. **31**(1): p. 32-49.

36. Klaine, S.J., A.A. Koelmans, N. Horne, S. Carley, R.D. Handy, L. Kapustka, B. Nowack, and F. von der Kammer, *Paradigms to assess the environmental impact of manufactured nanomaterials*. Env. Tox. & Chem., 2012. **31**(1): p. 3-14.

37. Weinberg, H., A. Galyean, and M. Leopold, *Evaluating engineered nanoparticles in natural waters*. Trac-Trends in Analytical Chemistry, 2011. **30**(1): p. 72-83.

38. Praetorius, A., M. Scheringer, and K. Hungerbuhler, *Development of Environmental Fate Models for Engineered Nanoparticles-A Case Study of TiO2 Nanoparticles in the Rhine River*. Env. Sci. & Tech., 2012. **46**(12): p. 6705-6713.

39. Neal, C., H. Jarvie, P. Rowland, A. Lawler, D. Sleep, and P. Scholefield, *Titanium in UK rural, agricultural and urban/industrial rivers: Geogenic and anthropogenic*

colloidal/sub-colloidal sources and the significance of within-river retention. Science of The Total Environment, 2011. **409**(10): p. 1843-1853.

40. Sanchís, J., N. Berrojalbiz, G. Caballero, J. Dachs, M. Farré, and D. Barceló, *Occurrence of Aerosol-Bound Fullerenes in the Mediterranean Sea Atmosphere*. Env. Sci. & Tech., 2011. **46**(3): p. 1335-1343.

41. Gottschalk, F., R.W. Scholz, and B. Nowack, *Probabilistic material flow modeling for assessing the environmental exposure to compounds: Methodology and an application to engineered nano-TiO(2) particles*. Environmental Modelling & Software, 2010. **25**(3): p. 320-332.

42. Gottschalk, F., T. Sonderer, R.W. Scholz, and B. Nowack, *Modeled Environmental Concentrations of Engineered Nanomaterials (TiO2, ZnO, Ag, CNT, Fullerenes) for Different Regions*. Env. Sci. & Tech., 2009. **43**(24): p. 9216-9222.

43. Gottschalk, F., T. Sonderer, R.W. Scholz, and B. Nowack, *Possibilities and Limitations of Modeling Environmental Exposure to Engineered Nanomaterials by Probabilistic Material Flow Analysis*. Env. Tox. & Chem., 2010. **29**(5): p. 1036-1048.

44. Mackay, D., *Multimedia environmental models : the fugacity approach*. 2nd ed. 2001, Boca Raton: Lewis Publishers. 261 p.

45. USEPA, *Testing for Field Applicability of Chemical Exposure Models*, 1982, US Environmental Protection Agency

46. Kauffman, R., M. Lee, R. Murphy, D. Burch, M. Fisher, A. Benjamin, and B. Jones, *Evaluation of TRIM.FaTE*, USEPA, Office of Air Quality Planning and Standards, and Emissions Standards & Air Quality Strategies and Standards Divisions, 2004,

47. Pistocchi, A., *Some considerations on the use of simple box models of contaminant fate in soils*. Environmental Monitoring and Assessment, 2013. **185**(3): p. 2855-2867.

48. Mackay, D. and S. Paterson, *Evaluating the Multimedia Fate of Organic-Chemicals - a Level-Iii Fugacity Model*. Env. Sci. & Tech., 1991. **25**(3): p. 427-436.

49. Liu, H.H., S. Surawanvijit, R. Rallo, G. Orkoulas, and Y. Cohen, *Analysis of Nanoparticle Agglomeration in Aqueous Suspensions via Constant-Number Monte Carlo Simulation*. Env. Sci. & Tech., 2011. **45**(21): p. 9284-9292.

50. Kajihara, M., *Settling velocity and porosity of large suspended particle*. Journal of Oceanography, 1971. **27**(4): p. 158-162.

51. Elimelech, M., *Particle deposition and aggregation : measurement, modelling, and simulation*. Colloid and surface engineering series. 1995, Oxford England ; Boston: Butterworth-Heinemann. xv, 441 p.

52. Areepitak, T. and J. Ren, *Model Simulations of Particle Aggregation Effect on Colloid Exchange between Streams and Streambeds*. Env. Sci. & Tech., 2011

53. Sharma, V.K., *Aggregation and toxicity of titanium dioxide nanoparticles in aquatic environment-A Review*. Journal of Environmental Science and Health Part a-Toxic/Hazardous Substances & Environmental Engineering, 2009. **44**(14): p. 1485-1495.

54. Petosa, A.R., D.P. Jaisi, I.R. Quevedo, M. Elimelech, and N. Tufenkji, *Aggregation and Deposition of Engineered Nanomaterials in Aquatic Environments: Role of Physicochemical Interactions*. Env. Sci. & Tech., 2010. **44**(17): p. 6532-6549.

55. Long, T.C., N. Saleh, R.D. Tilton, G.V. Lowry, and B. Veronesi, *Titanium dioxide (P25) produces reactive oxygen species in immortalized brain microglia (BV2): Implications for nanoparticle neurotoxicity*. Env. Sci. & Tech., 2006. **40**(14): p. 4346-4352.

56. Cohen, J., J. Teeguarden, and P. Demokritou, *An integrated approach for the in vitro dosimetry of engineered nanomaterials*. Particle and Fibre Toxicology, 2014. **11**(1): p. 20.

57. DeLoid, G., J.M. Cohen, T. Darrah, R. Derk, L. Rojanasakul, G. Pyrgiotakis, W. Wohlleben, and P. Demokritou, *Estimating the effective density of engineered nanomaterials for in vitro dosimetry*. Nat Commun, 2014. **5**.

58. Hinderliter, P., K. Minard, G. Orr, W. Chrisler, B. Thrall, J. Pounds, and J. Teeguarden, *ISDD: A computational model of particle sedimentation, diffusion and target cell dosimetry for in vitro toxicity studies*. Particle and Fibre Toxicology, 2010. **7**(1): p. 36.

59. Teeguarden, J.G., P.M. Hinderliter, G. Orr, B.D. Thrall, and J.G. Pounds, *Particokinetics In Vitro: Dosimetry Considerations for In Vitro Nanoparticle Toxicity Assessments*. Toxicological Sciences, 2007. **95**(2): p. 300-312.

60. Ji, Z., X. Jin, S. George, T. Xia, H. Meng, X. Wang, E. Suarez, H. Zhang, E.M.V. Hoek, H. Godwin, A.E. Nel, and J.I. Zink, *Dispersion and Stability Optimization of TiO2 Nanoparticles in Cell Culture Media*. Env. Sci. & Tech., 2010. **44**(19): p. 7309-7314.

61. Zhang, Y., Y. Chen, P. Westerhoff, K. Hristovski, and J.C. Crittenden, *Stability of commercial metal oxide nanoparticles in water*. Water Research, 2008. **42**(8-9): p. 2204-2212.

62. Guzman, K.A.D., M.P. Finnegan, and J.F. Banfield, *Influence of Sufface Potential on Aggregation and Transport of Titania nanoparticles*. Env. Sci. & Tech., 2006. **40**(24): p. 7688-7693.

63. Keller, A.A., H.T. Wang, D.X. Zhou, H.S. Lenihan, G. Cherr, B.J. Cardinale, R. Miller, and Z.X. Ji, *Stability and Aggregation of Metal Oxide Nanoparticles in Natural Aqueous Matrices*. Env. Sci. & Tech., 2010. **44**(6): p. 1962-1967.

64. Jiang, J.K., G. Oberdorster, and P. Biswas, *Characterization of size, surface charge, and agglomeration state of nanoparticle dispersions for toxicological studies*. Journal of Nanoparticle Research, 2009. **11**(1): p. 77-89.

65. Baveye, P. and M. Laba, *Aggregation and toxicology of titanium dioxide nanoparticles*. Environmental Health Perspectives, 2008. **116**(4): p. A152-A152.

66. French, R.A., A.R. Jacobson, B. Kim, S.L. Isley, R.L. Penn, and P.C. Baveye, *Influence of Ionic Strength, pH, and Cation Valence on Aggregation Kinetics of Titanium Dioxide Nanoparticles*. Env. Sci. & Tech., 2009. **43**(5): p. 1354-1359.

67. Chen, K.L. and M. Elimelech, *Aggregation and Deposition Kinetics of Fullerene (C60) Nanoparticles*. Langmuir, 2006. **22**(26): p. 10994-11001.

68. He, Y.T., J.M. Wan, and T. Tokunaga, *Kinetic stability of hematite nanoparticles: the effect of particle sizes*. Journal of Nanoparticle Research, 2008. **10**(2): p. 321-332.

69. Kim, T., C.H. Lee, S.W. Joo, and K. Lee, *Kinetics of gold nanoparticle aggregation: Experiments and modeling*. Journal of Colloid and Interface Science, 2008. **318**(2): p. 238-243.

70. Huynh, K.A. and K.L. Chen, *Aggregation Kinetics of Citrate and Polyvinylpyrrolidone Coated Silver Nanoparticles in Monovalent and Divalent Electrolyte Solutions*. Env. Sci. & Tech., 2011. **45**(13): p. 5564-5571.

71. Buettner, K.M., C.I. Rinciog, and S.E. Mylon, *Aggregation kinetics of cerium oxide nanoparticles in monovalent and divalent electrolytes*. Colloids and Surfaces a-Physicochemical and Engineering Aspects, 2010. **366**(1-3): p. 74-79.

72. Bos, R., H.C. van der Mei, and H.J. Busscher, *Physico-chemistry of initial microbial adhesive interactions – its mechanisms and methods for study*. Fems Microbiology Reviews, 1999. **23**(2): p. 179-230.

73. Grasso, D., K. Subramaniam, M. Butkus, K. Strevett, and J. Bergendahl, *A review of non-DLVO interactions in environmental colloidal systems*. Reviews in Environmental Science and Biotechnology, 2002. **1**(1): p. 17-38.

74. Hermansson, M., *The DLVO theory in microbial adhesion*. Colloids and Surfaces B-Biointerfaces, 1999. **14**(1-4): p. 105-119.

75. Hong, Y.S., R.J. Honda, N.V. Myung, and S.L. Walker, *Transport of Iron-Based Nanoparticles: Role of Magnetic Properties*. Env. Sci. & Tech., 2009. **43**(23): p. 8834-8839.

76. Honig, E.P., Roeberse.Gj, and P.H. Wiersema, *Effect of Hydrodynamic Interaction on Coagulation Rate of Hydrophobic Colloids*. Journal of Colloid and Interface Science, 1971. **36**(1): p. 97-109.

77. Hattemer-Frey, H.A. and C.C. Travis, *Benzo-a-Pyrene: Environmental Partitioning and Human Exposure*. Toxicology and Industrial Health, 1991. **7**(3): p. 141-157.

78. Yeo, H.-G., M. Choi, M.-Y. Chun, and Y. Sunwoo, *Gas/particle concentrations and partitioning of PCBs in the atmosphere of Korea*. Atmospheric Environment, 2003. **37**(25): p. 3561-3570.

79. Mackay, D. and W.Y. Shiu, *Aqueous solubility of polynuclear aromatic hydrocarbons*. Journal of Chemical & Engineering Data, 1977. **22**(4): p. 399-402.

80. Lazareva, A. and A.A. Keller, *Estimating Potential Life Cycle Releases of Engineered Nanomaterials from Wastewater Treatment Plants*. Acs Sustainable Chemistry & Engineering, 2014. **2**(7): p. 1656-1665.

81. Keller, A.A., W. Vosti, H.T. Wang, and A. Lazareva, *Release of engineered nanomaterials from personal care products throughout their life cycle*. Journal of Nanoparticle Research, 2014. **16**(7).

82. Cohen, Y., R. Rallo, R. Liu, and H.H. Liu, *In Silico Analysis of Nanomaterials Hazard and Risk*. Accounts of Chemical Research, 2013. **46**(3): p. 802-812.

83. Tsuji, J.S., A.D. Maynard, P.C. Howard, J.T. James, C.-w. Lam, D.B. Warheit, and A.B. Santamaria, *Research Strategies for Safety Evaluation of Nanomaterials, Part IV: Risk Assessment of Nanoparticles*. Toxicological Sciences, 2006. **89**(1): p. 42-50.

84. Colvin, V.L., *The potential environmental impact of engineered nanomaterials*. Nat Biotech, 2003. **21**(10): p. 1166-1170.

85. Gottschalk, F., T. Sun, and B. Nowack, *Environmental concentrations of engineered nanomaterials: Review of modeling and analytical studies*. Environmental Pollution, 2013. **181**(0): p. 287-300.

86. USEPA, *Lake Michigan mass budget/mass balance work plan*, USEPA and Great Lakes National Program Office, Editor 1997.

87. McKone, T.E., *CalTOX, a multimedia total exposure model for hazardous-waste sites; Part 1, Executive summary*, in *Other Information: PBD: Jun 1993*1993. p. Medium: ED; Size: 31 p.

88. USEPA, *Total Risk Integrated Methodology, TRIM.FaTE Technical Support Document, Volume I: Description of Modules*, USEPA, Office of Air Quality Planning and Standards, and Emissions Standards & Air Quality Strategies and Standards Divisions, 2002, USEPA

89. Van de Meent, D., *SimpleBox: a generic multimedia fate evaluation model*, 1993, National Institute of Public Health and the Environment (RIVM): Bilthoven, The Netherlands.

90. Giorgi, F., *A particle dry-deposition parameterization scheme for use in tracer transport models*. Journal of Geophysical Research: Atmospheres, 1986. **91**(D9): p. 9794-9806.

91. Williams, R.M., *A Model for the Dry Deposition of Particles to Natural-Water Surfaces*. Atmospheric Environment, 1982. **16**(8): p. 1933-1938.

92. Tsai, W., Y. Cohen, H. Sakugawa, and I.R. Kaplan, *Dynamic partitioning of semivolatile organics in gas/particle/rain phases during rain scavenging*. Env. Sci. & Tech., 1991. **25**(12): p. 2012-2023.

93. O'Dowd, C.D. and G. de Leeuw, *Marine aerosol production: a review of the current knowledge*. Philosophical Transactions of the Royal Society A: Mathematical, Physical and Engineering Sciences, 2007. **365**(1856): p. 1753-1774.

94. Sehmel, G.A. and W.H. Hodgson, *Model for predicting dry deposition of particles and gases to environmental surfaces*. 1978. Medium: P; Size: Pages: 44.

95. USDA-ARS, *A universal equation for measuring wind erosion*, United States Department of Agriculture - Agriculture Research Service, 1961,

96. Renard, K.G., G.R. Foster, and G.A. Weesies, *Predicting soil erosion by water : a guide to conservation planning with the Revised Universal Soil Loss Equation (RUSLE)*. Agriculture handbook;no. 703. 1997, Washington: USDA.

97. Wishmeier, W.H. and D.D. Smith, *Predicting rainfall erosion losses - a guide to conservation planning*, U.S. Department of Agriculture, 1978,

98. Slinn, W.G.N., *Predictions for Particle Deposition to Vegetative Canopies*. Atmospheric Environment, 1982. **16**(7): p. 1785-1794.

99. Luettich, R.A., D.R.F. Harleman, and L. Somlyody, *Dynamic Behavior of Suspended Sediment Concentrations in a Shallow Lake Perturbed by Episodic Wind Events*. Limnology and Oceanography, 1990. **35**(5): p. 1050-1067.

100. Grant, W.D. and O.S. Madsen, *Combined wave and current interaction with a rough bottom*. Journal of Geophysical Research: Oceans, 1979. **84**(C4): p. 1797-1808.

101. Bird, R.B., W.E. Stewart, and E.N. Lightfoot, *Transport phenomena*. 2nd, Wiley international ed. 2007, New York: J. Wiley. xii, 895 p.

102. Blanchard, D.C., *The Ejection of Drops from the Sea and Their Enrichment with Bacteria and Other Materials - a Review*. Estuaries, 1989. **12**(3): p. 127-137.

103. Dyer, K.R., *Review of Oceanographic Proccesses Influencing Radioactive Waste Dispersal In The Irish Sea*, 1986, Institute of Oceanographic Science.

104. Blanchard, D.C. and L.D. Syzdek, *Water-to-Air Transfer and Enrichment of Bacteria in Drops from Bursting Bubbles*. Applied and Environmental Microbiology, 1982. **43**(5): p. 1001-1005.

105. Buschiazzo, D.E. and T.M. Zobeck, *Validation of WEQ, RWEQ and WEPS wind erosion for different arable land management systems in the Argentinean Pampas*. Earth Surface Processes and Landforms, 2008. **33**(12): p. 1839-1850.

106. Fryrear, D.W., J.D. Ali Saleh, H.M. Bilbro, J.E.S. Schomberg, and T.M. Zobeck., *Revised Wind Erosion Equation (RWEQ)*, U.-A. Wind Erosion and Water Conservation Research Unit and Southern Plains Area Cropping Systems Research Laboratory, 1998,

107. Fryear, D.W., P.L. Sutherland, G. Davis, G. Hardee, and M. Dollar, *Wind Erosion Estimates with RWEQ and WEQ*. 10th International Soil Conservation Organization Meeting, 2001: p. 760-765.

108. Broadbridge, P. and I. White, *Time to ponding: Comparison of analytic, quasi-analytic, and approximate predictions*. Water Resources Research, 1987. **23**(12): p. 2302-2310.

109. Li, J. and C. Zhang, *Sediment resuspension and implications for turbidity maximum in the Changjiang Estuary*. Marine Geology, 1998. **148**(3–4): p. 117-124.

110. Holder, C.D., *Effects of leaf hydrophobicity and water droplet retention on canopy storage capacity*. Ecohydrology, 2013. **6**(3): p. 483-490.

111. Zhu, H., J. Han, J.Q. Xiao, and Y. Jin, *Uptake, translocation, and accumulation of manufactured iron oxide nanoparticles by pumpkin plants*. Journal of Environmental Monitoring, 2008. **10**(6): p. 713-717.

112. Servin, A.D., H. Castillo-Michel, J.A. Hernandez-Viezcas, B.C. Diaz, J.R. Peralta-Videa, and J.L. Gardea-Torresdey, *Synchrotron Micro-XRF and Micro-XANES Confirmation of*

the Uptake and Translocation of TiO2 Nanoparticles in Cucumber (Cucumis sativus) Plants. Env. Sci. & Tech., 2012. **46**(14): p. 7637-7643.

113. Lin, D. and B. Xing, *Root Uptake and Phytotoxicity of ZnO Nanoparticles*. Env. Sci. & Tech., 2008. **42**(15): p. 5580-5585.

114. Hischem, A. ller, J. Nordmann, rg, P. Ptacek, K. Mummenhoff, and M. Haase, *In-Vivo Imaging of the Uptake of Upconversion Nanoparticles by Plant Roots*. Journal of Biomedical Nanotechnology, 2009. **5**(3): p. 278-284.

115. Ma, X., J. Geiser-Lee, Y. Deng, and A. Kolmakov, *Interactions between engineered nanoparticles (ENPs) and plants: Phytotoxicity, uptake and accumulation*. Science of The Total Environment, 2010. **408**(16): p. 3053-3061.

116. Katsanevakis, S. and C.D. Maravelias, *Modelling fish growth: multi-model inference as a better alternative to a priori using von Bertalanffy equation*. Fish and Fisheries, 2008. **9**(2): p. 178-187.

117. Kent, R.D. and P.J. Vikesland, *Controlled Evaluation of Silver Nanoparticle Dissolution Using Atomic Force Microscopy*. Env. Sci. & Tech., 2011. **46**(13): p. 6977-6984.

118. Palmer, D.A. and P. Bénézeth, *Solubility of Copper Oxides in Water and Steam*. Proceedings of the 14th International Conference on the Properties of Water and Steam, 2004: p. 491-496.

119. Millero, F.J., *Solubility of Fe(III) in seawater*. Earth and Planetary Science Letters, 1998. **154**(1–4): p. 323-329.

120. David, C.A., J. Galceran, C. Rey-Castro, J. Puy, E. Companys, J. Salvador, J. Monné, R. Wallace, and A. Vakourov, *Dissolution Kinetics and Solubility of ZnO Nanoparticles Followed by AGNES*. The Journal of Physical Chemistry C, 2012. **116**(21): p. 11758-11767.

121. Kariuki, S. and H.D. Dewald, *Evaluation of diffusion coefficients of metallic ions in aqueous solutions*. Electroanalysis, 1996. **8**(4): p. 307-313.

122. Levenspiel, O., *Chemical reaction engineering*. 3rd ed. 1999, New York: Wiley. xvi, 668 p.

123. Seinfeld, J.H. and S.N. Pandis, *Atmospheric chemistry and physics : from air pollution to climate change*. 2nd ed. 2006, Hoboken, N.J.: J. Wiley. xxviii, 1203 p.

124. Socolofsky, S.A. and G.H. Jirka, *Environmental Fluid Mechanics 1: Mixing and Transport Processes in the Environment*. 2005.

125. Luketina, D., *Simple Tidal Prism Models Revisited*. Estuarine, Coastal and Shelf Science, 1998. **46**(1): p. 77-84.

126. Sun, T.Y., F. Gottschalk, K. Hungerbuhler, and B. Nowack, *Comprehensive probabilistic modelling of environmental emissions of engineered nanomaterials*. Environmental Pollution, 2014. **185**: p. 69-76.

127. Li, Q.L., B. Xie, Y.S. Hwang, and Y.J. Xu, *Kinetics of C-60 Fullerene Dispersion in Water Enhanced by Natural Organic Matter and Sunlight*. Env. Sci. & Tech., 2009. **43**(10): p. 3574-3579.

128. Fang, J., X.Q. Shan, B. Wen, J.M. Lin, and G. Owens, *Stability of titania nanoparticles in soil suspensions and transport in saturated homogeneous soil columns*. Environmental Pollution, 2009. **157**(4): p. 1101-1109.

129. Kennedy, A.J., M.S. Hull, J.A. Steevens, K.M. Dontsova, M.A. Chappell, J.C. Gunter, and C.A. Weiss, *Factors influencing the partitioning and toxicity of nanotubes in the aquatic environment*. Env. Tox. & Chem., 2008. **27**(9): p. 1932-1941.

130. Hyung, H., J.D. Fortner, J.B. Hughes, and J.H. Kim, *Natural organic matter stabilizes carbon nanotubes in the aqueous phase*. Env. Sci. & Tech., 2007. **41**(1): p. 179-184.

131. Liu, H.H. and Y. Cohen, *Multimedia Environmental Distribution of Engineered Nanomaterials*. Env. Sci. & Tech., 2014. **48**(6): p. 3281-3292.

132. Meesters, J.A.J., A.A. Koelmans, J.T.K. Quik, A.J. Hendriks, and D. van de Meentt, *Multimedia Modeling of Engineered Nanoparticles with SimpleBox4nano: Model Definition and Evaluation*. Env. Sci. & Tech., 2014. **48**(10): p. 5726-5736.

133. Blaser, S.A., M. Scheringer, M. MacLeod, and K. Hungerbuhler, *Estimation of cumulative aquatic exposure and risk due to silver: Contribution of nano-functionalized plastics and textiles*. Science of the Total Environment, 2008. **390**(2-3): p. 396-409.

134. Gottschalk, F., C. Ort, R.W. Scholz, and B. Nowack, *Engineered nanomaterials in rivers – Exposure scenarios for Switzerland at high spatial and temporal resolution*. Environmental Pollution, 2011. **159**(12): p. 3439-3445.

135. Alimohammadi, M. and K.A. Fichthorn, *Molecular Dynamics Simulation of the Aggregation of Titanium Dioxide Nanocrystals: Preferential Alignment*. Nano Letters, 2009. **9**(12): p. 4198-4203.

136. Maisels, A., F.E. Kruis, and H. Fissan, *Direct simulation Monte Carlo for simultaneous nucleation, coagulation, and surface growth in dispersed systems*. Chemical Engineering Science, 2004. **59**(11): p. 2231-2239.

137. Markutsya, S., S. Subramaniam, R.D. Vigil, and R.O. Fox, *On Brownian dynamics simulation of nanoparticle aggregation*. Industrial & Engineering Chemistry Research, 2008. **47**(10): p. 3338-3345.

138. Zhao, H., A. Maisels, T. Matsoukas, and C. Zheng, *Analysis of four Monte Carlo methods for the solution of population balances in dispersed systems*. Powder Technology, 2007. **173**(1): p. 38-50.

139. Peng, Z.B., E. Doroodchi, and G. Evans, *DEM simulation of aggregation of suspended nanoparticles*. Powder Technology, 2010. **204**(1): p. 91-102.

140. Jiang, W.T., G.L. Ding, H. Peng, and H.T. Hu, *Modeling of nanoparticles' aggregation and sedimentation in nanofluid*. Current Applied Physics, 2010. **10**(3): p. 934-941.

141. Lv, J., M. Bai, W. Cui, and X. Li, *The molecular dynamic simulation on impact and friction characters of nanofluids with many nanoparticles system*. Nanoscale Research Letters, 2011. **6**(1): p. 1-8.

142. Nguyen, N., R. Henning, and J. Wen, *Molecular dynamics simulation of iron nanoparticle sintering during flame synthesis*. Journal of Nanoparticle Research, 2011. **13**(2): p. 803-815.

143. Park, H., S. Kim, and H. Chang, *Brownian dynamic simulation for the aggregation of charged particles*. Journal of Aerosol Science, 2001. **32**(11): p. 1369-1388.

144. Lin, Y.L., K. Lee, and T. Matsoukas, *Solution of the population balance equation using constant-number Monte Carlo*. Chemical Engineering Science, 2002. **57**(12): p. 2241-2252.

145. Smith, M. and T. Matsoukas, *Constant-number Monte Carlo simulation of population balances*. Chemical Engineering Science, 1998. **53**(9): p. 1777-1786.

146. Lee, K. and T. Matsoukas, *Simultaneous coagulation and break-up using constant-N Monte Carlo*. Powder Technology, 2000. **110**(1-2): p. 82-89.

147. Kruis, F.E., A. Maisels, and H. Fissan, *Direct simulation Monte Carlo method for particle coagulation and aggregation*. AIChe Journal, 2000. **46**(9): p. 1735-1742.

148. Zhao, H.B., C.G. Zheng, and M.H. Xu, *Multi-Monte Carlo method for particle coagulation: description and validation*. Applied Mathematics and Computation, 2005. **167**(2): p. 1383-1399.

149. Friedlander, S.K., *Smoke, dust, and haze : fundamentals of aerosol dynamics*. 2nd ed. Topics in chemical engineering. 2000, New York: Oxford University Press. xx, 407 p.

150. Kruyt, H.R., *Colloid science*. 1949, New York,: Elsevier Pub. Co.

151. Israelachvili, J.N., *Intermolecular and surface forces*. 3rd ed. 2011, Burlington, MA: Academic Press. xxx, 674 p.

152. Li, K. and Y. Chen, *Effect of natural organic matter on the aggregation kinetics of CeO2 nanoparticles in KCl and CaCl2 solutions: Measurements and modeling*. Journal of Hazardous Materials, 2012. **209–210**(0): p. 264-270.

153. Li, Z., E. Sahle-Demessie, A.A. Hassan, and G.A. Sorial, *Aggregation, deposition and transport of CeO2 nanoparticles in a sand filtration process at water treatment facilities*. Abstracts of Papers of the American Chemical Society, 2011. **242**.

154. Lawrie, A.S., A. Albanyan, R.A. Cardigan, I.J. Mackie, and P. Harrison, *Microparticle sizing by dynamic light scattering in fresh-frozen plasma*. Vox Sanguinis, 2009. **96**(3): p. 206-212.

155. Röhder, L.A., T. Brandt, L. Sigg, and R. Behra, *Influence of agglomeration of cerium oxide nanoparticles and speciation of cerium(III) on short term effects to the green algae Chlamydomonas reinhardtii*. Aquatic Toxicology, 2014. **152**(0): p. 121-130.

156. Scheffold, F., A. Shalkevich, R. Vavrin, J. Crassous, and P. Schurtenberger, *PCS Particle Sizing in Turbid Suspensions: Scope and Limitations*, in *Particle Sizing and Characterization*. 2004, American Chemical Society. p. 3-32.

157. Provder, T., *Challenges in particle size distribution measurement past, present and for the 21st century*. Progress in Organic Coatings, 1997. **32**(1–4): p. 143-153.

158. Brar, S.K. and M. Verma, *Measurement of nanoparticles by light-scattering techniques*. TrAC Trends in Analytical Chemistry, 2011. **30**(1): p. 4-17.

159. Poda, A.R., A.J. Bednar, A.J. Kennedy, A. Harmon, M. Hull, D.M. Mitrano, J.F. Ranville, and J. Steevens, *Characterization of silver nanoparticles using flow-field flow fractionation interfaced to inductively coupled plasma mass spectrometry*. Journal of Chromatography A, 2011. **1218**(27): p. 4219-4225.

160. Filella, M., J.W. Zhang, M.E. Newman, and J. Buffle, *Analytical applications of photon correlation spectroscopy for size distribution measurements of natural colloidal suspensions: Capabilities and limitations*. Colloids and Surfaces a-Physicochemical and Engineering Aspects, 1997. **120**(1-3): p. 27-46.

161. Baalousha, M., *Aggregation and disaggregation of iron oxide nanoparticles: Influence of particle concentration, pH and natural organic matter*. Science of the Total Environment, 2009. **407**(6): p. 2093-2101.

162. Thio, B.J.R., D.X. Zhou, and A.A. Keller, *Influence of natural organic matter on the aggregation and deposition of titanium dioxide nanoparticles*. Journal of Hazardous Materials, 2011. **189**(1-2): p. 556-563.

163. Liu, R., R. Rallo, S. George, Z.X. Ji, S. Nair, A.E. Nel, and Y. Cohen, *Classification NanoSAR Development for Cytotoxicity of Metal Oxide Nanoparticles*. Small, 2011. **7**(8): p. 1118-1126.

164. Allouni, Z.E., M.R. Cimpan, P.J. Høl, T. Skodvin, and N.R. Gjerdet, *Agglomeration and sedimentation of TiO2 nanoparticles in cell culture medium*. Colloids and Surfaces B: Biointerfaces, 2009. **68**(1): p. 83-87.

165. Tiraferri, A., K.L. Chen, R. Sethi, and M. Elimelech, *Reduced aggregation and sedimentation of zero-valent iron nanoparticles in the presence of guar gum*. Journal of Colloid and Interface Science, 2008. **324**(1-2): p. 71-79.

166. Fedele, L., L. Colla, S. Bobbo, S. Barison, and F. Agresti, *Experimental stability analysis of different water-based nanofluids*. Nanoscale Research Letters, 2011. **6**(1): p. 300.

167. Li, X.F., D.S. Zhu, and X.J. Wang, *Evaluation on dispersion behavior of the aqueous copper nano-suspensions*. Journal of Colloid and Interface Science, 2007. **310**(2): p. 456-463.

168. Hunter, R.J., *Foundations of colloid science*. 2nd ed. 2001, Oxford ; New York: Oxford University Press. xii, 806 p.

169. Chen, K.J., S.M. Wolahan, H. Wang, C.H. Hsu, H.W. Chang, A. Durazo, L.P. Hwang, M.A. Garcia, Z.K. Jiang, L. Wu, Y.Y. Lin, and H.R. Tseng, *A small MRI contrast agent*

library of gadolinium(III)-encapsulated supramolecular nanoparticles for improved relaxivity and sensitivity. Biomaterials, 2011. **32**(8): p. 2160-2165.

170. Rapaport, D.C., *The art of molecular dynamics simulation*. 2nd ed. 2004, Cambridge, UK ; New York, NY: Cambridge University Press. xiii, 549 p.

171. Schlick, T., *Molecular modeling and simulation : an interdisciplinary guide*. 2nd ed. Interdisciplinary applied mathematics. 2010, New York: Springer. xlv, 723 p.

172. Schuss, Z., *Brownian dynamics at boundaries and interfaces : in physics, chemistry, and biology*. Applied mathematical sciences,. 2013, New York: Springer. xx, 322 pages.

173. Vold, R.D. and M.J. Vold, *Colloid and interface chemistry*. 1983, Reading, Mass.: Addison-Wesley. xxv, 694 p.

174. Bell, G.M., S. Levine, and L.N. McCartney, *Approximate methods of determining the double-layer free energy of interaction between two charged colloidal spheres*. Journal of Colloid and Interface Science, 1970. **33**(3): p. 335-359.

175. Ohshima, H., *Effective Surface-Potential and Double-Layer Interaction of Colloidal Particles*. Journal of Colloid and Interface Science, 1995. **174**(1): p. 45-52.

176. Schwarzer, H.C. and W. Peukert, *Prediction of aggregation kinetics based on surface properties of nanoparticles*. Chemical Engineering Science, 2005. **60**(1): p. 11-25.

177. Brant, J., H. Lecoanet, and M.R. Wiesner, *Aggregation and deposition characteristics of fullerene nanoparticles in aqueous systems*. Journal of Nanoparticle Research, 2005. **7**(4-5): p. 545-553.

178. Chen, K.L. and M. Elimelech, *Relating Colloidal Stability of Fullerene (C60) Nanoparticles to Nanoparticle Charge and Electrokinetic Properties*. Env. Sci. & Tech., 2009. **43**(19): p. 7270-7276.

179. Gomez-Merino, A.L., F.J. Rubio-Hernandez, J.F. Velazquez-Navarro, F.J. Galindo-Rosales, and P. Fortes-Quesada, *The Hamaker constant of anatase aqueous suspensions*. Journal of Colloid and Interface Science, 2007. **316**(2): p. 451-456.

180. Visser, J., *On Hamaker constants: A comparison between Hamaker constants and Lifshitz-van der Waals constants*. Advances in Colloid and Interface Science, 1972. **3**(4): p. 331-363.

181. Ackler, H.D., R.H. French, and Y.M. Chiang, *Comparisons of Hamaker constants for ceramic systems with intervening vacuum or water: From force laws and physical properties*. Journal of Colloid and Interface Science, 1996. **179**(2): p. 460-469.

182. Kim, T., C.-H. Lee, S.-W. Joo, and K. Lee, *Kinetics of gold nanoparticle aggregation: Experiments and modeling*. Journal of Colloid and Interface Science, 2008. **318**(2): p. 238-243.

183. Zhang, W., Y. Yao, K. Li, Y. Huang, and Y. Chen, *Influence of dissolved oxygen on aggregation kinetics of citrate-coated silver nanoparticles*. Environmental Pollution, 2011. **159**(12): p. 3757-3762.

184. Brunelli, A., G. Pojana, S. Callegaro, and A. Marcomini, *Agglomeration and sedimentation of titanium dioxide nanoparticles (n-TiO2) in synthetic and real waters*. Journal of Nanoparticle Research, 2013. **15**(6): p. 1-10.

185. Magdolenova, Z., A. Collins, A. Kumar, A. Dhawan, V. Stone, and M. Dusinska, *Mechanisms of genotoxicity. A review of in vitro and in vivo studies with engineered nanoparticles*. Nanotoxicology, 2013. **8**(3): p. 233-278.

186. Garner, K. and A. Keller, *Emerging patterns for engineered nanomaterials in the environment: a review of fate and toxicity studies*. Journal of Nanoparticle Research, 2014. **16**(8): p. 1-28.

187. Limbach, L.K., R. Bereiter, E. Müller, R. Krebs, R. Gälli, and W.J. Stark, *Removal of Oxide Nanoparticles in a Model Wastewater Treatment Plant: Influence of Agglomeration and Surfactants on Clearing Efficiency*. Env. Sci. & Tech., 2008. **42**(15): p. 5828-5833.

188. Hou, L., K. Li, Y. Ding, Y. Li, J. Chen, X. Wu, and X. Li, *Removal of silver nanoparticles in simulated wastewater treatment processes and its impact on COD and NH4 reduction*. Chemosphere, 2012. **87**(3): p. 248-252.

189. Surawanvijit, S., H.H. Liu, M. Kim, and Y. Cohen, *Removal of Metal Oxide Nanoparticles from Aqueous Suspensions*. Separation Science and Technology, 2013. **49**(2): p. 161-170.

190. Orts-Gil, G., K. Natte, D. Drescher, H. Bresch, A. Mantion, J. Kneipp, and W. Österle, *Characterisation of silica nanoparticles prior to in vitro studies: from primary particles to agglomerates*. Journal of Nanoparticle Research, 2011. **13**(4): p. 1593-1604.

191. Van Oss, C.J., *Interfacial forces in aqueous media*. 2nd ed. 2006, Boca Raton, Fla.: Taylor & Francis. 438 p.

192. Pashley, R.M., *Hydration forces between mica surfaces in aqueous electrolyte solutions*. Journal of Colloid and Interface Science, 1981. **80**(1): p. 153-162.

193. Petsev, D.N. and P.G. Vekilov, *Evidence for Non-DLVO Hydration Interactions in Solutions of the Protein Apoferritin*. Physical Review Letters, 2000. **84**(6): p. 1339-1342.

194. Pashley, R.M., *DLVO and hydration forces between mica surfaces in Li+, Na+, K+, and Cs+ electrolyte solutions: A correlation of double-layer and hydration forces with surface cation exchange properties*. Journal of Colloid and Interface Science, 1981. **83**(2): p. 531-546.

195. Molina-Bolívar, J.A., F. Galisteo-González, and R. Hidalgo-Álvarez, *Colloidal stability of protein-polymer systems: A possible explanation by hydration forces*. Physical Review E, 1997. **55**(4): p. 4522-4530.

196. Pettibone, J.M., D.M. Cwiertny, M. Scherer, and V.H. Grassian, *Adsorption of Organic Acids on TiO2 Nanoparticles: Effects of pH, Nanoparticle Size, and Nanoparticle Aggregation*. Langmuir, 2008. **24**(13): p. 6659-6667.

197. Murdock, R.C., L. Braydich-Stolle, A.M. Schrand, J.J. Schlager, and S.M. Hussain, *Characterization of Nanomaterial Dispersion in Solution Prior to In Vitro Exposure*

Using Dynamic Light Scattering Technique. Toxicological Sciences, 2008. **101**(2): p. 239-253.

198. Zook, J.M., V. Rastogi, R.I. MacCuspie, A.M. Keene, and J. Fagan, *Measuring Agglomerate Size Distribution and Dependence of Localized Surface Plasmon Resonance Absorbance on Gold Nanoparticle Agglomerate Size Using Analytical Ultracentrifugation*. ACS Nano, 2011. **5**(10): p. 8070-8079.

199. Suttiponparnit, K., J. Jiang, M. Sahu, S. Suvachittanont, T. Charinpanitkul, and P. Biswas, *Role of Surface Area, Primary Particle Size, and Crystal Phase on Titanium Dioxide Nanoparticle Dispersion Properties*. Nanoscale Res Lett, 2011. **6**(1): p. 27.

200. Metin, C., R. Bonnecaze, L. Lake, C. Miranda, and Q. Nguyen, *Aggregation kinetics and shear rheology of aqueous silica suspensions*. Applied Nanoscience, 2014. **4**(2): p. 169-178.

201. Grassian, V.H., *When Size Really Matters: Size-Dependent Properties and Surface Chemistry of Metal and Metal Oxide Nanoparticles in Gas and Liquid Phase Environments†*. The Journal of Physical Chemistry C, 2008. **112**(47): p. 18303-18313.

202. Li, X. and B.E. Logan, *Collision Frequencies of Fractal Aggregates with Small Particles by Differential Sedimentation*. Env. Sci. & Tech., 1997. **31**(4): p. 1229-1236.

203. Li, X.-Y. and B.E. Logan, *Permeability of Fractal Aggregates*. Water Research, 2001. **35**(14): p. 3373-3380.

204. Johnson, C.P., X. Li, and B.E. Logan, *Settling Velocities of Fractal Aggregates*. Env. Sci. & Tech., 1996. **30**(6): p. 1911-1918.

205. Virtanen, A., J. Ristimäki, and J. Keskinen, *Method for Measuring Effective Density and Fractal Dimension of Aerosol Agglomerates*. Aerosol Science and Technology, 2004. **38**(5): p. 437-446.

206. Rogak, S.N. and R.C. Flagan, *Stokes drag on self-similar clusters of spheres*. Journal of Colloid and Interface Science, 1990. **134**(1): p. 206-218.

207. Lee, D.J., G.W. Chen, Y.C. Liao, and C.C. Hsieh, *On the free-settling test for estimating activated sludge floc density*. Water Research, 1996. **30**(3): p. 541-550.

208. Veerapaneni, S. and M.R. Wiesner, *Hydrodynamics of Fractal Aggregates with Radially Varying Permeability*. Journal of Colloid and Interface Science, 1996. **177**(1): p. 45-57.

209. Woodfield, D. and G. Bickert, *An improved permeability model for fractal aggregates settling in creeping flow*. Water Research, 2001. **35**(16): p. 3801-3806.

210. Gmachowski, L., *Transport properties of fractal aggregates calculated by permeability*. Colloids and Surfaces A: Physicochemical and Engineering Aspects, 2003. **215**(1–3): p. 173-179.

211. Quik, J.T.K., I. Lynch, K.V. Hoecke, C.J.H. Miermans, K.A.C.D. Schamphelaere, C.R. Janssen, K.A. Dawson, M.A.C. Stuart, and D.V.D. Meent, *Effect of natural organic matter on cerium dioxide nanoparticles settling in model fresh water*. Chemosphere, 2010. **81**(6): p. 711-715.

212. Wang, X., Z. Ji, C.H. Chang, H. Zhang, M. Wang, Y.-P. Liao, S. Lin, H. Meng, R. Li, B. Sun, L.V. Winkle, K.E. Pinkerton, J.I. Zink, T. Xia, and A.E. Nel, *Use of Coated Silver Nanoparticles to Understand the Relationship of Particle Dissolution and Bioavailability to Cell and Lung Toxicological Potential*. Small, 2014. **10**(2): p. 385-398.

213. Fröhlich, E., G. Bonstingl, A. Höfler, C. Meindl, G. Leitinger, T.R. Pieber, and E. Roblegg, *Comparison of two in vitro systems to assess cellular effects of nanoparticles-containing aerosols*. Toxicology in Vitro, 2013. **27**(1): p. 409-417.

214. Nymark, P., K. Jensen, S. Suhonen, Y. Kembouche, M. Vippola, J. Kleinjans, J. Catalan, H. Norppa, J. van Delft, and J. Briede, *Free radical scavenging and formation by multi-walled carbon nanotubes in cell free conditions and in human bronchial epithelial cells*. Particle and Fibre Toxicology, 2014. **11**(1): p. 4.

215. Zhang, H.Y., Z.X. Ji, T. Xia, H. Meng, C. Low-Kam, R. Liu, S. Pokhrel, S.J. Lin, X. Wang, Y.P. Liao, M.Y. Wang, L.J. Li, R. Rallo, R. Damoiseaux, D. Telesca, L. Madler, Y. Cohen, J.I. Zink, and A.E. Nel, *Use of Metal Oxide Nanoparticle Band Gap To Develop a Predictive Paradigm for Oxidative Stress and Acute Pulmonary Inflammation*. Acs Nano, 2012. **6**(5): p. 4349-4368.

216. Lowry, G.V., K.B. Gregory, S.C. Apte, and J.R. Lead, *Transformations of Nanomaterials in the Environment*. Env. Sci. & Tech., 2012. **46**(13): p. 6893-6899.

217. Liu, J., K.G. Pennell, and R.H. Hurt, *Kinetics and Mechanisms of Nanosilver Oxysulfidation*. Env. Sci. & Tech., 2011. **45**(17): p. 7345-7353.

218. Liu, Y., S.A. Majetich, R.D. Tilton, D.S. Sholl, and G.V. Lowry, *TCE Dechlorination Rates, Pathways, and Efficiency of Nanoscale Iron Particles with Different Properties*. Env. Sci. & Tech., 2005. **39**(5): p. 1338-1345.

219. Hou, W.-C. and C.T. Jafvert, *Photochemical Transformation of Aqueous C60 Clusters in Sunlight*. Env. Sci. & Tech., 2008. **43**(2): p. 362-367.

220. Arvidsson, R., S. Molander, B.A. Sandén, and M. Hassellöv, *Challenges in Exposure Modeling of Nanoparticles in Aquatic Environments*. Human and Ecological Risk Assessment: An International Journal, 2011. **17**(1): p. 245 - 262.

221. Friedlander, S.K. and C.S. Wang, *Self-Preserving Particle Size Distribution for Coagulation by Brownian Motion*. Journal of Colloid and Interface Science, 1966. **22**(2): p. 126-&.

222. Farley, K.J. and F.M.M. Morel, *Role of Coagulation in the Kinetics of Sedimentation*. Env. Sci. & Tech., 1986. **20**(2): p. 187-195.

223. Spicer, P.T. and S.E. Pratsinis, *Coagulation and fragmentation: Universal steady-state particle-size distribution*. Aiche Journal, 1996. **42**(6): p. 1612-1620.

224. Walther, C., S. Büchner, M. Filella, and V. Chanudet, *Probing particle size distributions in natural surface waters from 15 nm to 2 μm by a combination of LIBD and single-particle counting*. Journal of Colloid and Interface Science, 2006. **301**(2): p. 532-537.

225. Reynolds, R.A., D. Stramski, V.M. Wright, and S.B. Woźniak, *Measurements and characterization of particle size distributions in coastal waters*. Journal of Geophysical Research: Oceans, 2010. **115**(C8): p. C08024.

226. Walling, D.E. and P.W. Moorehead, *The particle size characteristics of fluvial suspended sediment: an overview*. Hydrobiologia, 1989. **176-177**(1): p. 125-149.

227. Jacobs, M.B. and M. Ewing, *Suspended Particulate Matter: Concentration in the Major Oceans*. Science, 1969. **163**(3865): p. 380-383.

228. Susfalk, R.B., B. Fitzgerald, and A.M. Knust, *Characterization of Turbidty and Total Suspended Solids in the Upper Carson River, Navada*, N.D.o.E. Protection, 2008,

229. Ryan, P., *Review of mathematical models for health risk assessment: IV. Intermedia chemical transport*. Environmental Software, 1993. **8**(3): p. 157-172.

230. Darlington, T.K., A.M. Neigh, M.T. Spencer, O.T. Nguyen, and S.J. Oldenburg, *Nanoparticle Characteristics Affecting Environmental Fate and Transport through Soil*. Env. Tox. & Chem., 2009. **28**(6): p. 1191-1199.

231. Jaisi, D.P. and M. Elimelech, *Single-Walled Carbon Nanotubes Exhibit Limited Transport in Soil Columns*. Env. Sci. & Tech., 2009. **43**(24): p. 9161-9166.

232. ECB, *Technical Guidance Document on Risk Assessment*, 2003, European Chemicals Bureau. Institute for Health and Consumer Protection. European Commission

233. Priester, J.H., Y. Ge, R.E. Mielke, A.M. Horst, S.C. Moritz, K. Espinosa, J. Gelb, S.L. Walker, R.M. Nisbet, Y.-J. An, J.P. Schimel, R.G. Palmer, J.A. Hernandez-Viezcas, L. Zhao, J.L. Gardea-Torresdey, and P.A. Holden, *Soybean susceptibility to manufactured nanomaterials with evidence for food quality and soil fertility interruption*. Proceedings of the National Academy of Sciences, 2012. **109**(37): p. E2451–E2456.

234. Rico, C.M., S. Majumdar, M. Duarte-Gardea, J.R. Peralta-Videa, and J.L. Gardea-Torresdey, *Interaction of Nanoparticles with Edible Plants and Their Possible Implications in the Food Chain*. Journal of Agricultural and Food Chemistry, 2011. **59**(8): p. 3485-3498.

235. Holzworth, G.C., *Mixing Depths, Wind Speeds and Air Pollution Potential for Selected Locations in the United States*. Journal of Applied Meteorology, 1967. **6**(6): p. 1039-1044.

236. Asner, G.P., J.M.O. Scurlock, and J. A. Hicke, *Global synthesis of leaf area index observations: implications for ecological and remote sensing studies*. Global Ecology and Biogeography, 2003. **12**(3): p. 191-205.

237. Breuer, L., K. Eckhardt, and H.-G. Frede, *Plant parameter values for models in temperate climates*. Ecological Modelling, 2003. **169**(2–3): p. 237-293.

238. Hairer, E., S.P. Nørsett, and G. Wanner, *Solving ordinary differential equations*. Springer series in computational mathematics. 1987, Berlin ; New York: Springer-Verlag.

239. Simcik, M.F., T.P. Franz, H. Zhang, and S.J. Eisenreich, *Gas-Particle Partitioning of PCBs and PAHs in the Chicago Urban and Adjacent Coastal Atmosphere: States of Equilibrium*. Env. Sci. & Tech., 1998. **32**(2): p. 251-257.

240. Pirrone, N., G.J. Keeler, and T.M. Holsen, *Dry Deposition of Semivolatile Organic-Compounds to Lake Michigan*. Env. Sci. & Tech., 1995. **29**(8): p. 2123-2132.

241. Ryan, P.A. and Y. Cohen, *Multimedia transport of particle-bound organics: Benzo(a)Pyrene test case*. Chemosphere, 1986. **15**(1): p. 21-47.

242. Yaffe, D., Y. Cohen, J. Arey, and A.J. Grosovsky, *Multimedia Analysis of PAHs and Nitro-PAH Daughter Products in the Los Angeles Basin*. Risk Analysis, 2001. **21**: p. 275-294.

243. Harrison, R.M., D.J.T. Smith, and L. Luhana, *Source apportionment of atmospheric polycyclic aromatic hydrocarbons collected from an urban location in Birmingham, UK*. Env. Sci. & Tech., 1996. **30**(3): p. 825-832.

244. USEPA - Fate Exposure and Risk Analysis Group, *Total Risk Integrated Methodology. TRIM.Expo Technical Support Document. External Review Draft (EPA-453/D-99-001)*, USEPA - Fate Exposure and Risk Analysis Group, 1999, USEPA

245. ICF Consulting, *Air Toxics Risk Assessment Reference Library*, USEPA, Office of Air Quality Planning and Standards, 2004, USEPA

246. Albert, R., *Multimedia approaches to pollution control: a symposium proceedings*, National Research Council, Committee on Multimedia Approaches to Pollution Control, Board on Environmental Studies Toxicology, Commission on Physical Sciences, Mathematics, Resources, 1987, National Academy Press

247. California Environmental Protection Agency (CalEPA), *CalTox: A multimedia total exposure model for hazardous-waste sites*, Department of Toxic Substance Control and Office of Scientific Affairs, 1993,

248. *National Climatic Data Center*, 2013, National Oceanic And Atmospheric Admiinstration.

249. USCB, *United States Census Bureau QuickFacts*, 2012, United States Census Bureau.

250. Keller, A.A. and A. Lazareva, *Predicted Releases of Engineered Nanomaterials: From Global to Regional to Local*. Env. Sci. & Tech. Letters, 2013.

251. Hendren, C.O., X. Mesnard, J. Dröge, and M.R. Wiesner, *Estimating Production Data for Five Engineered Nanomaterials As a Basis for Exposure Assessment*. Env. Sci. & Tech., 2011. **45**(7): p. 2562-2569.

252. Piccinno, F., F. Gottschalk, S. Seeger, and B. Nowack, *Industrial production quantities and uses of ten engineered nanomaterials in Europe and the world*. Journal of Nanoparticle Research, 2012. **14**(9): p. 1-11.

253. USEPA. *Water: Sewage Sludge (Biosolids) Frequently Asked Questions*. 2012 10/08/2013]; Available from: http://water.epa.gov/polwaste/wastewater/treatment/biosolids/genqa.cfm.

254. Palmer, D.A. and P. Bénézeth, *Solubility of Copper Oxides in Water and Steam*. Proceedings of the 14th Int'l Conf on the Properties of Water and Steam, 2004: p. 491-496.

255. World Health Organization, *Zinc in Drinking-water, Background document for development of WHO Guidelines for Drinking-water Quality,*, World Health Organization, 1996,

256. *The World Factbook*, 2013, Central Intelligence Agency.

257. Van de Water, R.B., *Modeling the Transport and Fate of Volatile and Semi-volatile Organics in a Multimedia Environment*. 1995: University of California, Los Angeles.

258. United Nations, *Municipal waste treatment*, 2011, United Nations Statistics Division.

259. *Human Development Reports 2012. International Human Development Indicators: Inequality-adjusted HDI value.*, in *United Nations Development Programme*.2012: United Nations: New York.

260. NOAA, *Daily Observational Data: Global Summary of the Day (GSOD)*, National Oceanic and Atmospheric Administration.

261. American Meteorological Society, *Rain*, in *Glossary of Meteorology*2000.

262. *Fact sheet No. 3 - Water in the atmosphere*, N.M.L.a. Archive, 2011, Met Office

263. Cohen, Y. and P.A. Ryan, *Multimedia modeling of environmental transport: trichloroethylene test case*. Env. Sci. & Tech., 1985. **19**(5): p. 412-417.

264. Holden, P.A., F. Klaessig, R.F. Turco, J.H. Priester, C.M. Rico, H. Avila-Arias, M. Mortimer, K. Pacpaco, and J.L. Gardea-Torresdey, *Evaluation of Exposure Concentrations Used in Assessing Manufactured Nanomaterial Environmental Hazards: Are They Relevant?* Env. Sci. & Tech., 2014. **48**(18): p. 10541-10551.

265. Dale, A.L., G.V. Lowry, and E.A. Casman, *Modeling Nanosilver Transformations in Freshwater Sediments*. Env. Sci. & Tech., 2013. **47**(22): p. 12920-12928.

266. Kaegi, R., A. Ulrich, B. Sinnet, R. Vonbank, A. Wichser, S. Zuleeg, H. Simmler, S. Brunner, H. Vonmont, M. Burkhardt, and M. Boller, *Synthetic TiO2 nanoparticle emission from exterior facades into the aquatic environment*. Environmental Pollution, 2008. **156**(2): p. 233-239.

267. Park, B., K. Donaldson, R. Duffin, L. Tran, F. Kelly, I. Mudway, J.-P. Morin, R. Guest, P. Jenkinson, Z. Samaras, M. Giannouli, H. Kouridis, and P. Martin, *Hazard and Risk Assessment of a Nanoparticulate Cerium Oxide-Based Diesel Fuel Additive—A Case Study*. Inhalation Toxicology, 2008. **20**(6): p. 547-566.

268. Clay, E.R., *Multimedia Environmental Distribution of Gaseous, Dissolved, and Particle-bound Pollutants*, in *Department of Chemical Engineering*1992, University of California, Los Angeles: Los Angeles. p. 302.

269. Tranter, M., *Annual Bus Statistics: England 2012/13*, U.D.f. Transport, 2013,

270. Norton, P., *Demonstration of Caterpillar C-10 Dual-Fuel Engines in MCI 102DL3 Commuter Buses*, 2000, Natinoal Renewable Energy Laboratory: Golden, CO.

271. Office for National Statistics, *Population Estimates for UK, England and Wales, Scotland and Northern Ireland, Mid-2011 and Mid-2012*, 2013.

272. Office for National Statistics, *Census result shows increase in population of the North East*, 2012.

273. Khan, S., *Sub-national road transport fuel consumption statistics*, UK Department of Energy & Climate Change, 2012,

274. Atkinson, R., J. Arey, A.M. Winer, and B. Zielinska, *Ambient Concentrations of Polycyclic Aromatic Hydrocarbons (PAHs) at Selected Locations in California*, California Environmental Protection Agency and Air Resource Board, 1989,

275. Department for Transport, U., *Road Traffic Estimates 2010 (Revised)*, U. Department for Transport, 2010,

276. Marr, L.C., T.W. Kirchstetter, R.A. Harley, A.H. Miguel, S.V. Hering, and S.K. Hammond, *Characterization of Polycyclic Aromatic Hydrocarbons in Motor Vehicle Fuels and Exhaust Emissions*. Env. Sci. & Tech., 1999. **33**(18): p. 3091-3099.

277. Pirrone, N., G.J. Keeler, and T.M. Holsen, *Dry Deposition of Semivolatile Organic Compounds to Lake Michigan*. Env. Sci. & Tech., 1995. **29**(8): p. 2123-2132.

278. Hermanson, M.H., E.R. Christensen, D.J. Buser, and L.-M. Chen, *Polychlorinated Biphenyls in Dated Sediment Cores from Green Bay and Lake Michigan*. Journal of Great Lakes Research, 1991. **17**(1): p. 94-108.

279. Bank, T.W., *Average precipitation in depth (mm per year)*, 2013, The World Bank.

280. Aschberger, K. and F.M. Christensen, *Approaches for establishing human health no effect levels for engineered nanomaterials*. Journal of Physics: Conference Series, 2011. **304**(1): p. 012078.

281. Liu, R., H.Y. Zhang, Z.X. Ji, R. Rallo, T. Xia, C.H. Chang, A. Nel, and Y. Cohen, *Development of structure-activity relationship for metal oxide nanoparticles*. Nanoscale, 2013. **5**(12): p. 5644-5653.